TIARA-REP-WP9-2014-006

Test Infrastructure and Accelerator Research Area

Status Report

Technical Design Report of the Multi-MW test Irradiation Facility

Samec, K. (CERN) *et al*

11 February 2014

The research leading to these results has received funding from the European Commission under the FP7-INFRASTRUCTURES-2010-1/INFRA-2010-2.2.11 project TIARA (CNI-PP). Grant agreement no 261905.

This work is part of TIARA Work Package **9: TIHPAC R&D Infrastructure**.

The electronic version of this TIARA Publication is available via the *TIARA web site* at `http://www.eu-tiara.eu/database` or on the *CERN Document Server* at the following URL: `http://cds.cern.ch/search?p=TIARA-REP-WP9-2014-006`

Test Infrastructure and Accelerator Research Area

Final Report

Technical Design Report of the Multi-MW test Irradiation Facility T-MIF

K. Samec; Y. Kadi; Y. Fusco; R. Luis; M. Behzad; Y. Romanets

(CERN)

27. February 2014

The research leading to these results has received funding from the European Commission under the FP7-INFRASTRUCTURES-2010-1/INFRA-2010-2.2.11 project TIARA (CNI-PP).

Grant agreement no 261905.

This work is part of TIARA Work Package 9: TIHPAC R&D Infrastructure. The electronic version of this TIARA Publication is available on the TIARA web site at:

http://www.eu-tiara.eu/database

or on the CERN Document Server at the following URL:

http://cdsweb.cern.ch/search?p=TIARA-REP-WP9-2014-006

TIARA Project

Work Package 9: TIHPAC - Test Infrastructure for High Power Accelerator Components

Task 9.1: Multi MW Irradiation Facility for complex target testing

Deliverable D9.1: TDIF Technical Design Report of the Multi-MW test Irradiation Facility T-MIF

Planned Date (month):36

Achieved Date (month):38

Lead Contractor:CERN

Project acronym:	*TIARA*
Project full title:	*Test Infrastructure in Accelerator Research Area*
Start of the Project:	*1st January 2011*
Duration of the project:	*36 Months*
TDIF Author:	*Karel Samec*
	Nucl.&. Mech. Eng.
	CERN associate
Task Coordinator:	*Yacine Kadi*
	Prof. Dr. Phys.
	CERN staff physicist

Contents

F i g u r e s

T a b l e s

R e f e r e n c e s

Ref. 1: K. Samec: "Report on the Definition and Specifications of the Irradiation test Facilities", TIARA-REP-WP9-2012-001, FP7-Infrastructures-2010-1/INFRA-2010-2.2.11 project TIARA, 23 January 201

Ref. 2: K. Samec: "Preliminary Design report of the high power Irradiation test Facility", Milestone MS34, 25. February 2013

Ref. 3: Y. Fusco: "Detail Engineering Design T-MIF", 2. February 2014

Ref. 4: Y. Fusco, M. Behzad: "Thermal-hydraulic analysis of the neutron source for T-MIF", NT02, 10. February 2014

Ref. 5: R. Luis, Y. Romanets: "Neutronics FLUKA analysis of the Target section for T-MIF", NT03, 2. February 2014

Ref. 6: Y. Dai et al.: "FeCrAlY and TiN coatings on T91 steel after irradiation with 72 MeV protons in flowing LBE" , Journal of Nuclear Materials, Volume 431, Issues 1–3, December 2012, Pages 66–76

Ref. 7: K. Samec: "Analysis of the Lisor Experiment", PSI technical report TM-34-05-02, 7 March 2005

Ref. 8: Y. Dai et al.: "Tensile tests and TEM investigations on LiSoR-2 to -4", Journal of Nuclear Materials, Volume 356, Issues 1–3, September 2006, Pages 256–263

Ref. 9: F. Gröschel: MEGAPIE – A liquid target at SINQ, Workshop on High-Power Targetry for Future Accelerators, Ronkonkoma, 8.-12.9.2003

Ref. 10: K. Samec et. al. : "Designing Safety into a High-power Neutron Spallation Source" , Proceedings of ICAPP 2011, Nice, France, May 2-5, 2011

S y m b o l s

Parameters, variables and abbreviations:

CEA	Abbr.	Commissariat à l'Energie Atomique, France
CERN	Abbr.	Centre Européen de la Recherche Nucléaire, Switzerland
C_P	[J/kg/K]	Thermal capacity
CFD	Abbr.	Computational Fluid Dynamics
DPA	Abbr.	Displacement per atom
E	[MeV]	Beam energy
ESS	Abbr	European Spallation Source
FEM	Abbr.	Finite Element Method
f	[Hz]	Frequency
I	[mA]	Current
INFN	Abbr.	Instituto Nazionale de Fisica Nucleare, Italy
IPUL	Abbr.	Institute of Physics of the University of Latvia, Latvia
JAEA	Abbr	Japan Atomic Energy Agency
LBE	Abbr.	Lead Bismuth Eutectic
LM	Abbr.	Liquid Metal
p	[Bar]	Pressure
P	[W]	Beam Power
PSI	Abbr.	Paul Scherrer Institute, Switzerland
RCCMR	Abbr.	CEA design rules for mechanical components of FBR nuclear islands
T	[°C]	Temperature
t	[sec.]	Time
Δ	[-]	Discrete difference, change
ϕ	[$n/cm^3/s$]	Neutron flux
λ	[W/m/s]	Thermal conductivity
ρ	[kg/m^3]	Density
σ	[N/mm^2]	Stress
$\sigma_{x,y}$	[mm]	Gaussian half width

Executive Summary

Within the framework of the TIARA project, applications of accelerator technology has been investigated, which would benefit society and encourage progress in such diverse areas of technology as material science, medical sciences, or energy research. The design of a facility able to test materials under high irradiation doses is proposed as it will result in many possible applications in different areas of interest to science. Concentrating a high neutron flux over a small volume will be of interest to material studies, fundamental physics or radiopharmaceutical production. By sufficiently shielding the facility, an implementation in existing dedicated laboratories can be envisaged, which prioritises safety in order to fulfil rapidly regulatory requirements.

Overview of the proposed facility:

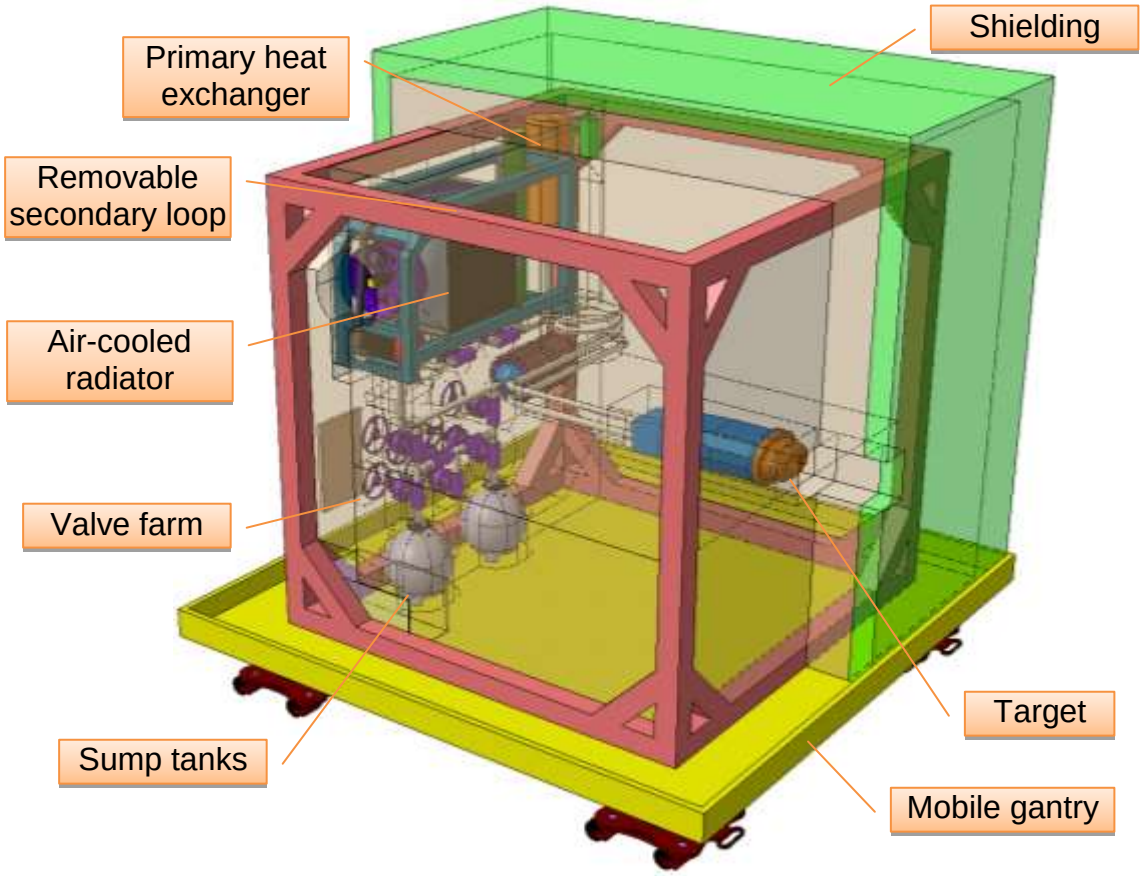

The heat deposited by the beam in the target is transferred by the primary fluid to a secondary fluid, Gallium in the secondary loop which is self-contained and detachable. The secondary loop is itself cooled by air blown through the fins of a radiator.

Testing section:

The facility comprises in its centre the spallation target containing liquid metal, in this case lead, which when hit by a proton beam emits spallation neutrons. Samples are placed in the centre of this spallation zone to maximise the DPA.

DPA production is maximised by orienting the samples in such a way that they are impacted side-on by a beam whose elliptical cross-section maximises irradiation in the samples.

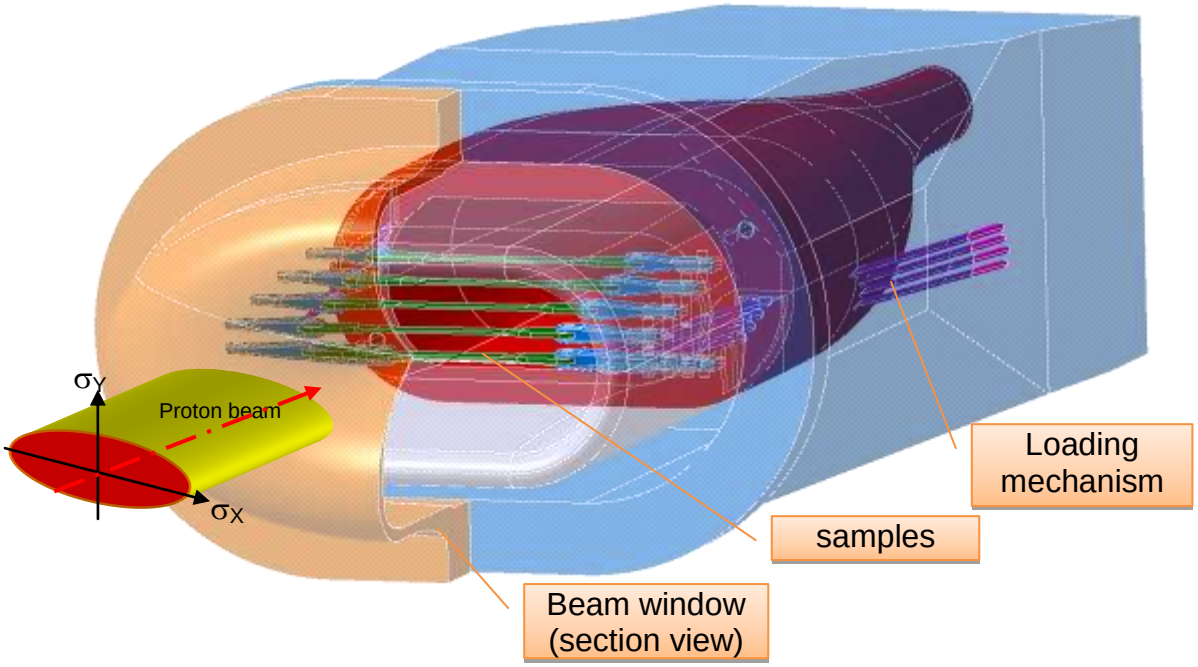

Expected irradiation performance in the samples

The neutronics analysis has focused on increasing the DPA in the samples by optimising the beam. The beam parameters have been varied with respect to energy, current and dimensions. Also different combinations of materials around the target have been studied. The beam has by far the greatest influence. An optimum is found with:

- Beam energy 200 MeV
- Beam cross section 1: 1.7 (height to width)

With such parameters and a beam power of 100 kW, a maximum of 25.7 DPA per annum can be reached in the most irradiated sample, the one closest to the beam window, using a beam energy of 200 MeV, a current of 500 μA and a beam spot of 1.7cm x 1.0cm. The long axis of the beam spot is parallel to the sample. The table below shows the average yearly DPAs over the sample for different settings of the beam. The figure alongside the table shows an example of the DPA mapping corresponding to the first column in the table and a period of one month. A more equal distribution of DPA would be achieved with a 400 MeV beam (middle column) and 200 MeV gives the highest DPA.

	DPA per year (stat. uncertainty < 1%)		
Beam spot	σ_X : 6 cm σ_Y : 1 cm	σ_X : 1.7 cm σ_Y : 1 cm	
Sample	600 MeV 166 μA	400 MeV 250 μA	200 MeV 500 μA
1	8.8	23.0	25.7
2	6.0	13.9	1.7
3	4.1	8.3	1.0
4	2.9	5.0	0.6

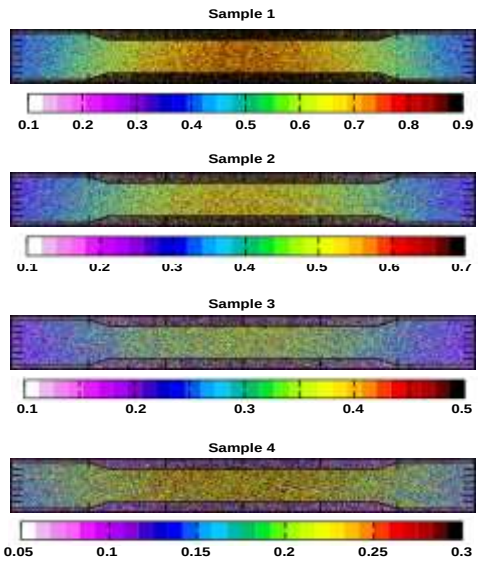

The ratio of DPA attributable to protons versus neutrons can vary quite considerably from one sample to the next, in some configurations 80% of the DPAs are due to protons in others 80% of DPA are due to neutrons. This gives the researcher great flexibility in choosing parameters in his material investigation.

Application to Fusion materials

Another significant achievement of the design is its ability to reproduce the spectrum required for the ITER development. This is demonstrated in the figure below where the spectrum of the T-MIF facility is compare against that of IFMIF (the ITER test facility) and MTS a 1 MW facility proposed by LANL. The baseline 100 kW version and a 1 MW high power version of T-MIF have been plotted; indeed although the design is documented for 100 kW the critical items such as the target and heat exchanger are easily adaptable to 1 MW. The figure demonstrates how the 100 kW version of T-MIF reaches the same values as the 1 MW facility MTS. And likewise the 1 MW version of T-MIF delivers the same spectrum and neutron flux intensity as the 5 MW IFMIF. The two curves for a 100 kW and 1 MW version of T-MIF envelop completely 90% of the spectrum that is sought for the DEMO pilot plant of ITER.

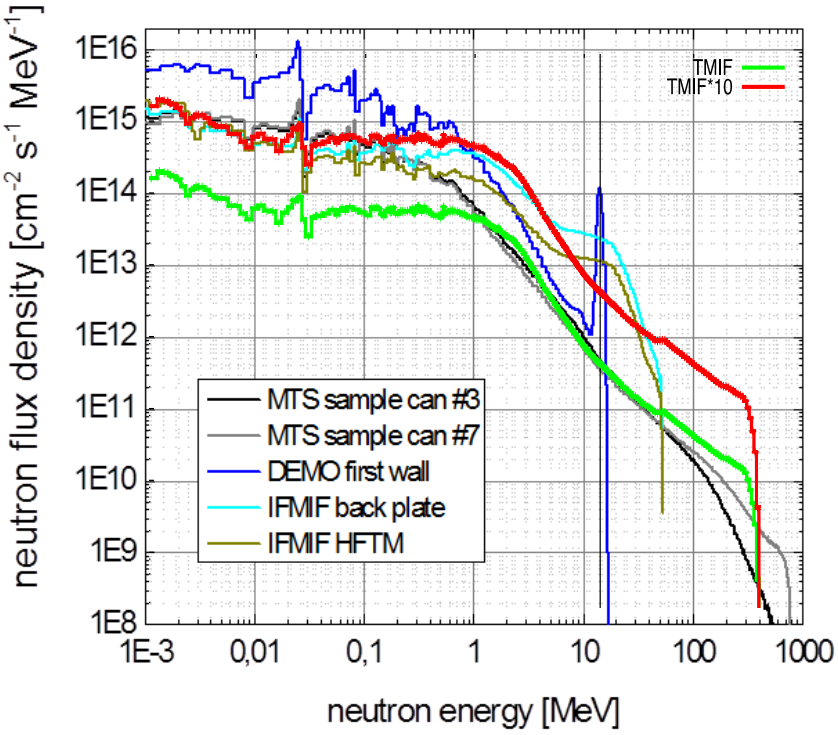

Safety considerations

Multiple containment strategies are implemented to prevent contamination from leaking out of the central spallation target. The spallation target itself possess high margins against safety, particularly on the window where stresse are well below allowable values, even at high irradiation doses. The primary heat exchanger between the primary and secondary loop has no common wall, such that any leak from one circuit does not penetrate into the neighbouring circuit, but instead enters a thin gap, where the leak can be immediately detected.

The T91 beam window has been proven to possess significat safety margins, due to very low stresses and allowing for effects such as increased radiation temperature embrittlement and lower strength at higher temperature.

The position of the primary heat exchanger above the target entails that in the event of a pump failure, the flow of cooling liquid metal would coast down gently, entrained by natural circulation since

the cold source is above the heat source. By having the target in a low position the effect of a primary LOCA is also mitigated since the liquid will first drain out of the primary circuit above the target leaving the target filled for a sufficiently long time to switch off the beam.

A significant effort was aimed at reducing the dose rates around the installation. During operation, the T-MIF facility would be housed inside a shielded laboratory. The use of a succession of different material layers has allowed the designers to significantly reduce the doses around the facility during operation even if shielded laboratory walls will still be needed. Reducing the beam energy also yields a significant improvement, since the DPAs remain quite high and more balance between the samples is achieved. This would be a strong argument in favour of a 200 MeV / 500μA beam.

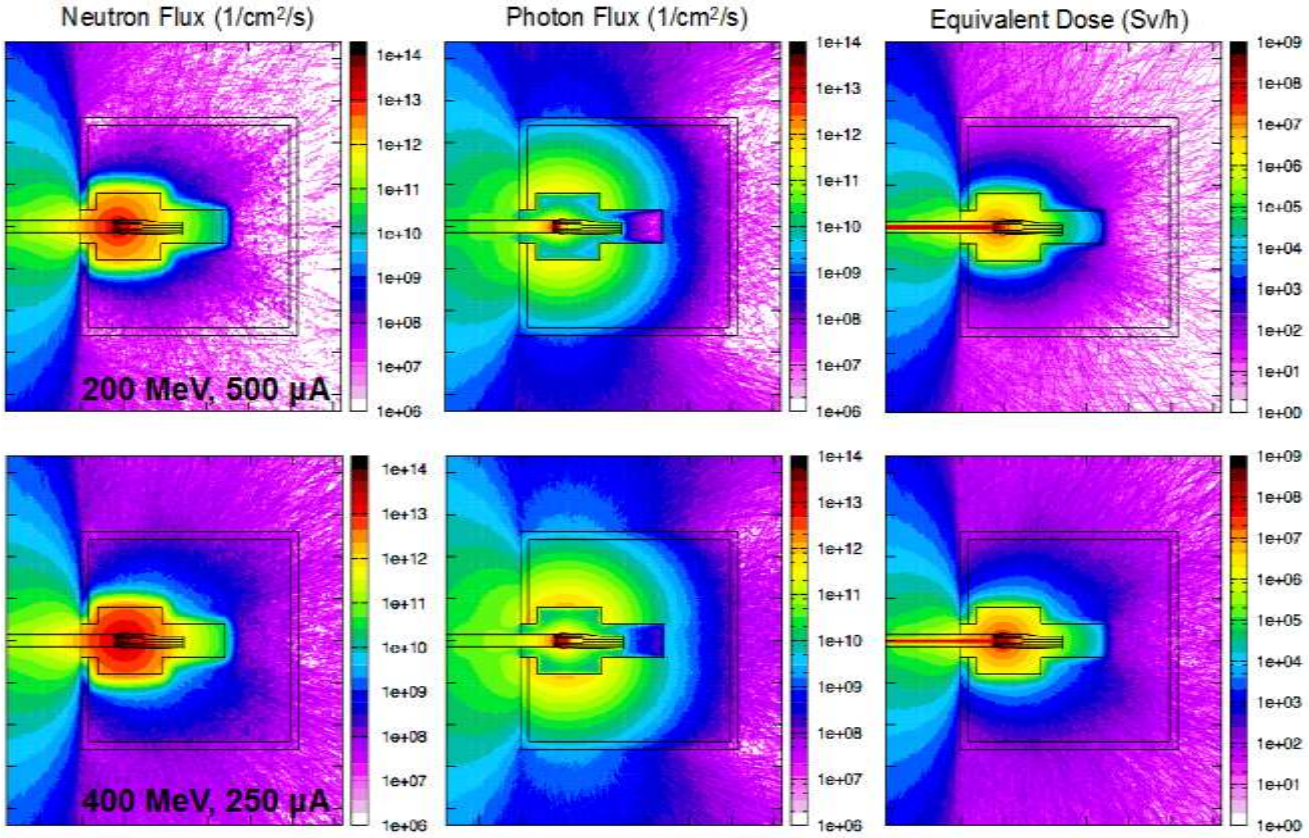

After operation, the activated primary fluid would be stored in heavily shielded tanks located inside the facility and the sample holder containing the samples would be withdrawn rapidly from the facility using robotics. The dose rates are compatible with such operations after a cooling period of a day. This would allow rapid reloading of the T-MIF with fresh samples, thus gaining a high level of availability.

Conclusions

A design for building a compact flexible facility allowing testing of samples at high dose rates is proposed with an overall budget of 7.5 M€ required for full-scale development over a period of three years. Possible applications include materials for Gen IV reactors, Accelerator-Driven Systems or the ITER program. Further developement towards the production of commercial-grade isotopes using an accelerator-based facility could be envisaged.

1 Scope of the project

1.1 Project specifications

In its early stages, the project examined various options for applying target technology to purposes that were deemed to be of general interest not only to the nuclear and physics research community but would also be of interest to industries such as the radio-pharmaceutical industry. A first specification document (Ref. 1) summed up the possible uses of target technology and centred on materials research. Subsequently, a proposal was put forward (Ref. 2) with a design which could possibly fulfil the specification.

The specification laid out a facility which would irradiate samples side-on with a steady static beam. Such a configuration is estimated to be more efficient than painting the sample with a mobile beam, such as in Lisor (Ref. 7). The required level of DPA was derived from the Megapie experience (Ref. 8 & 9) and an overall layout was proposed which would take into account the accumulated lessons from the past 10 years of liquid metal spallation source development in projects such as Megapie and Eurisol (Ref. 10). The environment needing to be reproduced with this facility should thus include at least:

- Neutron irradiation > 10 DPA total n+p
- Proton irradiation > 10 DPA total n+p
- Stress static/cyclic > 500 MPa
- Corrosion from liquid metal Lead or LBE
- High temperature 400-600°C

After a review of similar installations and in light of past experience, the parameters of the proton beam and circuits were chosen as follows:

Particles	Protons
Kinetic Energy	200MeV - 1 GeV
Beam shape	Elliptical cross-section σ_x / σ_y = 1.7 to 6 Parabolic density distribution
Current	< 500 μA
Power	100 kW in beam (70 kW thermal)

Table 1: Characteristics of the beam

Primary circuit and Spallation source inventory	Lead or LBE < 15 litre (150 kg)
Secondary circuit inventory	Gallium < 5 litre (25 kg)
Cold Source – open inventory	Air
Saturation radioactivity in primary	~ 20 - 30 TBq / kg
Decay Heat in primary	~ 1 - 2 W / kg
Neutron Flux density	~ 10^{13} n / cm^2 s

Table 2: Characteristics of the circuits

In addition to providing a facility for testing materials and sensors under high irradiation, the dense neutron flux in the facility could also be used for isotope production. This aspect was not covered in the present design study but it is entirely plausible, as the magnitude of the neutron flux in the core spallation region of the neutron source is similar to that of power reactors which are used for isotope production.

1.2 Project structure

The current design study is aimed at obtaining a design which is sufficiently mature to allow its evaluation by a review panel in order to determine whether it may justify further development. The design study is therefore focused on answering the following questions;

1. Can the samples be irradiated under the desired conditions?

2. Is the performance of all the systems in the facility attainable using existing technology?

3. Is the facility safe to operate?

4. What are the likely development costs?

The design proposed in Ref.2 has therefore been analysed in a series of iterative steps, focusing on distinct aspects such as structural mechanics, thermal hydraulics and neutronics, as outlined in the figure below. Inevitably, as one aspect is optimised, the design is changed; whereupon this change has an impact on another aspect. The iterations between the various specialties are therefore highly interdependent and need careful coordination

A typical example of such interdependence is the shielding which modifies not only the dose rate outside the facility but also the spectrum of the neutron field inside the sample irradiation area and hence the amount of DPA: Equally routing the piping through another area of the facility to help with shielding, changes the flow parameters in the primary circuit.

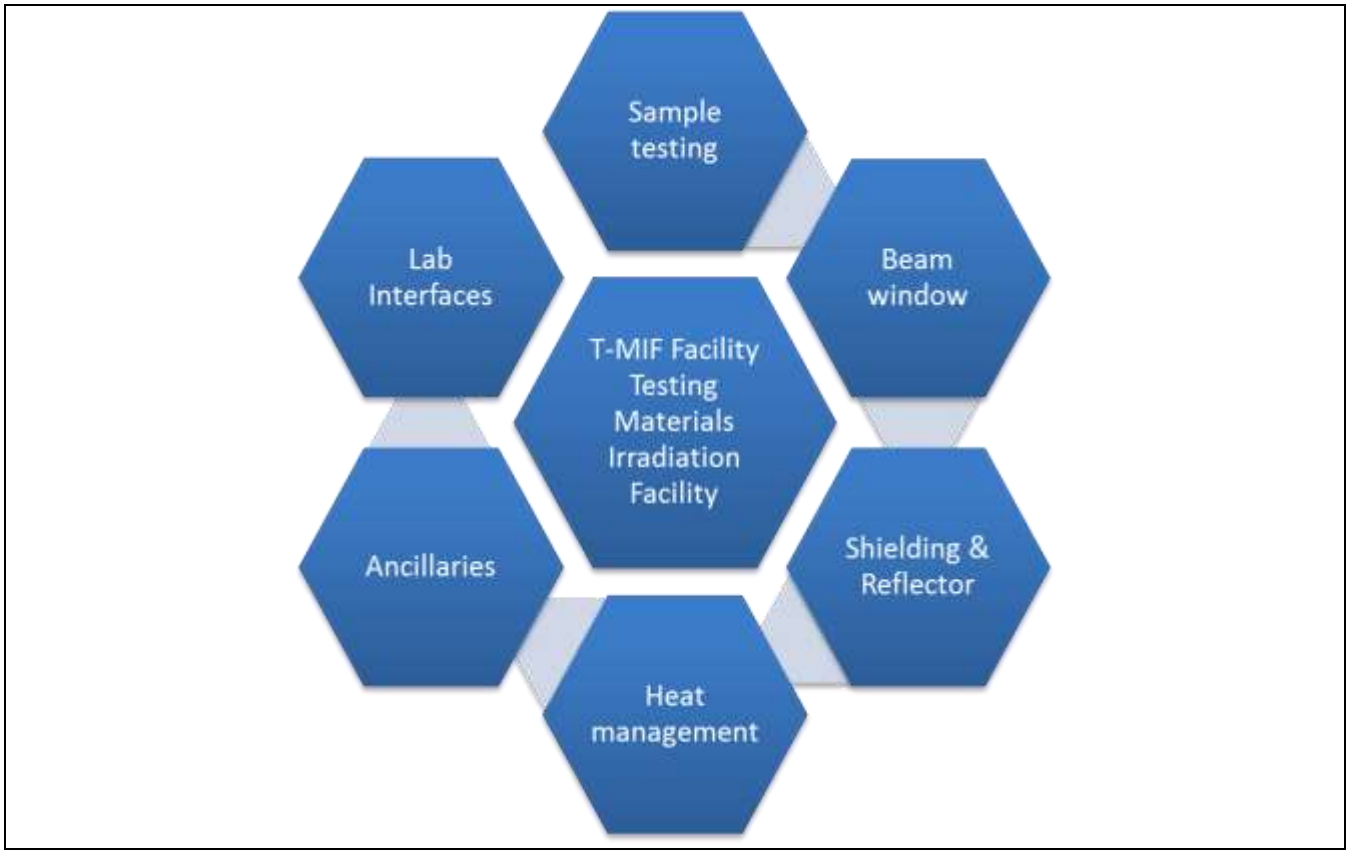

Figure 1: Iterative process

1.3 Project goals

Distinct work packages were therefore given to specialists in each field. Their work is documented in References 3, 4, 5. For convenience, the sum of this work has been integrated in the current report; it forms the essential argument in answering the questions posed here-above.

1. The sample irradiation dose rate may be found in section 2.13. They clearly exceed 10 DPA per annum as required. Furthermore the neutron spectrum is quite close to the requirements of projects such as IFMIF; refer to Figure 72.

2. The neutron source hydraulic performance is examined in chapter 4 and the heat exchanger performance in section 3.2.6 . These are deemed the most critical items of the T-MIF facility.

3. Shielding studies performed in section 2.9 indicate the facility can be operated in a suitable laboratory. The analysis of stresses in the beam window shows they remain below critical values (chapter 5.1). Typical accident cases studies were assessed qualitatively in section 3.4 and, although still requiring numerical analysis, do not raise any cause for concern.

4. Section 0 indicates development costs are well below 10 M€ if the participating institutes can share their existing resources in manpower. Thus the expenditure would be equivalent to that of similar projects such as Megapie.

The optimisation described in the following sections fully justifies the choices taken in the design.

2 Neutronics analysis of T-MIF

Source: The current chapter is reproduced from reference document 5.

2.1 Initial Design

As set out in the specification report (Ref. 1), the design of the T-MIF facility aims at obtaining the greatest possible flexibility in terms of its use in different beam irradiation facilities around the world, while ensuring safety and minimising down-time for repairs and maintenance. An overall concept for fulfilling these goals has been laid out in the preliminary design report for the entire facility (Ref. 2), which gives more detail on the engineering aspects of the various components.

At the heart of the facility rests the neutron source, where the test specimens are to be placed and subjected to proton and neutron bombardment. The neutron source is filled with liquid metal, which serves both as spallation material, issuing spallation neutrons produced by a proton beam, and as a means of cooling the impact of the beam.

From a thermodynamic point of view, the source is a liquid-metal filled vessel provided with a beam window at one end, through which the proton beam enters, and inlet/outlet fixtures at the other end, for circulating the liquid metal through the target and thus allowing the heat deposited by the beam to be carried away to a heat exchanger analysed in section 3.2.6. Specific cooling and fluid dynamic matters related to the source are studied in section 4.2. The initial design of the neutron source is summed up in Figure 2.

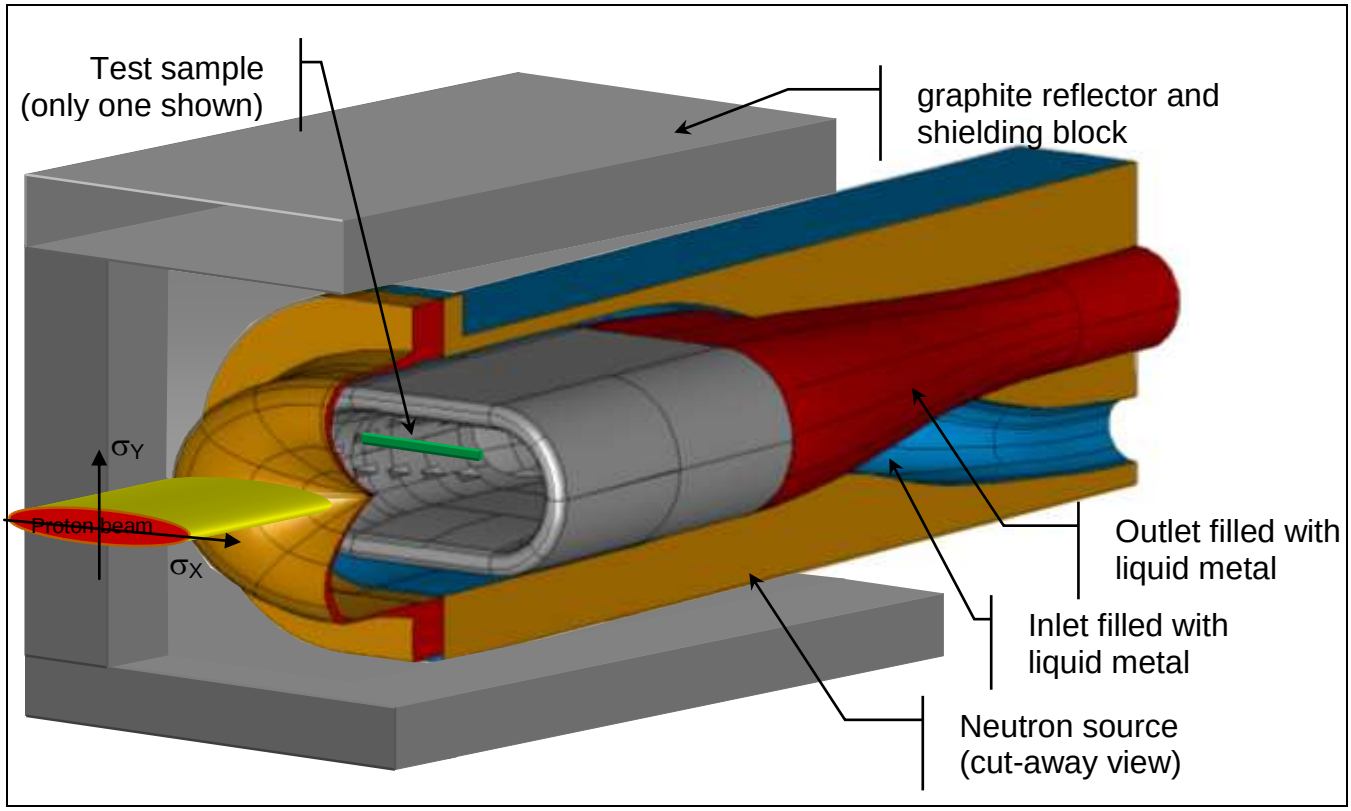

Figure 2: Neutron source for T-MIF embedded in a graphite reflector. (ref. 2)

The intense proton beam focused in the centre of the source is intended to procure a dense neutron flux over the small central volume of approximately 2 litres. It is in this small volume that the material samples (a representative shown above in green) are placed, in the hope of concentrating as high a

neutron flux as possible. An external thick graphite reflector is intended as a means of further increasing the neutron flux. The position of the various material samples, either directly in the path of the proton beam or slightly above and below it, will allow the study of samples both under mixed proton/neutron irradiation and pure neutron irradiation. This is an important scientific aspect of the experimental facility being proposed, which should help shed new light on the damage inflicted on materials by these different particles. It is therefore important to calculate the contribution in DPA from each of the different particles in the different locations foreseen for the samples.

2.2 Methodology of the investigations

The current technical note seeks to analyse the neutron source, from the point of view of neutron physics in order to report on the following primary matters:

1. Determine the heat deposition rates and DPAs in the liquid metal and beam window. A finer resolution is required in the latter case.

2. Resolve the spatial neutron field in and around the target.

3. Determine the dose rates spatial distribution at 1 second / 1 hour / 1 day / 1 week / 10 weeks after beam shutdown.

4. Establish the DPA (displacement per atom) rates from proton and neutron fluxes on the specimens placed in the target.

In addition, the secondary goals will be to:

5. Study the sensitivity of the results to the thickness of the surrounding graphite reflector.

6. Study alternative reflector materials such as Beryllium, heavy water and Iron.

7. Optimise the shielding by extending the model and incorporating layers of borated polyethylene around the facility.

The essential characteristics of the beam and neutron source are summarised in Table 3.

Particle	Proton
Power of the beam	100 kW
Current	166 μA
Energy	600 MeV
Time structure	Continuous
Beam Spot	Gaussian $\sigma_{x,}$ = 1.0 cm σ_{Y} = 6.0 cm
Liquid metal	LBE
Source structure	Stainless steel L316

Table 3: Essential characteristics of the neutron source.

2.3 Description of the FLUKA Model

2.3.1 Physics aspects

The Monte Carlo simulation program FLUKA was used to assess the neutronics performance of the system. The "Defaults" card in FLUKA was set to "Precision", activating the following physics parameters:

- EMF on (transport of photons and electrons activated);
- Rayleigh scattering and inelastic form factor corrections to Compton scattering activated;
- Detailed photoelectric edge treatment and fluorescence photons activated;
- Low-energy neutron transport on down to thermal energies included (high energy neutron threshold at 20 MeV);
- Fully analogue absorption for low-energy neutrons;
- Particle transport threshold set at 100 keV, except neutrons ($1x10^{-5}$ eV) and (anti)neutrinos (0, but they are discarded by default anyway);
- Multiple scattering threshold at minimum allowed energy, for both primary and secondary charged particles;
- Delta ray production on with threshold 100 keV (see option DELTARAY);
- Restricted ionisation fluctuations on, for both hadrons/muons and EM particles;
- Tabulation ratio for hadron/muon dp/dx set at 1.04, fraction of the kinetic energy to be lost in a step set at 0.05, number of dp/dx tabulation points set at 80 (see options DELTARAY, EMFFIX, FLUKAFIX);
- Heavy particle e^+e^- pair production activated with full explicit production (with the minimum threshold = 2 m_e);
- Heavy particle bremsstrahlung activated with explicit photon production above 300 keV;
- Muon photonuclear interactions activated with explicit generation of secondaries;
- Heavy fragment transport activated;

Besides the default definitions, the proton cut-off energy was set to 1 keV (instead of the 100 keV defined with the "Precision" defaults), in order to obtain more accurate results for the DPA calculations. No biasing options were activated.

For the "Beam**"** card, the following options were chosen:

- Energy: 0.6 GeV
- Shape (X): Gaussian with FWHM=14.13 cm (σ_x, = 6.0 cm)
- Shape (Y): Gaussian with FWHM=2.355 cm (σ_y, = 1.0 cm)
- Cantered on (x, y) = (0, 0) and travelling in the positive z direction

2.3.2 Geometry of the model

The geometry of the model as implemented in FLUKA is shown from Figure 3 to Figure 8 (it is a simplified version of the design presented in Figure 2). Figure 3 shows, on the left side, the plane x=0 with the whole target surrounded by a reflector of graphite. The right side of Figure 3 shows the

target window and a cut of the eight samples. The whole target, made of liquid lead (ρ=10.485 g/cm^3) in a container of L316 stainless steel, is shown in Figure 4.

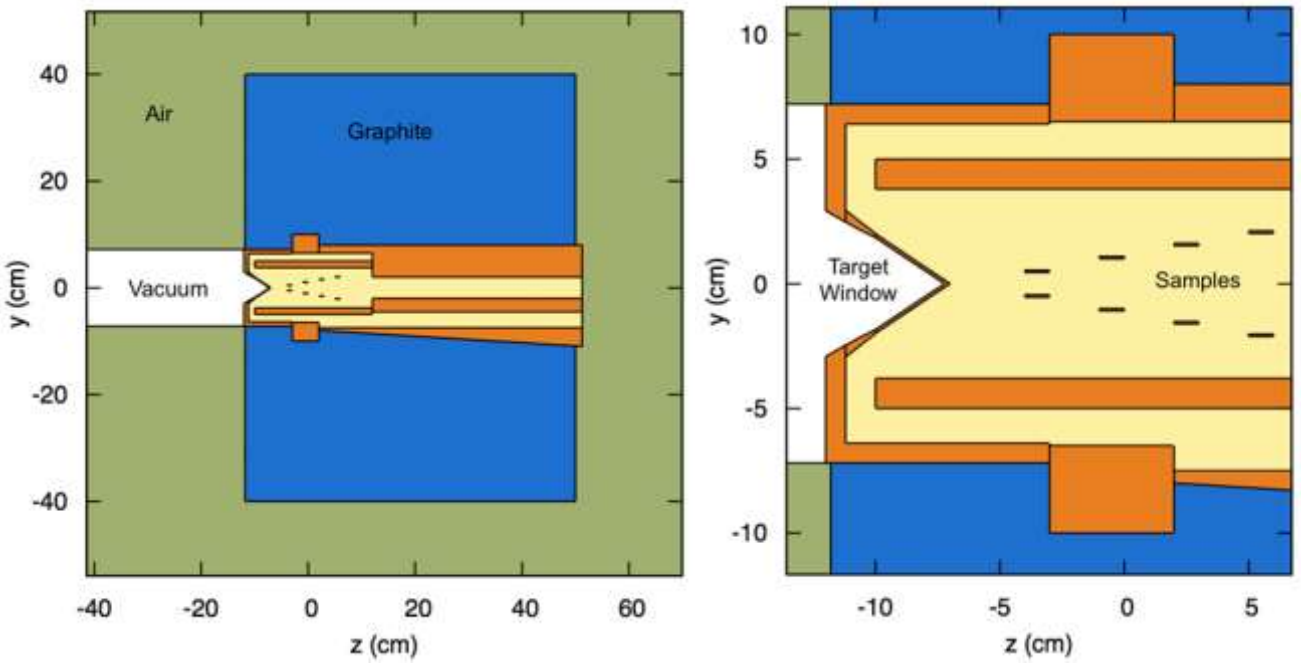

Figure 3 - Overview of the target area, with the target surrounded by a graphite reflector (left). Target window and samples region (right). Plane x=0.

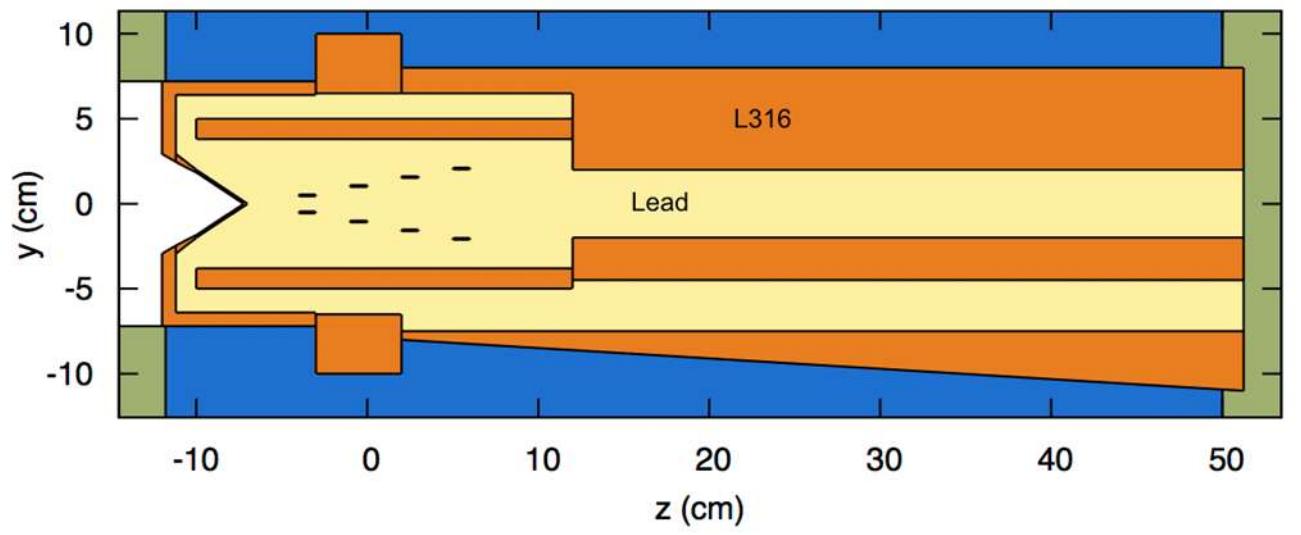

Figure 4 - Liquid lead target with L316 stainless steel enclosure, plane x=0.

The plane y=0.5, containing one of the eight samples, is shown in Figure 5, while a magnified version of the sample is represented in Figure 6. An effort was made in order to provide an accurate description of the samples, since the calculations of the DPA values in the samples will be of great importance in the assessment of the performance of the system.

Finally, the plane z=0 is represented in Figure 7, showing two of the eight samples (left) and the target window (right). A magnified version of the two samples is shown in Figure 8. The material used in the samples was L316 stainless steel.

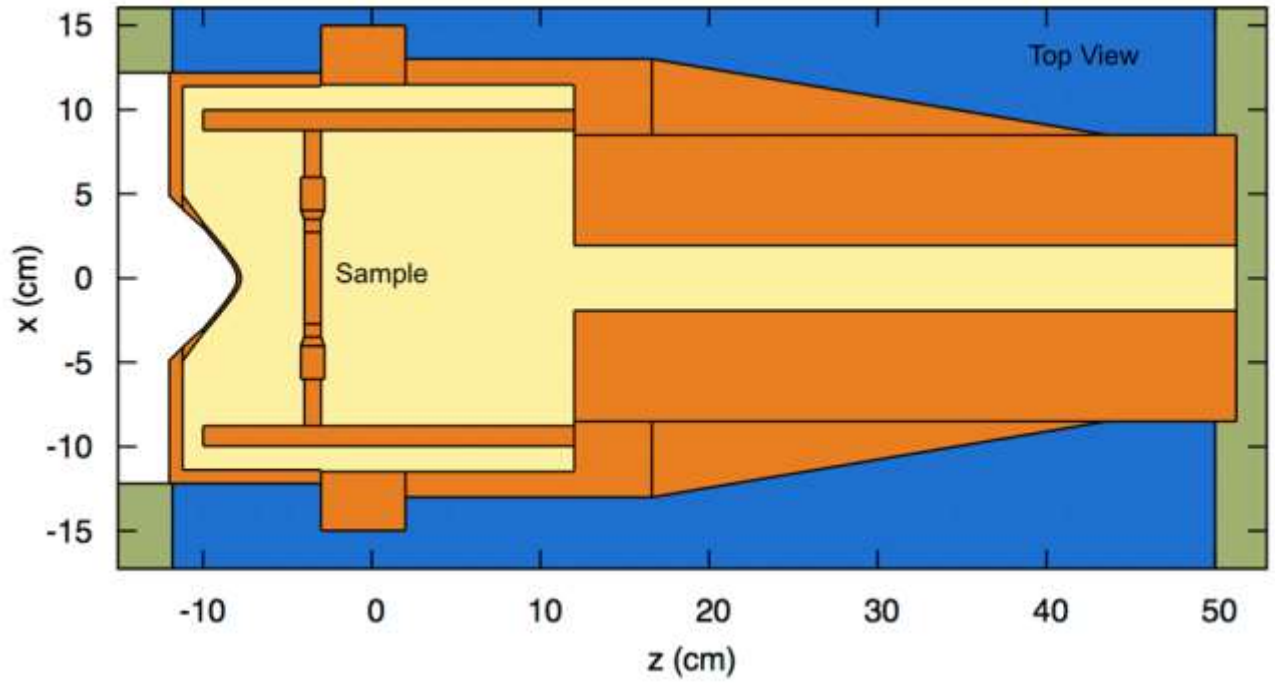

Figure 5 - Top View of the target, plane y=0.5 (one of the eight samples is shown in this plan).

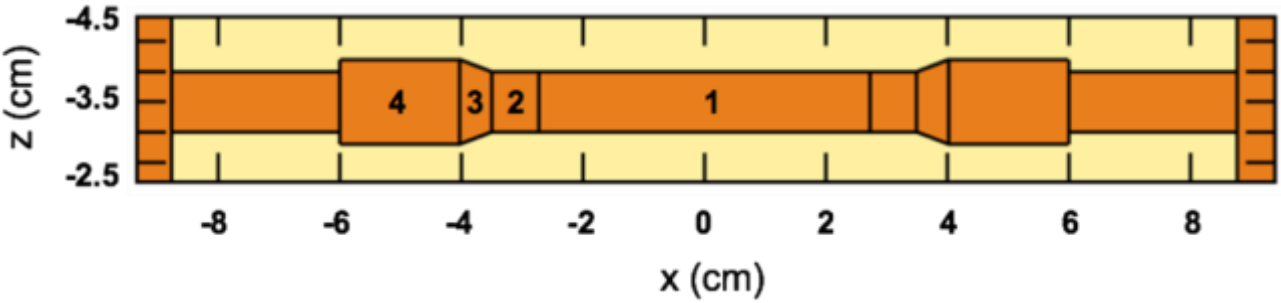

Figure 6 - Geometry of a sample, plane y=0.5. Each sample is divided into 4 regions, here numbered from 1 to 4.

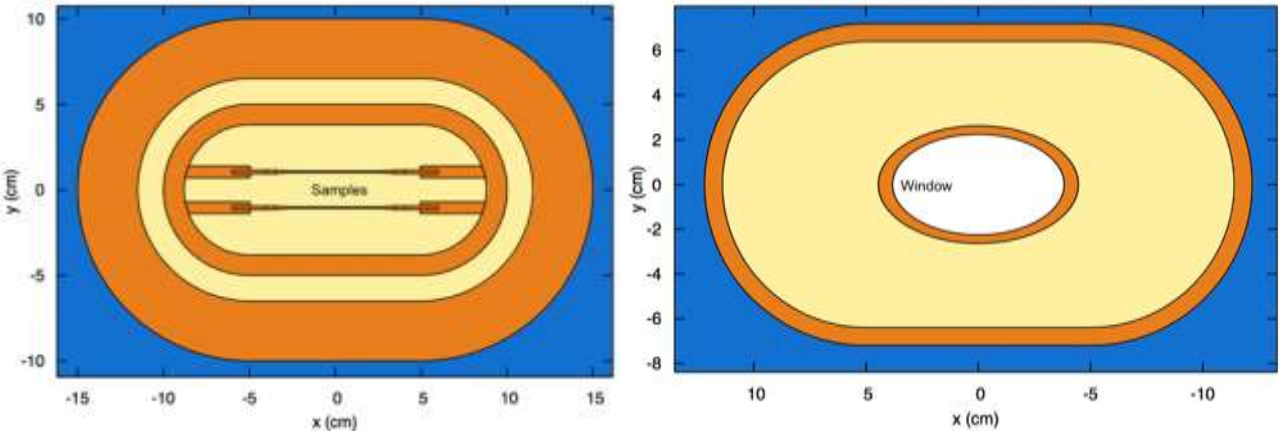

Figure 7 - Plane z=-3.5, showing two samples (left), and plane z=-10.8, showing the target window and the entrance point of the proton beam (right).

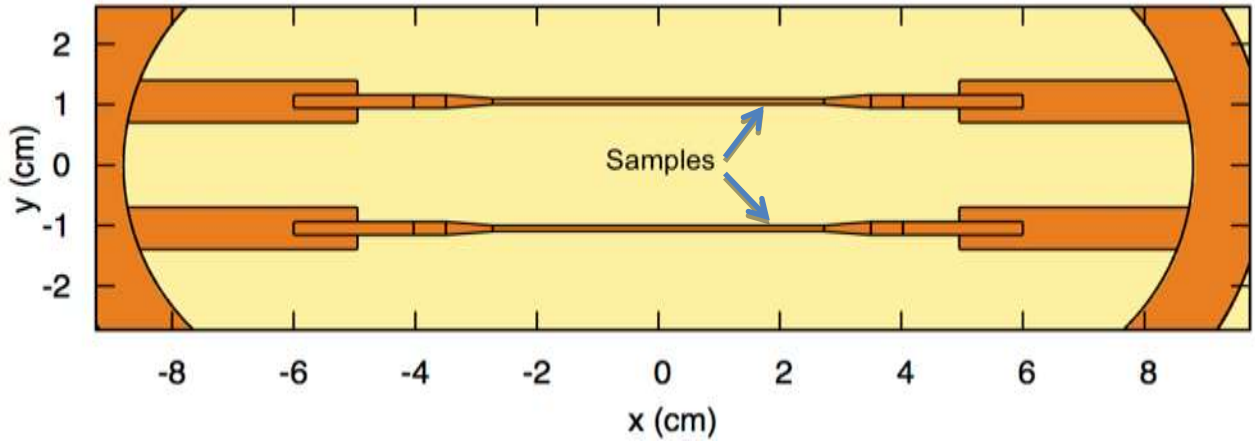

Figure 8 - Detailed view of the two samples and respective holders (plane z=-3.5).

2.4 Liquid metal and beam window evaluation

The power deposition (W/cm^3) in the liquid metal target is shown in Figure 9. A binning structure with 2mm bins in the z and y directions and 8 mm in the x direction was chosen. Peak values of up to 100 W/cm^3 are observed, in the impact point of the proton beam. Although the samples are well positioned to receive the highest power deposition possible, the power deposition inevitably decreases along the beam penetration path and thus the samples in the planes z=2.5 cm and z=5.5 cm receive less power than the samples in the planes z=-3.5 and z=0.5.

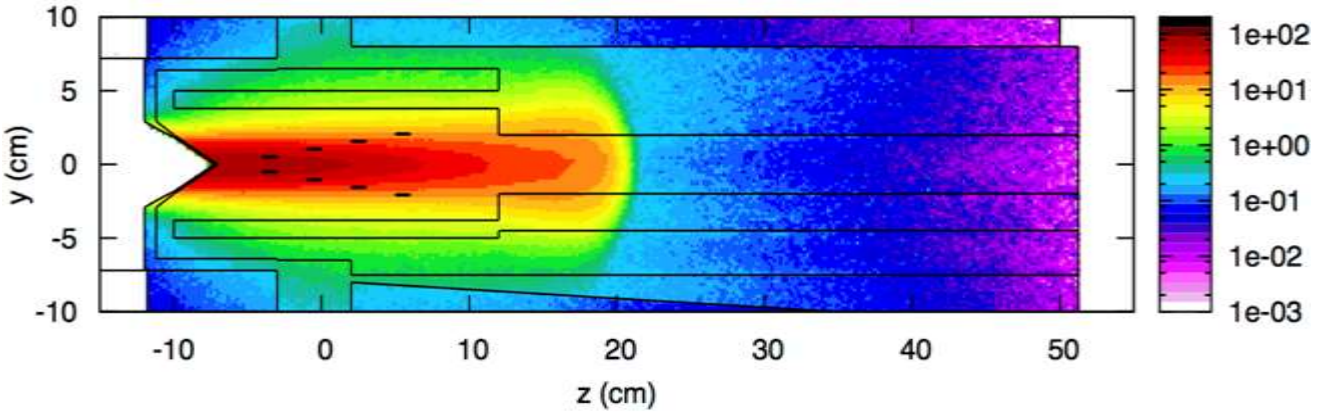

Figure 9 - Power deposition (W/cm^3) for a 100 kW beam (600 MeV, 166 µA), average values for a depth of 0.8 cm in the x direction.

The same binning structure was used to estimate the DPA in the liquid metal target. The results are presented in Figure 10, in DPA/month, and it is apparent that the DPA values are higher in the four samples closer to the window than in the remaining ones, as expected from the power deposition profile shown in Figure 9. The peak values are of the order of 2 DPA/month.

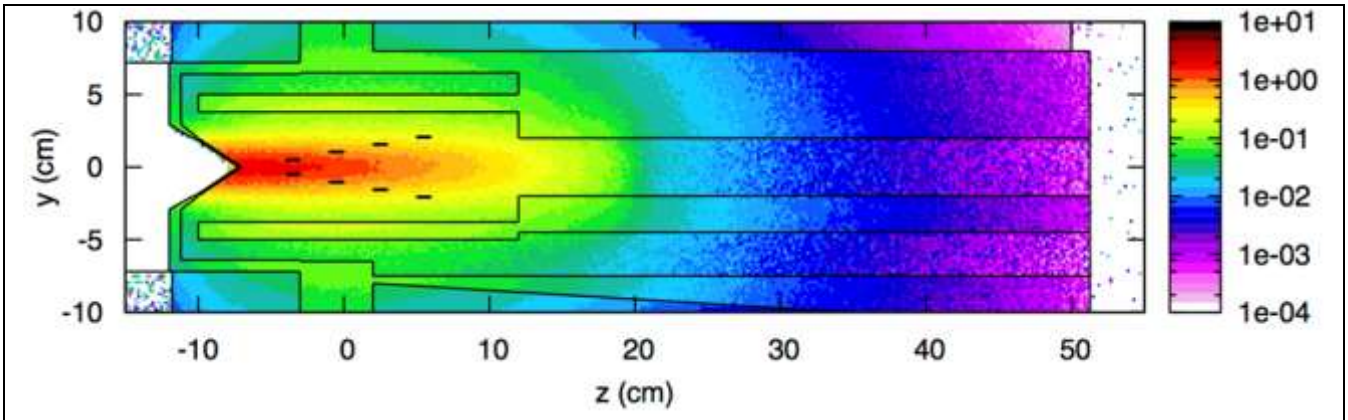

Figure 10 - DPA/month for a 100 kW beam (600 MeV, 166 µA), average values for a 1.2 cm depth in the x direction.

Additional simulations were carried out to determine the power deposition and DPA values in the target window, which are needed to assess its lifetime and durability. A different binning structure was required for these simulations, with 0.2 mm for each bin in the x, y and z directions, due to the thinness of the window. The results are displayed in Figure 11, for the thinnest part of the target window. While it is difficult to have appropriate statistics with such small bins, it is apparent that the values for energy deposition and DPA in the L316 stainless steel target window differ to some extent from those in the liquid metal immediately behind it. The difference is roughly in proportion to the difference in density of the materials.

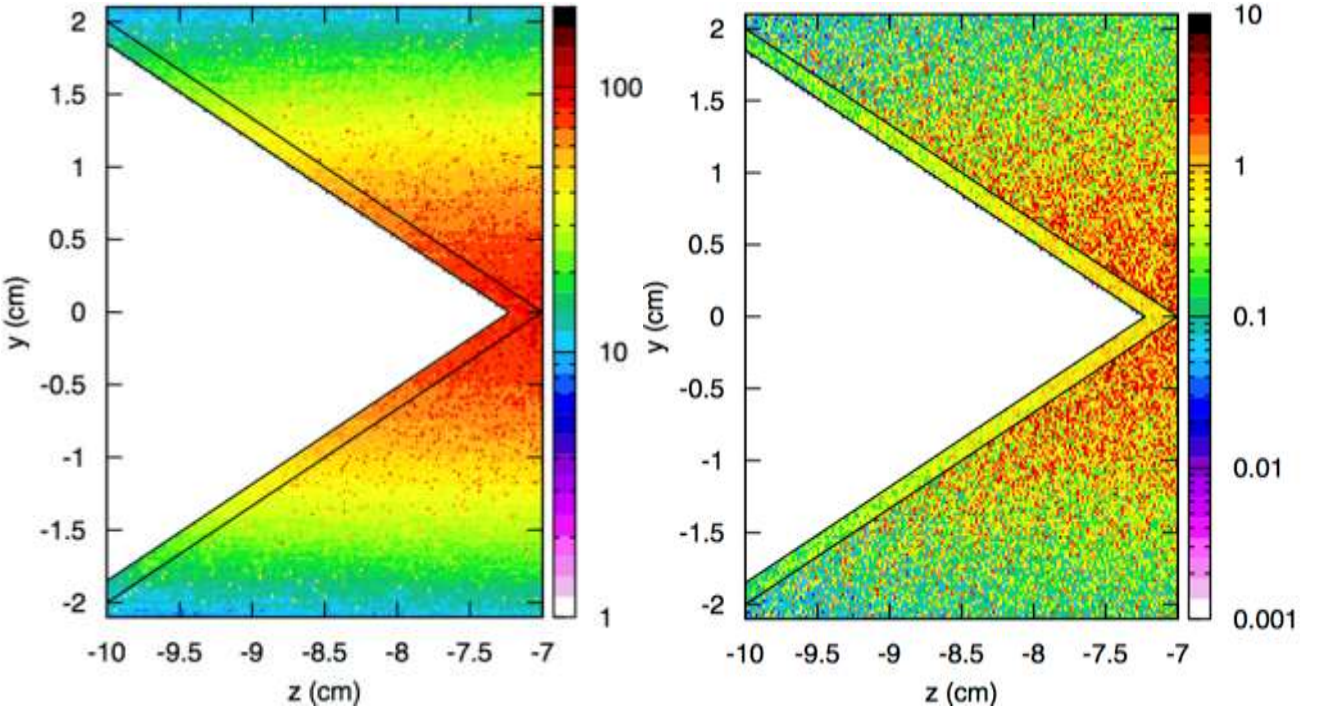

Figure 11 - Power deposition (W/cm^3) (left) and DPA/month (right) in the target window, for a 100 kW beam (600 MeV, 166 µA) and a 0.2 mm depth in the x direction.

The total power deposition and the average DPA in the window (total volume of 2.6 cm^3) were also calculated:

- Total power deposition in the window: 235 W (uncertainty: 0.1%) for a beam power of 100 kW

- DPA/month in the window: 2.25 (statistical uncertainty: 0.2%).

Figure 12 illustrates how the target window was subdivided into 15 different regions (with varying volumes) to calculate the DPA and energy deposition values as a function of z in the target window. The region of the liquid lead target located immediately behind the target window was also subdivided, into 16 regions, for the same purpose.

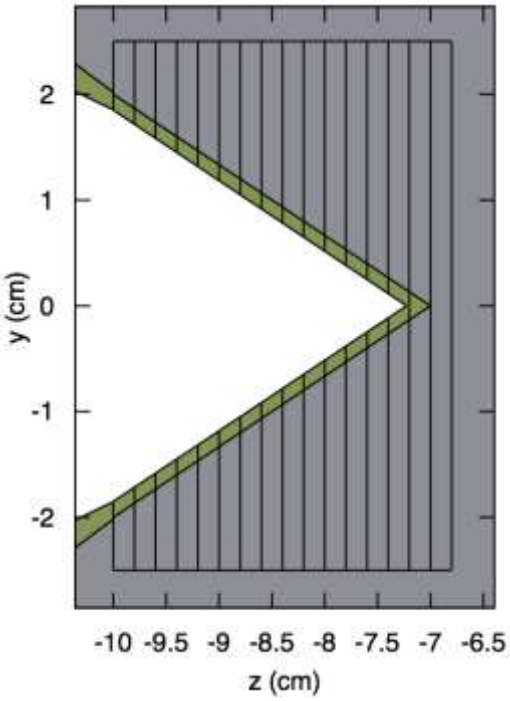

Figure 12 - Target window subdivided into regions, to calculate the DPA and energy deposition as a function of z.

Figure 13 and Figure 14 show the results for each region of the window. The power deposition per unit volume increases with z, since, as z increases, each region gets closer to the peak of the Gaussian beam profile. The absolute values decrease with increasing z, since each elliptical slice of the target window gets smaller as z increases. The same results for the liquid lead behind the target window are presented in Figure 15 and Figure 16.

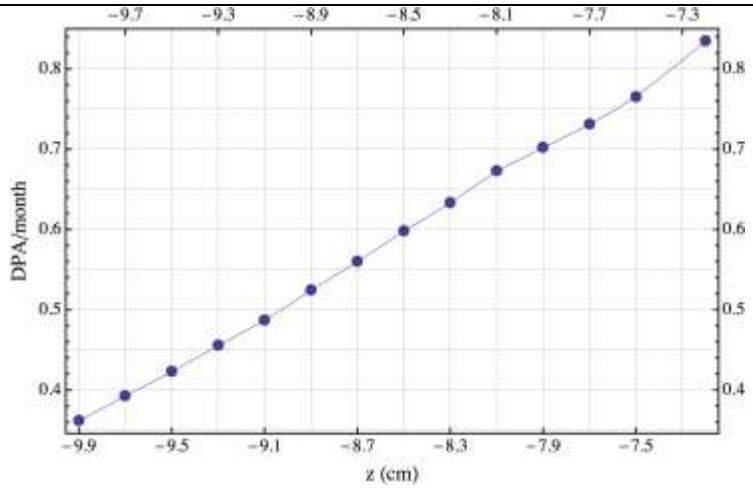

Figure 13 - DPA/month as a function of z in the target window.

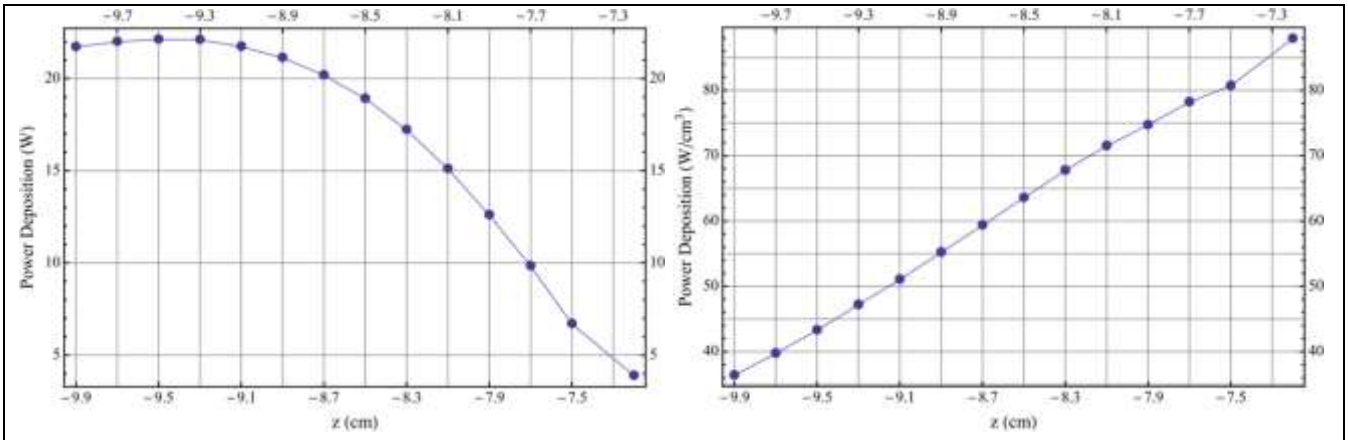

Figure 14 - Power Deposition as a function of z in the target window.

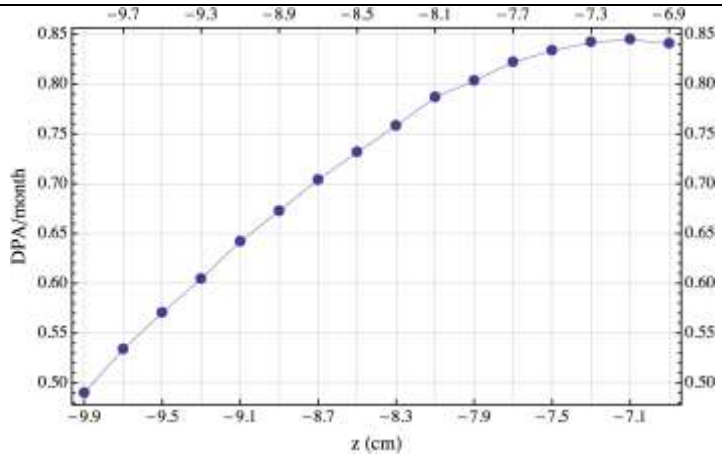

Figure 15 - DPA/month as a function of z in the liquid lead behind the target window.

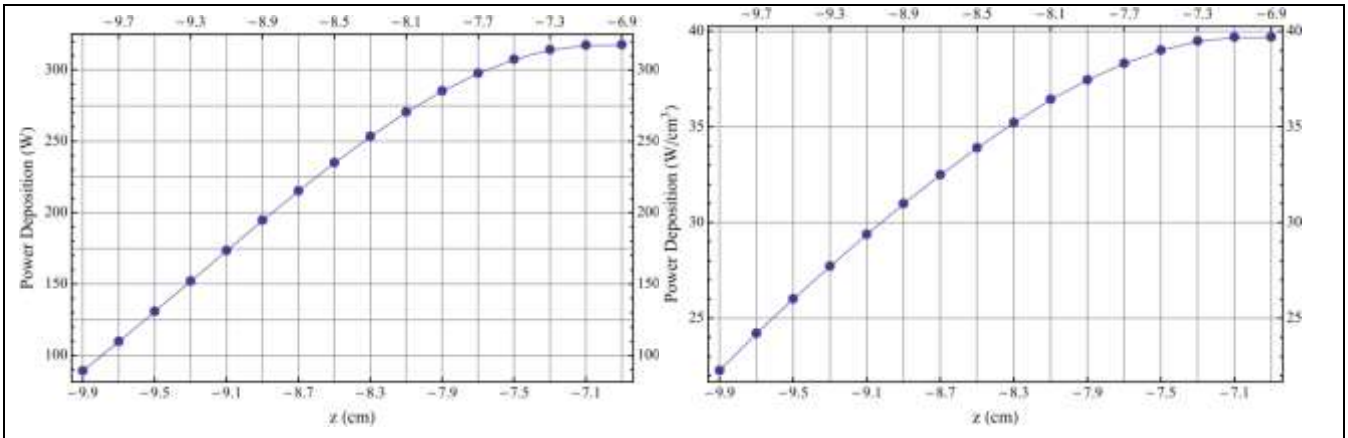

Figure 16 - Power Deposition as a function of z in the liquid lead behind the target window.

2.5 Neutron field in and around the target and proton beam profile

In this section, the neutron and proton fluxes in the target region are presented. For the neutron field in and around the target, three different binning structures were considered:

- 2 mm bins in the yz plane, with 1.2 cm of depth in the x direction (centred in the plane x=0). The results using this binning are presented in Figure 17, which shows the neutron fluxes inside the target;
- 4 mm bins in the yz plane, with 3.2 cm of depth in the x direction (centred in the plane x=0). The results are presented in Figure 18, showing the neutron fluxes in the target and surrounding graphite reflector;
- 6.4 mm bins in the yz plane, with 3.2 cm of depth in the x direction (centred in the plane x=0). The results are presented in Figure 19, showing the neutron fluxes in the target, the graphite reflector and the surrounding areas.

The neutron fluxes have peak values of the order of 10^{14} neutrons/cm^2/s, near the impact point of the proton beam. These values drop by approximately two orders of magnitude after 40 cm of graphite. These simulations also show the impact of the graphite reflector in the neutron fluxes around the target. The reflector will have to be extended well beyond the region z<-10, in order to reduce the dose rates outside of the target region. The strategy pursued in the first round of optimisation is to try and increase the neutron flux inside the material test zone at the expense of the neutron field outside the facility that contributes to the dose rate. As will be discussed in the following, the high beam power makes this option less attractive.

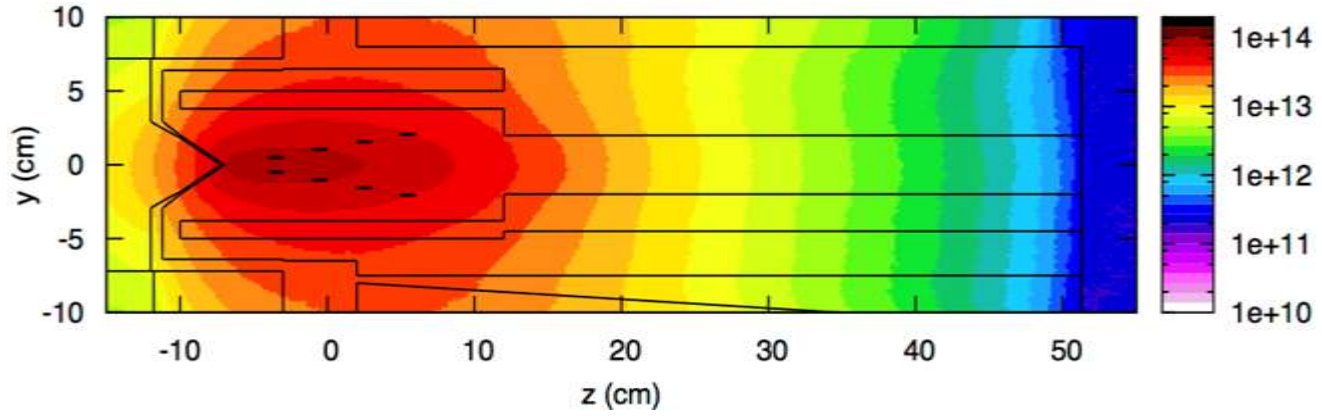

Figure 17 - Neutron flux (n/cm^2/s) in the target for a 100 kW beam (600 MeV, 166 μA), average values for a 1.2 cm depth in the x direction.

The following figures, showing the neutron fluxes during operation using a 40 cm reflector and no shielding, demonstrate the very high penetration of neutrons beyond the reflector, a damaging effect outside the facility.

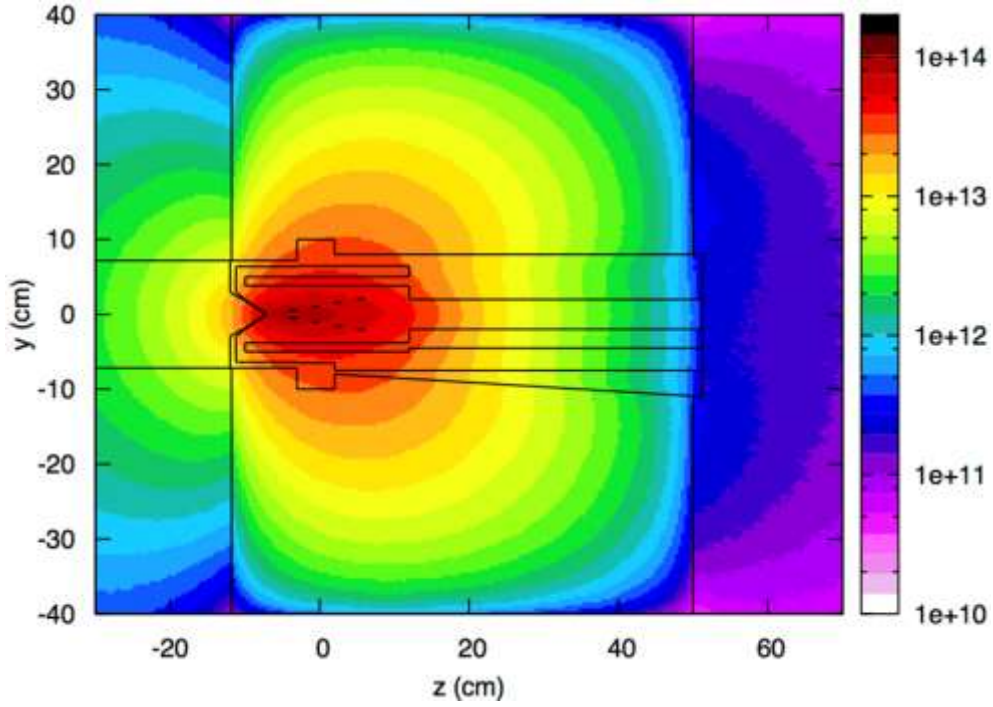

Figure 18 - Neutron flux (n/cm^2/s) in the target and graphite reflector for a 100 kW beam (600 MeV, 166 µA), average values for a 3.2 cm depth in the x direction.

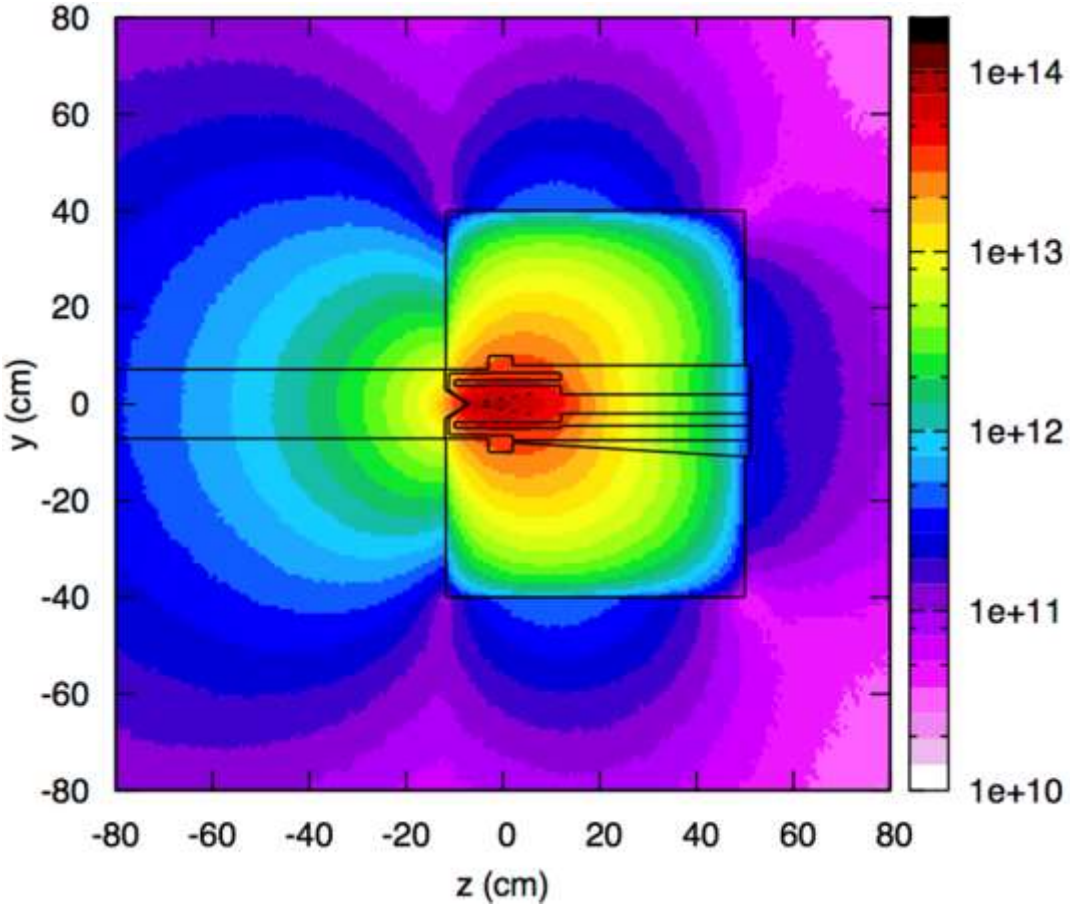

Figure 19 - Neutron flux (n/cm^2/s) in the target and surrounding regions for a 100 kW beam (600 MeV, 166 µA), average values for a 3.2 cm depth in the x direction.

The proton fluxes in the target are also included in this section, to show the beam profile and to provide an indication of the contribution of the proton beam to the power deposition in the target. Figure 20 shows the average values of the proton fluxes for a depth of 2 cm in the x direction, centred in the plane x=0. A perpendicular cut of the plane z=-11.5 is displayed in Figure 21, showing the profile of the beam in the x and y directions in the region of the target window.

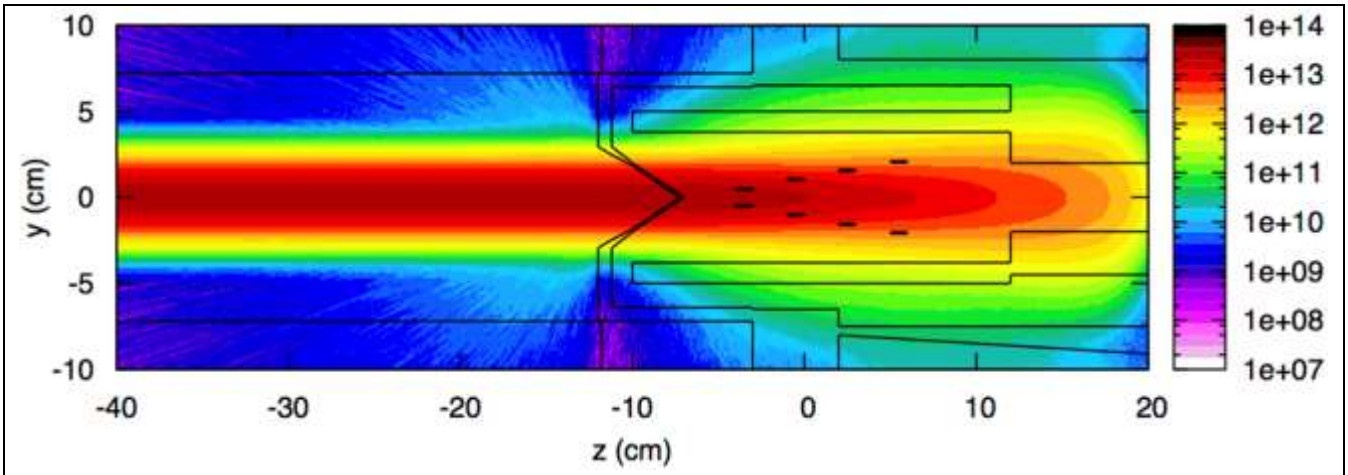

Figure 20 - Proton flux (p/cm^2/s) in the target for a 100 kW beam (600 MeV, 166 μA), average values for a 2 cm depth in the x direction.

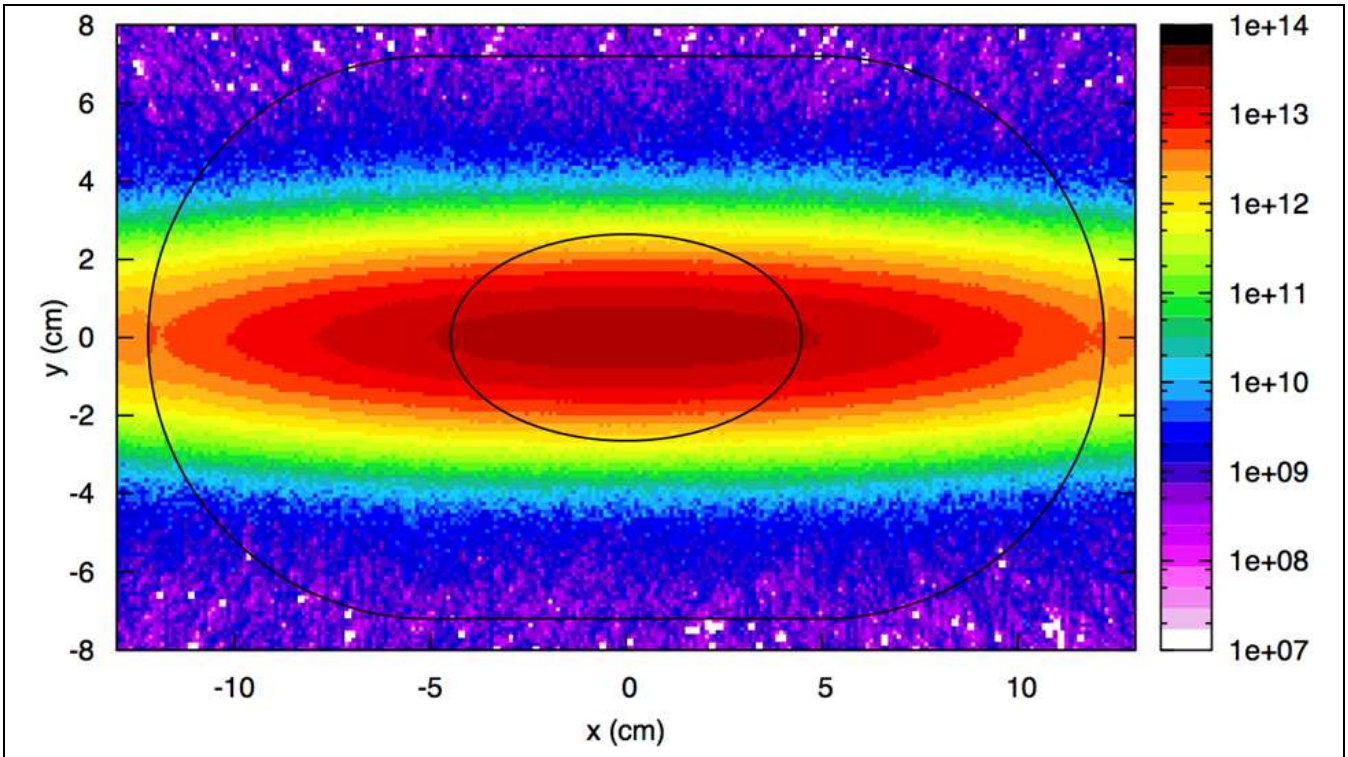

Figure 21 - Proton flux (p/cm^2/s) in the target for a 100 kW beam (600 MeV, 166 μA), average values for a 1 cm depth in the z direction.

2.6 Dose rates

The residual equivalent dose rates (Sv/h) due to the activation of the target and surrounding materials are shown in Figure 22 and Figure 23. The binning structure has 5 mm bins in the z and y directions and 8 cm bins in the x direction. The dose rates are calculated assuming no evacuation of the irradiated lead inside the target and primary circuit.

Four irradiation profiles were tested, both with a continuous 100 kW (600 MeV, 166 μA) proton beam: 1 day of irradiation (left side of Figure 22), 1 week of irradiation (right side of Figure 22), 1 month of irradiation (left side of Figure 23) and 1 year of irradiation (right side of Figure 23). Five cooling periods were considered: 1 second, 1 hour, 1 day, 1 week and 10 weeks.

A tolerable dose rate of 10^{-4} Sv/hr is only attained 10 weeks after shutdown assuming the facility has been operated only one week (Figure 22). For longer operation (Figure 23), the tolerable level cannot be reached even after 10 weeks. Since the duration of operation can certainly be projected to be in the order of months, shielding must clearly be given the greatest of attention.

The next section will examine to what extent the desired level of DPAs in the sample is attained, and how long the irradiation period must be to reach that level. Once this is known, a trade-off study will examine the relative merits of different materials to offset the needs of improving the shielding against the increased DPAs in the samples.

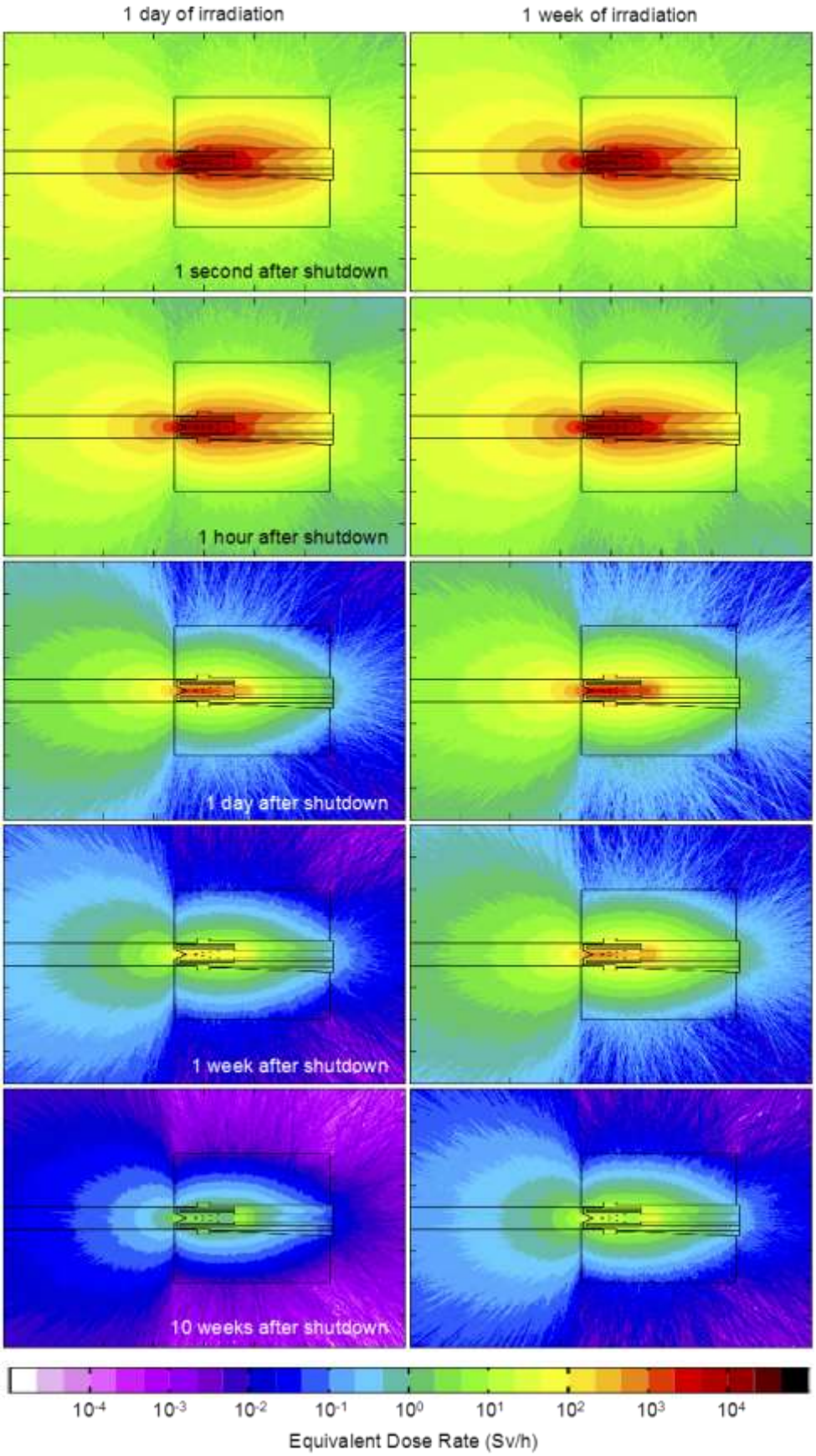

Figure 22 - Residual ambient dose equivalent rates (Sv/h) for several cooling periods (8 cm depth in the x direction, 100 kW beam). Left - 1 day of irradiation. Right - 7 days of irradiation.

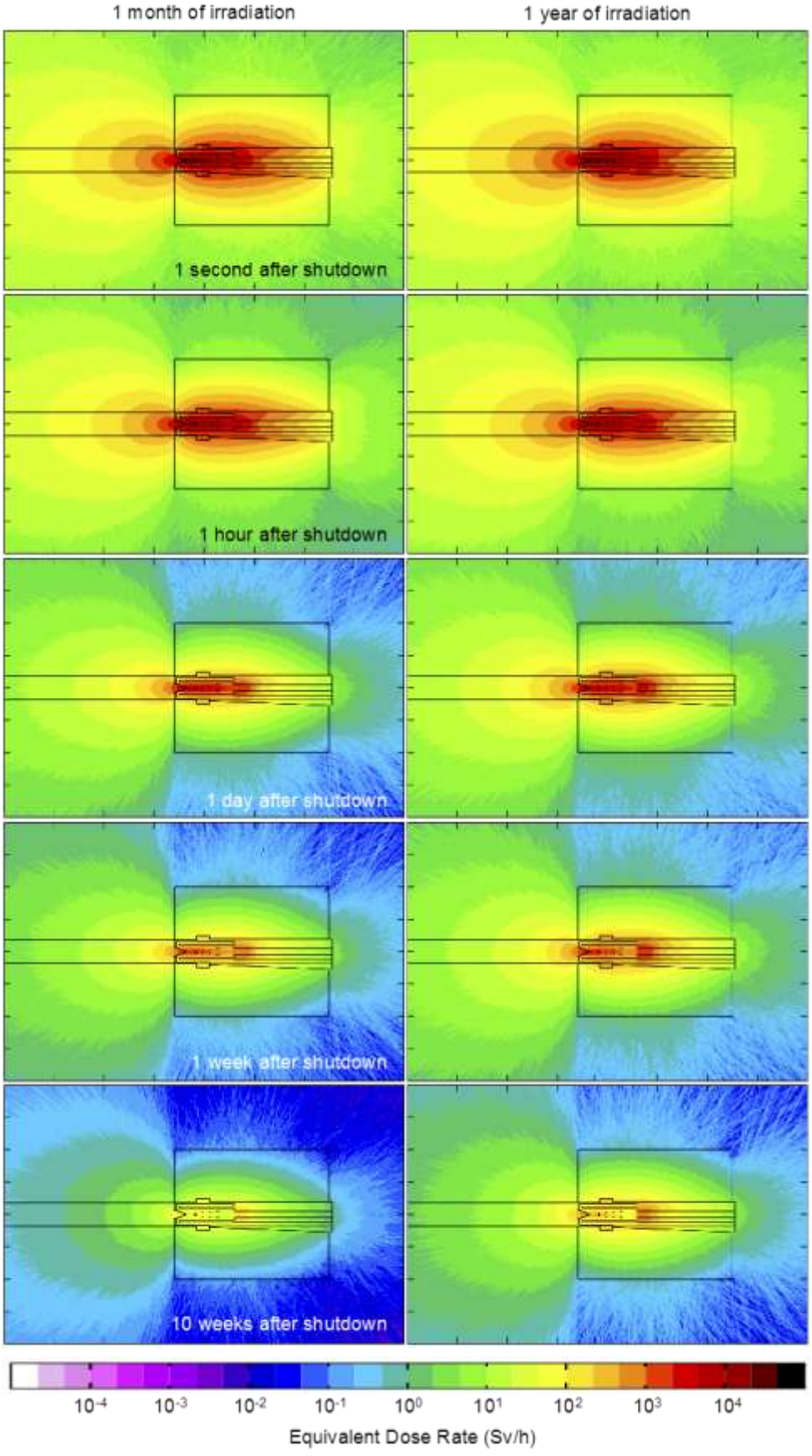

Figure 23 - Residual ambient dose equivalent rates (Sv/h) for several cooling periods (8 cm depth in the x direction, 100 kW beam). Left - 1 month of irradiation. Right - 1 year of irradiation.

2.7 Specimen Evaluation

2.7.1 DPA calculations

One of the most important objectives of this work was to estimate de DPA in the samples. For this analysis, four samples were chosen out of the total eight. These are the top four samples in the right side of Figure 3; the remaining ones are exposed to the same neutron and proton fluxes, due to the symmetry of the system.

Each bin has 0.1 mm in the x and z directions and 1 mm of depth in the x direction (the thickness of the thinnest part of the sample). The results, for the four samples, are shown in Figure 24 (logarithmic scale) and Figure 25 (linear scales), along with the basic dimensions of each sample. As expected, the DPA values decrease gradually along the beam penetration, since both the proton and neutron fluxes also decrease with this distance. The DPA values are between 0.1 and 1 DPA/month, for all samples.

More accurate DPA values in the samples and an estimation of the contributions from protons and neutrons to the total DPA can be seen in the table below. These calculations refer to the central part of each sample, the first of the four numbered regions in Figure 6.

In the first sample, the average DPA value is of 0.73 DPA/month. Protons are responsible for 44.3% of this value, while neutrons contribute with 55.5% (the remaining 0.2% of the total DPA value is due to other types of particles, like light ions). As the proton beam penetrates deeper into the target, the DPA decreases and the relative contribution from neutrons increases. In the fourth sample, neutrons are responsible for 79.1% of the DPA, while protons account for 20%. The overall DPA value in the fourth sample is of 0.24 DPA/month, approximately three times lower than in the first sample.

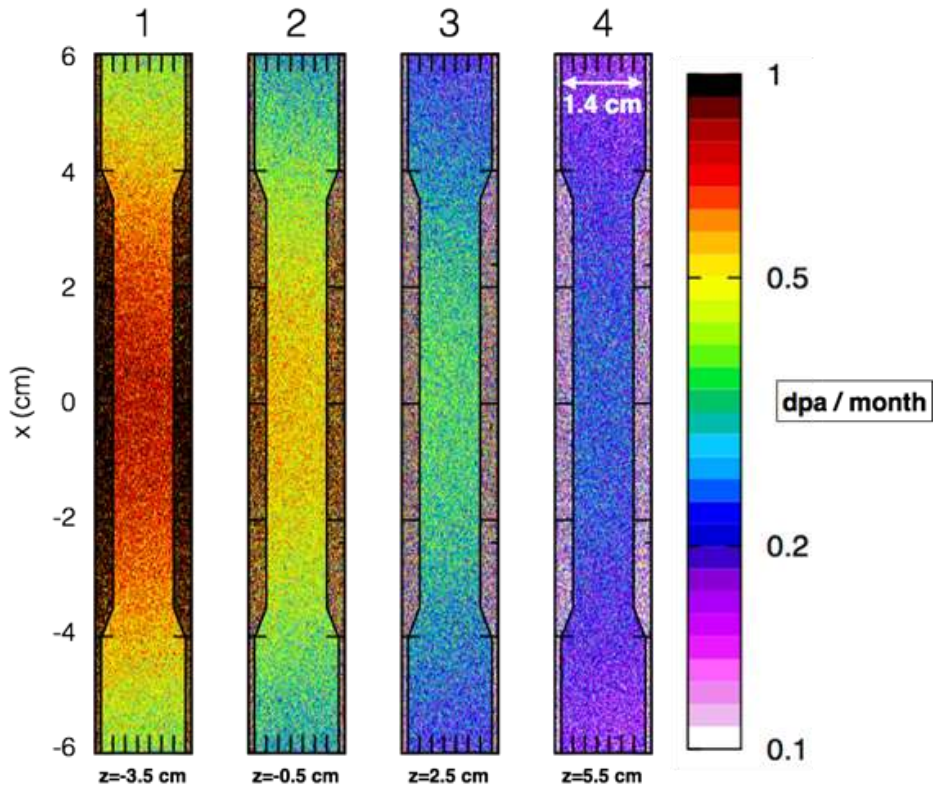

Figure 24 - DPA/month in 4 samples for a 100 kW beam (600 MeV, 166 μA), average values for a 1 mm depth in the y direction (log scale).

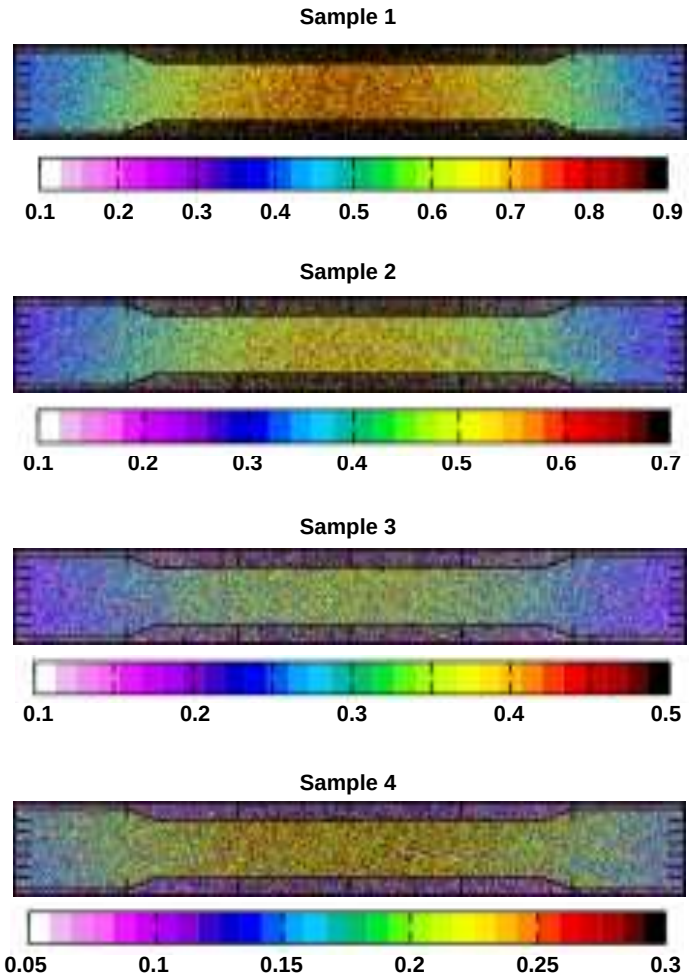

Figure 25 - DPA/month in 4 samples for a 100 kW beam (600 MeV, 166 μA), average values for a 1 mm depth in the y direction (linear scales).

Sample	DPA/month (stat. uncertainty)	Contribution from protons	Contribution from neutrons
1	0.73 (0.4%)	44.3%	55.5%
2	0.50 (0.5%)	34.9%	63.8%
3	0.34 (0.5%)	25.9%	73.2%
4	0.24 (0.6%)	20.0%	79.1%

Table 4 - DPA/month in the four samples and respective contributions from protons and neutrons.

Figure 26 shows how the first sample was subdivided into 15 different regions, in order to assess the power deposition and DPA in the sample along its transverse length. The results are shown in Figure 27 and Figure 28, and show that the energy deposition and the DPA are higher in the centre of the sample, as expected. The DPA and the energy deposition increase by approximately 20% from the edge to the centre of the sample.

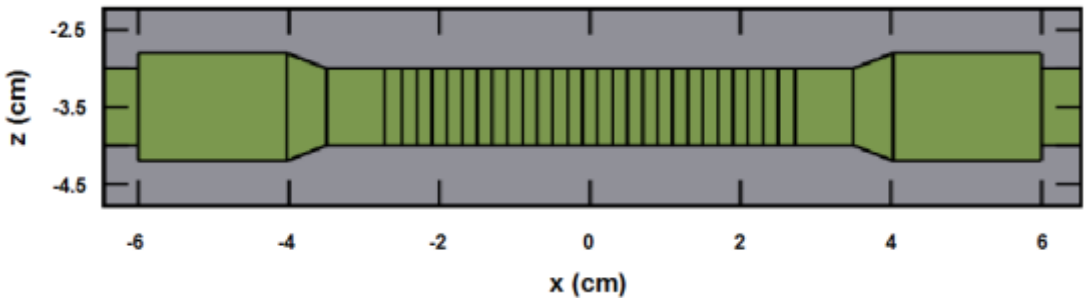

Figure 26 - First sample subdivided into regions, to calculate the DPA and energy deposition as a function of x.

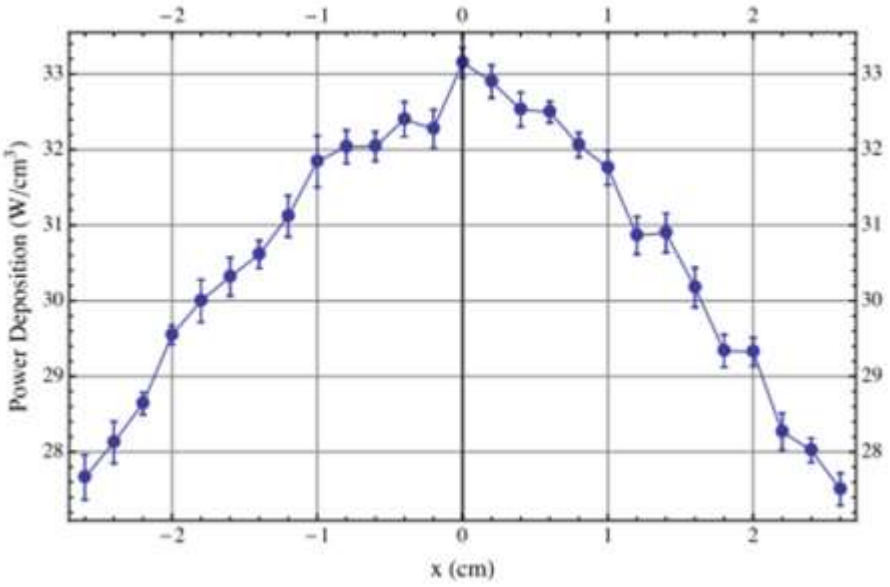

Figure 27 - Power deposition (W/cm^3) as a function of x in the first sample.

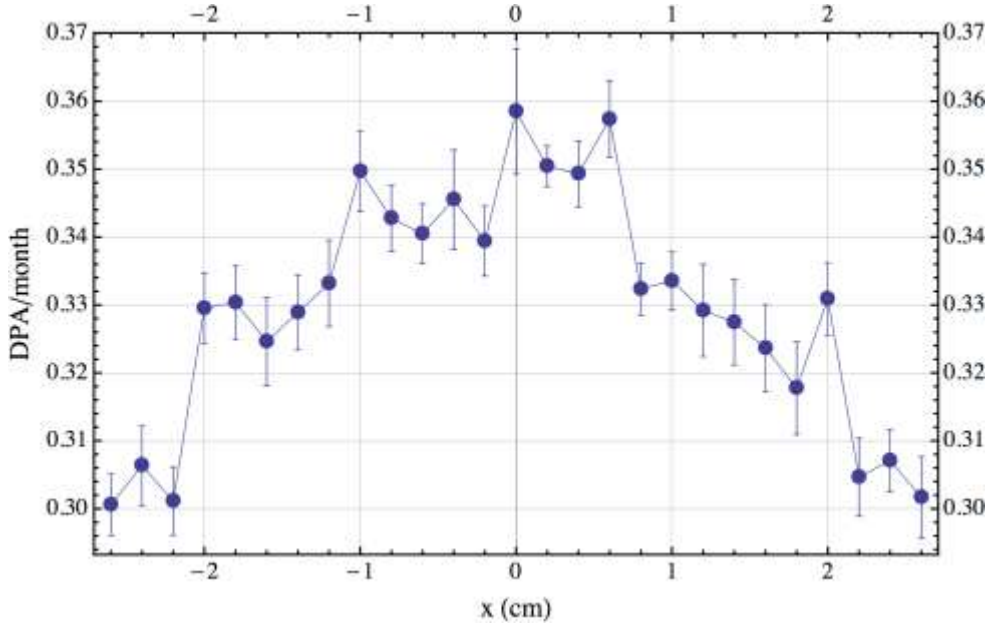

Figure 28 - DPA/month as a function of x in the first sample.

2.7.2 Neutron flux spectra in the samples

The neutron flux spectra in the four samples are represented in Figure 29. As expected, the fluxes of lower energy (<10 keV) neutrons in the samples increase along the path of the proton beam in the target, while the fluxes of higher energy (>1 MeV) neutrons decrease correspondingly. Hence one may assume that it is the high-energy neutrons that play the most important role in increasing the DPA count in the first sample, and not simply the higher overall neutron flux. Here lies a contradiction with the role of the reflector, which tends to moderate the neutrons reflected back into the target area. Therefore, the increase in the overall neutron flux provided by the reflector might not translate into higher DPA values, since the reflected neutrons will lie in the low-energy part of the spectrum.

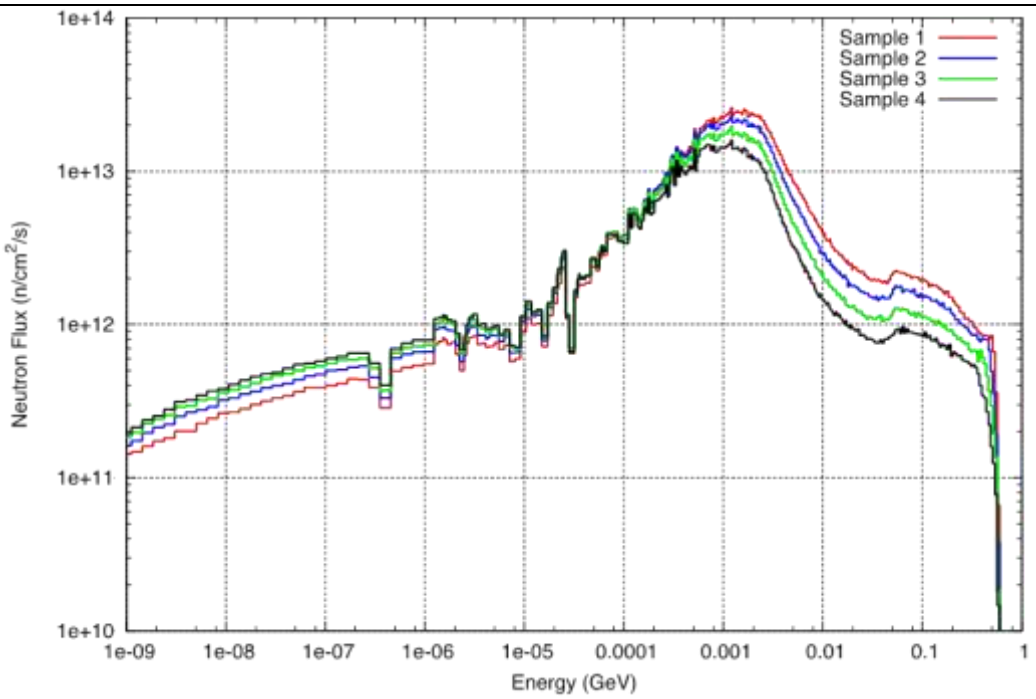

Figure 29 - Neutron flux spectra (n/cm^2/s) for each of the four samples.

One of the objectives of the facility is to extract the samples as quickly as possible to analyse in order to analyse them. This has been simulated, as shown in in the right side of Figure 30, by taking only into account the contributions from the sample to the equivalent dose rate taken into account. For this calculation of the residual ambient dose equivalent rates, the holder material was changed to vacuum. The first sample, the most activated one, was chosen for these calculations. For the decay period, FLUKA allows the material of every component of the geometry to be changed. In the left side of Figure 30 the case where the sample is left in the sample holder was calculated (but with both sample and sample holder outside the facility. For this calculation every material was changed to vacuum except the sample and sample holder materials, where L316 was kept unchanged.

In all calculations, a period of 1 month of irradiation was considered and the cooling periods were, once again, 1 second, 1 hour, 1 day, 1 week and 10 weeks. Furthermore, the contributions from gamma photons and neutrons were discriminated, since these cannot be easily shielded if the samples are manipulated in a hot-cell; the residual dose rates, however, are essentially due to gamma decay, and no neutrons are emitted from the sample after the stoppage of the beam. L316 stainless steel is highly activated, with activities of the order of 100 Sv/h in the sample after ten weeks of cooling. Hence from these results, it would be highly recommended to remove the samples and manipulate them without the holder, since the residual dose rates are greatly reduced if the contribution of the holder is removed. Hot-cell remote manipulators will be needed in any case.

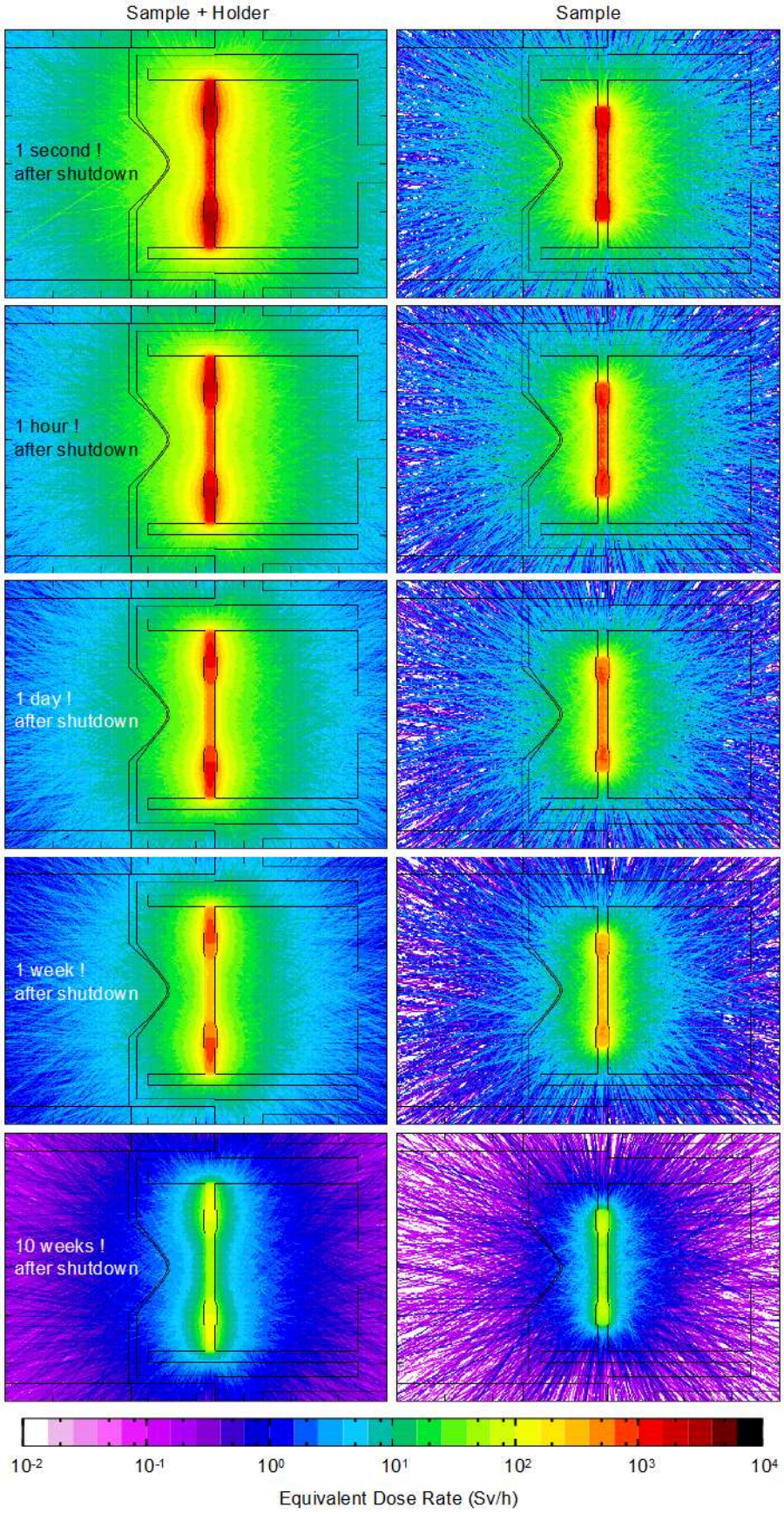

Figure 30 - Residual ambient dose equivalent rates (Sv/h) for several cooling periods (7 mm depth in the y direction, 100 kW beam) after 1 month of irradiation. Left - Contributions from sample 1 and respective holder. Right – Contribution only from sample 1.

2.8 Reflector studies

In this section, a study of the neutron reflector is presented. Five different materials were tested in this component of the target system: graphite, iron, lead, water and marble. The case without a neutron reflector was also tested. For each material, three reflector thicknesses were used, to provide a sensitivity analysis of the impact of the reflector material and dimensions in the neutron fluxes and DPA in the samples. The three configurations are presented in Figure 31: they will be referred to as "20 cm", "25 cm" and "30 cm", their respective distances from the centre of the target to the edge of the reflector. The results are presented in the following five sections and summarised and discussed in Section 2.8.7.

The material used in the shielding surrounding the reflector was polyethylene (C_2H_4) with a density of 1.11 g/cm^3. It is important, at this stage, to mention that this material, being a neutron moderator, also acts as a neutron reflector, with characteristics similar to those of light water.

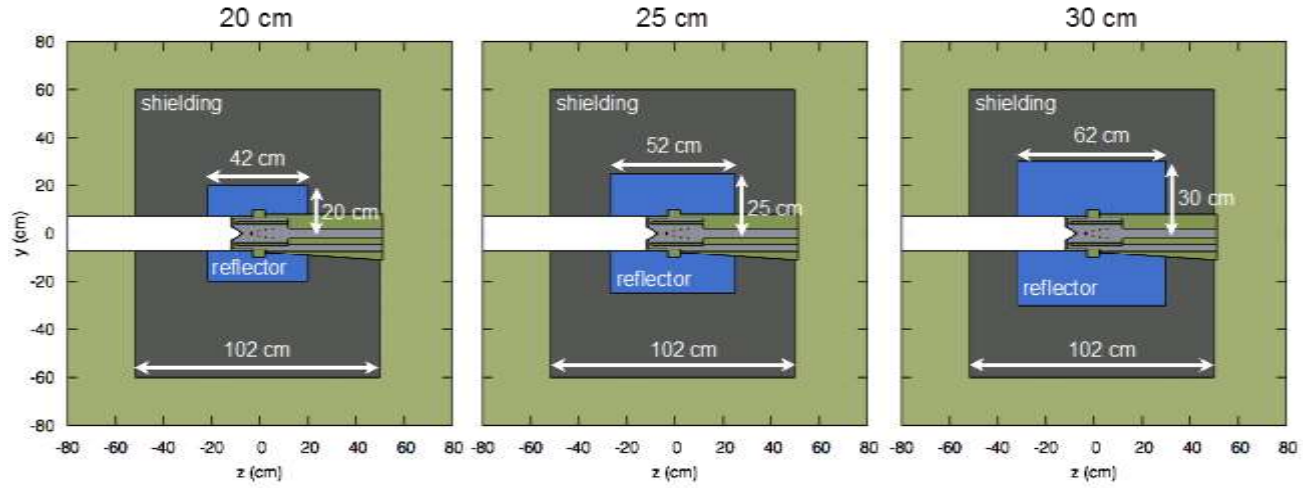

Figure 31 - Shielding and reflector dimensions, plane x=0. Three configurations are shown, with different reflector dimensions.

2.8.1 Graphite reflector

Figure 32 shows the neutron and photon fluxes and the equivalent dose rate in the target, reflector and shielding regions. The results are presented for the three previously mentioned configurations. For shielding considerations, there is no observable effect between the different thicknesses; the dose rates and the neutron and photon fluxes are similar between the three configurations. The neutron flux spectra, presented in Figure 33, show that the reflector thickness only affects the spectra for neutrons with energies below 10 keV, for all samples. When the thickness of the reflector increases, the number of low energy neutrons crossing the samples also increases, but no effect is seen at high energies. A comparison between the different reflectors is provided in Section 2.8.7.

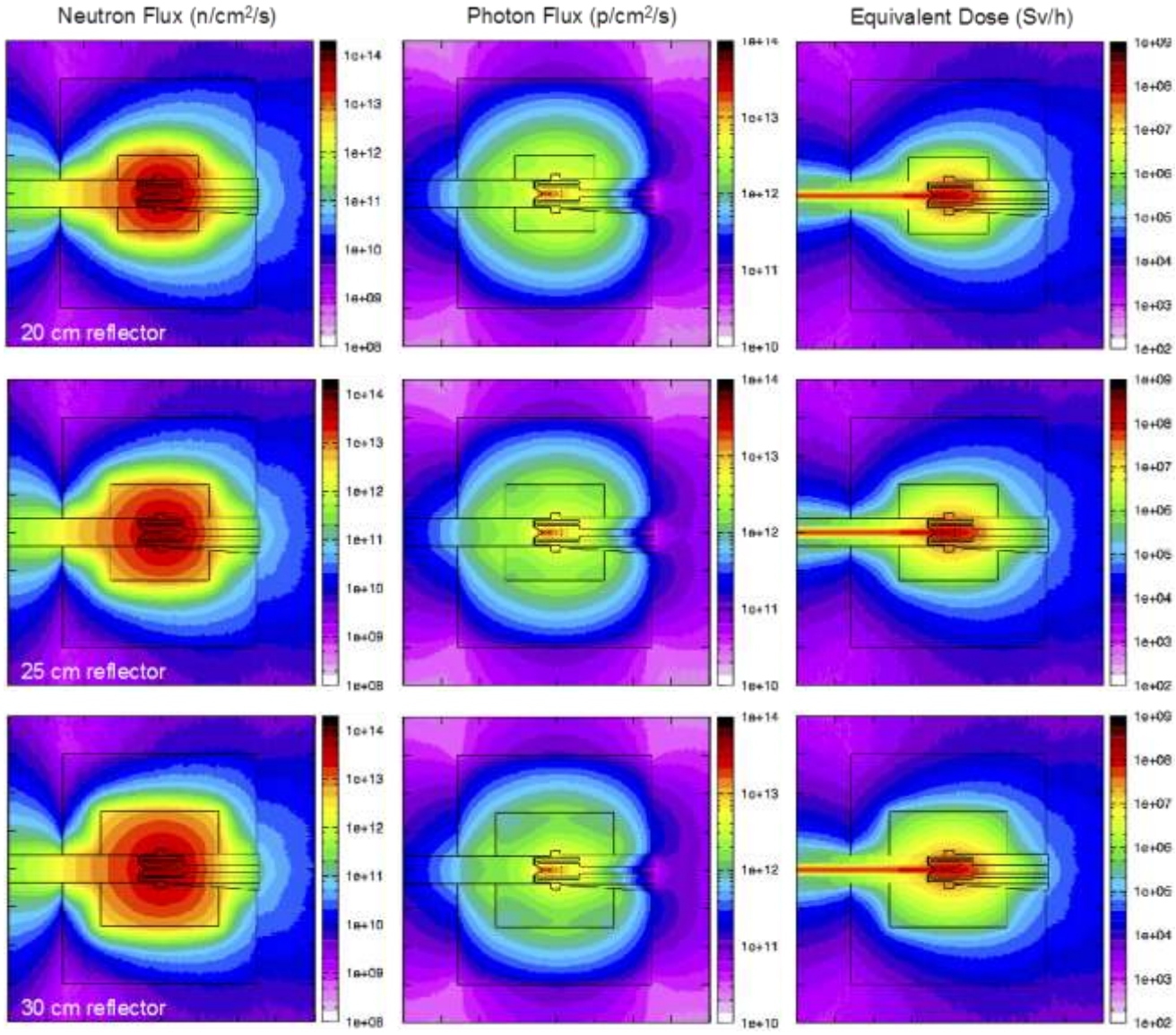

Figure 32 - Neutron and photon fluxes (1/cm^2/s) and ambient dose equivalent rates (Sv/h) in the target, graphite reflector and shielding regions, for a 100 kW beam (average values for an 8 cm thickness in the x direction).

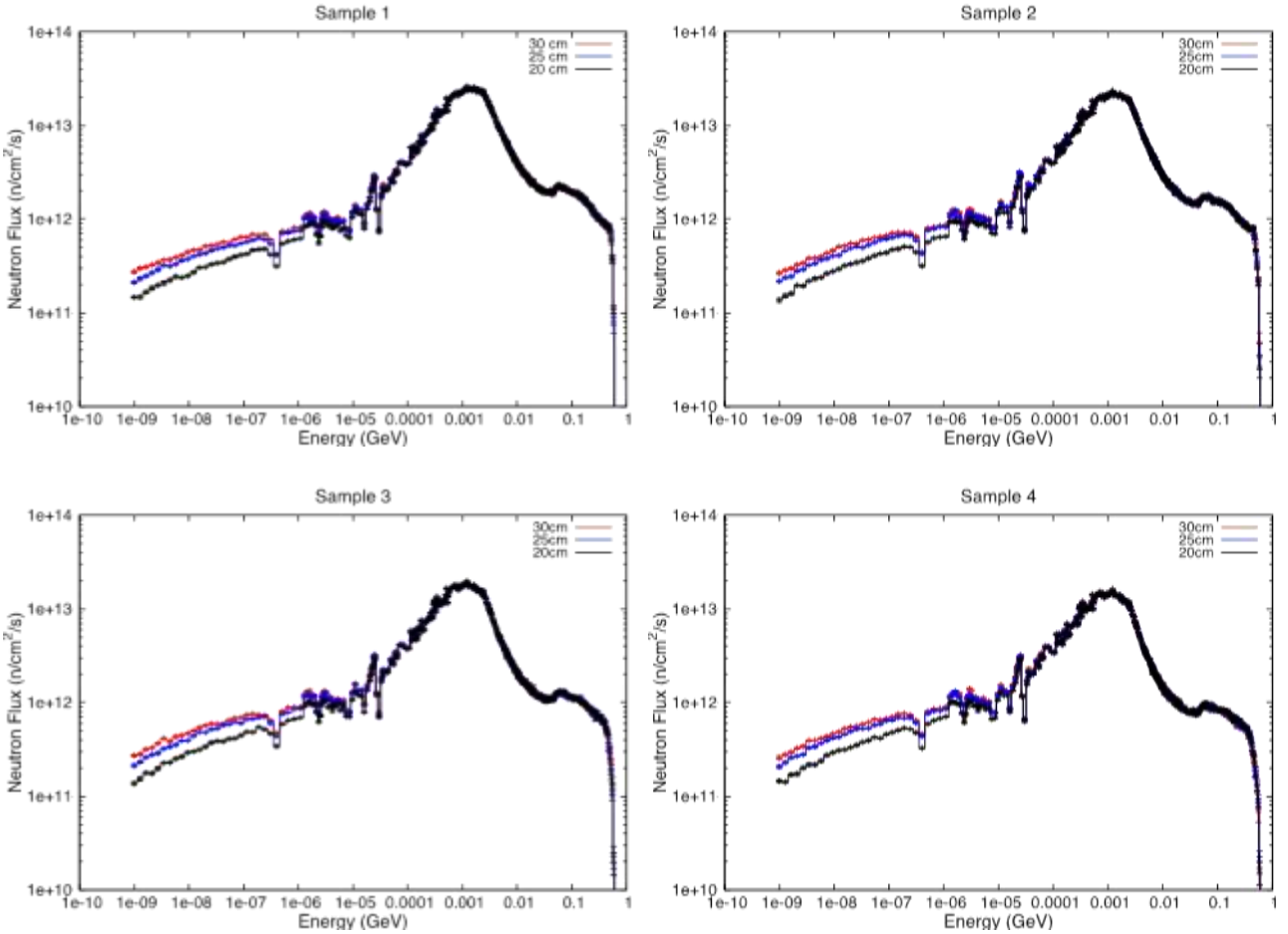

Figure 33 - Neutron flux spectra (n/cm^2/s) in the four samples, using a graphite reflector.

The reflector thickness does not affect the DPA in any of the four samples, as shown in Table 5. The DPA values are mainly due to high-energy neutrons and protons, and since the reflector does not affect the high-energy regions of the neutron spectra, there is no effect in the DPA when the reflector thickness is changed.

Table 5 - DPA/month in the four samples using graphite as reflector.

	DPA per month (stat. uncertainty < 1%)		
Sample	30 cm graphite	25 cm graphite	20 cm graphite
1	0.73	0.73	0.73
2	0.51	0.51	0.51
3	0.35	0.35	0.35
4	0.25	0.25	0.25

2.8.2 Iron reflector

The objective of using iron in the reflector is to increase the number of high-energy neutrons crossing the samples, since neutrons lose less energy when scattered off heavy nuclei. Figure 34 shows the same results as Figure 33 with iron in the reflector instead of graphite. A reduction in the neutron fluxes and equivalent dose rates outside the shielding is seen when the thickness of iron increases. The photon flux changes are more complex: although the photons are strongly attenuated in the iron, the fluxes are larger after the reflector. This is due to the emission of gamma photons in neutron capture reactions in polyethylene, an effect not so easily seen with graphite as reflector since the photons coming from the target were less attenuated, overshadowing the contribution of polyethylene as a gamma source.

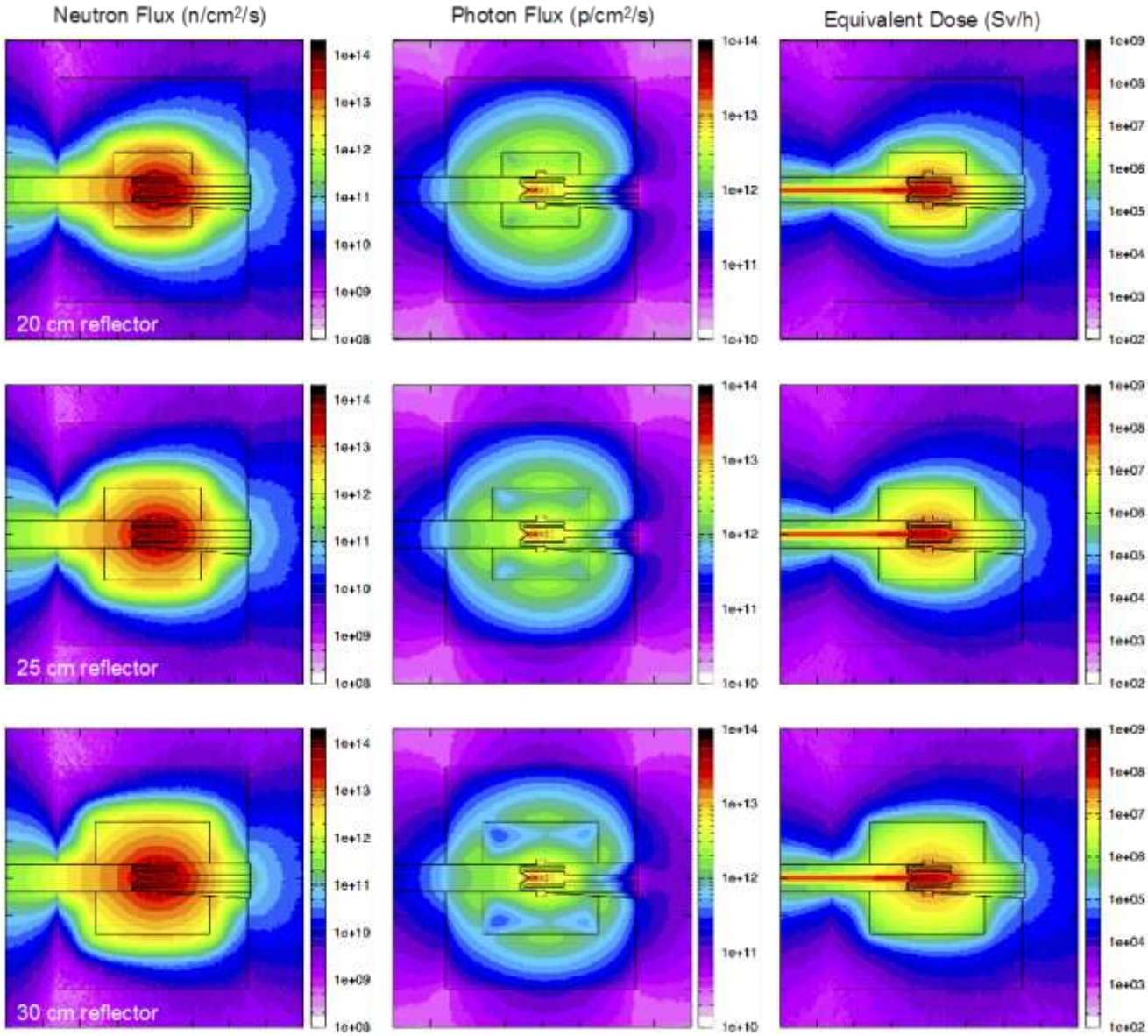

Figure 34 - Neutron and photon fluxes (1/cm^2/s) and ambient dose equivalent rates (Sv/h) in the target, iron reflector and shielding regions, for a 100 kW beam (average values for an 8 cm thickness in the x direction).

Regarding the neutron flux spectra in the samples, presented in Figure 35, the greatest differences between configurations are for energies below 100 keV. For energies up to 200 eV, a smaller reflector provides higher neutron fluxes; the opposite happens for energies between 200 eV and 20 keV. Once again, no effect is seen at higher energies. The DPA values, presented in Table 6, are also unaffected.

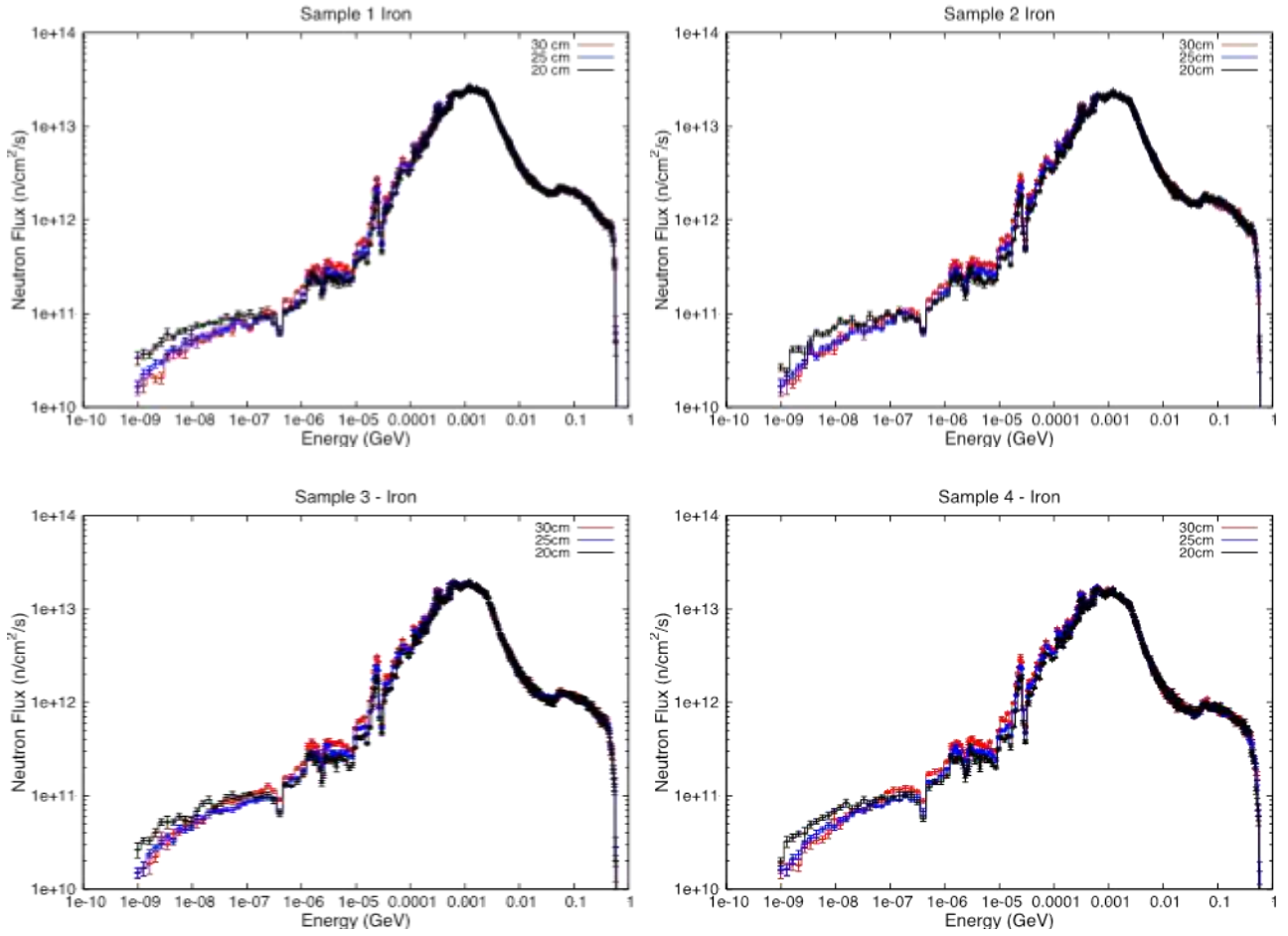

Figure 35 - Neutron flux spectra (n/cm^2/s) in the four samples, using an iron reflector.

Table 6 - DPA/month in the four samples using iron as reflector.

	DPA per month (stat. uncertainty < 1%)		
Sample	30 cm iron	25 cm iron	20 cm iron
1	0.73	0.74	0.73
2	0.52	0.51	0.51
3	0.35	0.35	0.35
4	0.25	0.25	0.25

2.8.3 Lead Reflector

Lead was also tested as reflector, and its effect in shielding neutrons and photons is seen in Figure 36. It is comparable to iron when shielding neutrons, and more effective when shielding photons, as expected. The effect on the neutron fluxes (Figure 37) is also similar to the one seen with the iron reflector, and the DPA (Table 7) are also approximately the same.

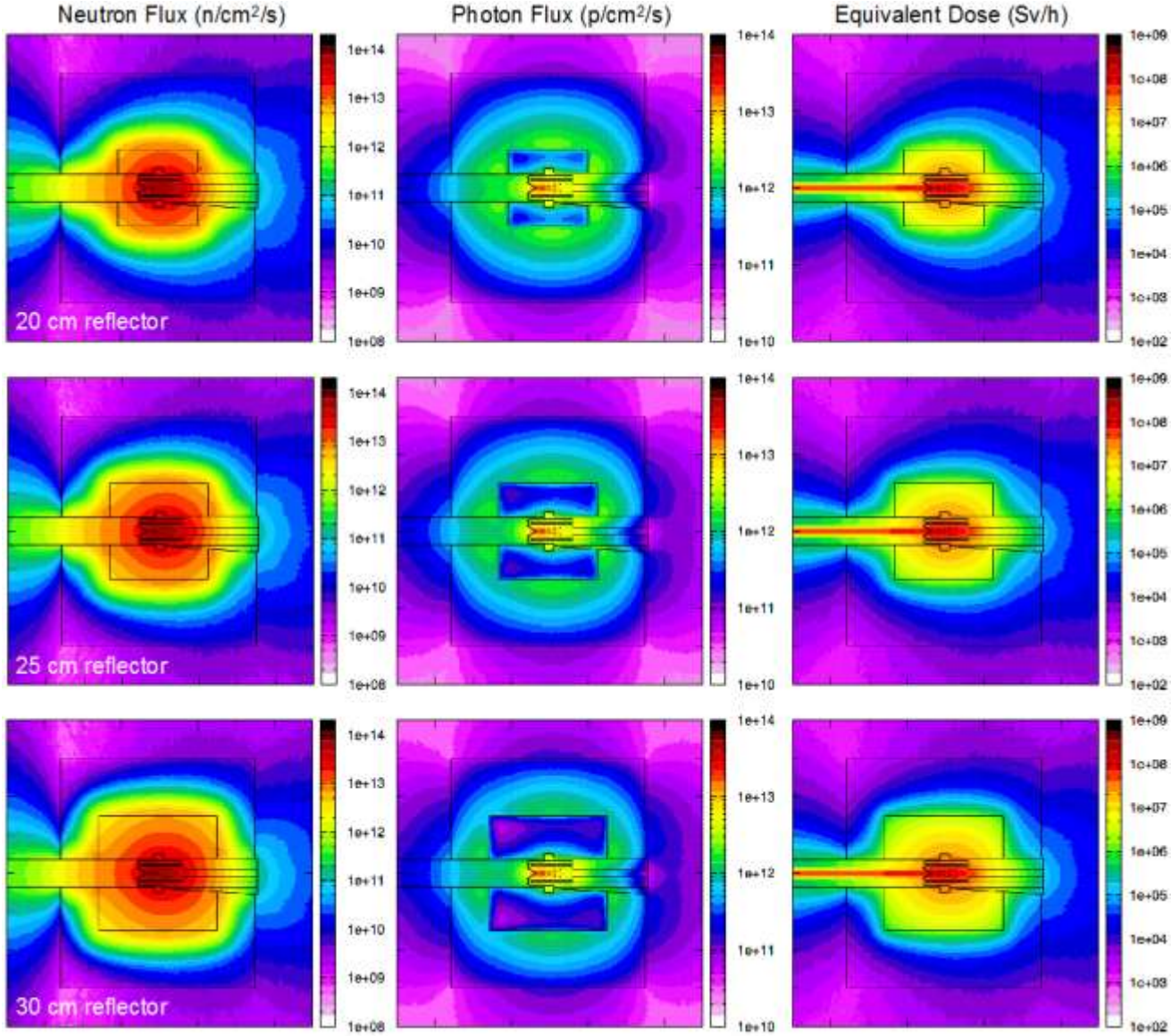

Figure 36 - Neutron and photon fluxes (1/cm^2/s) and ambient dose equivalent rates (Sv/h) in the target, lead reflector and shielding regions, for a 100 kW beam (average values for an 8 cm thickness in the x direction).

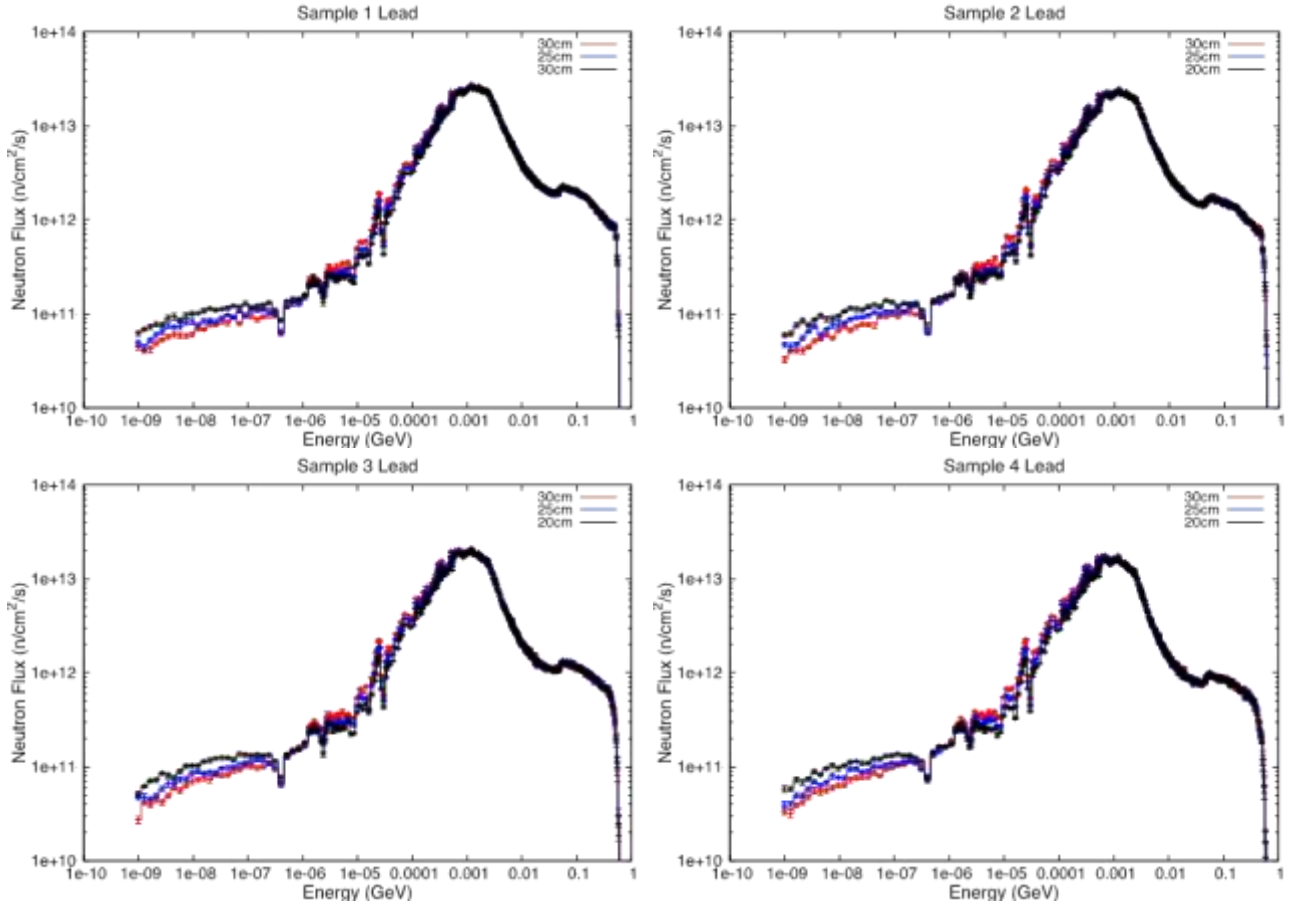

Figure 37 - Neutron flux spectra (n/cm^2/s) in the four samples, using a lead reflector.

	DPA per month (stat. uncertainty < 1%)		
Sample	30 cm lead	25 cm lead	20 cm lead
1	0.74	0.73	0.73
2	0.52	0.52	0.51
3	0.35	0.35	0.35
4	0.25	0.25	0.25

Table 7 - DPA/month in the four samples using lead as reflector.

2.8.4 Water reflector

Using water in the reflector has approximately the same effect as using only polyethylene and removing the reflector, since as previously mentioned, the two materials have approximately the same density and similar characteristics. This is confirmed by Figure 39, which shows that the neutron flux spectra are not affected by the thickness of the water reflector. The same applies for shielding considerations (Figure 38) and for the DPA values (Table 8).

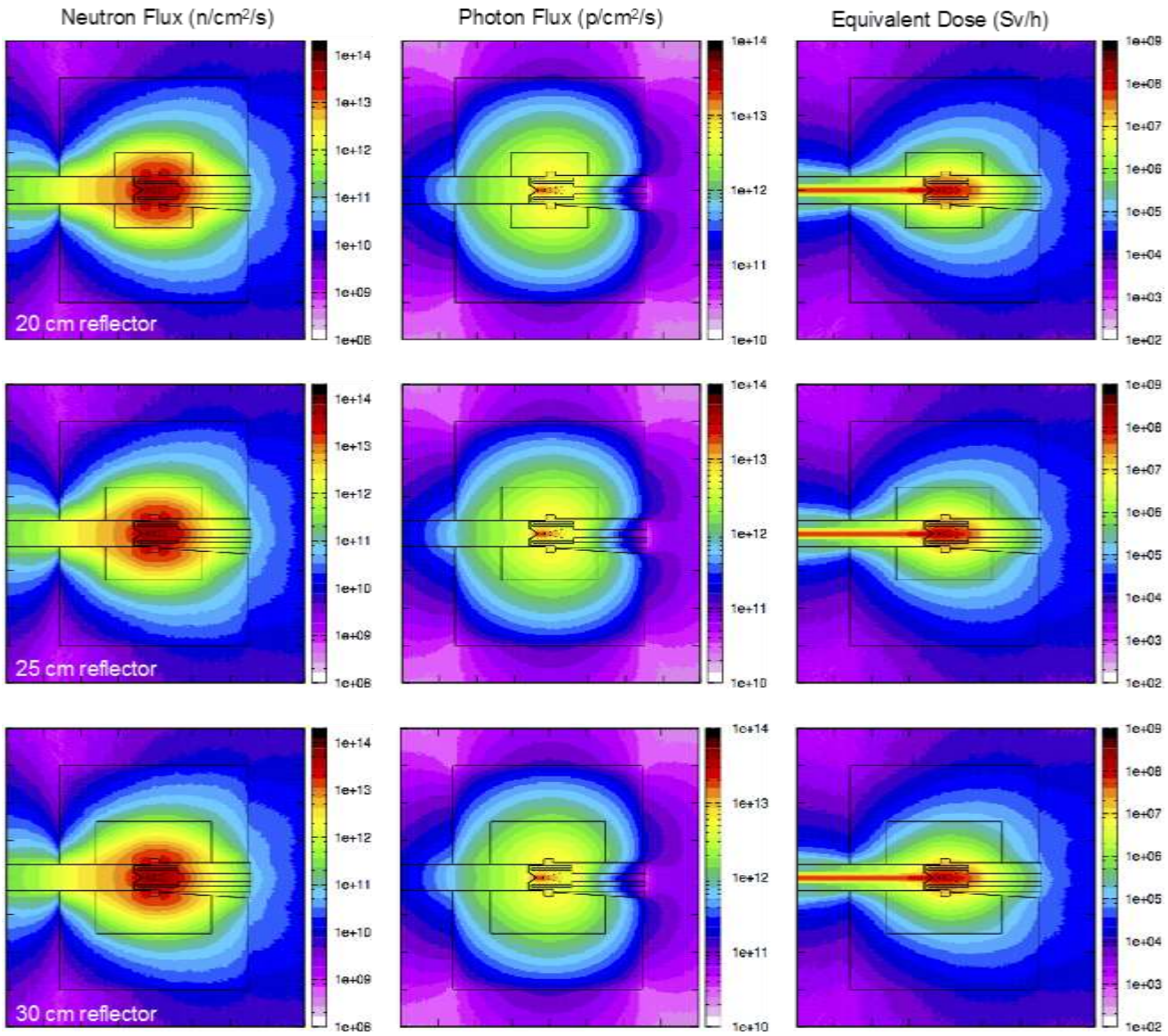

Figure 38 - Neutron and photon fluxes (1/cm^2/s) and ambient dose equivalent rates (Sv/h) in the target, water reflector and shielding regions, for a 100 kW beam (average values for an 8 cm thickness in the x direction).

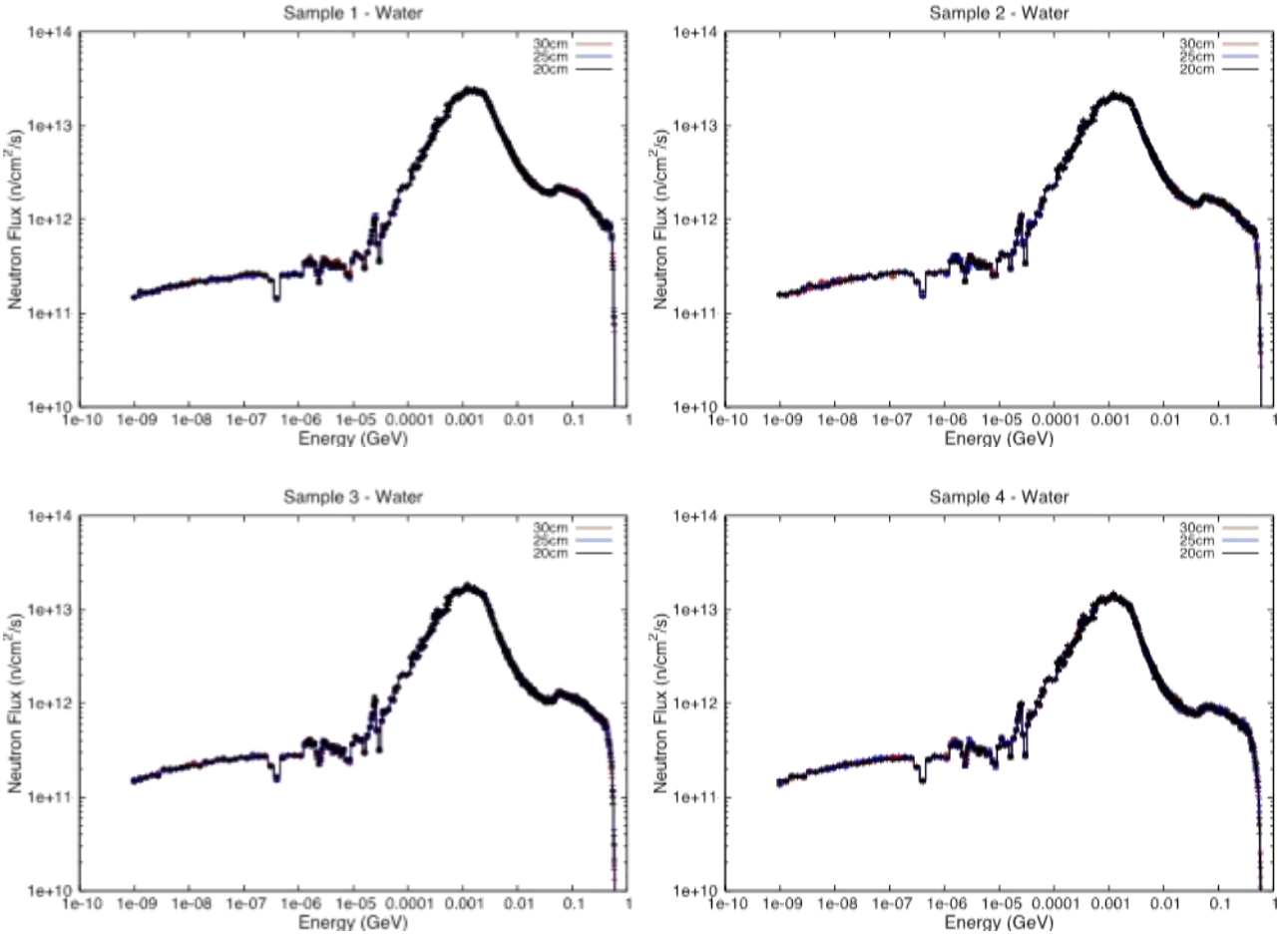

Figure 39 - Neutron flux spectra (n/cm^2/s) in the four samples, using a water reflector.

Table 8 - DPA/month in the four samples using water as reflector.

	DPA per month (stat. uncertainty < 1%)		
Sample	30 cm water	25 cm water	20 cm water
1	0.71	0.71	0.71
2	0.49	0.49	0.49
3	0.33	0.33	0.33
4	0.23	0.23	0.23

2.8.5 Marble reflector

The last material tested in the reflector was marble ($CaCO_3$), which has a high density (2.7 g/cm^3) when compared to the other light-nuclei reflectors. For shielding purposes (Figure 40), there is little difference between using marble, light water or graphite. The neutron flux spectra are also not changed in the high-energy part of the spectrum, as shown in Figure 41, nor the DPA values, presented in the table

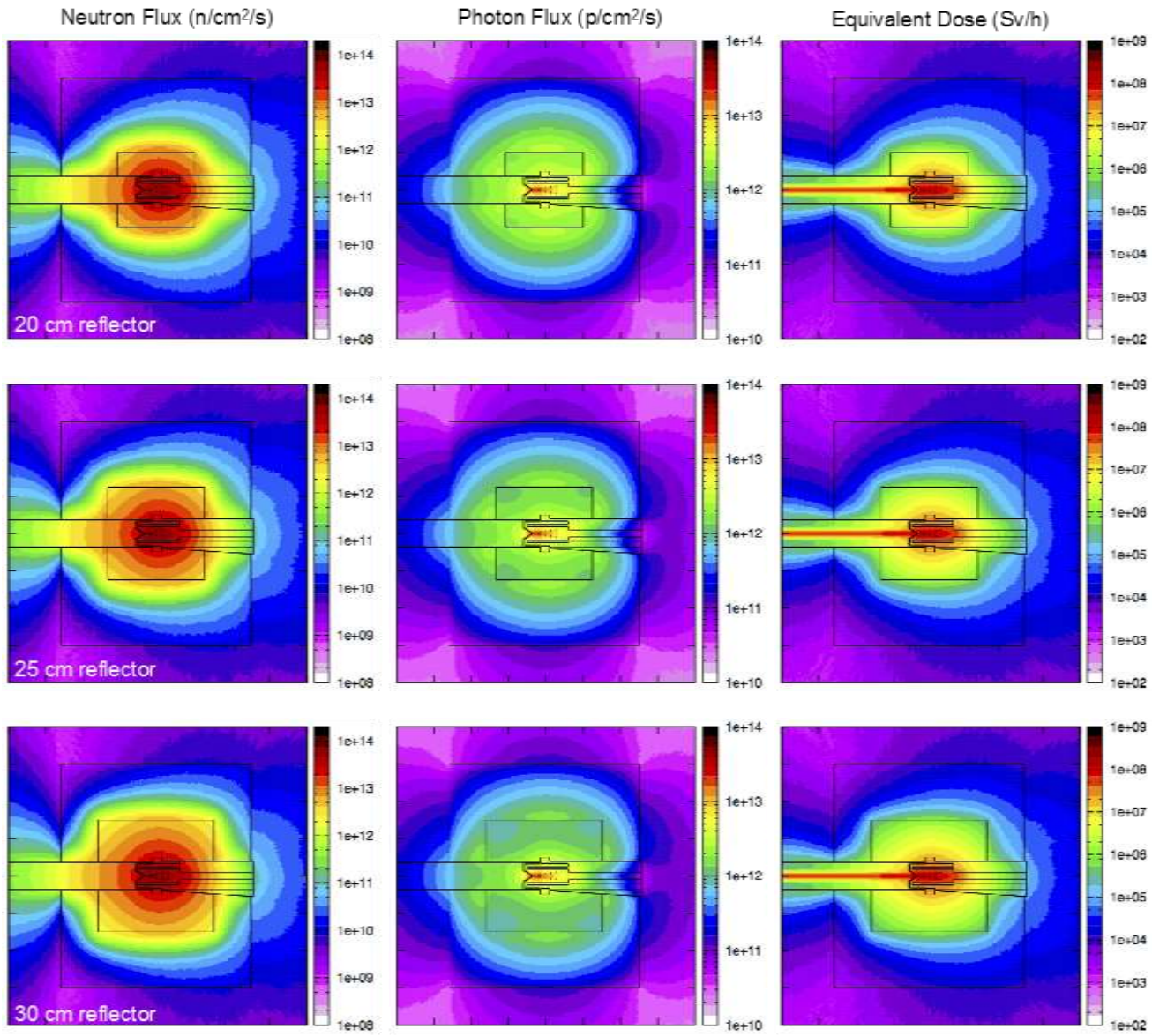

Figure 40 - Neutron and photon fluxes (1/cm^2/s) and ambient dose equivalent rates (Sv/h) in the target, marble reflector and shielding regions, for a 100 kW beam (average values for an 8 cm thickness in the x direction).

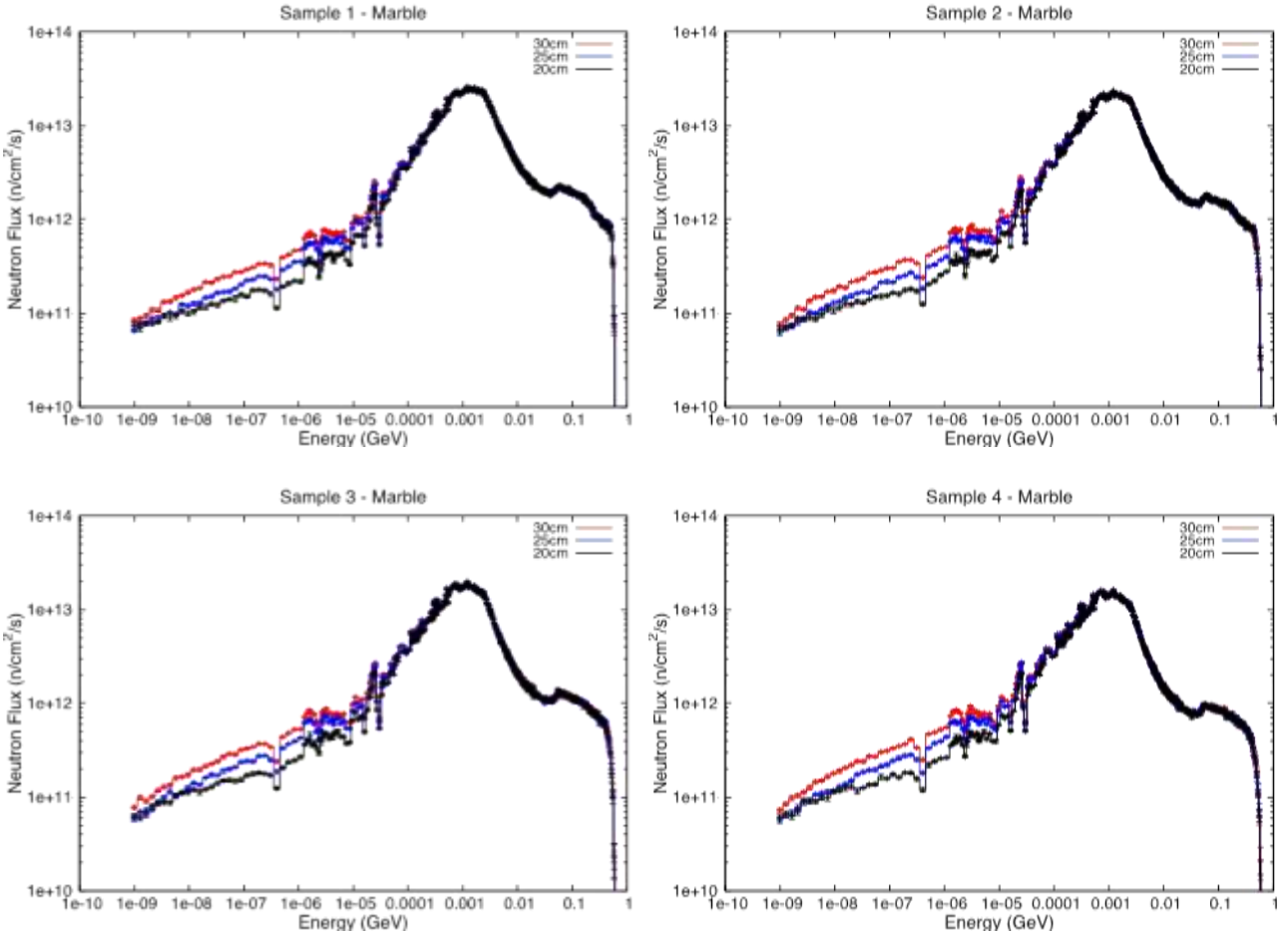

Figure 41 - Neutron flux spectra (n/cm^2/s) in the four samples, using a marble reflector.

	DPA per month (stat. uncertainty < 1%)		
Sample	30 cm marble	25 cm marble	20 cm marble
1	0.73	0.71	0.71
2	0.51	0.51	0.50
3	0.35	0.34	0.34
4	0.24	0.25	0.24

Table 9 - DPA/month in the four samples using marble as reflector.

2.8.6 No reflector (target surrounded by polyethylene only)

Finally, using polyethylene in the reflector is similar to using water, as previously mentioned. The results are shown in Figure 43, Figure 44 and Table 10.

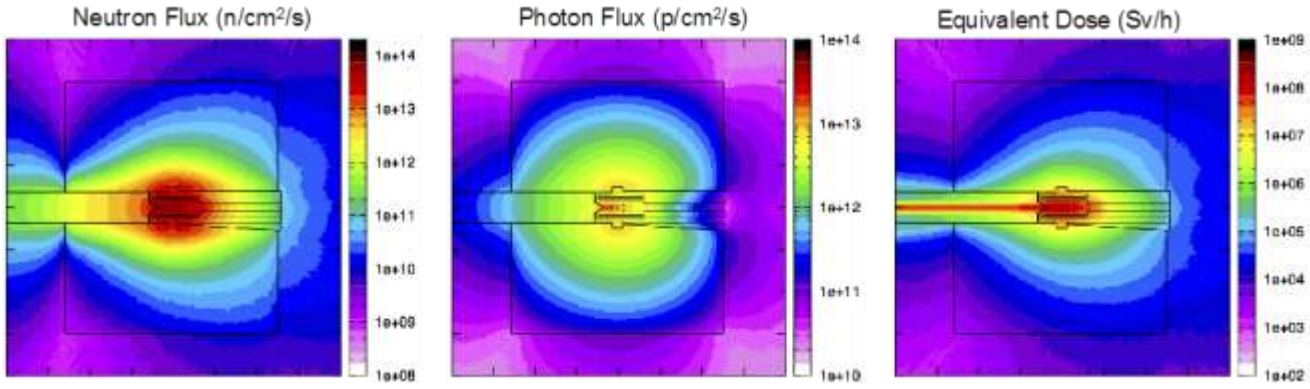

Figure 42 - Neutron and photon fluxes (1/cm^2/s) and ambient dose equivalent rates (Sv/h) in the target and shielding regions without reflector, for a 100 kW beam (average values for an 8 cm thickness in the x direction).

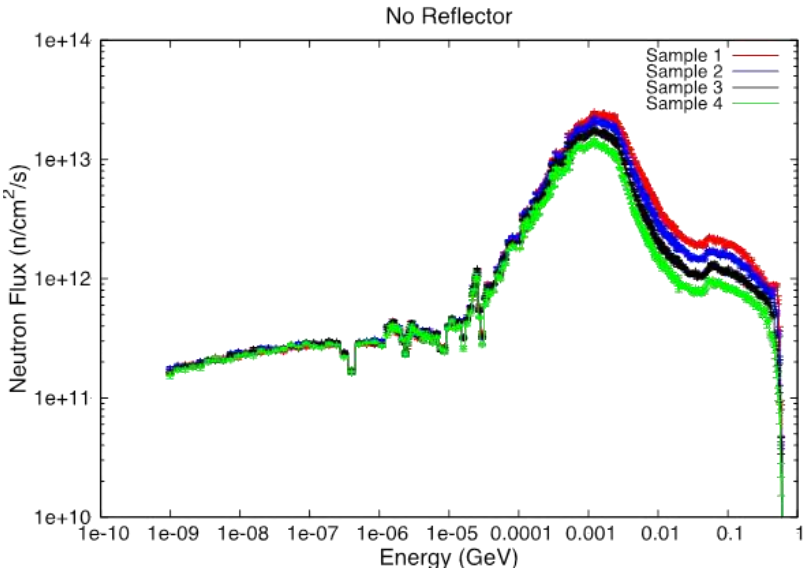

Figure 43 - Neutron fluxes (n/cm^2/s) in the four samples without reflector.

Table 10 - DPA/month in the four samples, without reflector.

Sample	DPA per month
1	0.71
2	0.49
3	0.34
4	0.23

2.8.7 Summary and Conclusions of the reflector studies

The first and most important conclusion of the study presented in this section is that using graphite, iron, lead, water or marble in the reflector has no effect in the DPA values in the samples, since the most energetic neutrons are not affected by the reflector material. For the shielding, the lowest neutron fluxes were obtained with the configuration with the thickest lead reflector. Since the reflector material does not affect the DPA values, this would be a good reason to choose a dense material for the reflector in order to shield against gammas from the target after shutdown.

A direct comparison between the neutron flux spectra in the four samples using the different tested reflectors is presented in Figure 44. For comparison, the case when no reflector or shielding is used is also presented, with the target surrounded by vacuum. It shows that the amount of reflected neutrons with energies above 1 MeV is negligible, for all tested materials. For lower energies, the highest fluxes are obtained with graphite. Nevertheless, these neutrons are a small fraction of the total number of neutrons and have no effect on the DPA values.

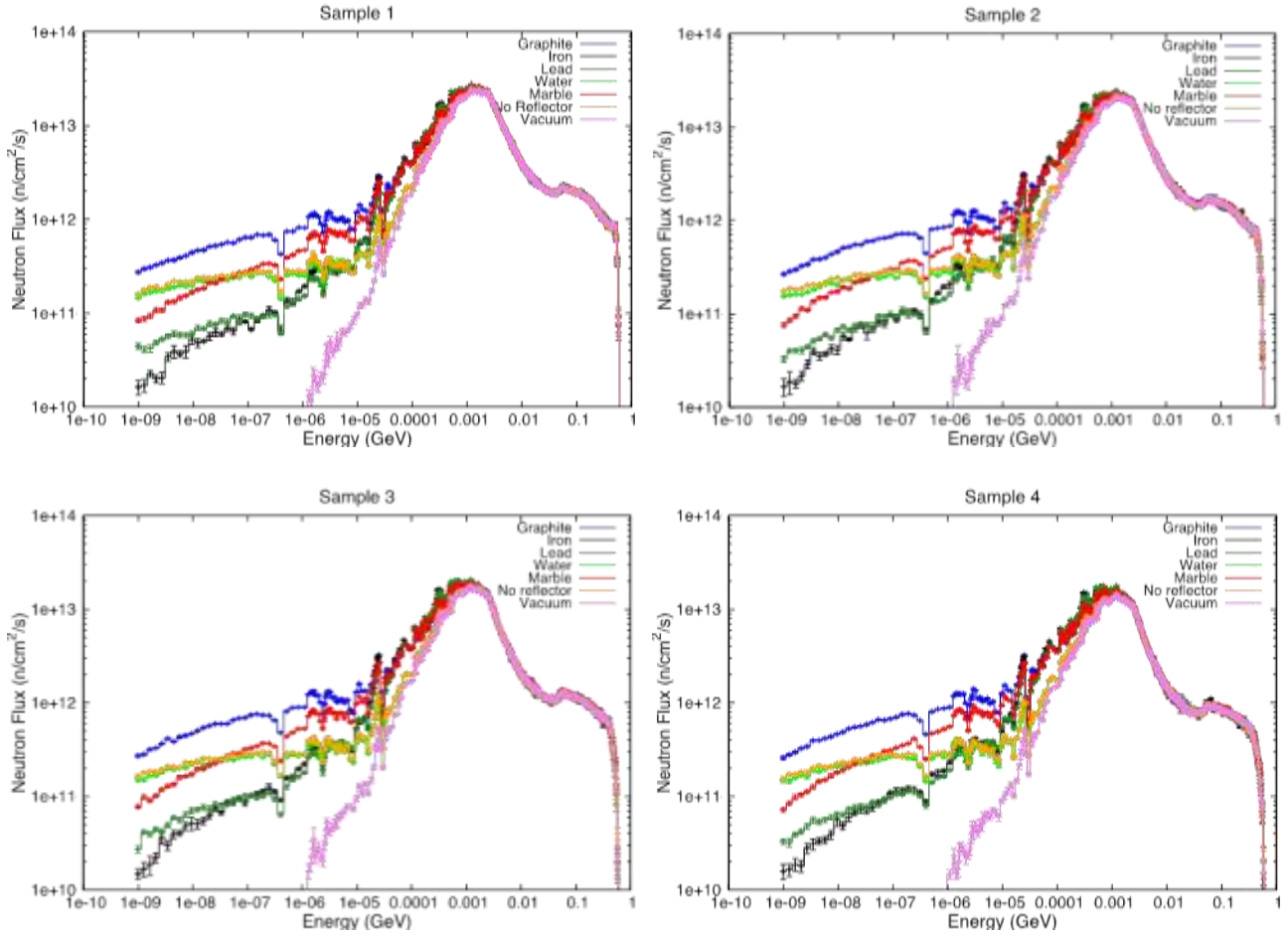

Figure 44 - Neutron flux spectra (n/cm^2/s) in the four samples - direct comparison between different reflectors.

2.9 Shielding Studies

The first step in the shielding studies was to update the design of the target, which evolved from the previous configuration to the one presented in Figure 45. The main differences are in the back part of the target and do not affect the results presented in the previous sections.

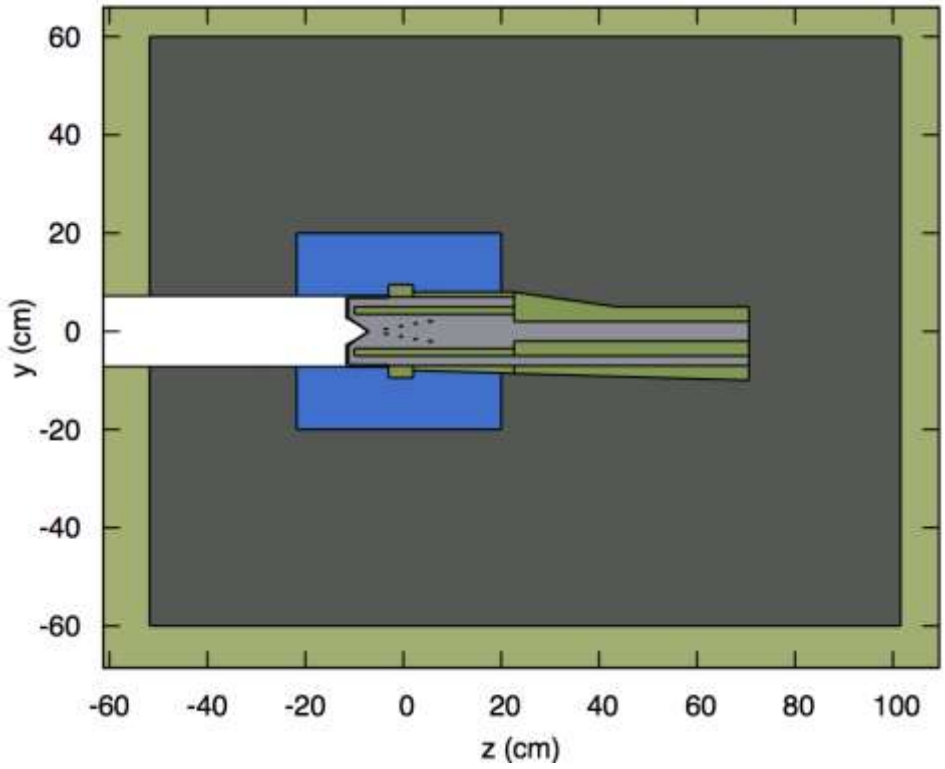

Figure 45 - New design of the target, used for dimensioning the shielding.

The objective of the first simulations was to assess the effect of using borated polyethylene in the neutron and photons fluxes and ambient equivalent dose rates outside the target. Four simulations were run for this purpose, using simple polyethylene and borated polyethylene with 5%, 10% and 30% of boron-10. The thickness of the polyethylene shielding is as shown in Figure 45, with a total thickness of 120 cm in the x and y directions and 152 cm in the z direction. In the first round of simulations, graphite was kept as the reflector material, and the smallest thickness was chosen.

There is no significant reduction in the neutron fluxes and dose rates outside the shielding when borated polyethylene is used instead of simple polyethylene. The reason is that the neutrons are very energetic, and the neutron absorption cross-section in boron-10 is small for high-energy neutrons. Furthermore, when the weight fraction of boron is increased, the corresponding weight fractions of carbon and hydrogen decrease; thus, increasing the weight fraction of boron decreases the moderating power of the shielding material. A better alternative could be to increase the thickness of polyethylene and add an outer layer of borated polyethylene to absorb the moderated neutrons. Since the neutron fluxes outside the shielding are still in the interval 10^9-10^{11} neutrons/cm^2/s, more shielding will be necessary.

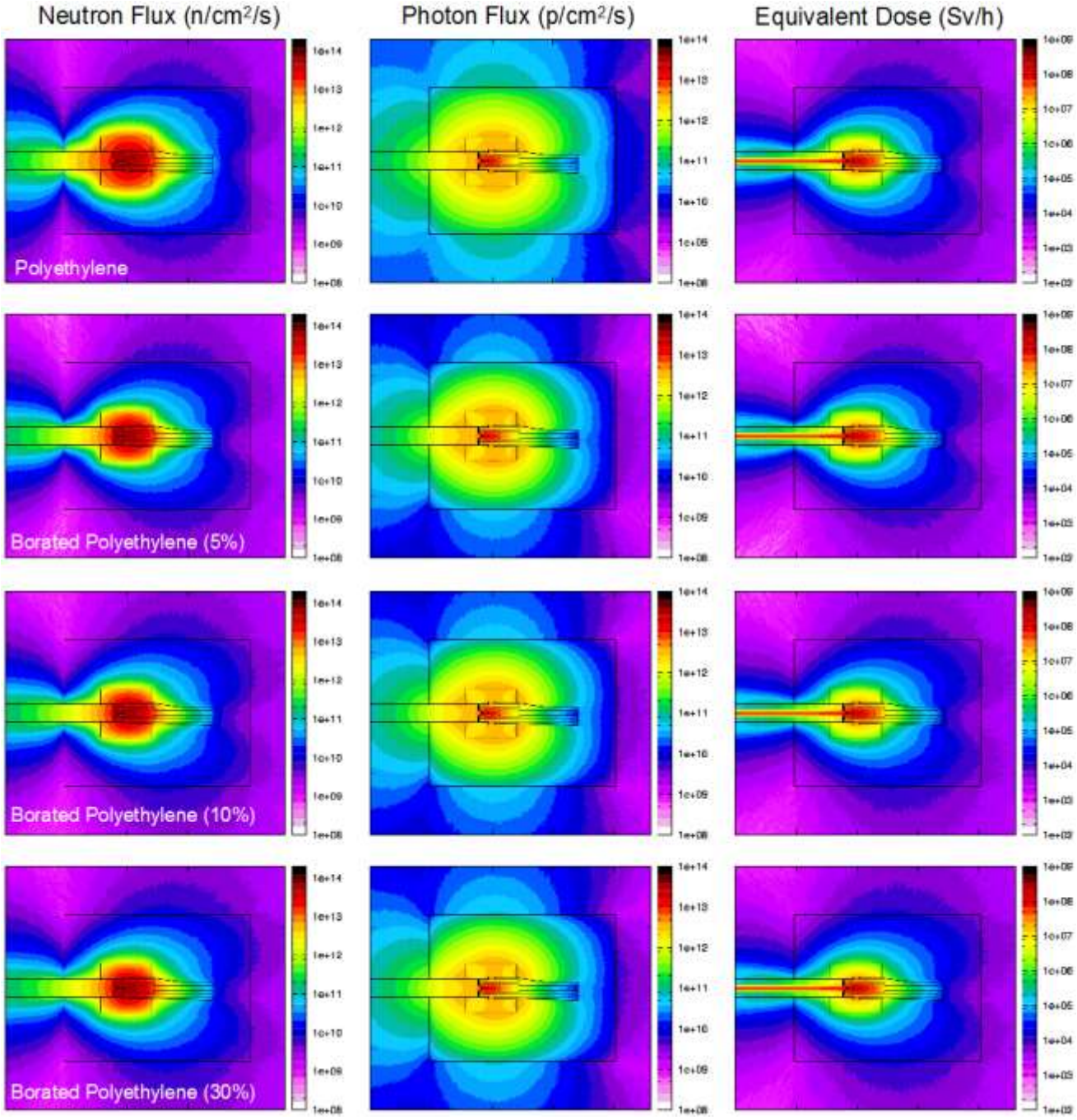

Figure 46 - Neutron and photon fluxes (1/cm^2/s) and ambient dose equivalent rates (Sv/h) in the target and shielding regions using four shielding materials: polyethylene and borated polyethylene with three different weight fractions of boron (5%, 10% and 30 %).

The next step consisted in increasing the thickness of the shielding to 200 cm in the x and y directions and to 182 cm in the z direction. The reflector was changed to iron, since the previous section demonstrated that iron would be better to decrease the particle fluxes and dose rates outside the shielding. Four simulations were run, with the following shielding dimensions:

- 2 m of polyethylene shielding;
- 2 m of shielding with polyethylene and an outer 10 cm thick layer of 10% borated polyethylene (the total thickness of the shielding was kept the same)
- 3 m of polyethylene shielding;

- 3 m of shielding with polyethylene and an outer 20 cm thick layer of 10% borated polyethylene

In all cases, the shielding is thicker in the x and y directions than in the z direction. The results are shown in Figure 47. Once again, no significant difference in the fluxes appears when using the outer layer of borated polyethylene. The neutron fluxes outside the shielding are still in the order of 10^8 n/cm^2/s, which indicates that the shielding thickness must be further increased.

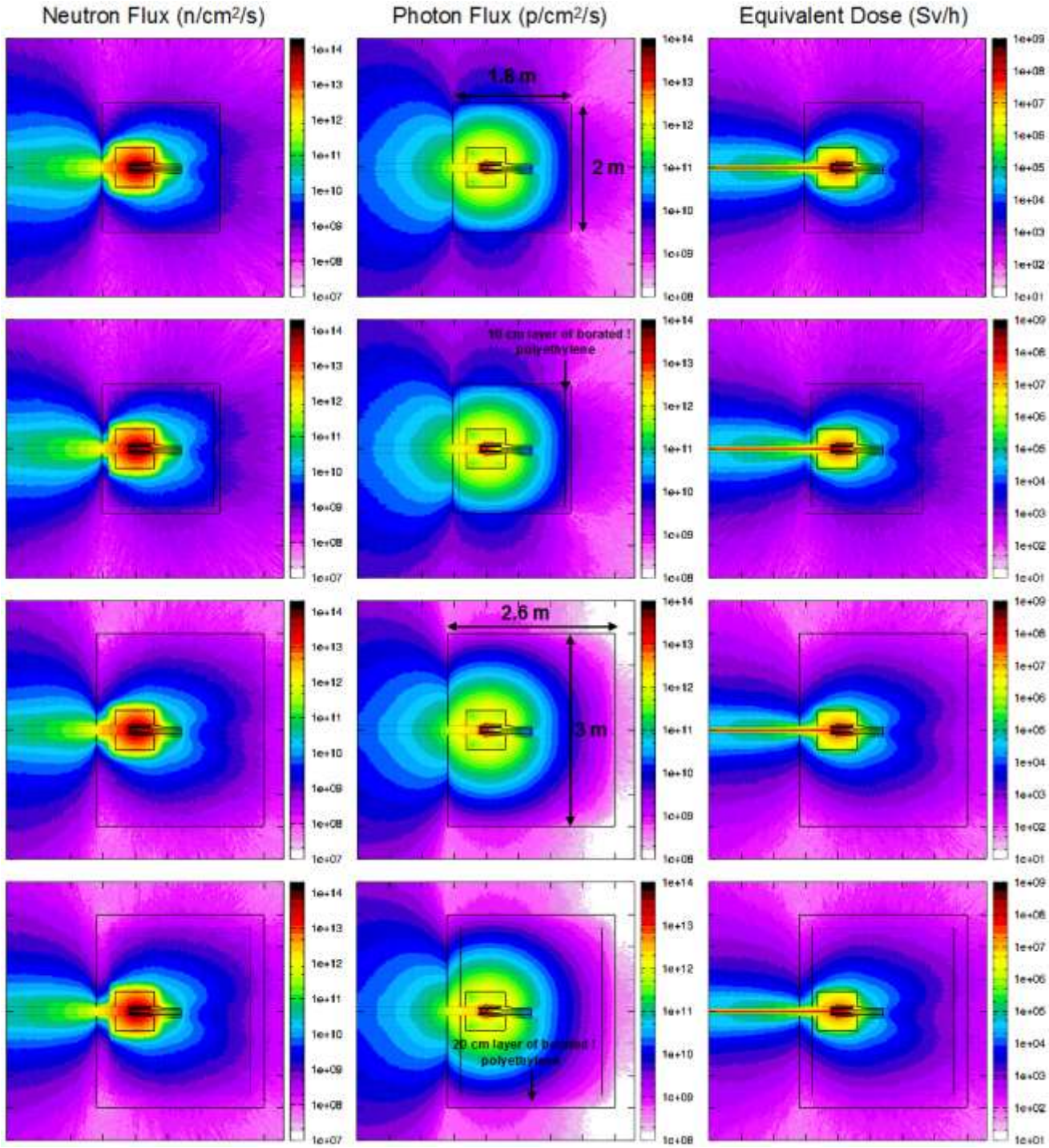

Figure 47 - Neutron and photon fluxes (1/cm^2/s) and ambient dose equivalent rates (Sv/h) in the target and shielding regions for four shielding configurations.

The neutron fluxes after the shielding were examined, by adding two neutron detectors to the simulations: one behind the target and the other above the target, at z=0 (both after the shielding). The results (Figure 48) show that high-energy neutrons account for most of the neutron fluxes, even above the target. The outer layer of borated polyethylene removes the peak of low-energy neutrons, but the effect on the integrated flux is not significant, since low-energy neutrons account for a small fraction of the total flux. These results show clearly that the first priority must be to find a design solution to moderate the high-energy neutrons.

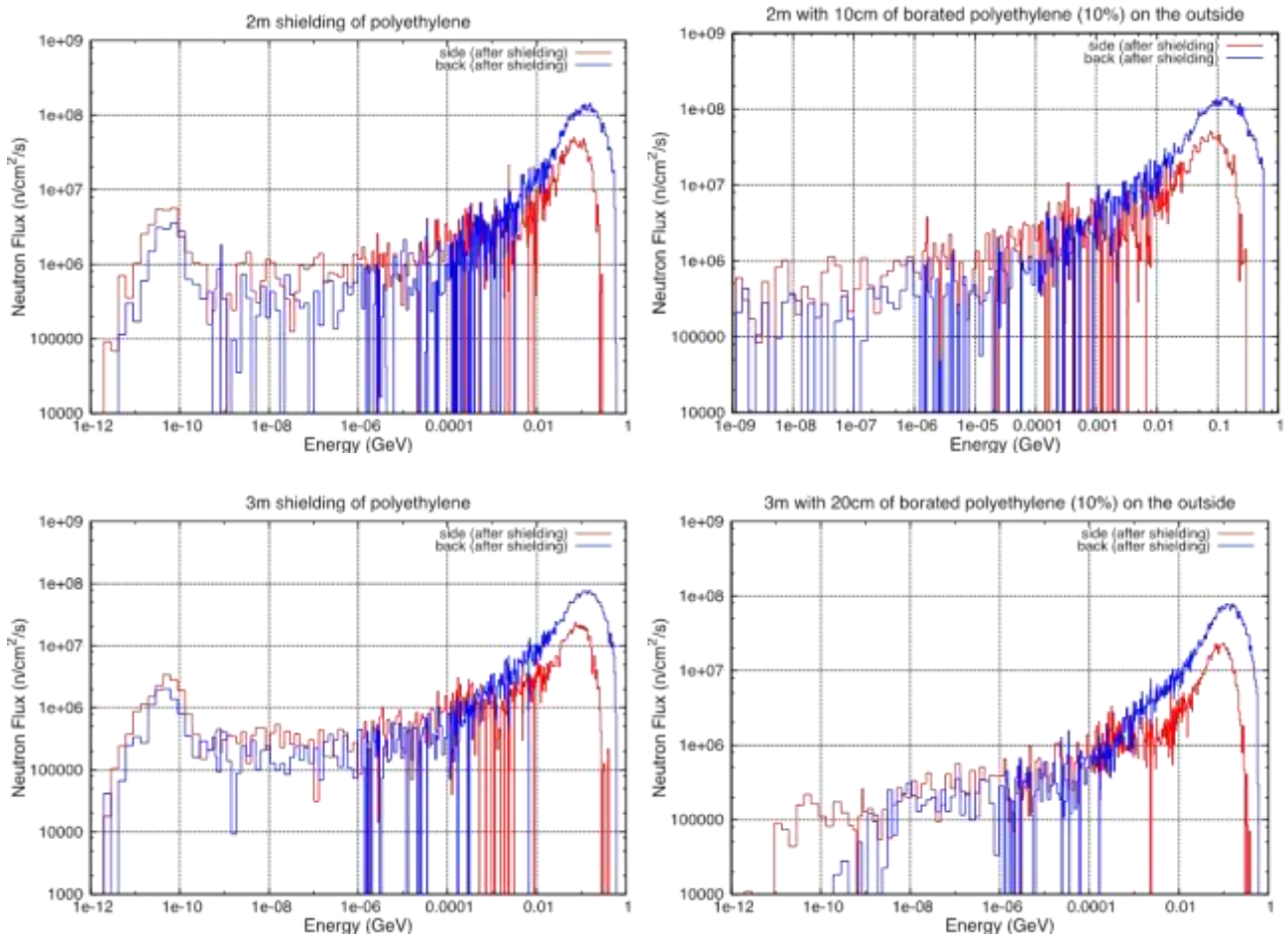

Figure 48 - Neutron flux spectra after the shielding, behind the target ("back") and above the target ("side"), for four shielding configurations.

The introduction of a layer of lead after the iron reflector was also tested, to reduce the photon fluxes and to check the effect of this reduction in the equivalent dose. The results, presented in Figure 49, show that the photon fluxes are indeed reduced by the introduction of this layer, but the neutron fluxes for energies between 100 keV and 10 MeV are increased (Figure 50). Overall, the equivalent dose rate is slightly increased with the introduction of a thin 5 cm layer of lead around the target.

In all the attempts to reduce the shielding requirements, it seems clear that the high-energy neutrons play a major role in the dose rates. Hence, the next question to be examined was whether the beam energy could be reduced, to lower the energies of the neutrons exiting the central spallation region, making shielding an easier task. The effect of reducing the proton beam energy in the fluxes and doses outside the shielding and the corresponding impact on the DPA values in the samples are addressed in the next section.

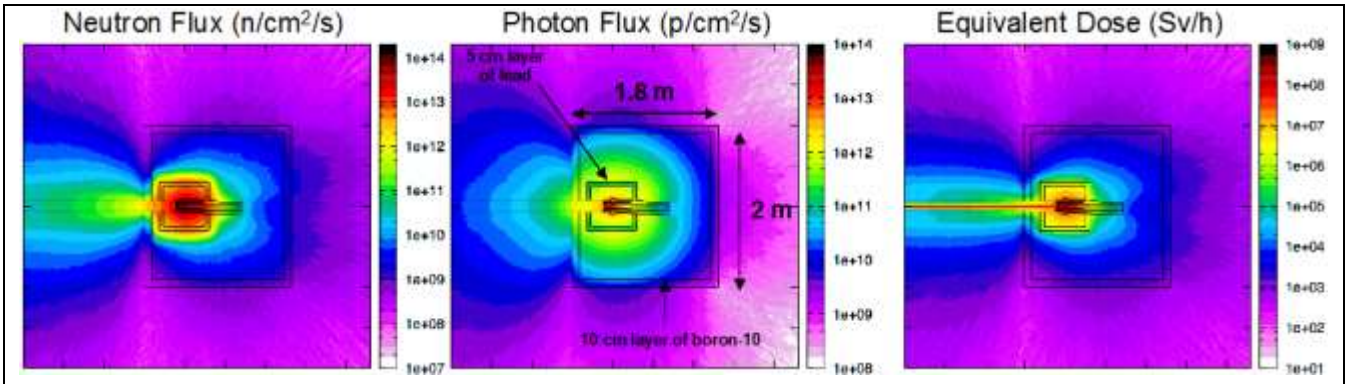

Figure 49 - Neutron and photon fluxes (1/cm^2/s) and ambient dose equivalent rates (Sv/h) in the target and shielding regions, using a 5 cm layer of lead and a 10 cm outer layer of boron-10.

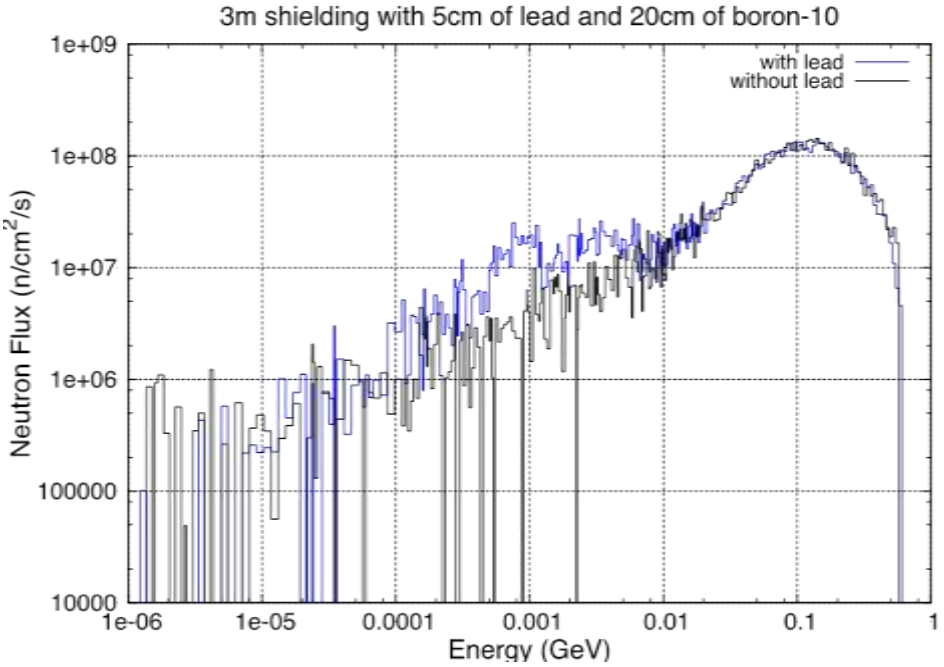

Figure 50 - Neutron flux spectra after the shielding, behind the target, using a 10 cm outer layer of boron-10. In one of the configurations ("with lead"), a 5 cm layer of lead surrounds the reflector material.

2.10 Beam Analysis

2.10.1 Beam Energies

The beam energy was varied from 1 GeV to 200 MeV. In order to be consistent, the beam current was adapted so that the overall beam power is the same. This was necessary for a fair comparison, as the overall costs of such a facility are roughly proportional to the power of the beam. The figures below demonstrate quite clearly the beneficial effect of lowering the beam energy, since there is a clear improvement in lowering the dose rate due to the spectrum (Figure 52).

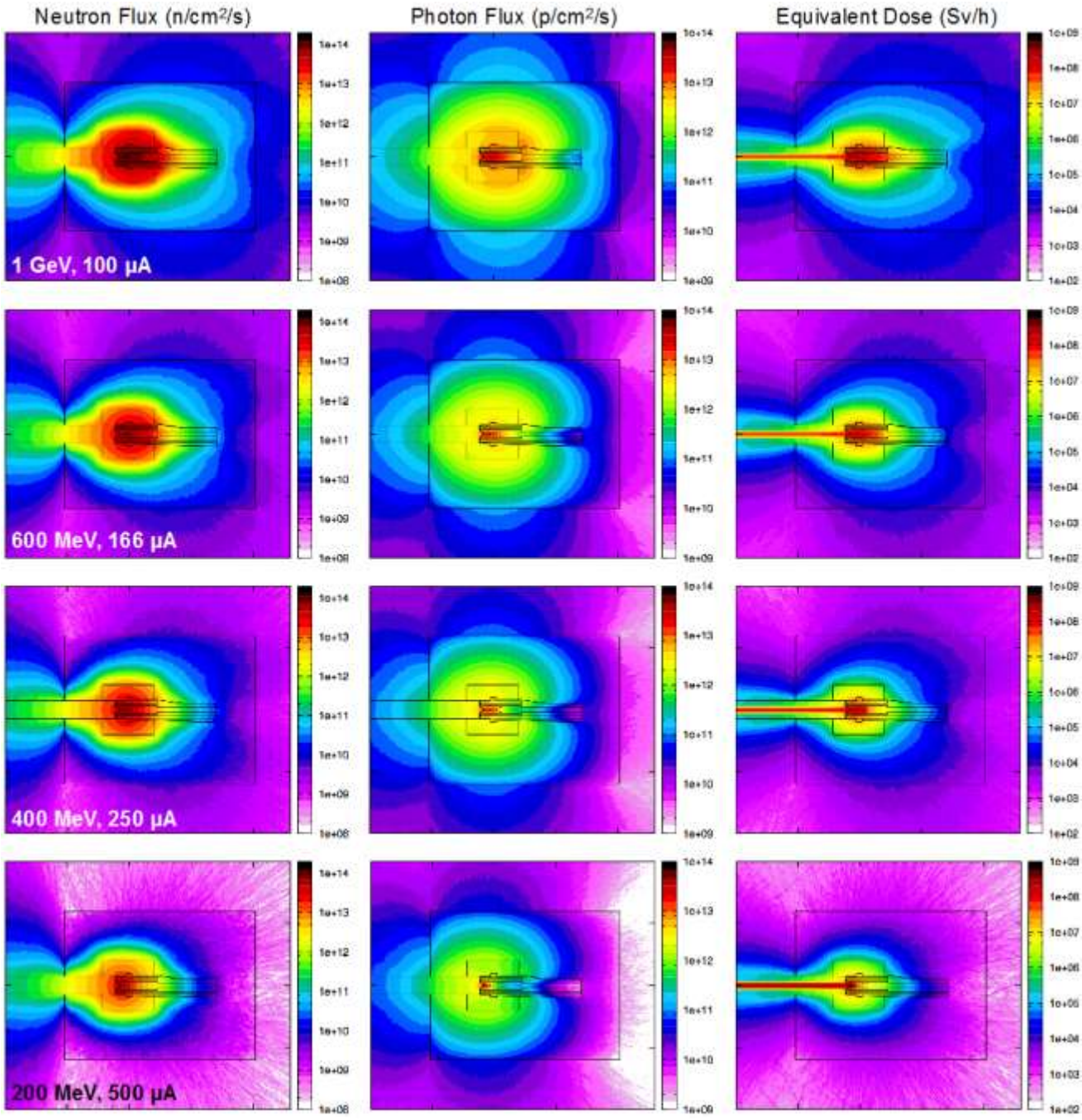

Figure 51 - Neutron and photon fluxes (1/cm^2/s), ambient dose rates (Sv/h) for four primary beam energies and intensities at same power, with 20 cm graphite reflector, 40 cm polyethylene shielding.

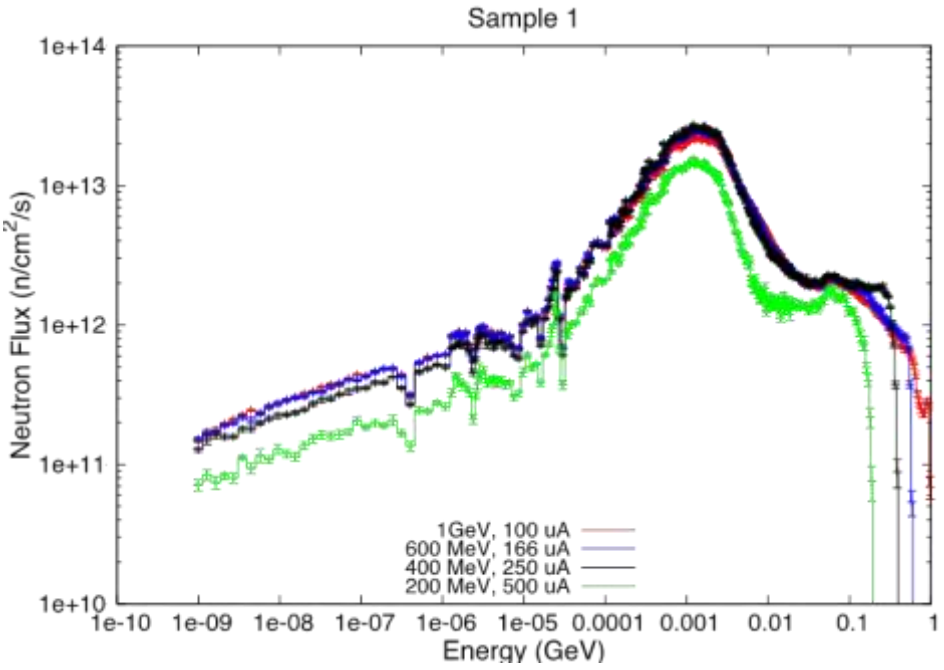

Figure 52 - Neutron flux spectra (n/cm^2/s) in sample 1 - comparison between different beam energies and intensities.

The reduced spallation production at lower beam energies could be feared to result in less DPAs in the sample. Remarkably, this is not the case; indeed, the DPA values are maximised for a beam energy around 400 MeV. This may be in part due to the fact that spallation production rates only reduce markedly below 200 MeV, and at 400 MeV the proportion of reflected neutrons might be slightly higher. The spectrum in Figure 52 shows a tail end in the high-energy regions for 400 MeV that is clearly superior to the 600 MeV and 1 GeV case; a reasonable explanation for the higher DPA values shown in Table 11. Given that the 200 MeV case has the same DPA production rate as at 600 MeV but is far superior in shielding, an optimum beam may be found in the region between 200 and 400 MeV.

	DPA per month (stat. uncertainty < 1%)			
Sample	1 GeV 100 µA	600 MeV 166 µA	400 MeV 250 µA	200 MeV 500 µA
1	0.60	0.73	0.85	0.72
2	0.45	0.51	0.54	0.08
3	0.33	0.34	0.35	0.04
4	0.25	0.25	0.20	0.03

Table 11 - DPA/month in the four samples using 1GeV, 600 MeV, 400 MeV and 200 MeV proton beams.

Another possibility for increasing the DPA without further complicating the shielding requirements may be to reduce the width of the beam to concentrate more proton damage on the central part of the sample at the expense of its extremities. Micro-testing of samples barely 2 mm in length is

common, such that although the number of samples would be reduced, this may be of interest for material scientists.

2.10.2 Beam Dimensions

The ratio of long axis to short axis was changed from 6 to 1.7; the latter ratio matches exactly the elliptical geometry of the beam window. Hence it is hoped that apart from increasing the DPAs on the sample, a beneficial effect will also ensue in terms of the thermal stresses in the window.

The DPA values with a 400 MeV proton beam and a Gaussian profile with σ_x = 1.7 cm and σ_y = 1.0 cm are shown in the table Indeed, the DPA values are greatly increased with the new beam dimensions. In the first sample, the DPA is more than doubled, with both the contributions from protons and from neutrons above the total DPA with the previous beam. The contributions from protons and neutrons vary from 58.1%-40.6% in the first sample to 45.1%-54% in the fourth sample, a less pronounced variation than with the previous beam. Nonetheless, it is clear the new beam shape should be preferred to the previous one, since it will allow the production of up to 23 DPA per year in the first sample. The detailed results for power deposition and DPA in the samples and window are presented from Figure 53 to Figure 57.

Sample	DPA/month (stat. uncertainty)	Contribution from protons	Contribution from neutrons
1	1.91 (0.1%)	58.1%	40.6%
2	1.16 (0.3%)	49.8%	49.2%
3	0.70 (0.3%)	44.5%	54.5%
4	0.41 (0.4%)	45.1%	54.0%

Table 12 - DPA/month in the four samples and respective contributions from protons and neutrons with a 400 MeV proton beam (σ_x = 1.7 cm, σ_y = 1.0 cm).

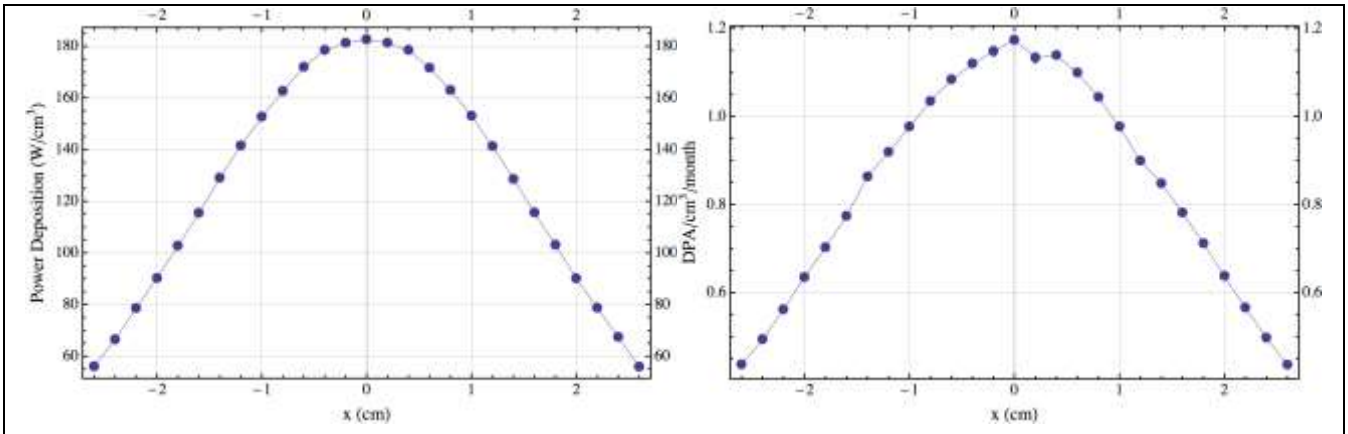

Figure 53 - Power deposition (W/cm^3) and DPA/cm^3/month as a function of x in the first sample.

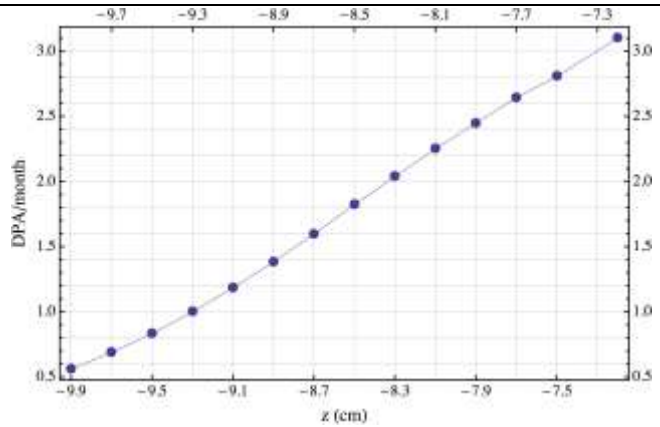

Figure 54 - DPA/month as a function of z in the target window.

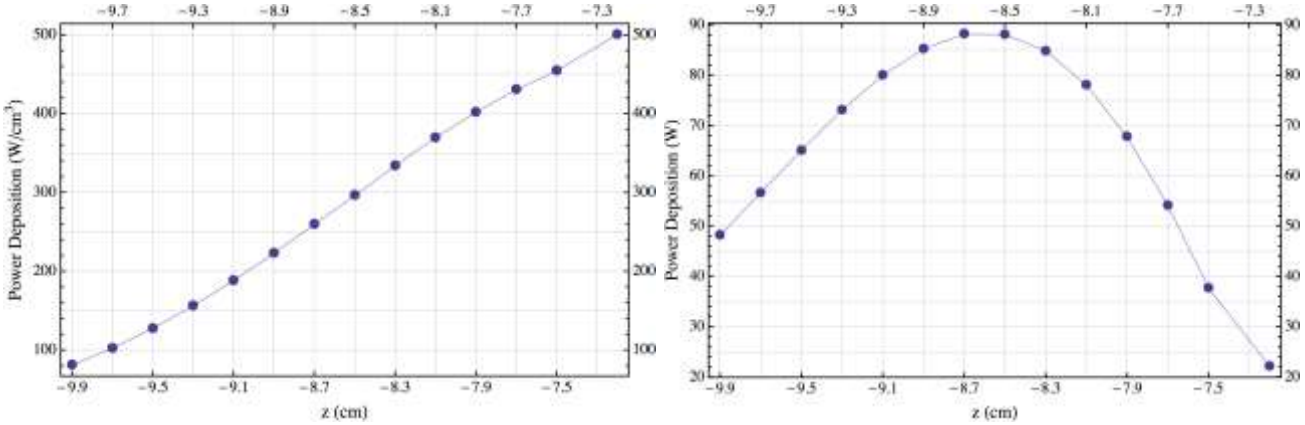

Figure 55 - Power Deposition as a function of z in the target window.

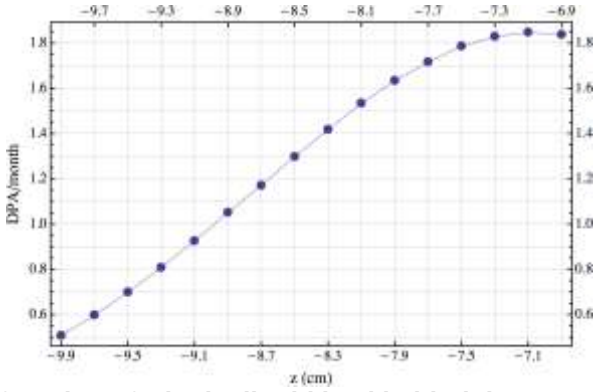

Figure 56 - DPA/month as a function of z in the liquid lead behind the target window.

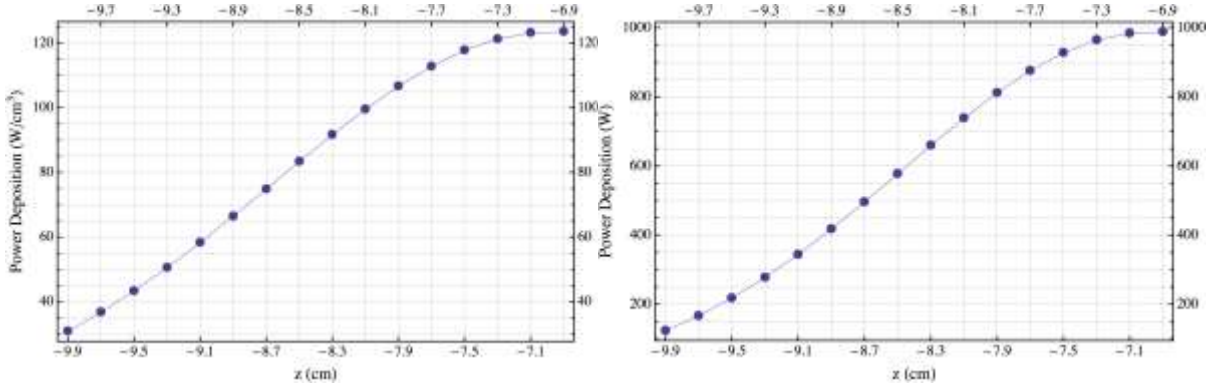

Figure 57 - Power Deposition as a function of z in the liquid lead behind target window.

2.10.3 Deuteron Beam

It is well known that at lower energies deuteron beams may be superior to proton beams in terms of neutron production. Hence an attempt was made to study the effect of low-energy deuteron beams. The negative effect of the short stopping ranges is apparent in the following figures, in terms of high heat deposition rates in the materials and nevertheless low neutron production rates. Although substances such as Lithium may prove superior, the option was not pursued.

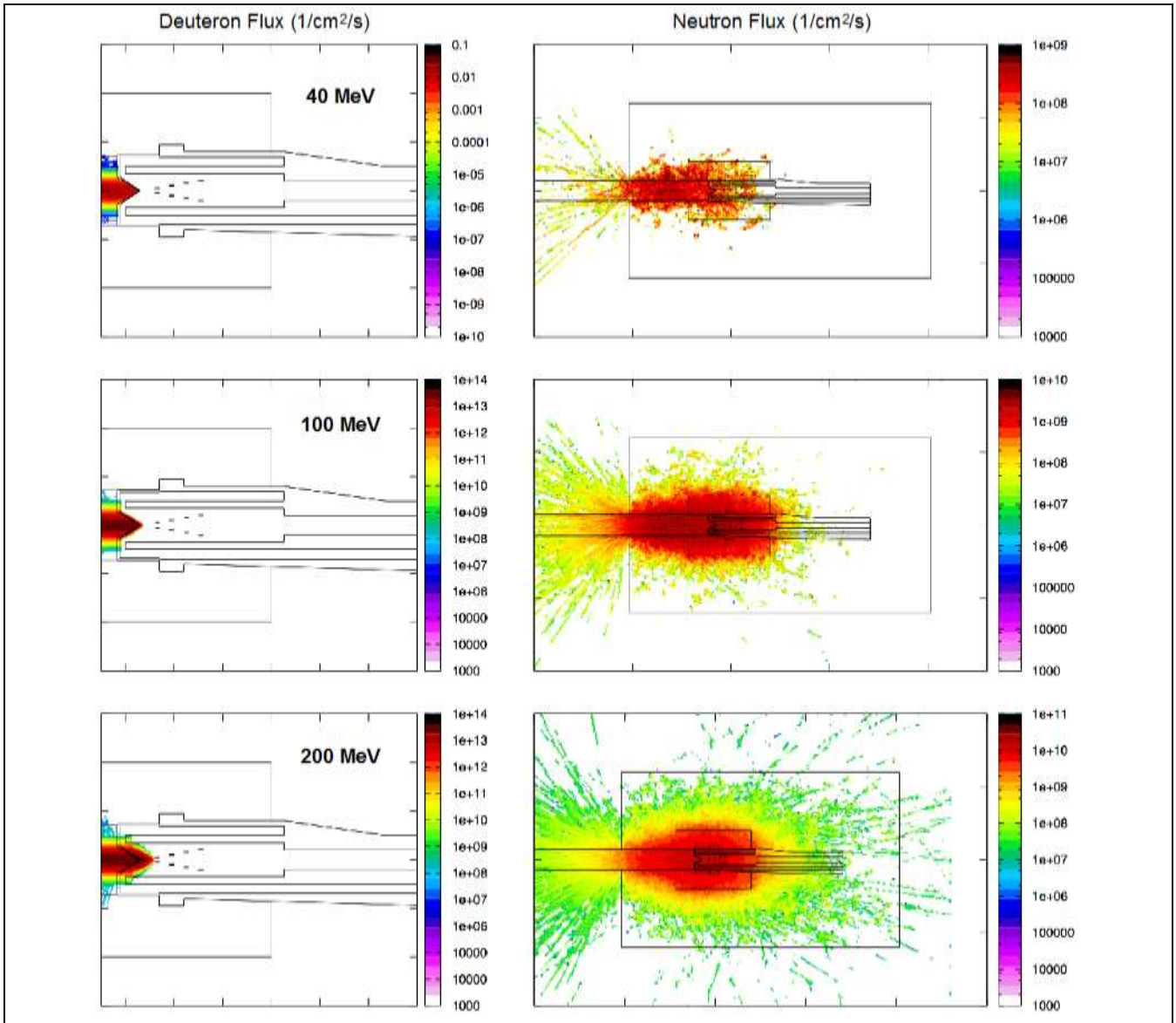

Figure 58 - Deuteron and neutron fluxes (1/cm^2/s) in the target and shielding regions for three deuteron beam energies. The reflector is made of graphite with a thickness of 20 cm and the polyethylene has 40 cm of thickness

2.11 Optimised Configuration Studies

2.11.1 Lead Shielding around the Target

The remainder of the study chooses to focus on the beam energy band of interest in terms of good shielding properties and attractive DPA production capacity. As discussed above, this would appear to be between 200 and 400 MeV of proton beam energy.

The previous discussion has also shown the necessity of using a heavy element surrounding the target to moderate the high-energy neutrons and also to shield against gamma production during operation and, most importantly, after shutdown. Finally the differences highlighted before between the dose rates exiting the sides of the facility and the rear and front section are the reason for adopting different thicknesses in these areas. These considerations are illustrated in Figure 59:

-Lead is used around the target to reduce gammas from activation during cool-down and moderate effectively the high-energy neutrons during operation before they cross the shielding.
-The front section of the target, which must remain open to allow the penetration of the beam, is shielded with an additional length of lead tube that should reduce the gammas from the target beam window by restricting its externally visible aspect ratio.
-The sides are shielded conventionally, first with lead and then with polyethylene.
-The back of the target has an additional thickness of both lead and polyethylene to reflect the fact that the spectrum is harder at the back of the target, due to the neutrons propelled forward by the impacting protons.
-Finally a layer of borated polyethylene is meant to capture exiting slow neutrons.

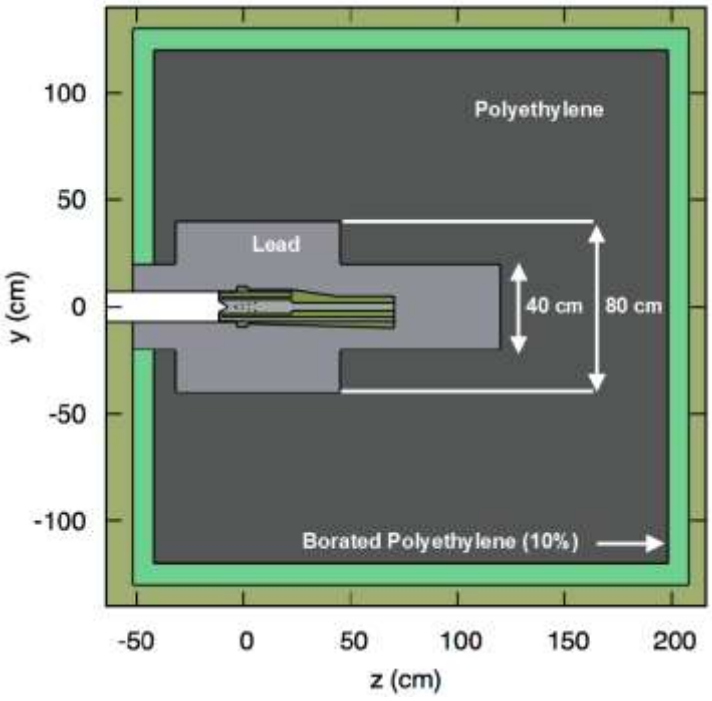

Figure 59 - Shielding dimensions using lead around the target.

The configuration shown above was investigated in a final round of neutronics calculations to examine the effect on shielding. The two beam dimensions studied in the previous sections were simulated, and the results are presented in Sections 2.11.2 and 2.11.3. Although the immediate vicinity is still exposed to lethal dose levels during operation, they have been decreased significantly. Hence the testing facility could be placed in a shielded area, as are common in accelerator laboratories.

2.11.2 Beam Dimensions: σ_x, = 1.7 cm, σ_y, = 1.0 cm

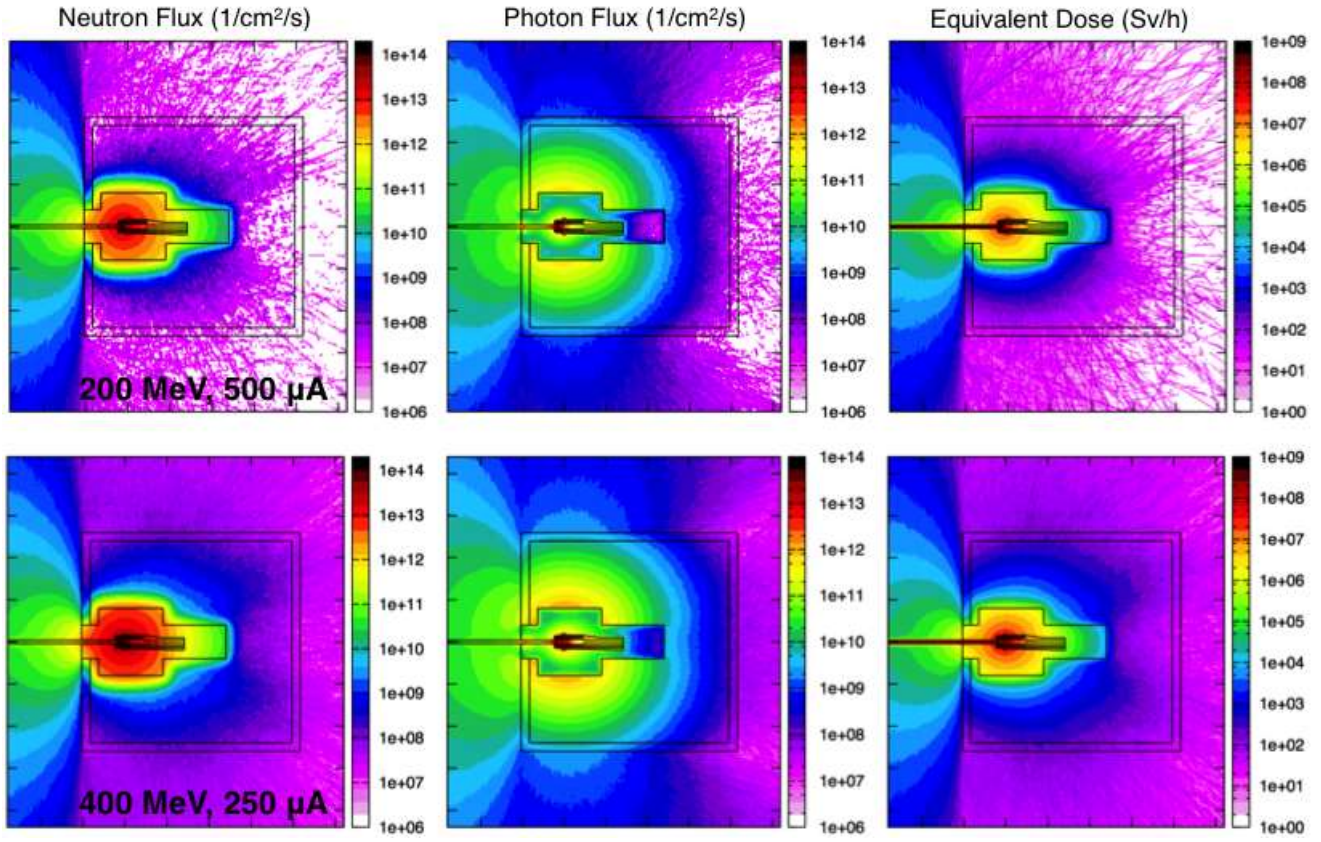

Figure 60 - Neutron and photon fluxes (1/cm^2/s) and ambient dose equivalent rates (Sv/h) in the target and shielding, using lead around the target, for 200 MeV (top) and 400 MeV (bottom) beams (σ_x, = 1.7 cm, σ_y, = 1.0 cm).

The fluxes and dose rates presented in Figure 60 relate to the operation period, for which no human intervention is necessary. Conserving a low enough dose rate is therefore primarily intended to prevent the activation of the laboratory components and do not contemplate human presence. A dose rate in the order of < 100 Sv/hr may be considered satisfactory in this respect. The doses rates above show a cross-section and are therefore dominated by the high dose rates inside the testing facility.

Of interest are also the exiting dose rates, as they will affect the environment around the testing facility, as shown in Figure 61. The dose rates are taken at contact in a 1 cm thick slice along the sides of the shielding. The back end shows greatly reduced dose rates thanks to the increased shielding depth. At contact there are some hot spots along the sides of the facility, up to 100 Sv /hr for a 400 MeV beam; however this decreases rapidly with distance, as shown in Figure 60, and a 200 MeV beam brings some definite advantages.

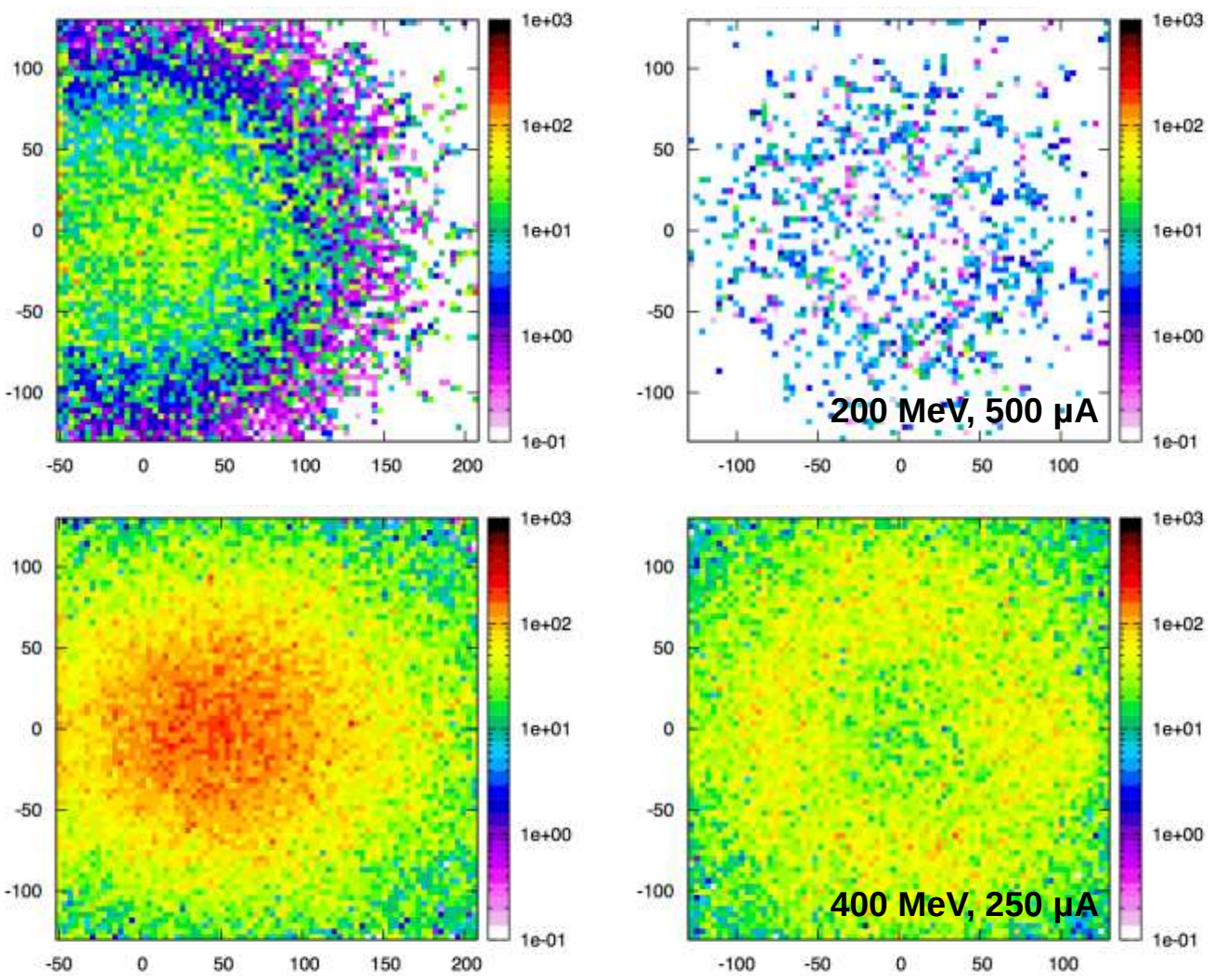

Figure 61 - Ambient equivalent dose rates (Sv/h) after the shielding, in 1 cm slices of air, for 200 MeV (top) and 400 MeV (bottom) proton beams (σ_x, = 1.7 cm, σ_y, = 1.0 cm). Left side – lateral side of the TMIF facility. Right side back end of the T-MIF facility.

The phase after operation is also of great interest, as the target will have to be opened and the samples extracted. Thereafter new samples will be placed for the next round of testing. The level of radiation after a certain cool-down period will determine to a large extent the degree to which robotics are needed for this phase. This aspect is examined in Figure 62, where different cooling times are calculated. In this calculation it is assumed that the liquid lead will be evacuated from the target and will be contained in the sump tanks. The corresponding calculations are shown in Section 2.12.

The ambient dose rate at contact after shutdown is shown in Figure 63 and demonstrates that the testing facility is approachable after one day, irrespective of the beam energy. In this case, the evacuation of the irradiated liquid metal to the sump tank is the key to restricting the dose rate. Since the sump tanks can thereby be expected to irradiate, they are examined in Section 2.12.

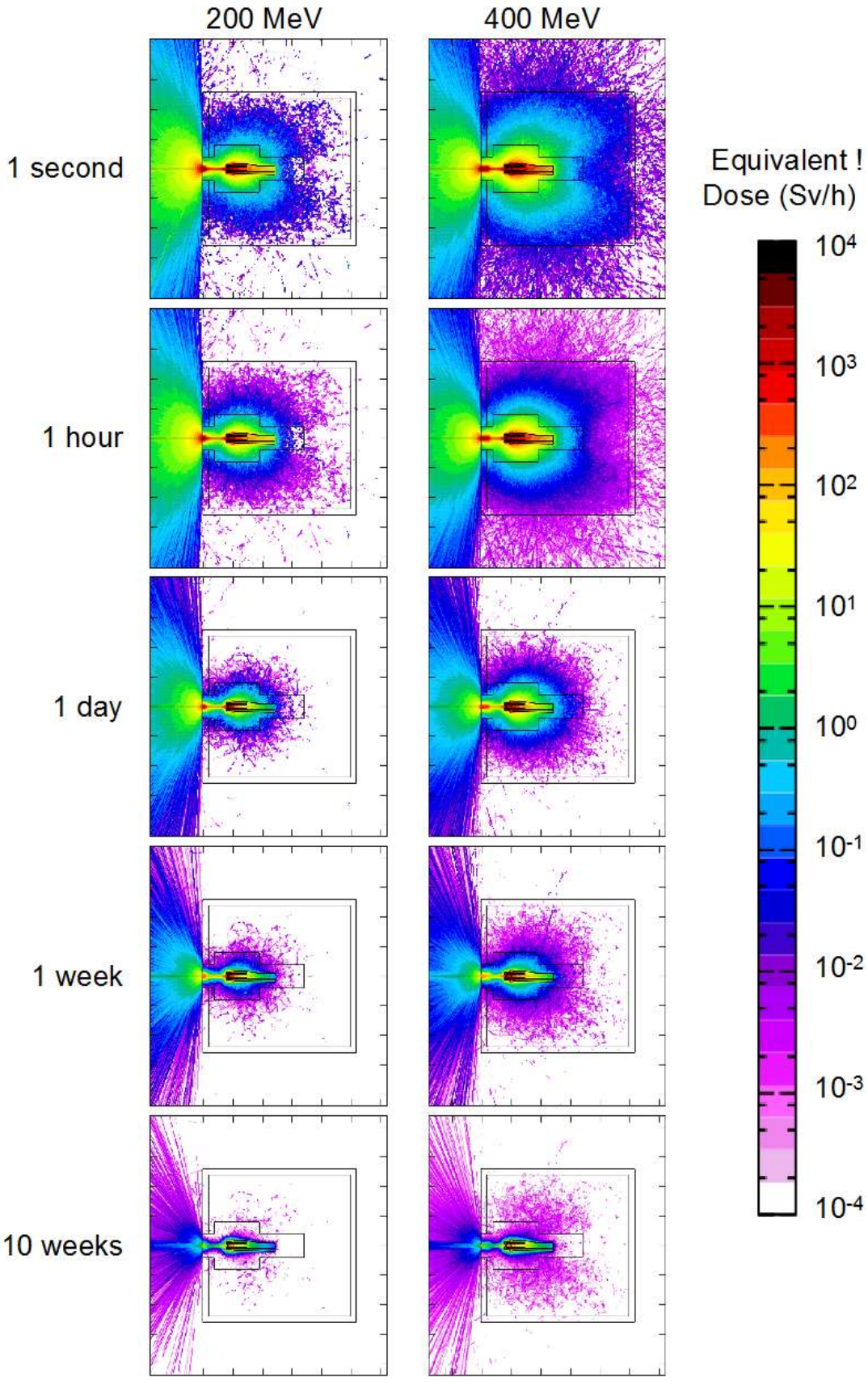

Figure 62 - Residual ambient dose equivalent rates (Sv/h) for several cooling periods (8 cm depth in the x direction, 100 kW beam, 1 year of irradiation, (σ_x, = 1.7 cm, σ_y, = 1.0 cm). Left - 200 MeV. Right - 400 MeV.

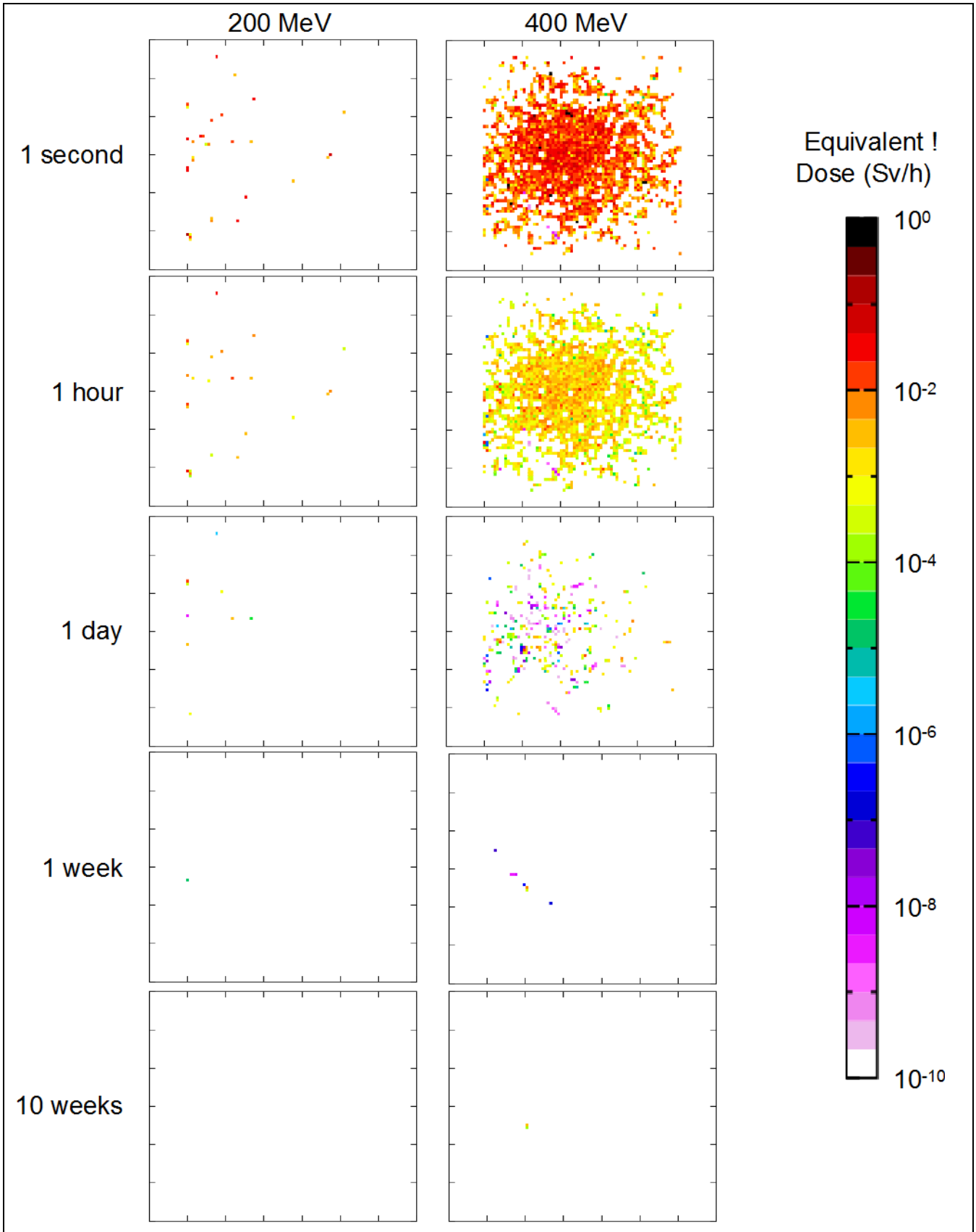

Figure 63 - Residual ambient dose equivalent rates (Sv/h) for several cooling periods in 1 cm slices of air on the lateral side of the target (100 kW beam, 1 year of irradiation, σ_x = 1.7 cm, σ_y = 1.0 cm). Left - 200 MeV. Right - 400 MeV.

2.11.3 Beam Dimensions: σ_x, = 6.0 cm, σ_y, = 1.0 cm

This section shows the same results as the previous one for the beam with σ_x, = 6.0 cm, σ_y, = 1.0 cm. It can be seen, from Figure 64 to Figure 67, that changing the beam dimensions has no significative impact in the fluxes and dose rates outside the shielding, during operation or after shutdown. Furthermore, the configuration with the narrower beam makes it possible to reduce the dimensions of the beam entrance, thus reducing the amount of backscattered protons and neutrons.

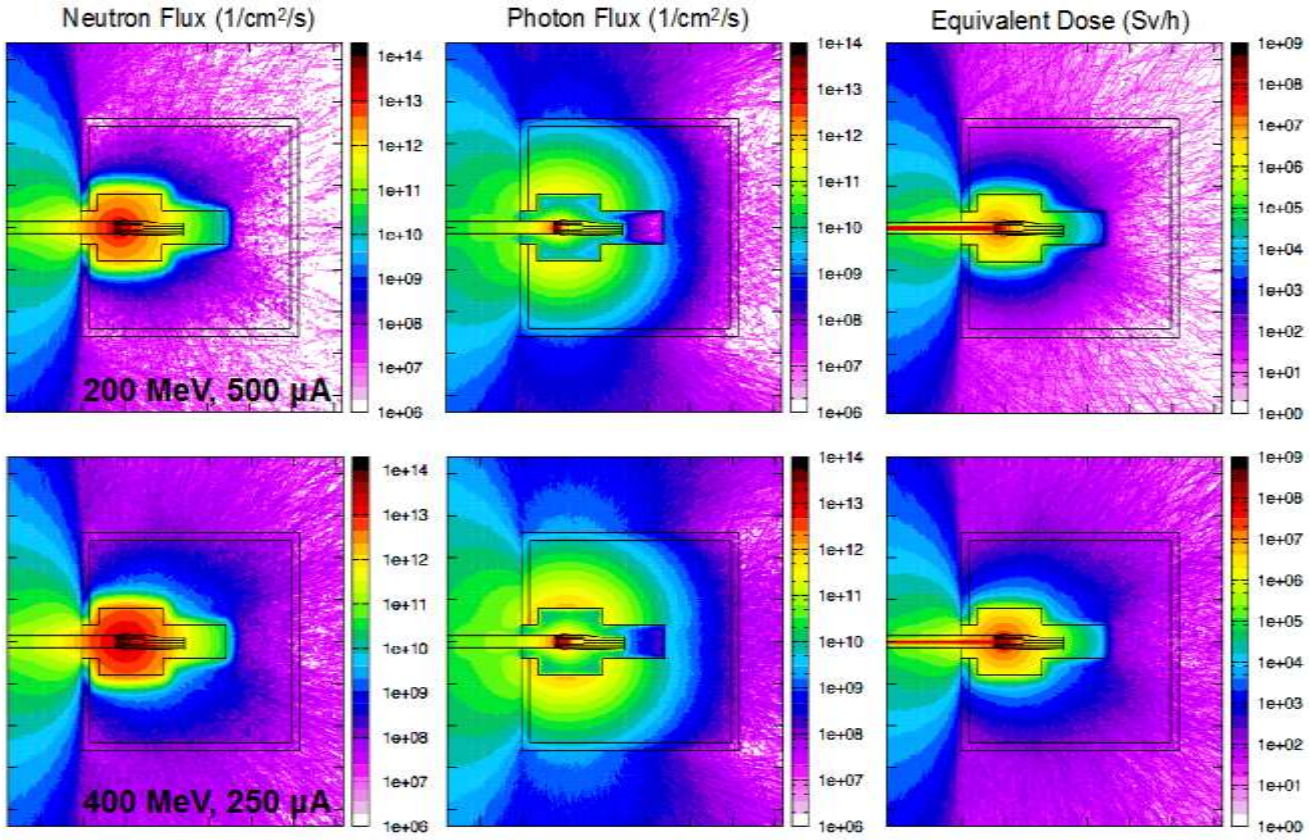

Figure 64 - Neutron and photon fluxes (1/cm^2/s) and ambient dose equivalent rates (Sv/h) in the target and shielding, using lead around the target, for 200 MeV (top) and 400 MeV (bottom) beams (σ_x = 6.0 cm, σ_y = 1.0 cm).

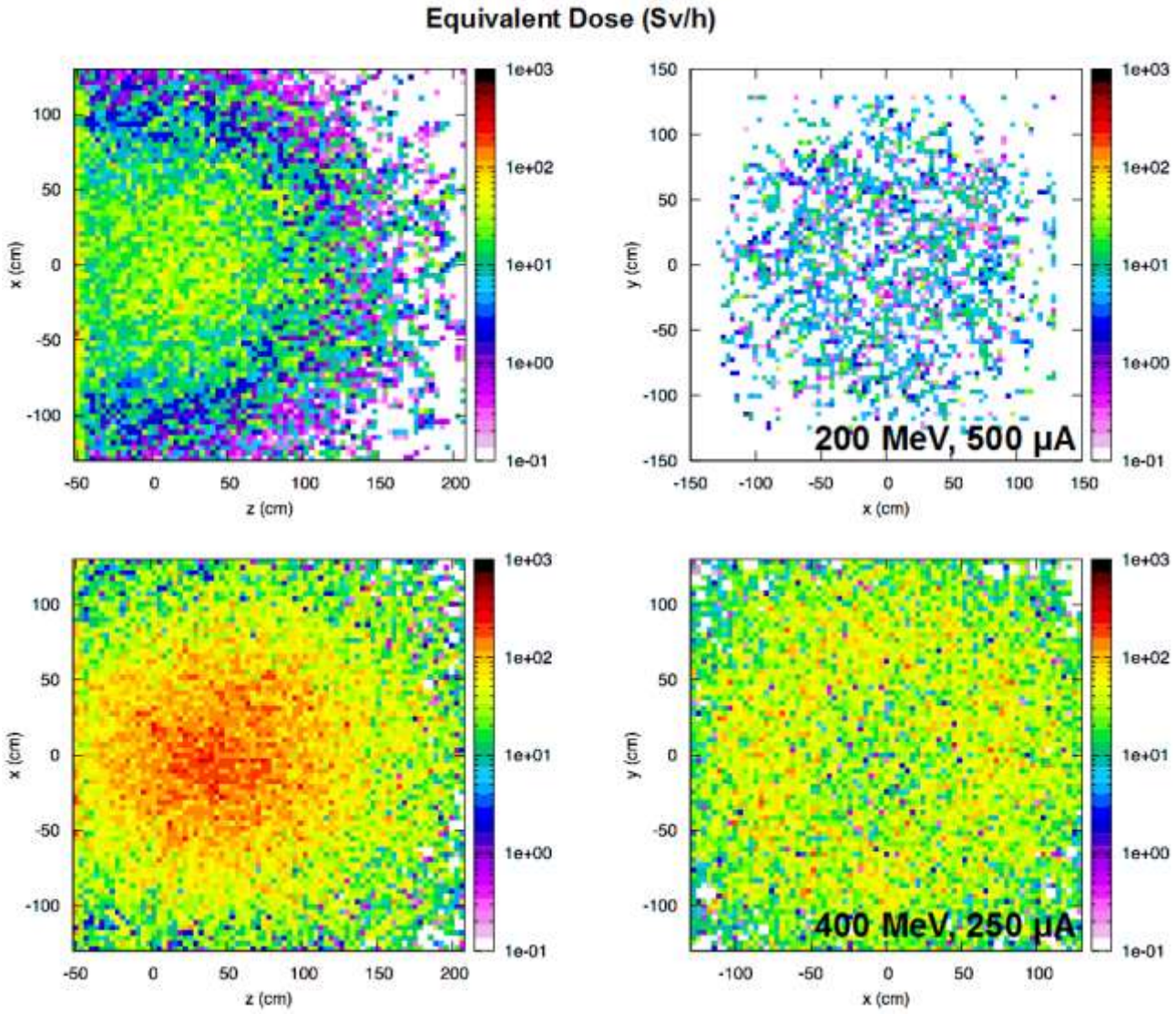

Figure 65 - Ambient equivalent dose rates (Sv/h) after the shielding, in 1 cm slices of air, for 200 MeV (top) and 400 MeV (bottom) proton beams (σ_x = 6.0 cm, σ_y = 1.0 cm). Left side – lateral side of the TMIF facility. Right side back end of the T-MIF facility.

.

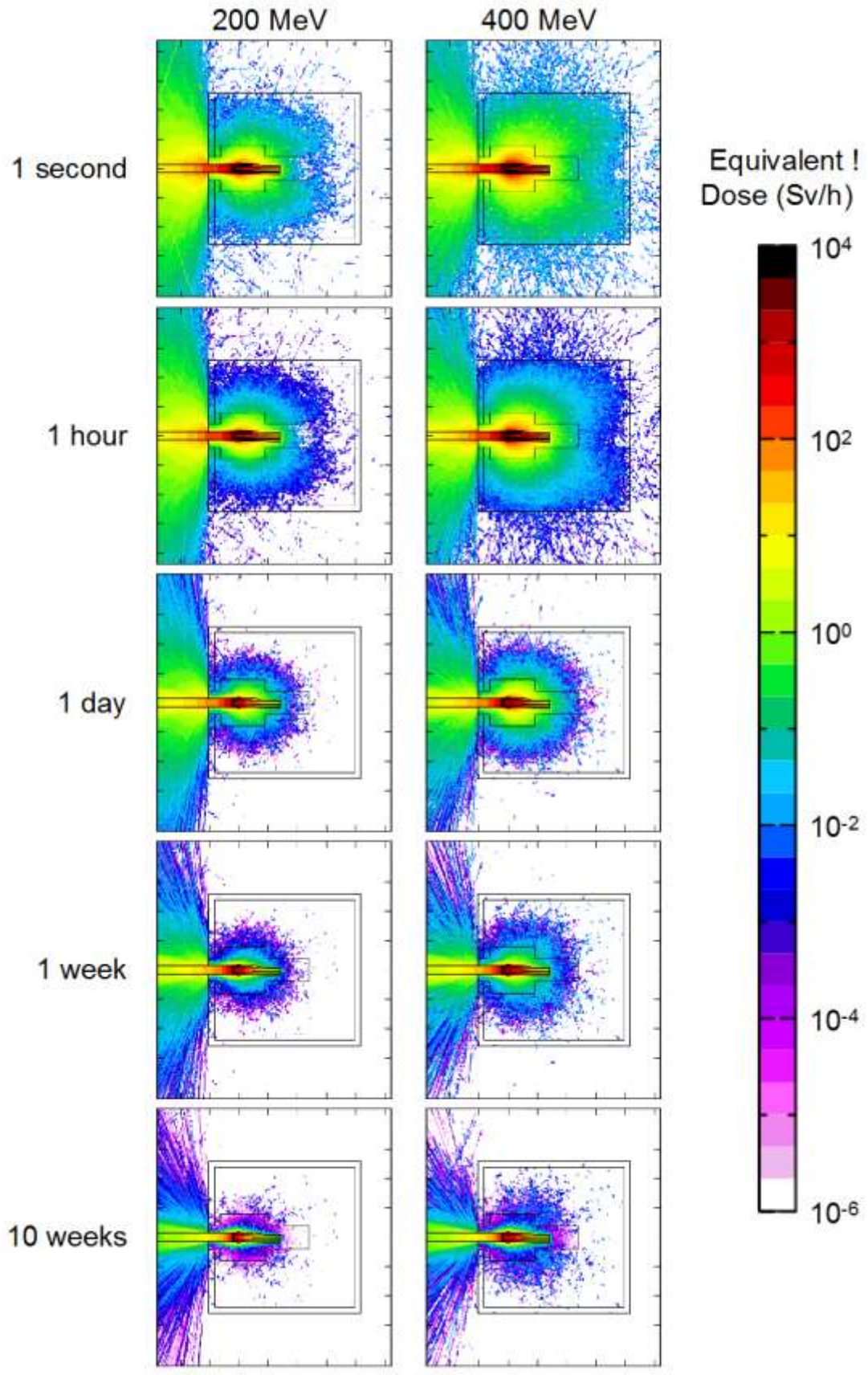

Figure 66 - Residual ambient dose equivalent rates (Sv/h) for several cooling periods (8 cm depth in the x direction, 100 kW beam, 1 year of irradiation, σ_x = 6.0 cm, σ_y = 1.0 cm). Left - 200 MeV. Right - 400 MeV.

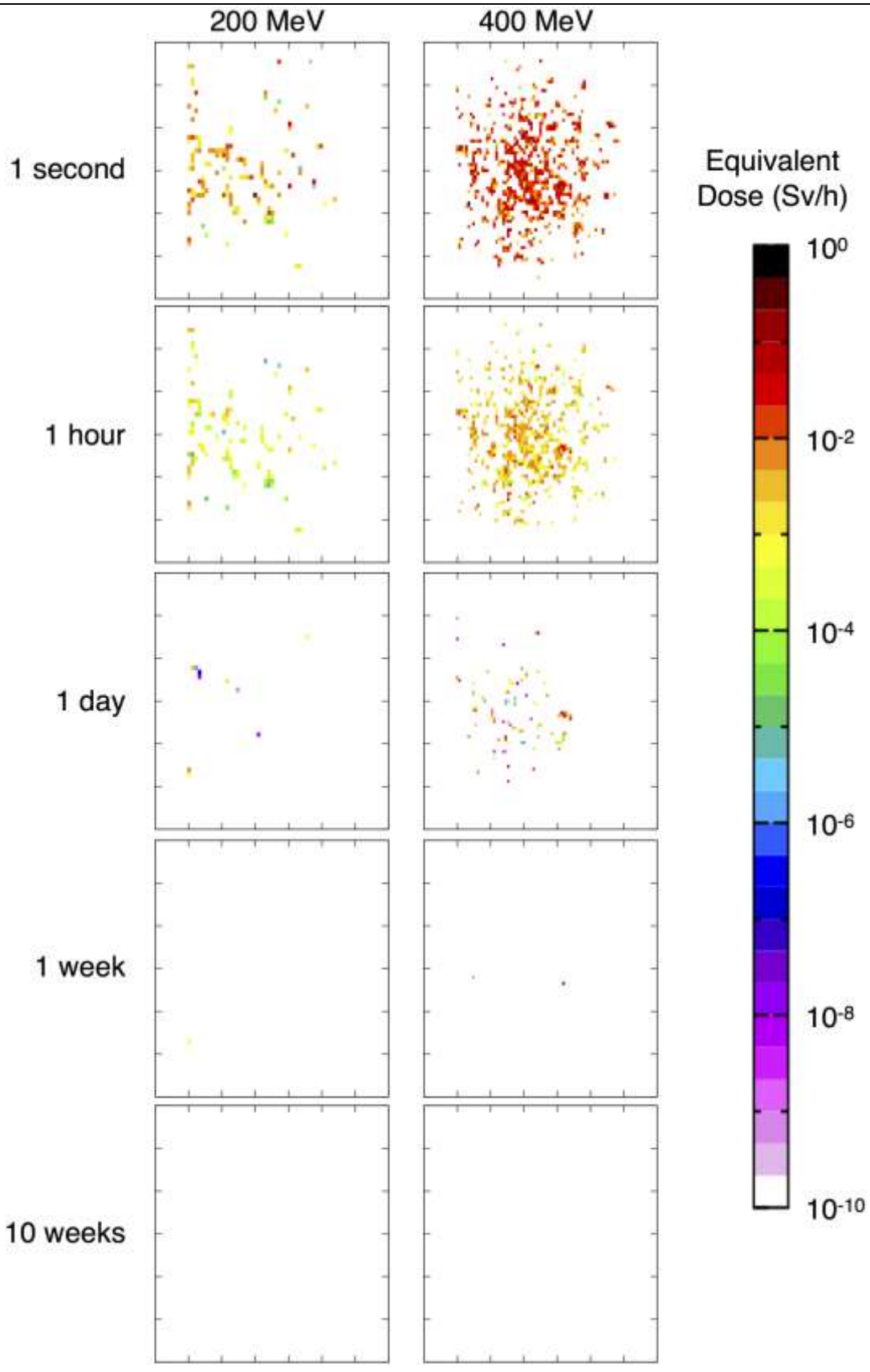

Figure 67 - Residual ambient dose equivalent rates (Sv/h) for several cooling periods in 1 cm slices of air on the lateral side of the target (100 kW beam, 1 year of irradiation, σ_x = 6.0 cm, σ_y = 1.0 cm). Left - 200 MeV. Right - 400 MeV.

2.12 Liquid Lead Container

The liquid metal contained in the sump tanks after evacuation from the target and primary loop must be shielded if the facility as a whole is to be useable. Their position close to the floor and their compact shape make this task relatively less complex. Furthermore as they are only used after shutdown and not in operation, the shielding can be optimised to serve against only against gamma radiation, for which heavy elements such as lead are optimal.

Essentially, three different thicknesses of lead have been studied, as shown from Figure 68 to Figure 70. In line with trying to access the facility 1 day after shutdown, it would appear that a 25 cm lining of lead around the tanks would provide sufficient shielding.

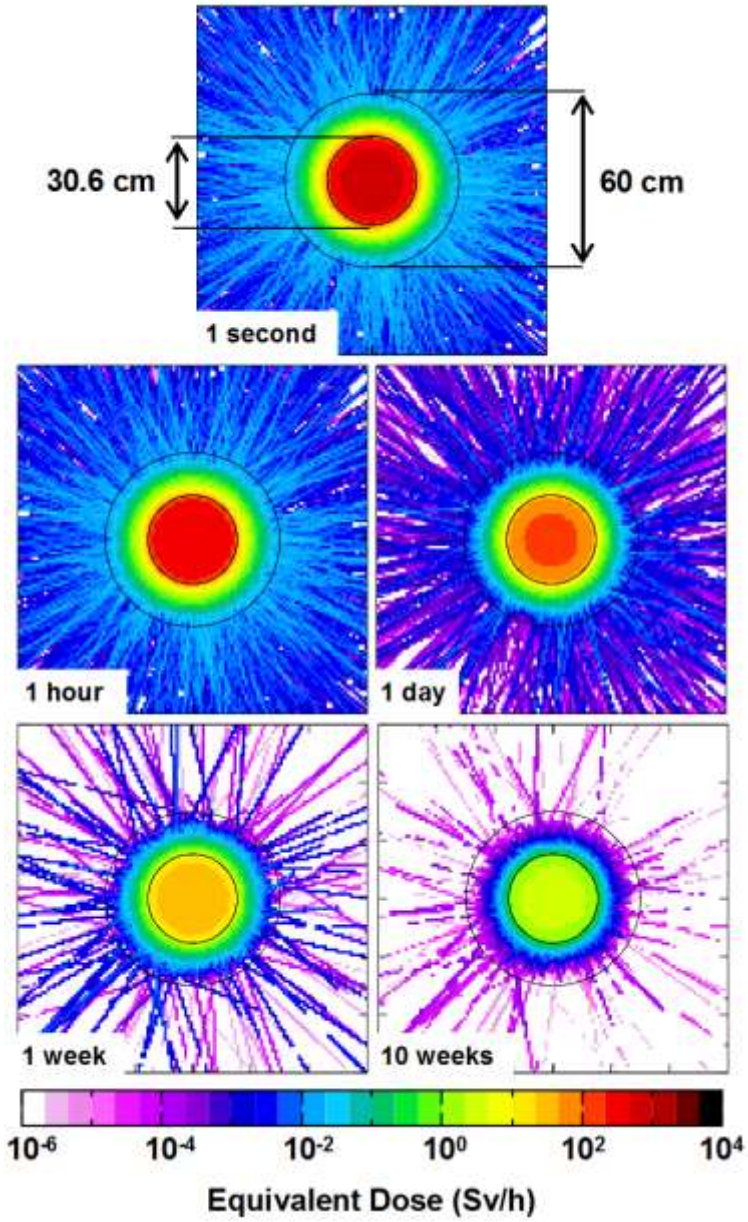

Figure 68 - Residual ambient dose equivalent rates (Sv/h) in the liquid lead container for several cooling periods (average values for a depth of 120 cm) and 1 year of irradiation with a 400 MeV, 250 mA beam. Container thickness: 15 cm.

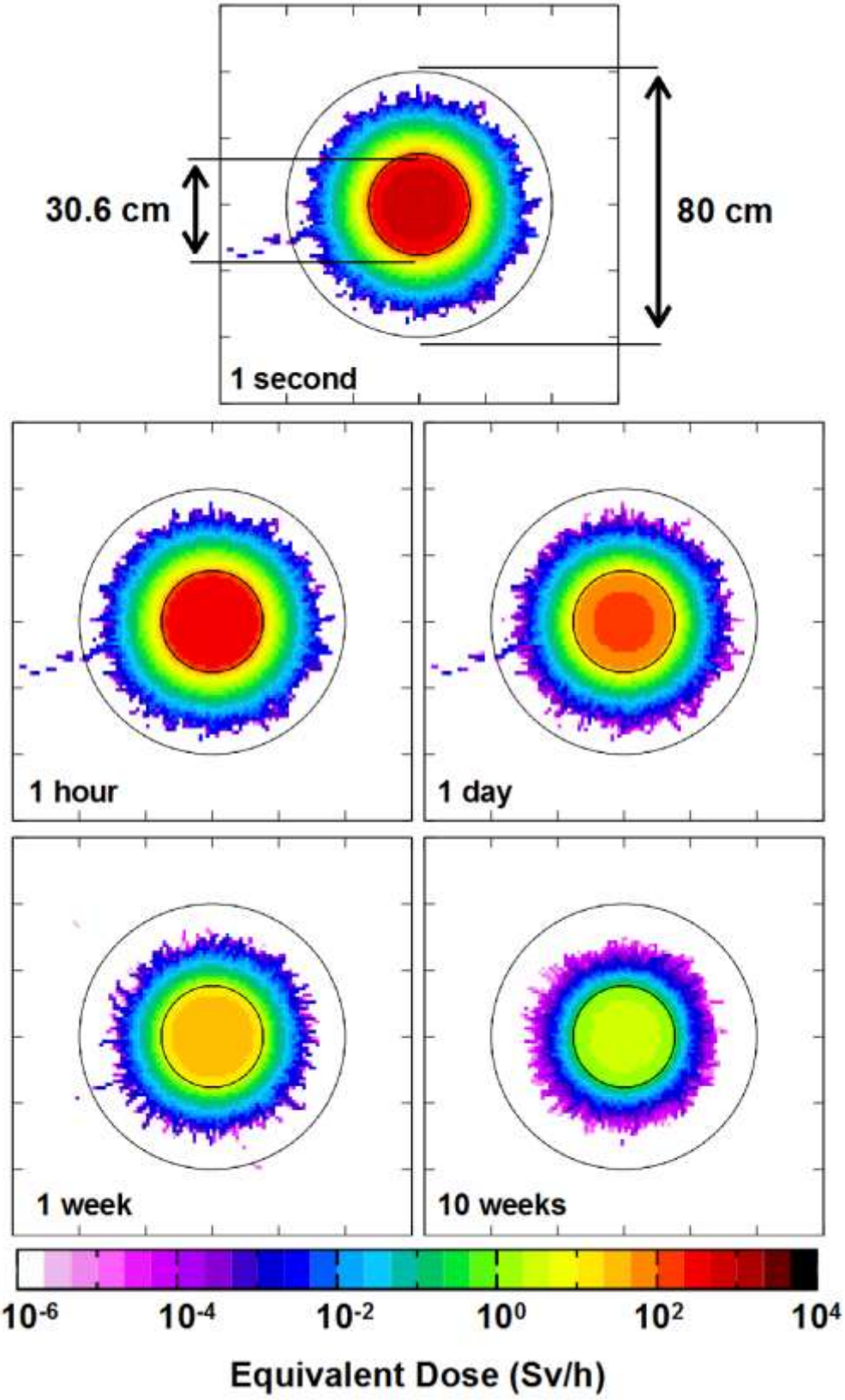

Figure 69 - Residual ambient dose equivalent rates (Sv/h) in the liquid lead container for several cooling periods (average values for a depth of 120 cm) and 1 year of irradiation with a 400 MeV, 250 mA beam. Container thickness: 25 cm.

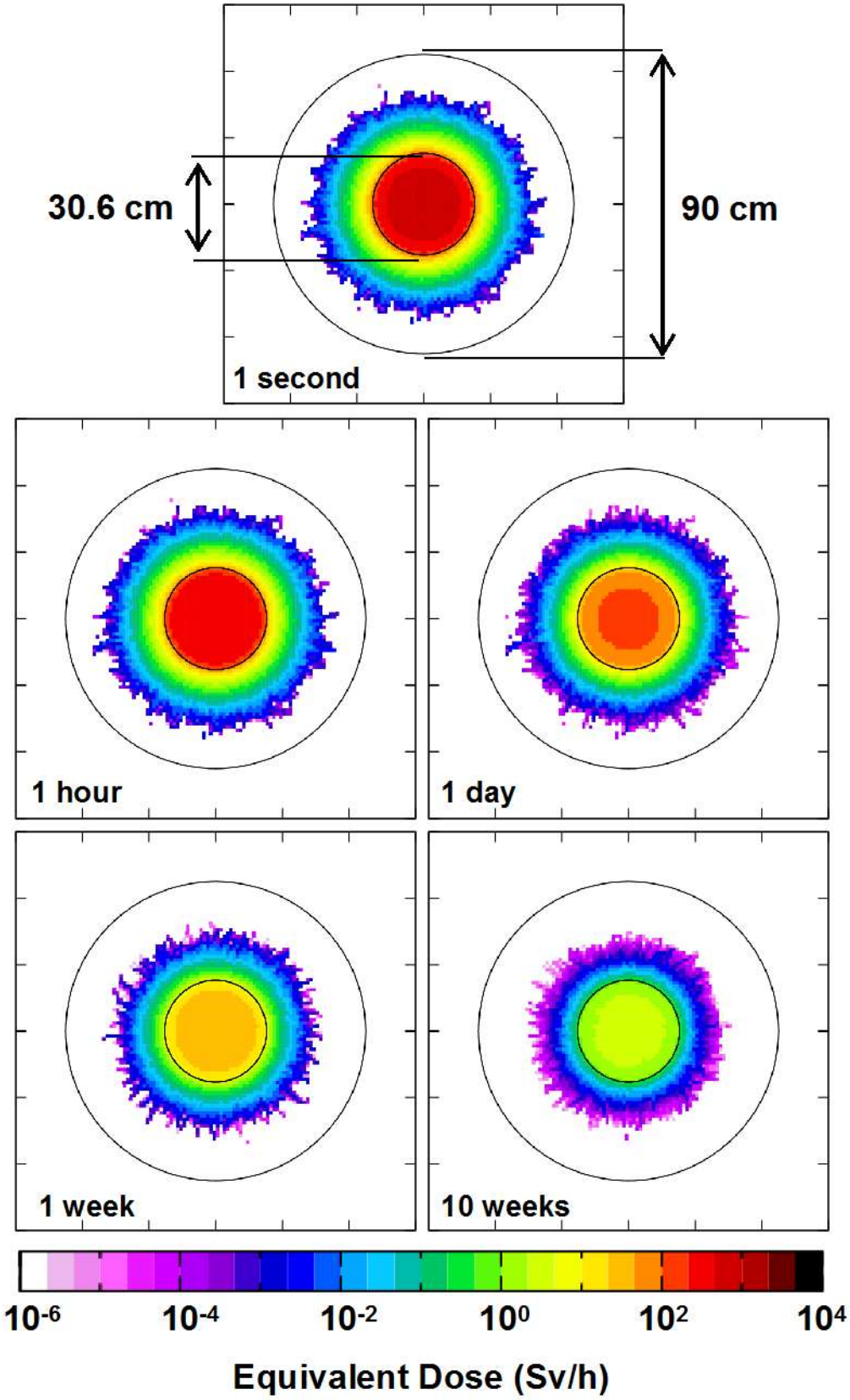

Figure 70 - Residual ambient dose equivalent rates (Sv/h) in the liquid lead container for several cooling periods (average values for a depth of 120 cm) and 1 year of irradiation with a 400 MeV, 250 mA beam. Container thickness: 30 cm.

2.13 Sample DPA production

The same calculations for DPA (Table 13) and neutron flux spectra (Figure 71) in the four samples were repeated with the optimized configuration, for 200 MeV and 400 MeV proton beams with σ_x = 1.7 cm and σ_y = 1.0 cm. For the 400 MeV beam, the DPA values are basically the same as the ones presented in the table below which means that the sample and beam window analyses presented in Section 2.10.2 remain valid for the final configuration. It is also seen that with a 200 MeV beam the DPAs in the first sample go up to 2.14 DPA/month, or approximately 26 DPA/year. The DPAs are greatly reduced in the remaining samples, as seen before, a fact that can be explained by the reduction of the neutron fluxes in those samples.

	DPA per month (stat. uncertainty < 1%)	
Sample	400 Me 250 µA	200 MeV 500 µA
1	1.92	2.14
2	1.16	0.14
3	0.69	0.08
4	0.42	0.05

Table 13 - DPA/month in the four samples 200 MeV and 400 MeV proton beams with σ_x = 1.7 cm and σ_y = 1.0 cm.

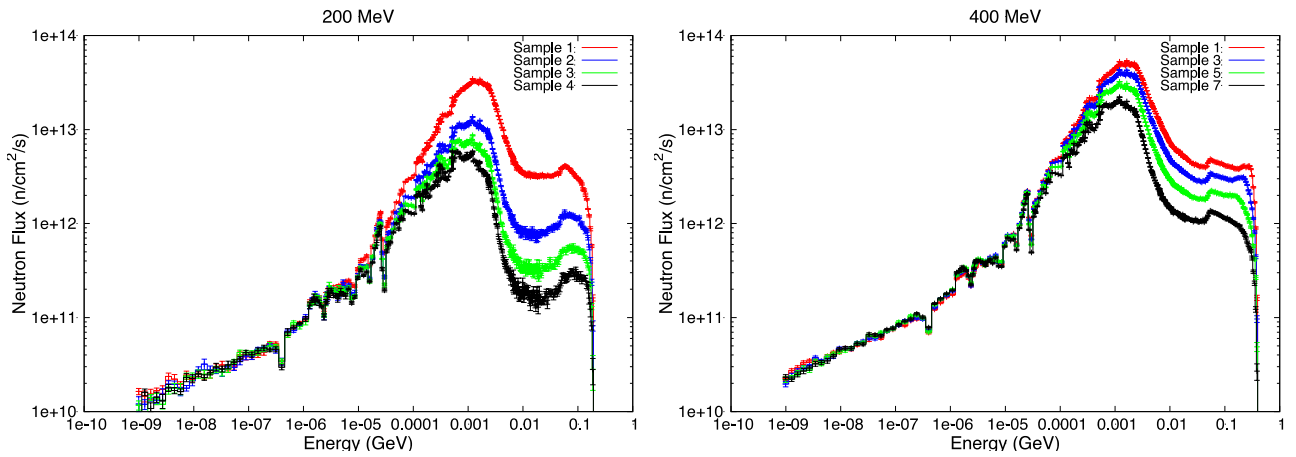

Figure 71 - Neutron flux spectra (n/cm^2/s) in the four samples, for 200 MeV (left) and 400 MeV (right) proton beams with σ_x = 1.7 cm and σ_y = 1.0 cm.

In Figure 72 the neutron flux densities in the first sample of the proposed T-MIF facility (400 MeV / 100 kW beam) are compared to those foreseen for facilities such as MTS, IFMIF and DEMO. At 14 MeV, the neutron fluxes predicted for the first sample in the T-MIF facility are similar to those

expected for the MTS facility (1 MW beam): However, TMIF can achieve this with ten times less beam power. When compared to IFMIF, the difference in the flux densities is not so great if the 10xT-MIF curve is considered, i.e. if the power applied to the facility is multiplied by ten, an option which is technically feasible by revising some of the parameters of T-MIF. These results highlight the potential of the T-MIF target station for testing fusion materials.

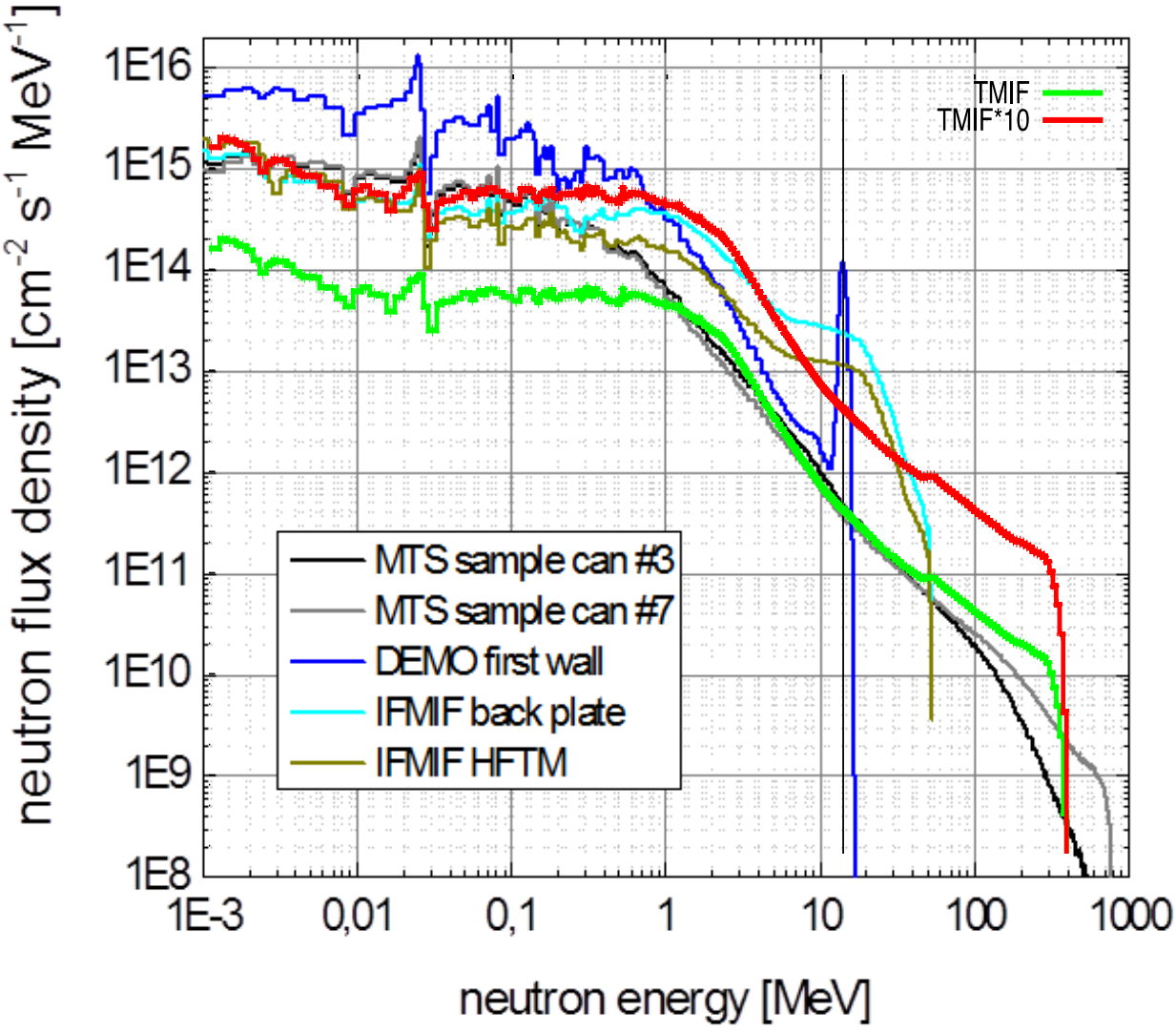

Figure 72 - Neutron flux density (n/cm^2/s/MeV) in the four samples for a 400 MeV beam (left), compared with the neutron flux densities foreseen for MTS, IFMIF and DEMO (right).

Finally, the residual dose rates in the first sample were also calculated again, to check if they increase with a narrower beam. The results shown in Figure 73 indicate that the residual dose rates will be essentially similar with the two beams, the only difference being that with the narrower beam the gamma source will be more concentrated in the centre of the sample (for a comparison, see Figure 30).

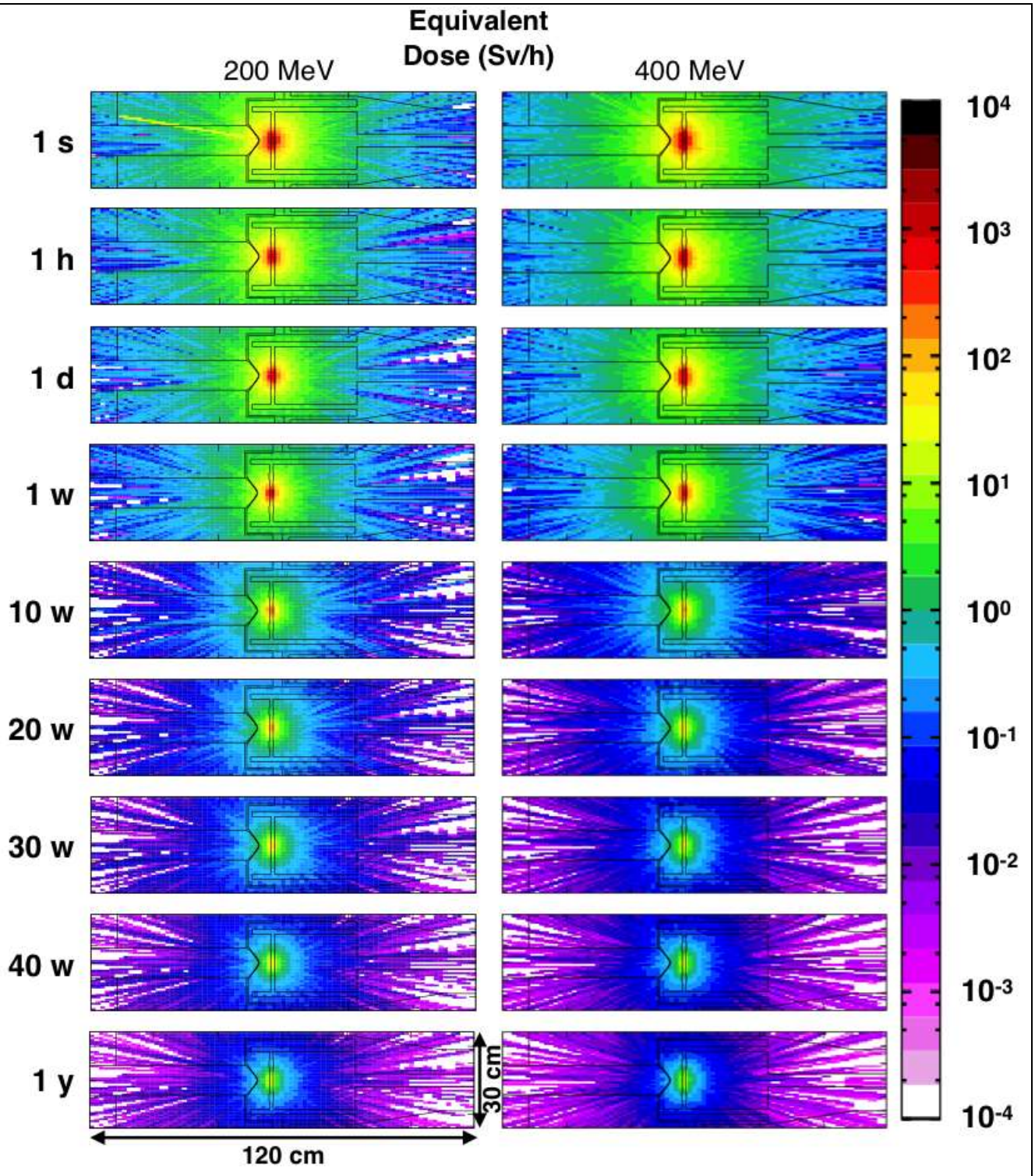

Figure 73 - Residual ambient dose equivalent rates (Sv/h) in the first sample for several cooling periods (2 cm depth in the y direction, 100 kW beam) after 1 month of irradiation with 200 MeV (left) and 400 MeV (right) proton beams (σ_x = 1.7 cm and σ_y = 1.0 cm).

2.14 Concluding remarks on the neutronics analysis

Many optimisations were necessary to arrive at a satisfactory design of the T-MIF testing facility, from a neutronics point of view. The essential features of the design as listed in the initial specification [Ref.1] and laid out in the initial design [Ref.2] have been validated.

Balancing the need for increasing the DPAs on the sample against the wish to minimise dose rates has resulted in a design that will achieve the desired goal of allowing samples to be exposed to over 20 DPA/year and yet minimise the need for robotics, while preserving the health of the operators and the environment of the laboratory.

The bulk of the active substances will be in the liquid metal, which can be stored separately in tanks, and in the samples and sample holders, which will need dedicated handling tools. Apart from these two components, it appears that the rest of the T-MIF facility is accessible to human operators for maintenance, reloading of the samples and repositioning or relocation of the facility.

The next step in the neutronics design and analysis will be to incorporate the results from the current study into a detailed CAD design of T-MIF with the shielding, and also to perform a stress analysis of the target window. Once the detailed design has been firmed up, a second examination of the neutronics aspects would be advisable, in a follow-on stage to the current project.

3 System-level study of the T-MIF facility

The current chapter is reproduced from reference document 3.

As set out in the specification report (Ref. 1) the design of the T-MIF facility aims at obtaining the greatest possibility flexibility in terms of its use in different beam irradiation facilities around the world, while ensuring safety and minimising down-time for repairs and maintenance.

Research establishments where the test facility would be installed would not necessarily dispose of the full range of nuclear installations such as hot cells that are usually required for maintenance of installations under high irradiation. Therefore a modular solution has been proposed, in which the most activated components can be disassembled and stored for a period of time until the activity has decayed sufficiently that they may be accessed under less stringent requirements. The modular construction also helps in cases of accidents by isolating the most affected equipment which may then be disposed of as a global waste package.

An overall concept for fulfilling these goals has been laid out in the preliminary design report for the entire facility (Ref.2) which gives more detail on the engineering aspects of the various components. After a review of similar installations and in light of past experience, the essential parameters of the facility are chosen as follows:

Power Exchanged	100 kW
Primary side fluid	Lead or LBE or Mercury
Secondary side fluid	Gallium
Specific requirements	Leak-proof Leak detection Able to disconnect primary/secondary Gravity-fed in case of pump trip
Pressure	12 Bar

Table 14: Essential thermal hydraulic characteristics of the facility

The primary side fluid was given much thought. The choice of primary liquid depends on the type of application pursued, i.e. material research, radio-pharmaceutical production or rare isotope research. In the present case, both LBE and lead were calculated in subsequent sections in terms of heat exchange and found to be acceptable. Mercury was not calculated but would also be acceptable in that respect since it imposes fewer difficulties, due to its state as a liquid at room temperature.

Analysis proved Gallium to be an adequate choice for evacuating the heat from the primary fluid and passing it on to the cold source, materialised in the facility by an air-cooled heat exchanger.

The next following pages detail the overall concept. The final design shown in the figure hereafter is the result of an optimisation which by virtue of conflicting demands has had to make some compromises, the most challenging of which was to fit the entire facility within a very tight space. The components were placed in a manner to optimise space requirements whilst taking into account the necessities of shielding. The process for arriving at an optimal solution in terms of shielding may be found in chapter 2, whilst the process of optimising the target is detailed in chapter 4. Hence these aspects will not be addressed in detail in the current chapter.

3.1 Shielding

The shielding encompasses the full dimensions of the frame, absorbing all the components within it. It has been optimised as explained in section 2.9, by dedicated shielding around the target and by heavily shielding the two decay tanks at the bottom of the facility which receive the entire content of the primary loop after shut-down. Indeed, the hydrogen-rich polyethylene serves to moderate the neutrons escaping the central spallation target, while the last layer of borated polyethylene helps in neutron capture and the lead around the target and tanks shields from gammas due to activation. The shielding requires a large volume and thus absorbs many components of the facility in which access holes and recesses have to be designed to allow operation and maintenance of the facility.

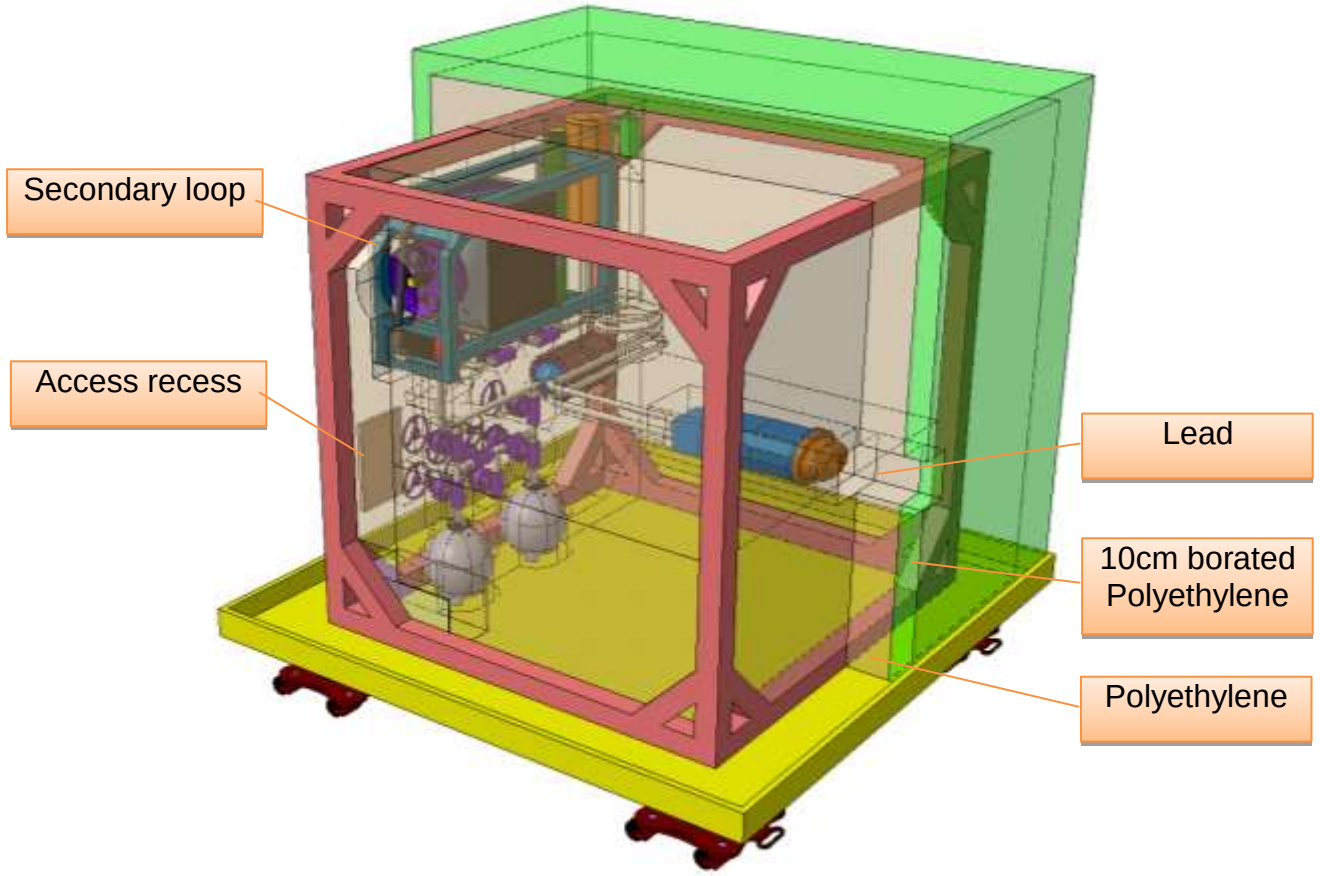

Figure 74: Facility shielding
Note that in the figure above the secondary loop is also shown (refer to subsequent sections)

Special dedicated robotic tools will be necessary to extract the samples from the target. This will entail withdrawing part of the shielding at the front of the facility to allow the dismounting of the target window which once the target is open gives access to the sample holder. The samples contained in the sample holder can then all be removed in one operation to a hot-cell for final manipulation. Thus the parts that need manipulating are fairly large and should not pose a major problem in terms of the robotics needed to handle them. Indeed it is anticipated that standard industrial robots fitted out with the necessary shielding to protect the electronics will be sufficient for this task.

Once the sample holder is removed, a new sample holder with fresh samples can be mounted, the target window replaced and the target closed. The front beam tube in the facility will then be “plugged” with a dummy lead/polyethylene insert to decrease the environmental doses sufficiently to allow access for manual maintenance of the remainder of the facility.

3.2 Primary loop

The primary loop and its component are shown below, separate from the secondary loop and without any shielding for greater clarity. Individual aspects of the different components are explained in greater detail in the following sections. The circulation of the fluid is highlighted by the arrows.

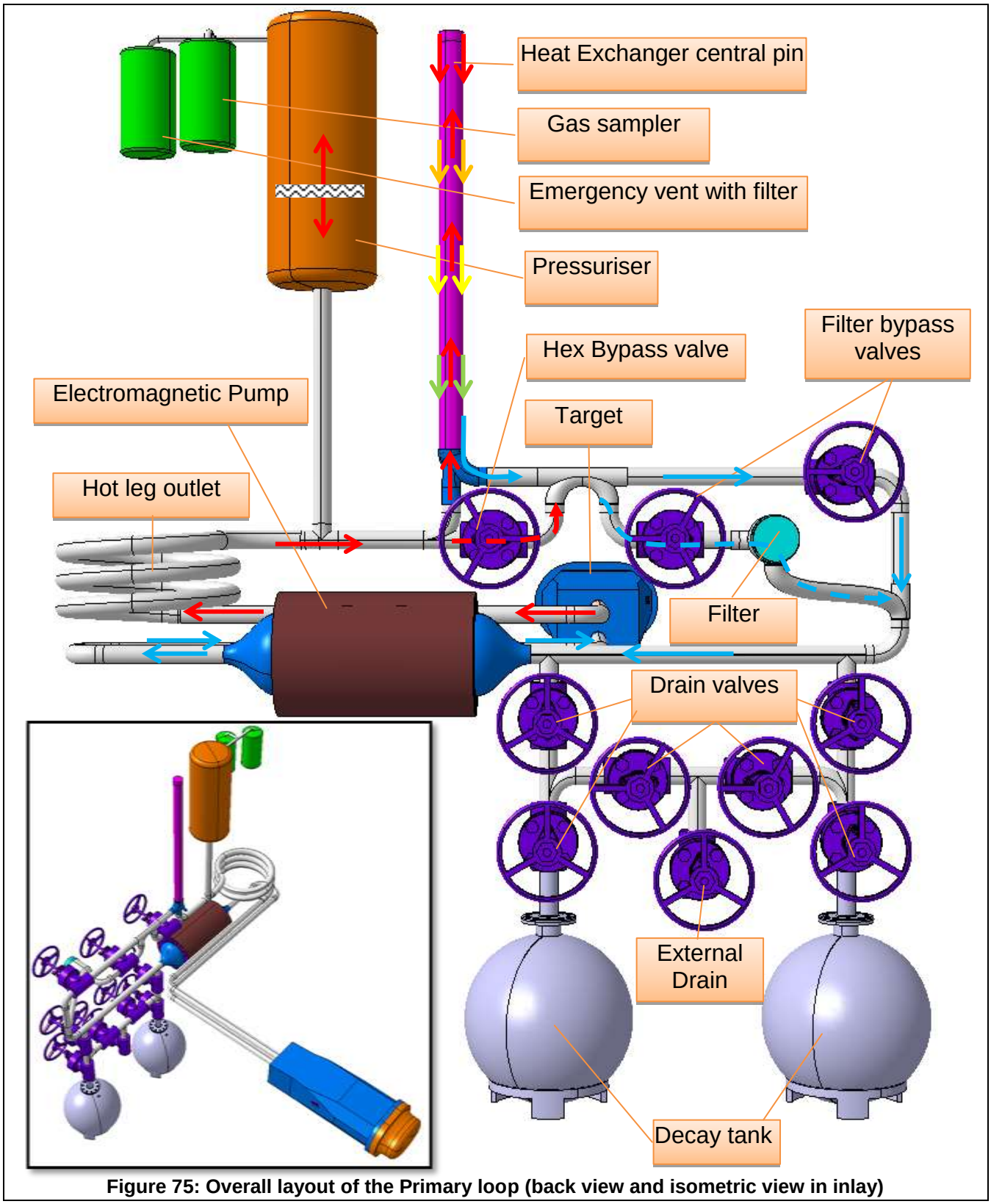

Figure 75: Overall layout of the Primary loop (back view and isometric view in inlay)

As may be seen in the figure above, all the components of the primary loop are organised in such a manner to facilitate operation and maintenance. In particular;

-Pipe lengths are minimized to keep the volume of activated liquid in the primary circuit low.
-The assembly is as compact as possible; all is fitted in a cube, 2 meter on a side.
-The decay sump tanks are at the lowest position to ensure that all the liquid in the primary flows out of the loop by gravity when it is drained.
-The pump is situated in the cold leg just before the target station, to provide maximum protection against thermal transients by using the inertia of the loop.
-The target outlet hot leg features a series of hoops to absorb any thermal expansion due to the temperature variations and to minimise associated stresses in the system.
-The pressuriser tank, gas sampler and emergency venting system are located at the highest point of the primary loop, which is essential for maintaining pressure equilibrium in the loop and ensuring spallation gases are continuously vented from the liquid.
-The heat exchanger is located at the highest position to allow gravity-driven flow to continue cooling the target in the event of a pump failure.
-A heat exchanger by-pass is implemented as a simple means of controlling the temperature in the loop by allowing a variable portion of the hot fluid leaving the target to bypass the heat exchanger. Thus the temperature can be controlled independently of the flow-rate.
-Ease of access to all the components needed for operation such as valves and the filter is ensured by locating them in the same plane at the back of the facility.

This facility is designed to be transportable; the entire components are fixed to a frame in the shape of a 2 metre cube. A sump plate below the frame is foreseen collect any eventual leaks. A system of articulated roller transport trollies or air-pads is designed to allow transport and positioning.

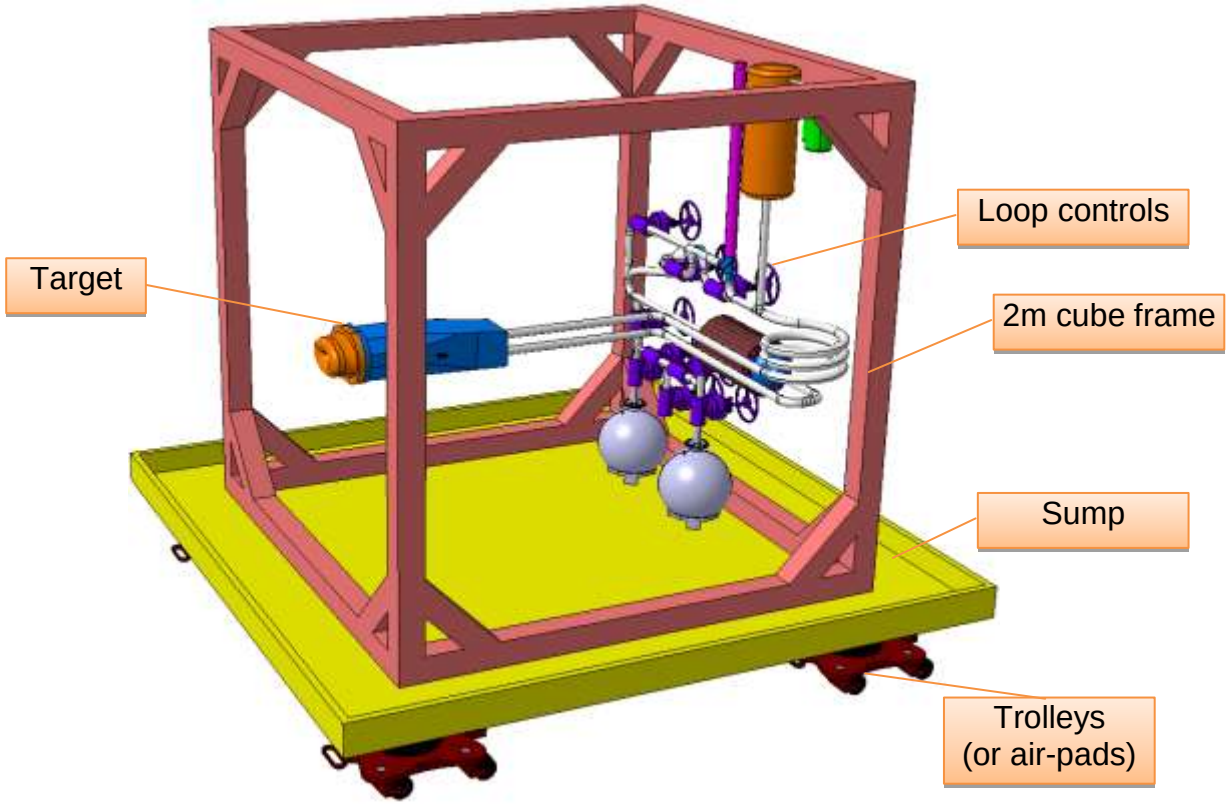

Figure 76: Facility support frame

3.2.1 The spallation target and sample loading

The target is the focus of extensive investigations in chapter 4 from a fluid dynamic point of view to optimise the flow inside the target and create the best conditions for cooling the beam window and the samples. The current section sums up the current state of the design and refers the reader back to chapter 4 for more details.

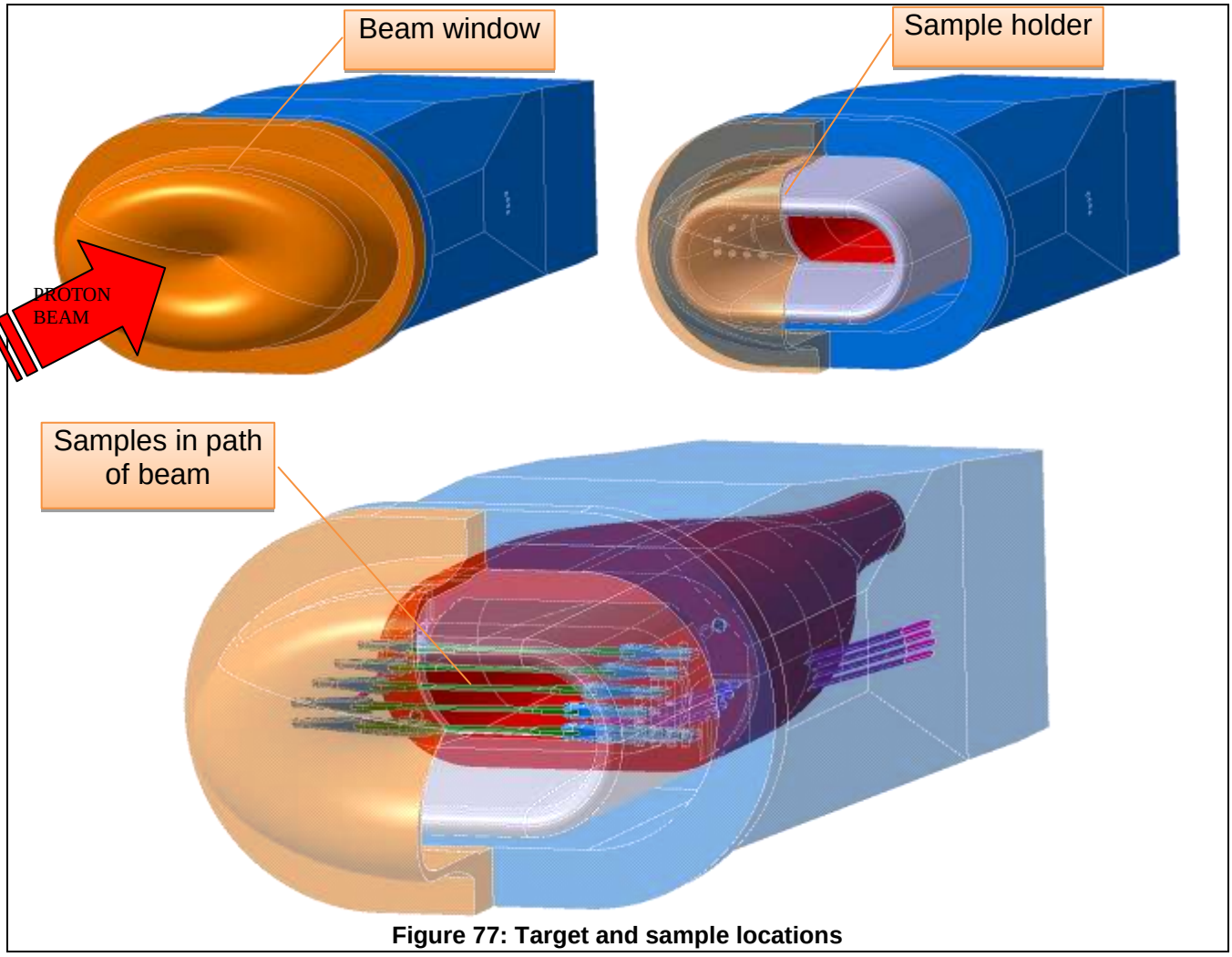

Figure 77: Target and sample locations

Upon impact the beam passes first through the beam window which is cusp shaped and thus optimally cooled by the reversing flow of fluid passing on from the annulus (refer to analysis in chapter 4). The beam then impacts directly the samples imposing DPA from proton interaction. The beam also impacts the surrounding primary fluid, a heavy nuclei, resulting in the production of a large number of spallation neutrons which also contribute to the DPA irradiation damage in the samples.

The samples are held in a sample holder which is an integral part of the internal guide tube through which the fluid flows out of the target towards the heat exchanger. Hence the samples are cooled by the reversing primary fluid. In this manner an environment replicating the use of these materials in fast reactors or ADS type application is created.

The irradiation, temperature and corrosive effects are all represented in the current design. In addition a mechanical system allows a stress to be imposed on the samples, either constant or cyclical. This aspect is particularly important to material embrittlement studies or fatigue studies. The method of applying stress to the samples is illustrated in the next following figures.

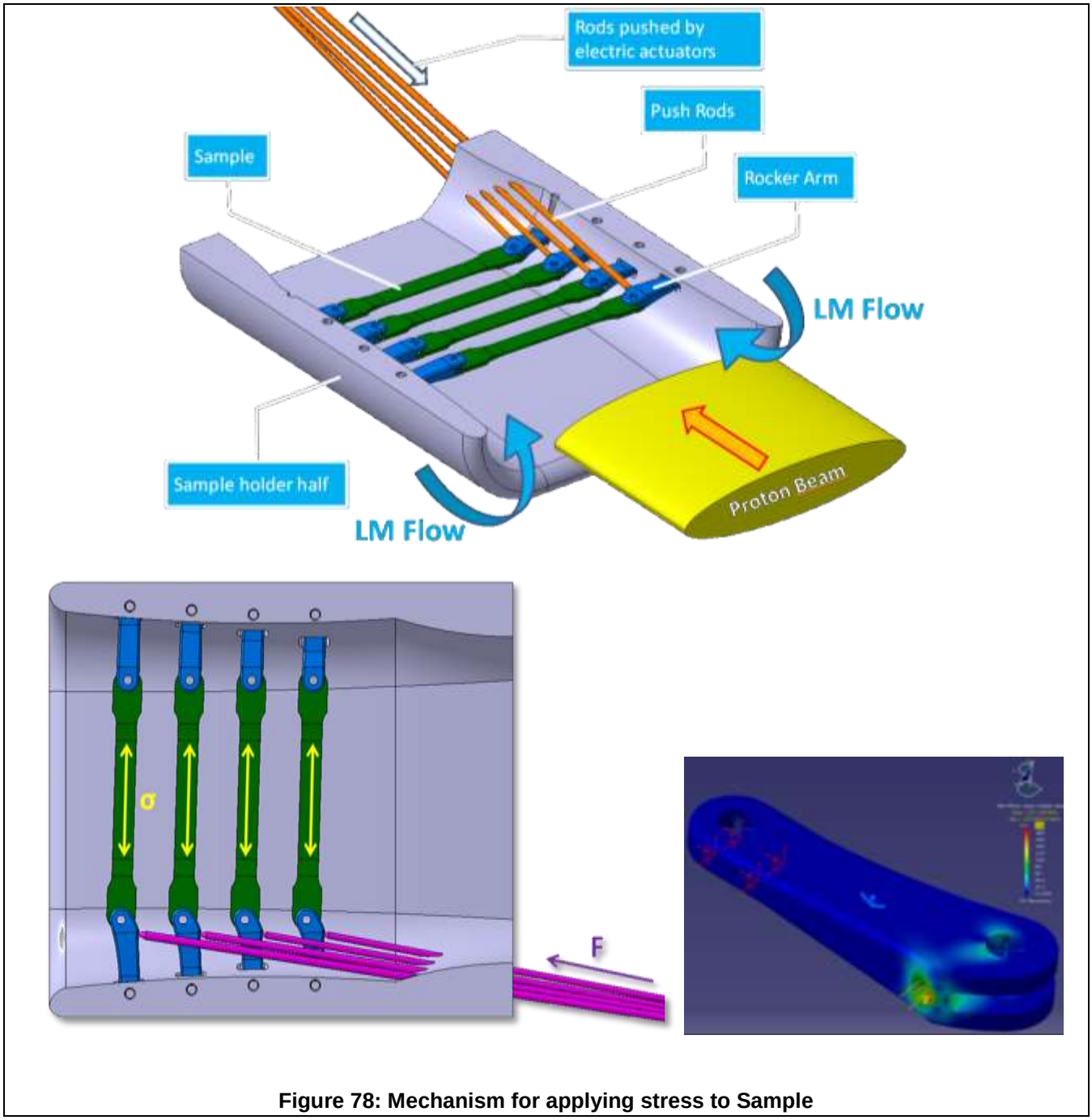

Figure 78: Mechanism for applying stress to Sample

As seen above, push rods are pushed by actuators situated outside the target. The push rods are able to penetrate through dedicated channels isolated by bellows ensuring leak-tightness of the primary circuit. The actuators are themselves located well beyond the maximum neutron flux to preserves their electrical components. Alternately, pneumatic actuators may be used.

The push rods are segmented, one part remaining attached to the target, the other to the sample holder. Since the push rods apply only compression loads, the interface between the two sets of push rods at the interface between the dismountable sample holder is easy to disconnect; the interface being merely a compression face.

The final sets of push rods located in the sample holder then apply a compressive force to a rocker arm which de-multiplies the load into a tensile stress applied to the sample. A relatively modest load from the actuator (~ 850 N) is sufficient to guarantee 500 MPa is attained in the samples.

3.2.2 Primary loop pressurisation

In order to dampen volume variations in the primary circuit due to the fluctuation of the temperature inside the loop, a pressuriser tank is added at the top of the facility, which can at the same time serve to collect all the hazardous gases resulting from the spallation process in the target.

With this implementation of the pressuriser it is possible to control pressure by simply either bleeding or feeding inert gas into the tank. An alternative method in the case of mercury would be the use of an electric heater to create a mercury vapour however this would create a chemical hazard. The method of pressure control through inert gas is well established and if properly implemented with appropriate venting can be made safe against the leaking of radioactive gases.

In parallel to the venting function, a control of any sudden overpressure must be guaranteed to protect the primary circuit against pressure rupture. Such rapid pressure shocks are always possible in a liquid as a result mainly of power excursions, which are always envisaged as part of the safety cases. A first level of protection is afforded by a spring-loaded valve which evacuate the over pressurized gases up to a certain level, above which a second protection measure in the form of a burst disk takes over should the pressure continue to rise. The first level serves to protect against most anticipated accidental scenarios and has the property of both opening and closing again, which allows the facility to continue to be operational. The second device may only open, hence once that ultimate pressure level has been reached, a total overhaul of the facility is mandatory. Both devices must feature a filtering system to provide some degree of retention of gaseous products, as large as reasonably feasible.

Another function of the pressuriser is to allow the sampling of the gases which are expected to collect at the top of the pressuriser. A dismountable gas sample bottle is therefore foreseen to allow these gaseous spallation products to be collected, analysed and then transported to a treatment plant where they are allowed to decay as the isotopes are usually short-lived before reaching admissible activity levels suitable for their release into the environment.

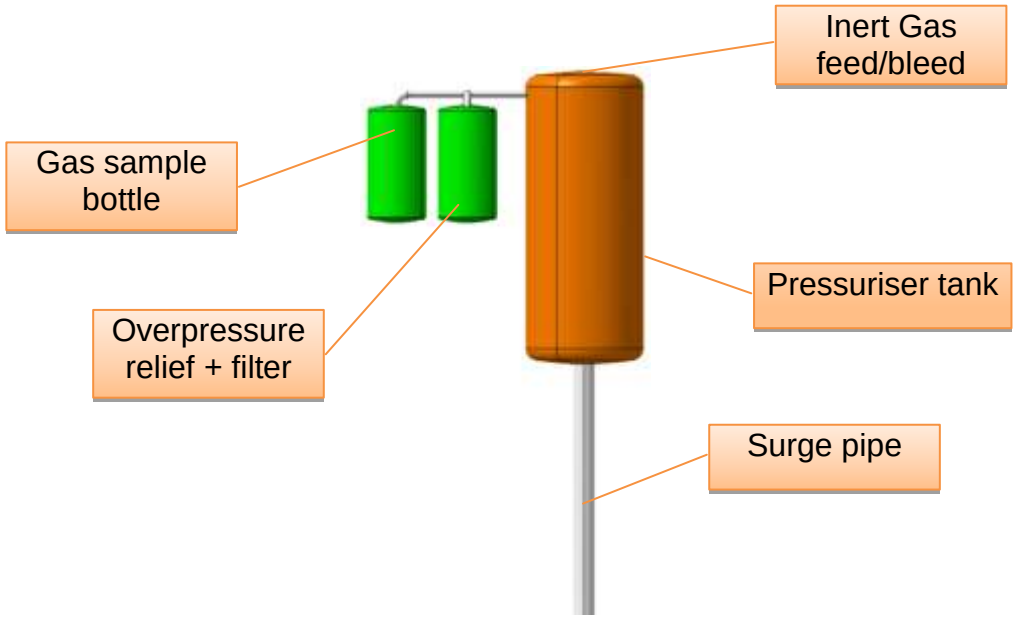

Figure 79: Pressuriser and venting systems

The design study has currently not yet examined these components at great length and they are merely represented in the figure above in terms of their expected volume and position. A deeper analysis of these components will be necessary in the next stage of the project.

3.2.3 Filtering and cleaning

During the operation of the target impurities are created in the liquid metal in part because of the transmutation effect induced by spallation and also the chemical corrosion caused by oxygen present in the loop. As they tend to concentrate activity they must be regularly withdrawn from the loop by filtering. To avoid it becoming a significant important source of pressure loss during operation, the filter is not inserted on the main route but on a by-pass section.

Whenever considered necessary, an appropriate selection of by-pass valves allows the primary liquid to flow through the filter. Once sufficient activity has been accumulated in the filter, the bypass is closed and the flow returned to normal operation. Regular use of the filter should prevent the deposition of active corrosion products along the walls in the primary circuit which can in the long terms contaminate the facility to such an extent that it can no longer be maintained or relocated to another facility. The filter can be exchanged during shutdown periods, using robotics.

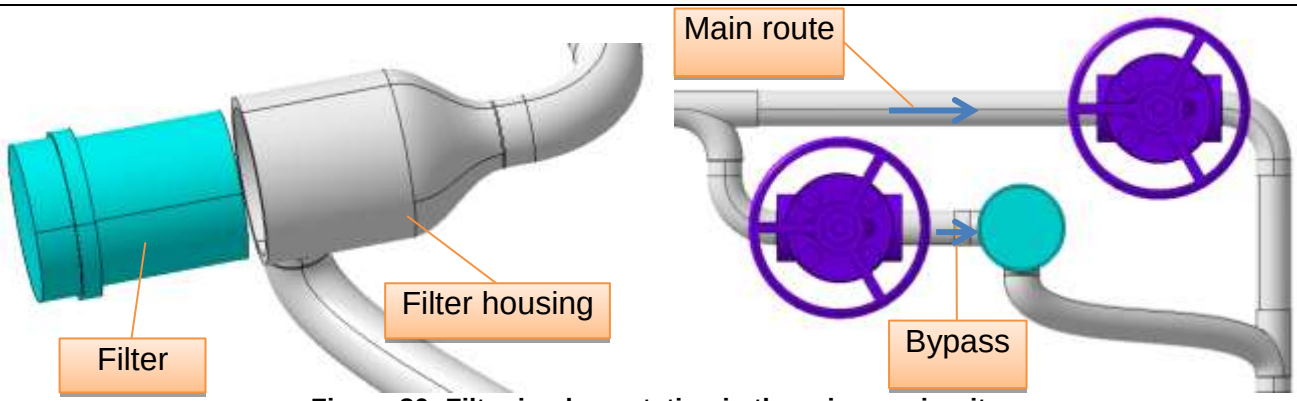

Figure 80: Filter implementation in the primary circuit

3.2.4 Electromagnetic Pump

In the primary loop, an electromagnetic pump is selected as it contains no moving parts, an important consideration when dealing with a highly radioactive environment in terms of maintenance and reliability. The working principle based on magneto hydrodynamics has a fairly low efficiency, resulting in high power consumption. A flow rate of 1.4 m^3/h is required.

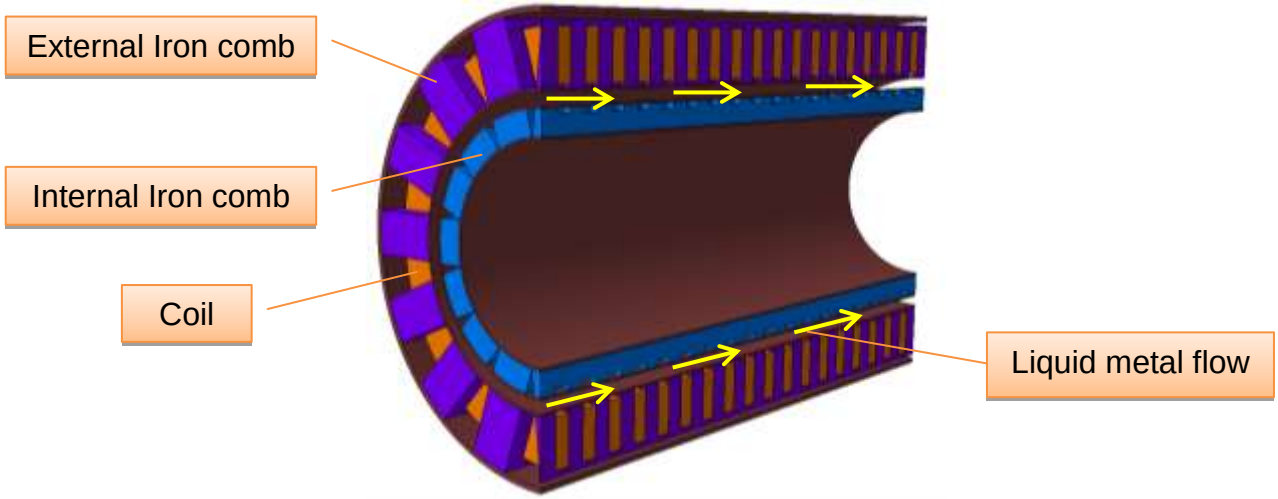

Figure 81: Electromagnetic Pump

3.2.5 Decay tank

The decay tank collects all the liquid in the primary circuit during the shutdown to allow the opening of the primary circuit in order to access the samples but also to decrease the overall activity around the target area. Sizing the decay tank is directly related to the total volume of liquid in the primary circuit with some margin. The shape giving the greatest capacity with the smallest overall dimensions is a sphere; it's also the optimal configuration for shielding because much of the radioactive fluid is then self-shielded by the surrounding fluid and the total surface irradiating out into the environment is minimised compared to the volume it contains. The decay tank features:

-A main pipe for filling and draining the tank. This pipe must reach the very bottom of the tank to be able to evacuate the totality of the liquid when it is drained by applying over-pressure in the tank compared to the primary circuit.

-Sufficient access in terms of an observation hole to permit inspection using a bore scope camera. In the current design the inspection hole stoppers are identical and the decay tank would need to be dismounted for inspection.

-A gas plug at the top of the tank to pressurize the tank allowing it to be drained. It can also be used to extract the gases which accumulate in the liquid due to radioactive decay.

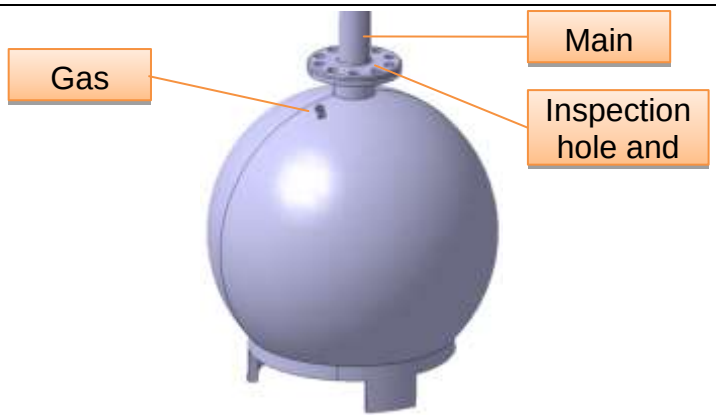

Figure 82: Decay tank

There are two decay tanks in the facility for reasons of safety, notably redundancy and operational maintenance since it allows fresh liquid to be pumped into the primary circuit while the used fluid is allowed to decay. An external interface also allows evacuation of the liquid for external disposal. A series of valves allows redundancy in operation and exchange of fluids.

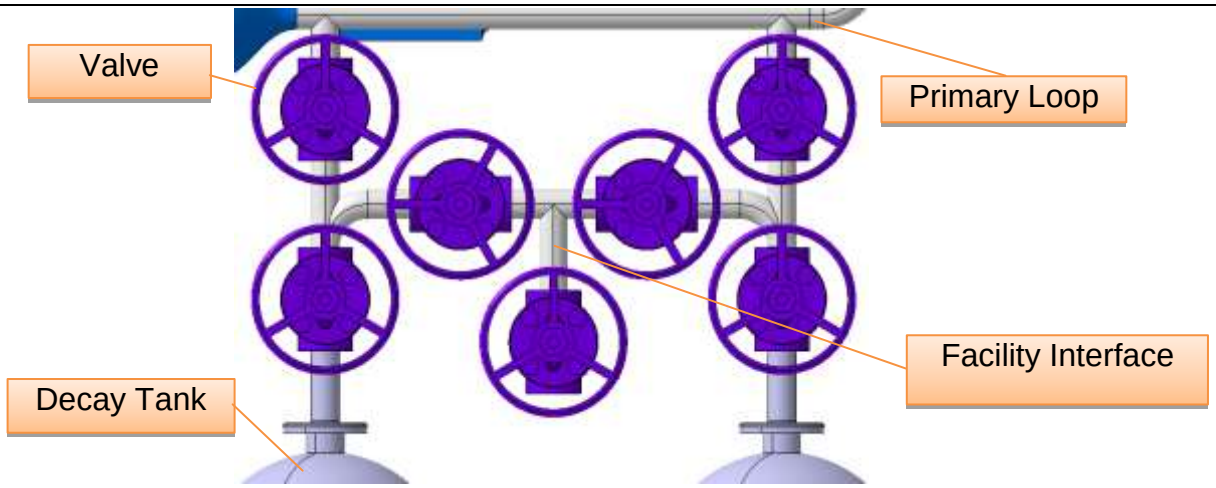

Figure 83: Valve control for decay tanks

3.2.6 Heat Exchanger

The design of the heat exchanger is explained at greater length as the design is somewhat novel featuring a dismountable interface between the primary and secondary side.

3.2.6.1 Design concept of the heat exchanger

The heat exchanger design is addressed in section 2.2.1 of Ref.2 and a broad concept is proposed which features a central pin containing the primary fluid centrally located inside an outer spiral containing the secondary fluid. The spiral shape permits to extend the path length, therefore the efficiency increases and the volume stays compact. The two components are in thermal contact but are physically distinct, having no common wall as is often the case in traditional heat exchangers.

The concept is summed up in figure 11 below.

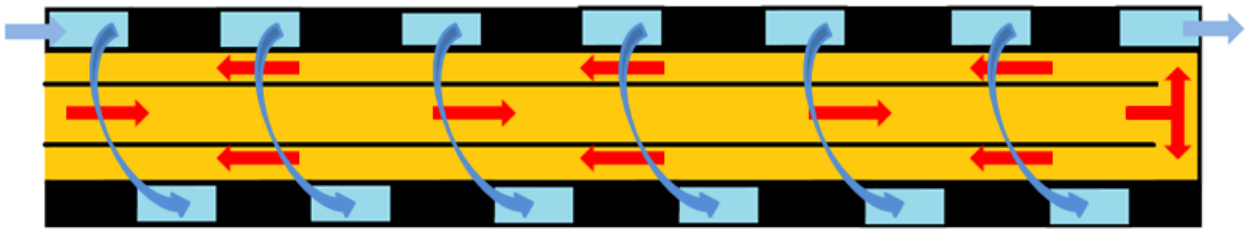

Figure 84: Heat Exchanger concept for T-MIF

A primary-side (orange) pin is inserted inside a secondary-side (blue) barrel with a spiral flow

The main advantage of this arrangement is its inherent safety. The two sides can be disassembled easily from one another by removing the pin from the barrel since the two are not attached.

Furthermore the small gap between the external wall of the primary-side pin and the secondary-side spiral-flow barrel can be filled with a thermally conductive gas which in the event of a leak from either side will catch the leaking fluid without breaking through to the other side, thus preventing contamination from the primary fluid from reaching the secondary circuit. In addition the leak will provoke an immediate rise in the gas pressure of the interface gap, a very robust leak detection device which was proven to work quite well both in the safety test of MEGAPIE and in the MEGAPIE test itself.

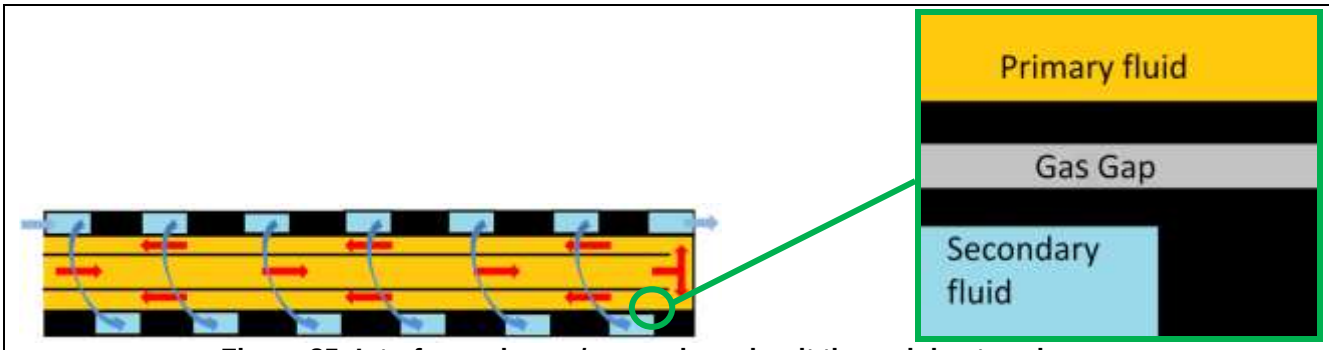

Figure 85: Interface primary / secondary circuit through heat exchanger

3.2.6.2 One dimensional Calculations of the heat exchange

The initial design of the heat exchanger has been optimised using one dimensional theory in which both fluids are considered as circulating in conformal tubes

3.2.6.2.1Theory

In order to gain a first insight into the performance of the heat exchanger, simple one-dimensional calculations are performed using the LMTD method (Log Mean Temperature Difference). This method computes the exchanged power and subsequently the necessary exchange surface based on the in- and output temperature of both primary heater-side and secondary cooling fluids.

According to the primary specifications for this heat exchanger, liquid metal fluids are used such as Lead, Lead-Bismuth Eutectic and Gallium, the exchanged power will be approximately 100 kW and temperatures on the primary side should not exceed 600°C to avoid Polonium evaporation from the LBE in the target. Obviously, the considered range of temperature needs to reflect the fact that the metals must remain in their liquid state.

Thus, the process envisaged is to create an Excel sheet following the LMTD method from which the in- and output temperatures of both fluids may be derived to obtain the required heat exchange. From this configuration, the exchange surface and then the exchanger dimensions may be deduced.

3.2.6.2.2Fluid properties

Before starting any calculation, some characteristics of the potential fluids used in the thermal exchanger must be collated. Indeed, these potential fluids that best fit the desired configuration are Gallium, Lead and Lead-Bismuth Eutectic and the needed characteristics are:

-Maximum and minimum operational temperatures (T°) that will a liquid state.

-Density (ρ)

-Specific heat capacity (C_p)

-Thermal conductivity (λ)

-Dynamic viscosity (μ)

-Molar mass (M)

Fluid:	Gallium			
Inlet T°	T_e	Min 30	°C	http://jpcrd.aip.org/resource/1/jpcrbu/v41/i3/p033101_s1
Outlet T°	T_s	Max 1227	°C	
Density	ρ	6033	kg/m3	
Specific heat capacity	C_P	381	J/(kg.K)	At 373 °K
Thermal conductivity	λ	41	W/(m.K)	
Dynamic viscosity	μ	0.001263	Pa.s	
Molar Mass	M	69.723	g/(mol)	

Fluid:	Lead			
Inlet T°	T_e	Min 327.46	°C	http://www.oecd-nea.org/science/reports/2007/pdf/
Outlet T°	T_s	Max 1027	°C	
Density	ρ		kg/m3	11367-(1,1944.T)
Specific heat capacity	C_P		J/(kg.K)	175,1-(0.04961.T)+(0.00001985.T^2)-(0.000000002099.T^3)-(1524000.T^-2)
Thermal conductivity	λ		W/(m.K)	9,2+(0,011.T)
Dynamic viscosity	μ		Pa.s	0,000455.exp(1069/T)
Molar Mass	M	207.2	g/(mol)	

Fluid:	Lead-Bismuth Eutectic			
Inlet T°	T_e	Min 130	°C	http://www.oecd-nea.org/science/reports/2007/pdf/
Outlet T°	T_s	Max 1000	°C	
Density	ρ		kg/m3	11096-(1,3236.T)
Specific heat capacity	C_P		J/(kg.K)	159-(0,0272.T)+(0,00000712.T^2)
Thermal conductivity	λ		W/(m.K)	3,61+(0,01517.T)-(0,000001741.T^2)
Dynamic viscosity	μ		Pa.s	0,000494.exp(754,1/T)
Molar Mass	M	208.21	g/(mol)	

Table 15: Calculation sheet extract - Fluids properties

In addition, the thermal conductivity (λ_p) and the roughness index (k) of the Stainless Steel that will be used as the piping material are also needed.

Material	Stainless steel		
Thermal conductivity	λ_p	60.5	W/(m.K)
Roughness index	k	0.1	mm

Table 16: Calculation sheet extract - Material properties

3.2.6.3 Simplified calculation for scoping analysis

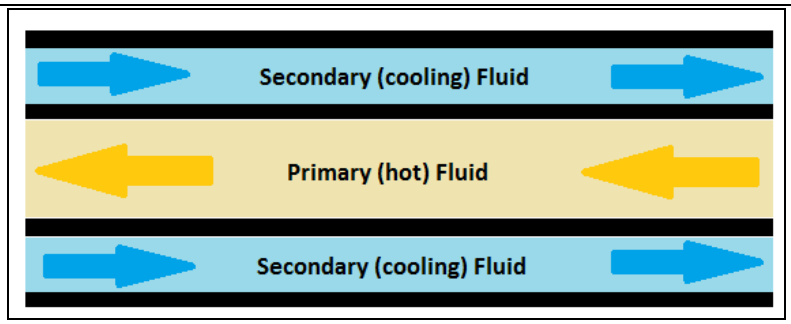

Figure 86: Initial simplified model

In a first calculation, the heat exchanger is represented by 2 concentric pipes, the primary fluid flowing through the inner pipe and the secondary (or cooling) fluid flowing counter-current through the outer pipe as represented above. However, it should be borne in mind that these results relate to an ideal concentric tube model and do not take into account every parameter of the real configuration. However it gives a good first approach of the exchanger specifications and the fluids conditions, which is to be completed by a 3D model later in the analysis.

The following simulation uses LBE as the primary fluid due to its wide liquid state temperature range and Gallium as the secondary fluid for its superior conductivity properties.

Primary fluid:	LBE		
Inlet T°	T_{e1}	550	°C
Outlet T° $T_{s1} < T_{e1}$	T_{s1}	300	°C
Volumetric flow rate	Q_1	1	m3/h
Density	ρ_1	10171.92866	kg/m3
Specific heat capacity	C_{p1}	143.4807036	J/(kg.K)
Thermal conductivity	λ_1	13.35234873	W/(m.K)
Dynamic viscosity	μ_1	0.001454876	Pa.s
Prandtl's number $\mu_1.C_{p1}/\lambda_1$	Pr_1	0.015634	
Mass flow $Q_1.\rho_1$	m_1	2.825536	kg/s
Flow capacity $m_1.C_{p1}$	C_1	405.409856	J/(s.K)

Secondary fluid:	Gallium		
Inlet T°	T_{e2}	75	°C
Outlet T° $T_{s2} > T_{e2}$	T_{s2}	120	°C
Volumetric flow rate $m_2.\rho_2$	Q_2	3.527492	m3/h
Density	ρ_2	6033	kg/m3
Specific heat capacity	C_{p2}	381	J/(kg.K)
Thermal conductivity	λ_2	41	W/(m.K)
Dynamic viscosity	μ_2	0.001263	Pa.s
Prandtl's number $\mu_2.C_{p2}/\lambda_2$	Pr_2	0.011737	
Mass flow	m_2	5.911488	kg/s
Flow capacity $m_2.C_{p2}$	C_2	2252.28	J/(s.K)

Exchange surface:	Stainless steel		
Thermal conductivity	λ_p	60.5	W/(m.K)
Wall thickness	e	5	mm

Fluid average T° 1	T_{moy1}	425	°C
Fluid average T° 2	T_{moy2}	97.5	°C

Exchanged power $C_1(T_{e1}-T_{s1})=C_2(T_{s2}-T_{e2})$	ϕ	101352.463943	W	≈ 100kW
Mass flow $\varphi/(C_{p2}.(T_{s2}-T_{e2}))$	m_2	5.911488	kg/s	
Flow capacities ratio C_1/C_2	R	0.18		
Exchanger efficiency $(T_{e1}-T_{s1})/(T_{e1}-T_{e2})$	ε	0.526316		
> According to Kern's literature, corrective coef	F	0.97		

The green cells are the input data needed to drive the computation; they are the only parameters to be modified. The grey cells are taken from the materials properties seen above; the values depend on the fluid average temperatures. All the other cells of this sheet are computed and cannot be manually changed.

The exchanged power is directly linked to the working temperatures and current settings lead to a value close to the required 100 kW.

Table 17: Heat Exchanger results with LBE

In the configuration shown, an exchanged power close to 100kW is reached, within temperatures limitations. Thus almost all the information needed is available for a final calculation of the exchanger specifications. Beforehand, the pipes diameters must be chosen.

Exchange pipe 1's diameter	D_1	0.025	m
Exchange hydraulic diameter 1	D_{h1}	0.025	m
Exchange hydraulic flow area 1	A_1	0.000491	m2
Exchange pipe 2's diameter	D_2	0.05	m
Exchange hydraulic diameter 2	D_{h2}	0.02475	m
Exchange hydraulic flow area 2	A_2	0.000481	m2

The hydraulic diameter is obtained by computing 4*area/perimeter. The hydraulic area is then derived from the hydraulic diameter.

Table 18: Heat Exchanger dimensions with LBE

Logarithmic average T° $(Te1-Ts2)-(Ts1-Te2)/ln((Te1-Ts2)/(Ts1-Te2))$	ΔT_{ML}	316.51	°C
Fluid velocity 2 Q_2/A_2	v_2	2.036266	m/s
Reynolds' number 2 $\rho_2.v_2.D_2/\mu_2$	Re_2	240759.857448	
Colburn's correlation > exchange coef $(\lambda_2/D_2).0,023.(Re_2^{0,8}).(Pr_2^{(1/3)})$	h_2	174853.474138	W/(m2.K)
Fluid velocity 1 Q_1/A_1	v_1	0.565884	m/s
Reynolds' number 1 $\rho_1.v_1.D_1/\mu_1$	Re_1	98911.084371	
Nusselt's number 1 $0.36.(Re_1^{0.55}).(Pr_1^{(1/3)})$	Nu_1	50.316199	
Exchange coef $\lambda_1.Nu_1/D_1$	h_1	26873.577352	W/(m2.K)
Global exchange coef inverse $1/(h_1.(D_1/D_2))+(1/h_2)+(D_2/2.\lambda_p).ln(D_1/D_2)$	1/K	0.000045	
Then	K	22422.991856	W/(m2.K)
Exchanger's surface $\varphi/(F.K.\Delta T_{ML})$	S	0.014722	m2
Exchanger length	L	0.133893949	m

From the 2 flows specifications and the piping dimensions, both fluids velocities are obtained and subsequently their Reynolds' numbers.

The aim of this sheet is to obtain the global power exchanged to finally derive the heat exchanger dimensions.

Table 19: Heat Exchanger specifications with LBE

The configuration with LBE above ties in well with project needs from a thermal-hydraulic point of view. Liquid LBE as a primary fluid enters the inner part of the exchanger at 550°C at 1 m^3/h and exits at 300°C. On the secondary side liquid Gallium as a cooling fluid enters the outer part of the exchanger at 75°C and approximately 3.5 m^3/h and leaves at 120°C. In the actual configuration, the LBE needs to share 0.0147 m2 with the Gallium to shed the100 kW deposited by the beam in the target.

However, after discussion with the management of the PSI Hotlab, a consensus was reached to replace LBE by Lead as the primary fluid, to avoid any production of polonium which would impose a higher classification of the laboratory where the facility may be positioned. Since lead will freeze at a higher temperature than LBE, the temperature range of the primary side exchanger needs to be adapted. Hence, instead of cooling the primary fluid down to 300°C, a minimum of 380°C is chosen; 327°C being the solidification temperature of lead.

A repeat of the calculations with the tables above yields the following results

Primary fluid:	Lead		
Inlet T°	T_{e1}	550	°C
Outlet T° $T_{s1} < T_{e1}$	T_{s1}	380	°C
Volumetric flow rate	Q_1	1.4	m3/h
Density	ρ_1	10485.35364	kg/m3
Specific heat capacity	C_{p1}	145.6547343	J/(kg.K)
Thermal conductivity	λ_1	17.31965	W/(m.K)
Dynamic viscosity	μ_1	0.001936258	Pa.s
Prandtl's number $\mu_1.C_{p1}/\lambda_1$	Pr_1	0.016284	
Mass flow $Q_1.\rho_1$	m_1	4.077638	kg/s
Flow capacity $m_1.C_{p1}$	C_1	593.927211	J/(s.K)

Secondary fluid:	Gallium		
Inlet T°	T_{e2}	75	°C
Outlet T° $T_{s2} > T_{e2}$	T_{s2}	120	°C
Volumetric flow rate $m_2.\rho_2$	Q_2	3.514098	m3/h
Density	ρ_2	6033	kg/m3
Specific heat capacity	C_{p2}	381	J/(kg.K)
Thermal conductivity	λ_2	41	W/(m.K)
Dynamic viscosity	μ_2	0.001263	Pa.s
Prandtl's number $\mu_2.C_{p2}/\lambda_2$	Pr_2	0.011737	
Mass flow	m_2	5.889042	kg/s
Flow capacity $m_2.C_{p2}$	C_2	2243.73	J/(s.K)

Exchange surface:	Stainless steel		
Thermal conductivity	λ_p	60.5	W/(m.K)
Wall thickness	e	3	mm

Fluid average T° 1	T_{moy1}	465	°C
Fluid average T° 2	T_{moy2}	97.5	°C

Exchanged power $C_1(T_{e1}-T_{s1})=C_2(T_{s2}-T_{e2})$	Φ	100967.625800	W	= 100kW
Mass flow $\varphi/(C_{p2}.(T_{s2}-T_{e2}))$	m_2	5.889042	kg/s	
Flow capacities ratio C_1/C_2	R	0.26		
Exchanger efficiency $(T_{e1}-T_{s1})/(T_{e1}-T_{e2})$	ε	0.357895		
> According to Kern's literature, corrective coef	F	0.97		

Table 20: Heat Exchanger results with Lead

Exchange pipe 1's diameter	D_1	0.025	m
Exchange hydraulic diameter 1	D_{h1}	0.025	m
Exchange hydraulic flow area 1	A_1	0.000491	m2
Exchange pipe 2's diameter	D_2	0.05	m
Exchange hydraulic diameter 2	D_{h2}	0.02511	m
Exchange hydraulic flow area 2	A_2	0.000495	m2

Table 21: Heat Exchanger dimensions with Lead

Logarithmic average T° $(Te1-Ts2)-(Ts1-Te2)/ln((Te1-Ts2)/(Ts1-Te2))$	ΔT_{ML}	363.93	°C
Fluid velocity 2 Q_2/A_2	v_2	1.971393	m/s
Reynolds' number 2 $\rho_2.v_2.D_2/\mu_2$	Re_2	236443.440552	
Colburn's correlation > exchange coef $(\lambda_2/D_2).0,023.(Re_2^{0,8}).(Pr_2^{(1/3)})$	h_2	169896.401187	W/(m2.K)
Fluid velocity 1 Q_1/A_1	v_1	0.792238	m/s
Reynolds' number 1 $\rho_1.v_1.D_1/\mu_1$	Re_1	107254.491972	
Nusselt's number 1 $0,36.(Re_1^{0.55}).(Pr_1^{(1/3)})$	Nu_1	53.327014	
Exchange coef $\lambda_1.Nu_1/D_1$	h_1	36944.208521	W/(m2.K)
Global exchange coef inverse $1/(h_1.(D_1/D_2))+(1/h_2)+(D_2/2.\lambda_p).ln(D_1/D_2)$	1/K	0.000032	
Then	K	31083.695473	W/(m2.K)
Exchanger's surface $q/(F.K.\Delta T_{ML})$	S	0.009202	m2
Exchanger length	L	0.094482056	m

Table 22: Heat Exchanger specifications with Lead

The configuration with Lead above ties in also well with project needs from a thermal-hydraulic point of view. Liquid Lead as a primary fluid enters the inner part of the exchanger at 550°C at 1,4 m^3/h and exits at 380°C. On the secondary side liquid Gallium as a cooling fluid enters the outer part of the exchanger at 75°C and approximately 3.5 m^3/h and leaves at 120°C. In the actual configuration, the Lead needs to share 0.0092 m2 with the Gallium to shed the100 kW deposited by the beam in the target.

3.2.6.4 Heat exchanger Design in 3D using CFD

3.2.6.4.1HEX Design

As mentionned in the design concept of the heat exchanger, the actual heat echanger model will be more complex than the one used in the Excel sheet calculation. The primary and secondary part of the exchanger must be simple to assemble, for easy maintenance and to improve security. Thus both the in-and outlet of the primary side are at the same location, in the form of two concentric pipes.

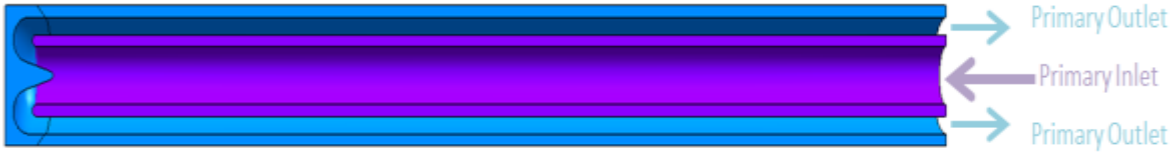

Figure 87: Primary part of the exchanger – sectional view

Furthermore, the secondary fluid flows in a spiral pipe wrapped around the central primary fluid barrel. The part shown in is basically a cylinder that close the upper spiral surface shown in orange.

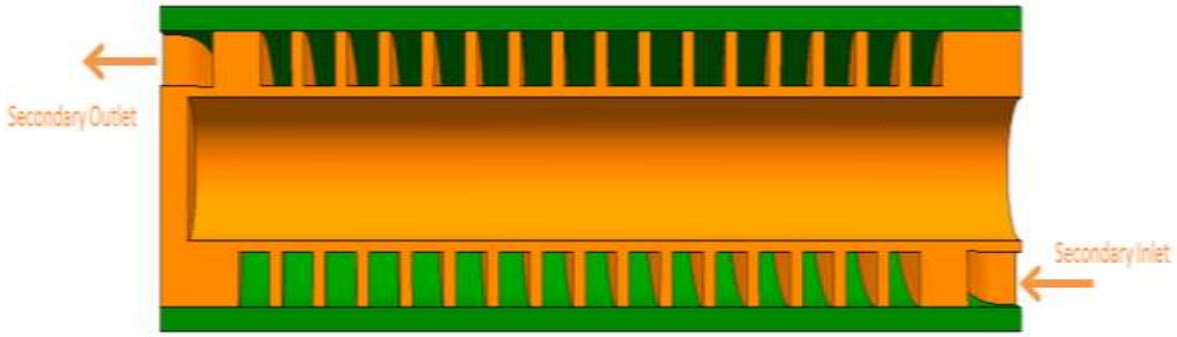

Figure 88: Secondary part of the exchanger – sectional view

Hence primary and secondary parts are fully independent and can be isolated in an emergency or for maintenance. Indeed the exchanger can be easily disassembled by sliding the inner primary part out of the outer secondary part.To improve the exchange efficiency, the fluids are running counter-current along almost the entire exchange surface. A wall at the extremity permit to close the volume between the 2 parts of the exchanger. It prevents an unexpected leak from the primary canal to flow down out of the securized volume and contains the gas used for leak detection.

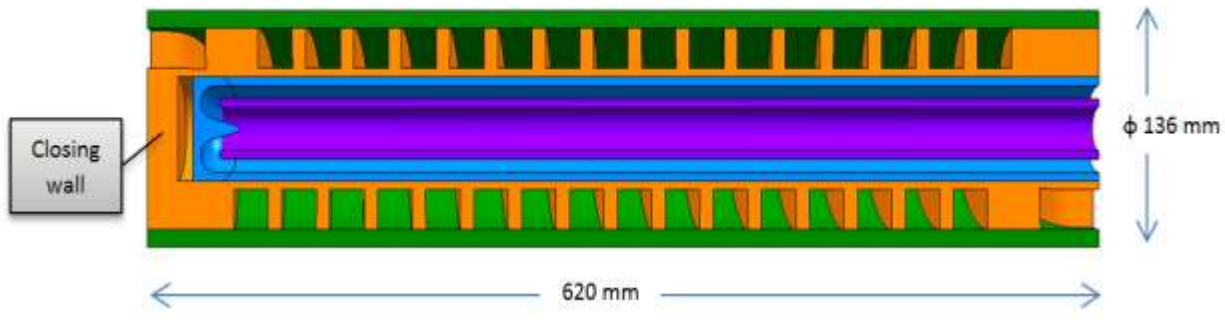

Figure 89: Complete Heat Exchanger – sectional view

This design construction differs slightly from the one used in the Excel simulation. And hence dimension s will differ slightly. Thus the pipe hydraulic flow areas are the same but the diameters are larger. Hence the heat exchange is less efficient than expected. Therefore, in a first instance a longer exchange surface (approximately 500 mm) is set and the resulting heat exchange is checked in a CFD analysis. Then, through iterations, this length may be adapted to the desired specified perofrmance of 100 kW, since the heat exchanged will be roughly proportional to the length.

3.2.6.4.2CFD Analysis

In the CFD analysis, excluding the secondary fluid velocity, all the input parameters are from the Excel calculation. Indeed for the secondary fluid velocity, as the spiral path is longer and the walls drag more important, it has been forced at 4 m/s instead of 2 m/s at the in- and outlet. In a first calculation, only the heat flux is monitored, the outer wall in contact with the environment is taken as adiabatic.

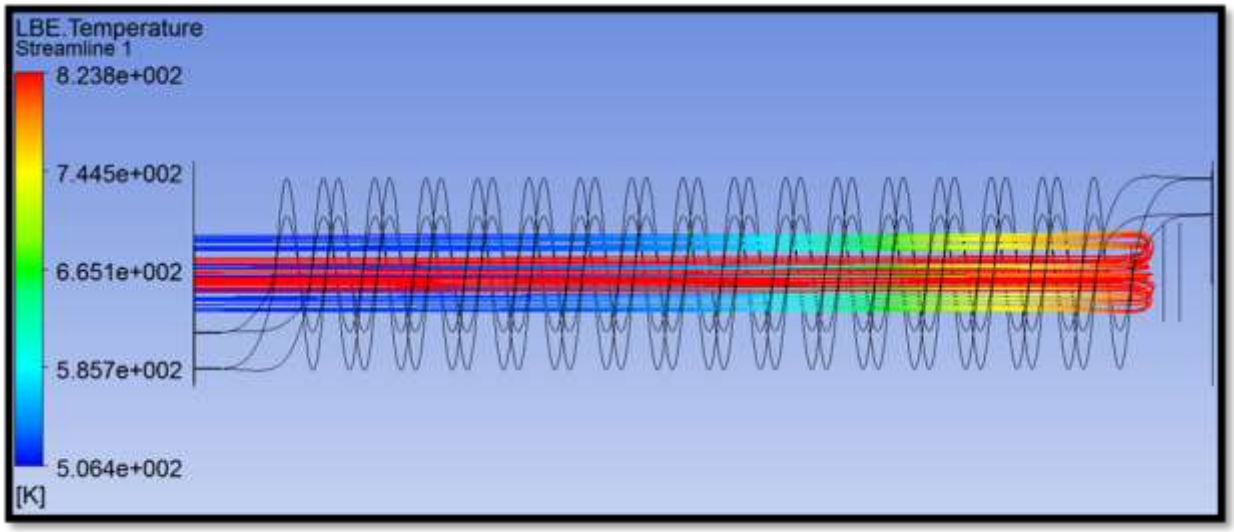

Figure 90: LBE temperature in primary circuit

On the CFD result above, the temperature variation in the primary fluid (LBE) is shown. The inlet temperature is set at 550°C (823°K - 273 = 550°C). The temperature is fairly constant in the first part of the channel because there is no contact with a cold source but it is clear that the LBE cools down along its way back down the outer annulus due to the proximity with the spiral. The LBE leaves the exchanger at a temperature of 233°C. This means the exchanged power is about 130 kW instead of the required 100kW.

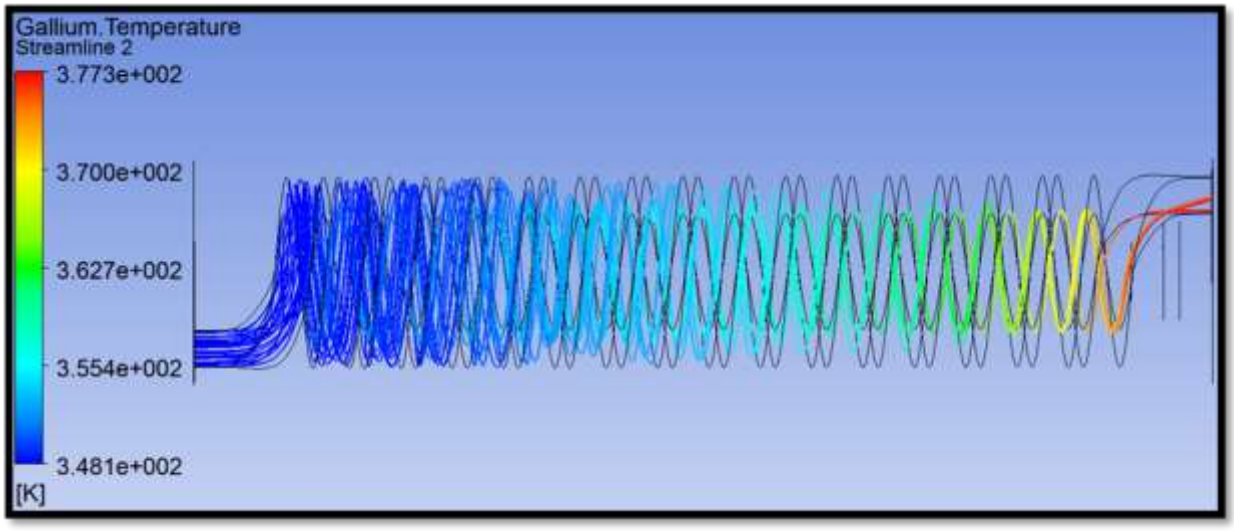

Figure 91: Gallium temperature in secondary circuit

In the figure above the secondary fluid temperature variation along the Gallium flow is shown. As set, the inlet temperature is 75 °C. The heat exiting the LBE warms up the Gallium up and finally reaches the outlet at 104°C.

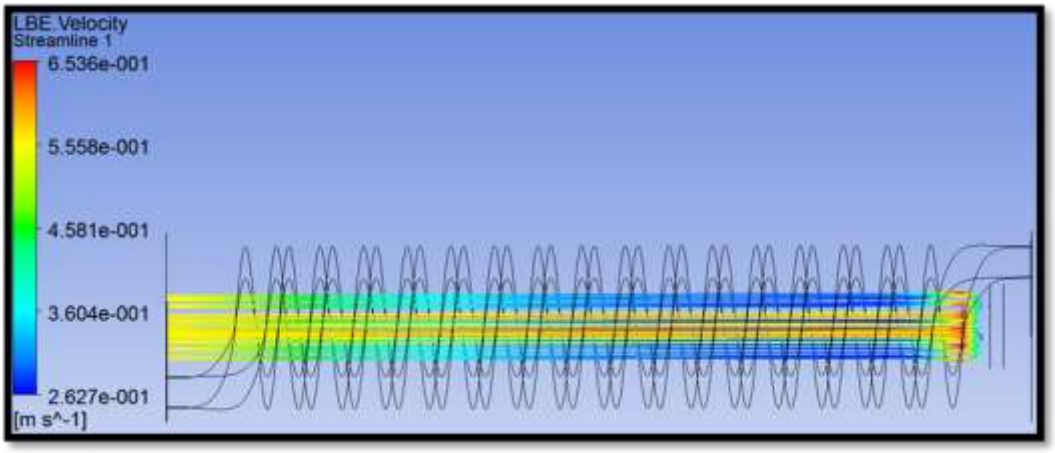

Figure 92: LBE velocity in primary circuit

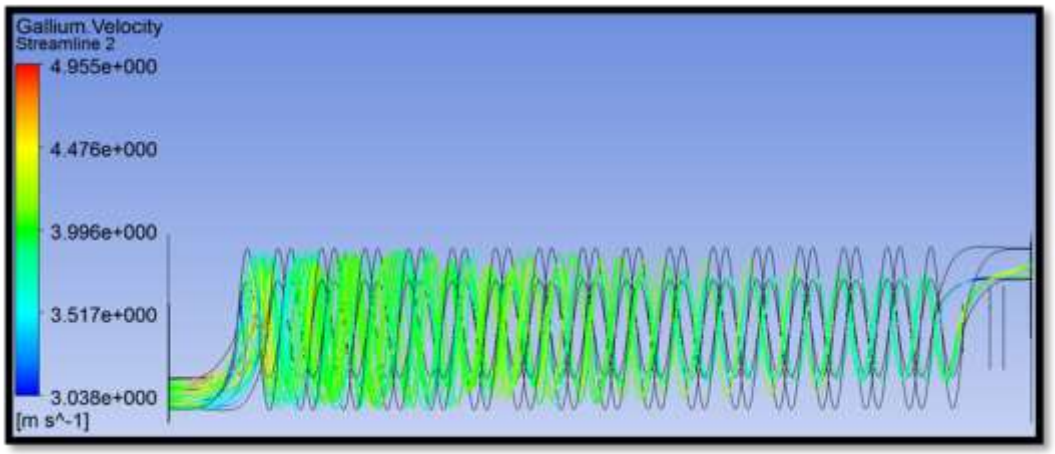

Figure 93: Gallium velocity in secondary circuit

By examining the velocity, it seems the secondary fluid flow is quite constant; the primary fluid tends to slow down after the turn back. It seems to speed up again before the outlet probably due to a homogenous velocity boundary condition.

In conclusion the primary fluid is cooled down more than needed. This means that there is enough scope for reducing the dimensions of the heat exchanger or including a small gas gap between the two parts which would lower efficiency but increase safety by separating the boundaries of the primary and secondary containments. Such a small gas-filled gap between primary and secondary containments would serve both as a barrier and a leak detection device.

3.2.6.4.3Variation study of the gap width

The previous calculations demonstrated an increase in exchanged power beyond 100 kW. It may therefore be possible to implement a gap between the spiral and the pin, which will have several effects:

-Adds thermal resistance. Hence thermal performance is degraded. This may be acceptable since the previous calculation showed the target of 100 kW was exceeded.

-Acts as buffer to prevent a crack from the primary side from propagating into the secondary side. If the gap is sufficient, there will be no direct contact between the two and hence no thermal stresses.

-Acts as a leak detection device, any leak provokes an increase in pressure.

-Allows controlling the direction of the leak by managing the pressure in each circuit. For instance if $P_{secondary} > P_{gas} > P_{primary}$, then radioactive volatiles will remain confined in the event of any breach of the containments. The strategy of stratifying the pressure levels is used with success in conventional nuclear power plants to prevent leaks of radioactivity during operation and minor deviations.

The first simulations show that the heat exchanged between the two parts becomes almost insignificant as soon as the two surfaces are physically completely separated, even if this gap is filled by a conductive gas such as Helium and reduced to a minimum, constrained by manufacturing tolerances.

Since the advantages listed above seem desirable, an alternative design has been sought which conserves these desirable properties whilst enabling the flow of heat.

3.2.6.5 Inlaid copper conduction strap

A new component is needed in order to insure a good heat contact between the primary and the secondary containment while conserving the gas gap. This new component is a highly conductive copper strap inserted between the two containments. However, to keep the same exchange surface and the same exchanged power of 100kW, the heat exchanger flow needs to be increased as the contact surface decreases.

After several simulations of gas thermal exchange, it seems adequate to assume that the whole power of 100kW is transferred by the copper strap and that the gas conduction may be neglected in the simulations. The copper strap is coiled inside the gas gaps and has the additional advantage of aiding in correctly positioning the primary inside the secondary.

As a first test to ensure good thermal contact between the primary and secondary parts of the exchanger, a simulation is carried with a simple spiral wire. This wire is 1mm in diameter and is rolled up around the pin like a spring. This solution proves to be not efficient enough, because of the very small contact surface between the cylinder and a plane, as shown below.

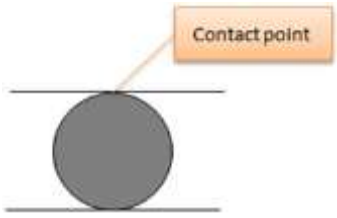

Figure 94: spiral wire in the gas gap

Hence, in the next attempt, the circular section is replaced by a rectangular section, more like a strap (2mm x 0,8mm) to increase thermal contact. This configuration is much more efficient but computations show the exchanged power still needs to be improved. Another design is tested, represented by straight rectangular (1,5mm x 0.5mm) lamellas parallel to the axis of the containment cylinder, in order to observe the effect of the orientation of the material on the exchange efficiency. It appears that the exchange is thus significantly improved, even with a smaller total contact surface.

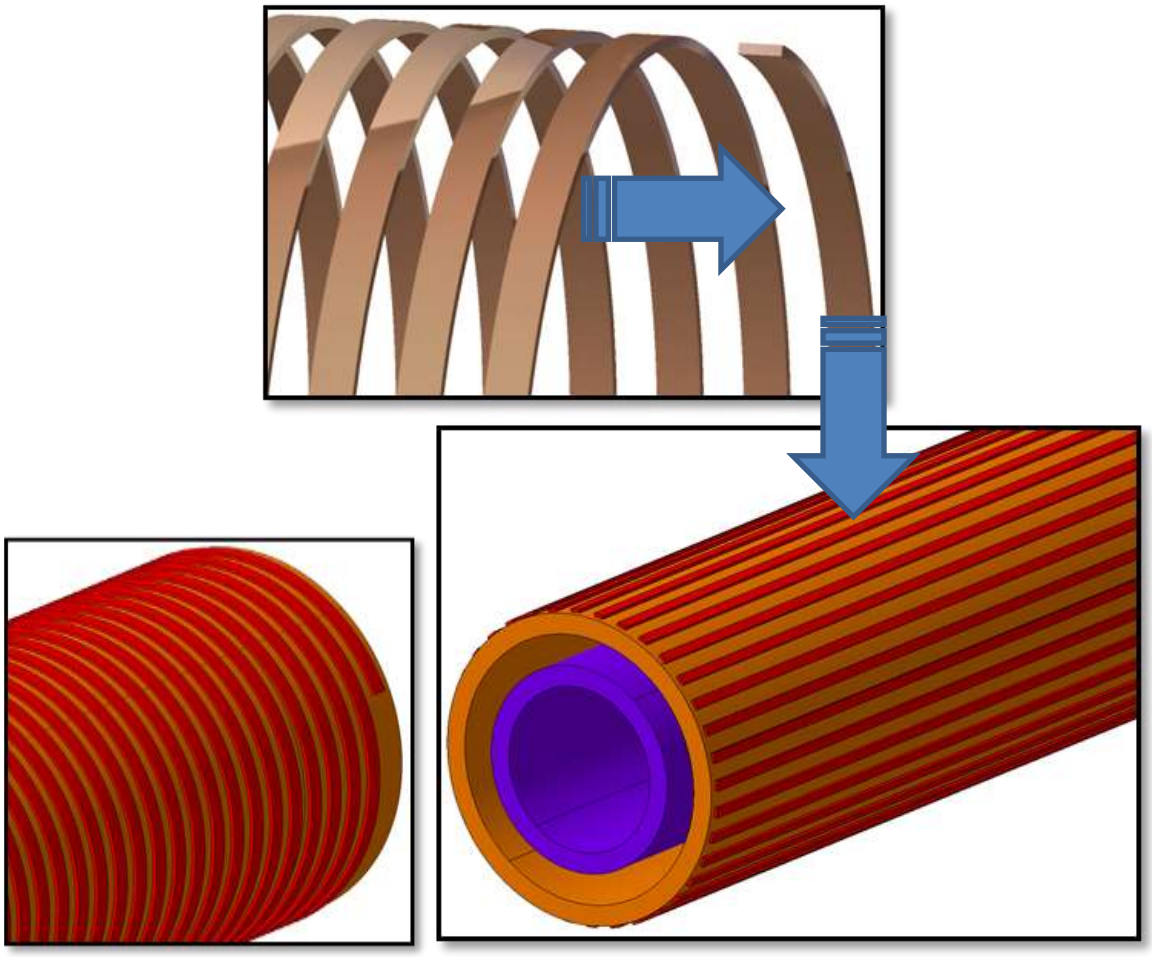

Figure 95: improved conductance strap

These lamellas are a valid thermal design but would be difficult to align in a real design, particularly if the two containments are to be separated for maintenance. A corrugated copper sheet concept (0,2mm thickness) is proposed as a feasible design which conserves this lamellas heat exchange properties. The corrugated cylindrical sheet can be placed in the gap materialising a good thermal contact surface between the primary and the secondary containments of the heat exchanger. It also ensures to a fair degree that both components be well located coaxially. The small thickness of the sheet and the small stiffness of the copper allow it to be deformed by differential thermal expansions without producing too much stress while keeping an optimum thermal contact. This final variant is kept for the next optimization simulations.

3.2.6.5.1CFD Analysis with corrugated copper sheet in gas gap

The same calculations are repeated, assuming the modified design as described previously. The effect of the heat exchange is documented in the figures hereafter. The primary fluid constituted now by Lead (Pb) which replaces the LBE, enters the heat exchanger at 550°C and its' outlet mean temperature reaches 377°C. The lead flows at a fairly constant velocity of 0.8 m/s.

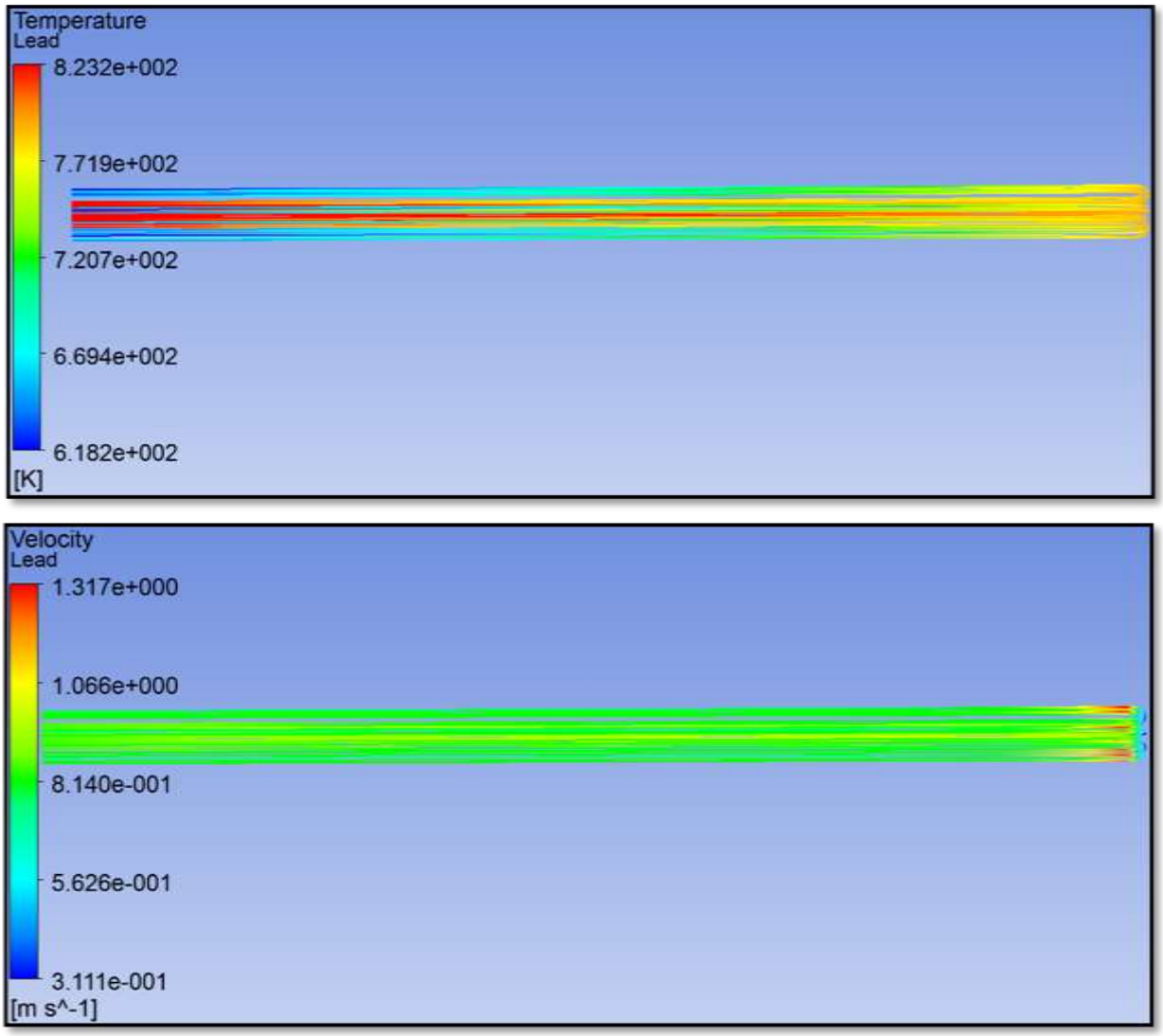

Figure 96: Liquid Lead temperature and velocity in primary circuit

On the secondary side, Gallium enters the spiral at 75°C and exits at a mean value of 119°C. The gallium passes through the spiral at a fairly constant velocity with an average of 2,9 m/s.

In this configuration, the heat exchanger is able to extract 100kW from the primary fluid and thus fully matches its specifications.

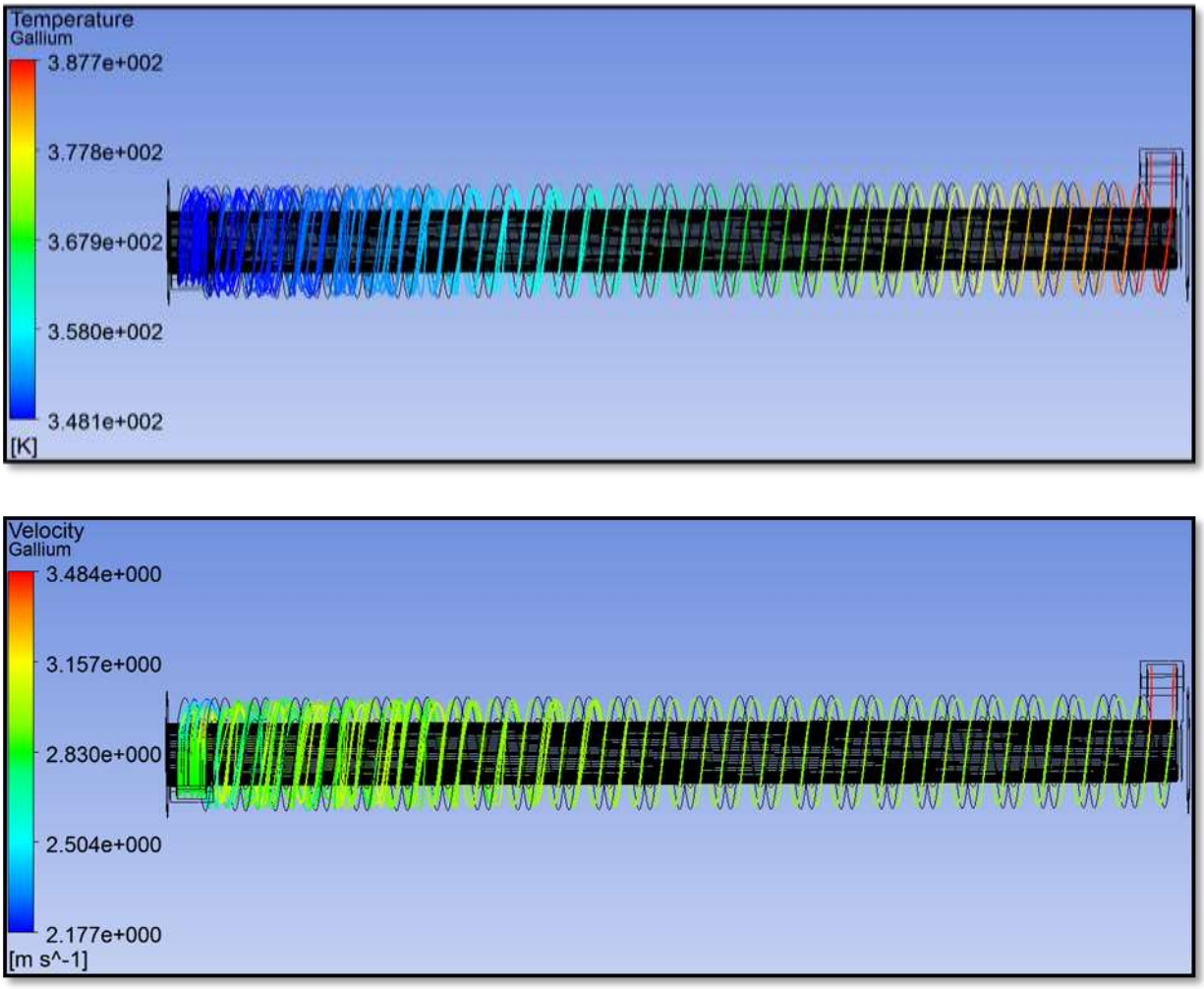

Figure 97: Liquid Gallium temperature and velocity in secondary circuit

3.3 Overall layout of the secondary loop

The secondary loop is an entirely removable component, which interface with the primary via the primary heat exchanger. The interface constituted by a hollow barrel which slots over the pin of the primary circuit allows the extraction of the entire secondary loop which is located inside a separate truss.

The heat that is extracted by the gallium from the primary loop is passed on to a secondary fin-type heat exchanger which is simply air cooled. There is therefore no need for any connection to the cold source, which is essentially the air of the lab. This air will have to be cooled by the environmental systems of the lab. These systems need to be dimensioned so as to cope with the extra 100 kW. This is a conservative figure, given that in reality only 70% of the 100 kW beam is dumped as heat, the remaining 30% are extracted by the energy of the escaping neutrons.

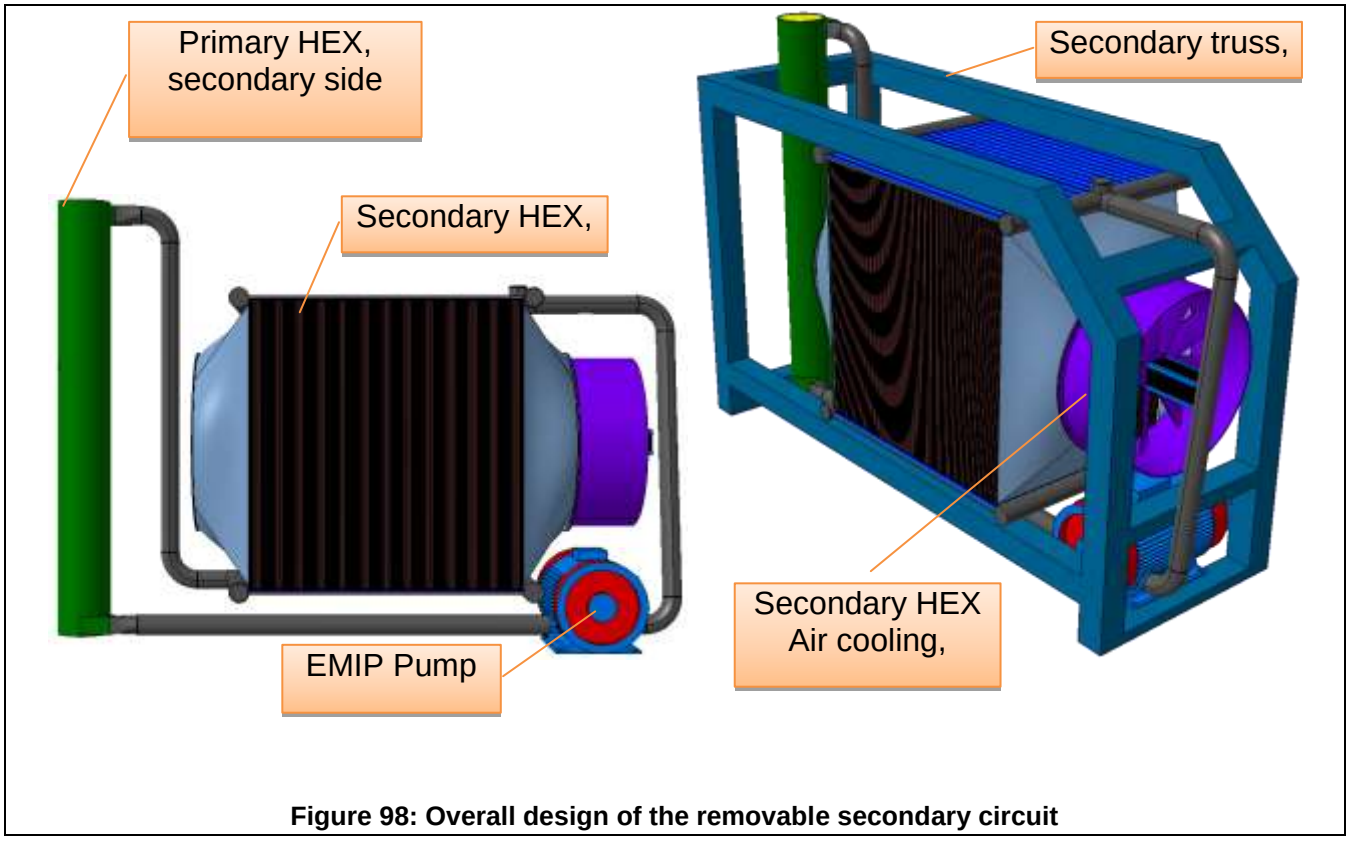

Figure 98: Overall design of the removable secondary circuit

The secondary loop has been sketched out in its most important aspects, however not with the degree of detail of the primary circuit. The heat exchanger, air circulation system and pump are examined.

In addition, the control systems for regulating the flow and secondary pressure still need to be examined and are not included in the scope of this study. Since the secondary circuit is not activated, and the presence of radioactive gases is excluded, it is reasonable to assume that the design of these remaining components will be simpler that in the primary circuit.

The method for extracting the secondary loop from the overall facility is illustrated in the next following figures.

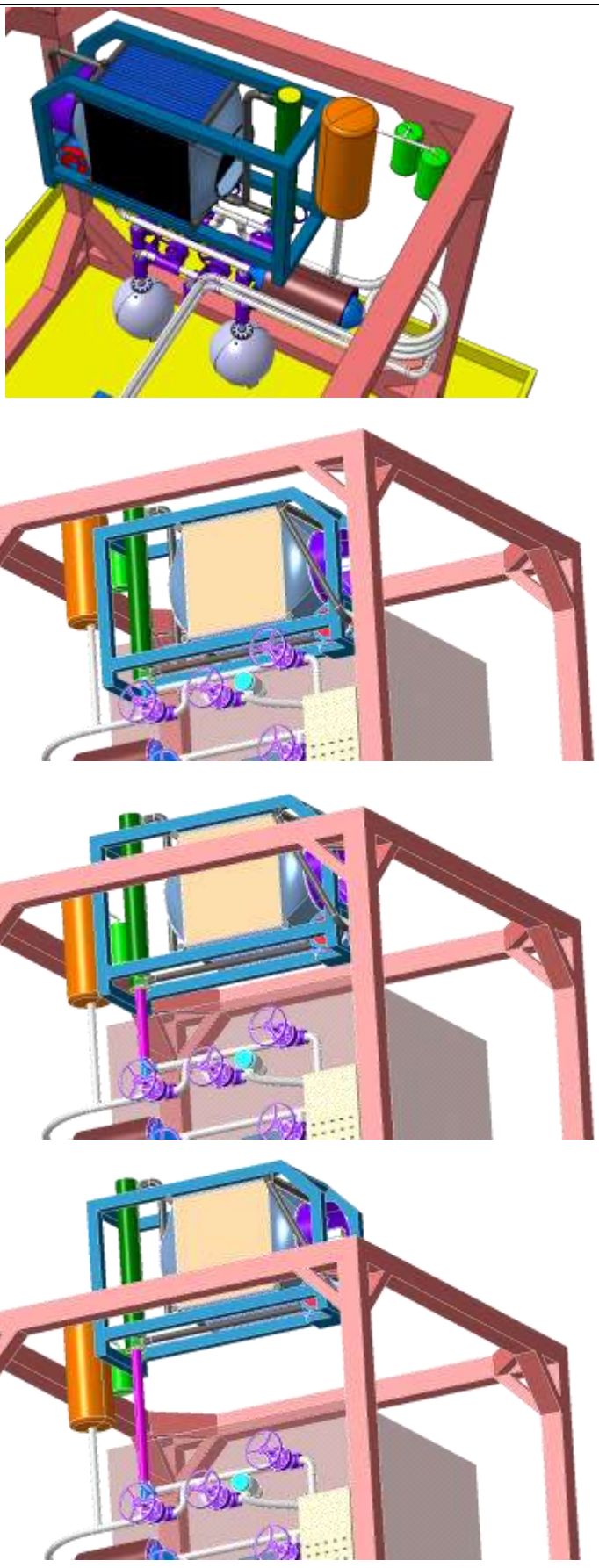

Figure 99: Extraction of the secondary circuit

3.3.1 Secondary heat exchanger

The secondary heat exchanger cools the secondary fluid down to 75°C after being heated to 120°C by the primary fluid in the primary heat exchanger. The proposed design is a plate heat exchanger cooled by forced convection air at 20°C. In these conditions, approximately 10 m^2 of exchange surface allows 100 kW of heat to be extracted.

The secondary fluid flows from a collector at the bottom of the plate exchanger to the top collector from where it passes back on to the inlet of the primary heat exchanger as indicated by the arrows in the figure below.

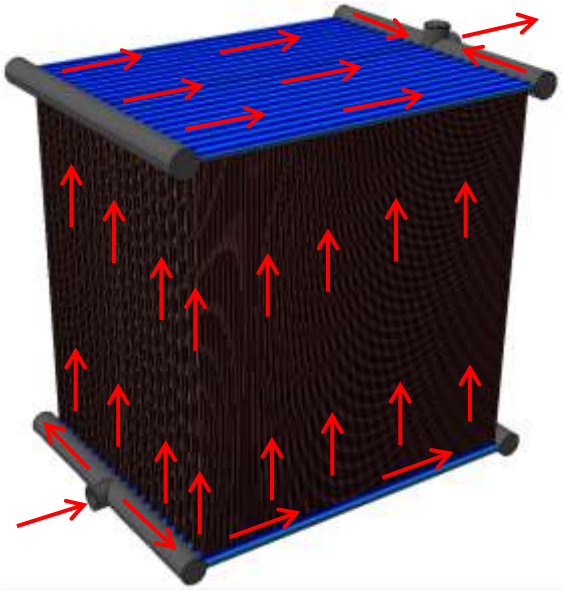

Figure 100: Secondary heat exchanger

The airflow along the plates is channelled by an inlet and outlet cone driven by an electrically motorized propeller.

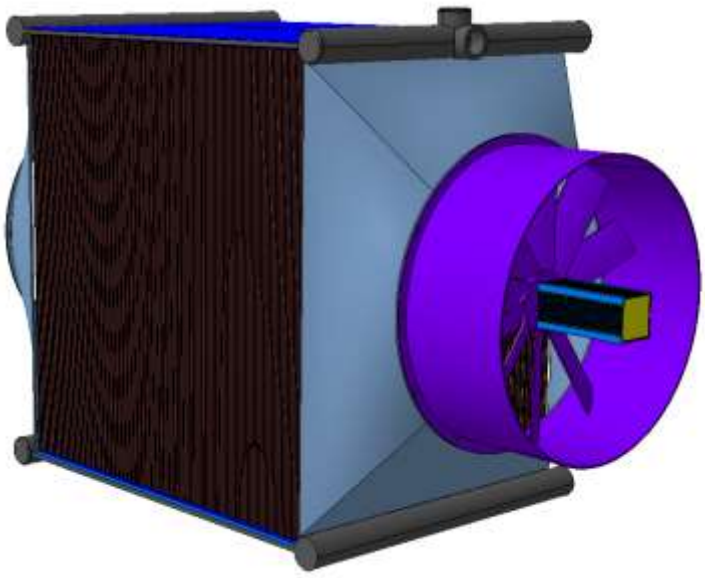

Figure 101: Secondary heat exchanger air cooling

3.3.2 Permanent magnet electromagnetic induction pump

As in the primary loop, a pump is needed for the secondary loop able to cope with liquid metal. The working principle is slightly different from the electromagnetic pump in the secondary and is driven by rotating permanent magnets as shown in the reference http://ipul.lv/main/?nav=imants

The pump must be able to provide a flow rate of 3,5 m3/h with sufficient power to overcome the drag losses in the fin plates. This matter will be analysed in the second stage of the project.

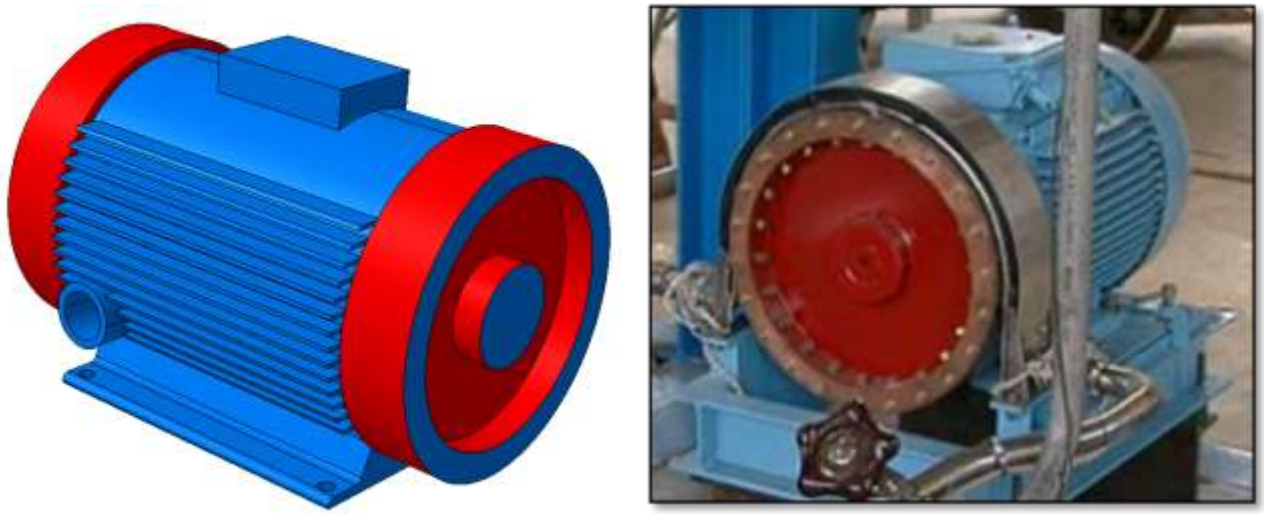

Figure 102: Permanent magnet electromagnetic induction pump

3.3.3 Pneumatic power

The power for actuating the valves should come in part from a pneumatic accumulator with a corresponding power panel and gas compressor. This will provide some redundancy in terms of not relying only on electric power which is susceptible to damage from radiation. To allow easy access, the power panel is positioned below the valve farm and the compressor should be placed in the lower corner as illustrated in the figure below.

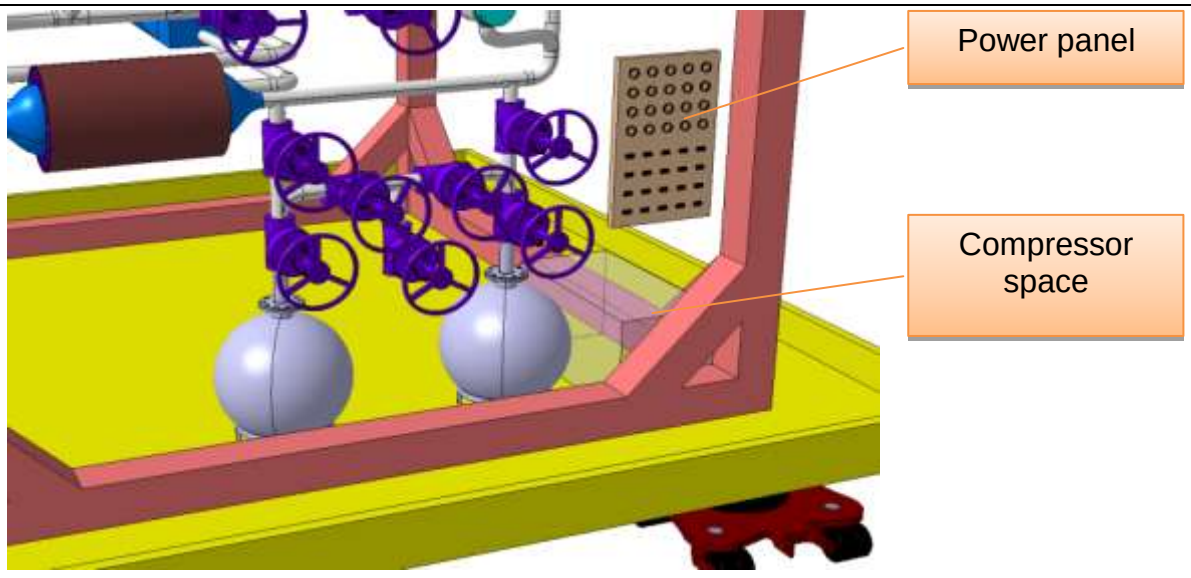

Figure 103: Pneumatic power

3.4 Effect of transients in the facility

The calculation of transients in the heat exchanger could not fit within the scope of the current engineering concept phase. It is therefore discussed qualitatively.

3.4.1 Loss of flow

The immediate effect of the loss of the EMP is a coast down until natural circulation conditions are reached. As in a conventional NPP, the cold source in effect the heat exchanger is situated at the top of the loop. The heat source on the other hand is at almost the lowest position in the loop.

A gravity driven flow may therefore be expected due to the effects of buoyancy. Since every effort has been made to keep the drag penalty in the primary circuit small, the progression from driven flow thru coast-down to gravity-driven flow may be expected to be progressive, giving ample time to switch off the beam before the reduced flow on the window may lead to its failure.

A full study of this effect would include using traditional safety codes such as RELAP/CATHARE/NRC-TRACE and extracting the integrated time-dependent flow rates to apply as boundary conditions to a full CFD couple with a thermal-stress analysis of the beam window area.

3.4.2 Beam transient

Occurrences of the beam switching off and then back on are certain; in which case a “cold slug” followed by a “hot slug” will flow through the primary circuit when the beam switches on again. This can be simulated by starting a calculation in steady state at the low temperature and then increasing suddenly the temperature at the inlet to hot temperature over a period of roughly 1 [ms].

The most sensitive elements in the loop will be the beam window and to a lesser degree the heat exchanger, which will be protected by the inertia of the loop.

The study should also cover thermal stresses. Natural circulation is less severe for stresses and can be neglected. The effects on the gap in the heat exchanger are possible, although stresses are likely to be small due to the compensating effect of the corrugated copper sheet. In any case it is necessary to transfer the temperature maps to a structural model along with the pressure maps and calculate the stresses.

3.5 Instrumentation and control

The issues of instrumentation and control are generic in nature and have been subject to numerous studies in previous programs such as Megapie and Eurisol. They necessitate the development of specific controls and dedicated testing facilities. The following comments give a short outline of the development work foreseen for the next step in the development of a T-MIF facility and are intended to demonstrate that no show-stoppers are to be expected in this area.

3.5.1 Instrumentation

Thermocouples have proven essential under irradiated conditions both in experimental facilities and in conventional nuclear power plants. Today thermocouples are still the instrumentation of choice for monitoring the enthalpy changes in a nuclear reactor, alongside the neutron flux monitors (not covered here as they necessitate detailed neutronics design). Care has to be taken with time lag effect and it is therefore vital to ensure good thermal contact and a low resistive path to the temperature source. An example of implementation is shown in the figure below.

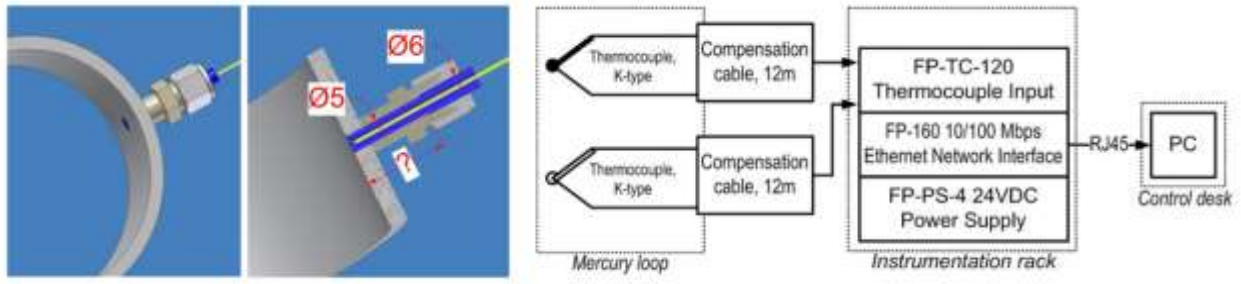

Figure 104: Thermocouples for temperature measurements / R. Milenkovic

Systems-level measurements are necessary to monitor adequately the health of the primary loop. A gradual increase in pressure drop is an indication of corrosion problem leading to the accumulation of oxidation on the walls. A sudden increase could be due to a mechanical rupture inside the loop, on the contrary a sudden increase could signal a LOCA. A simple differential manometer as shown below could be implemented. Here the challenge is the effect of radiation on the piezo-electric components.

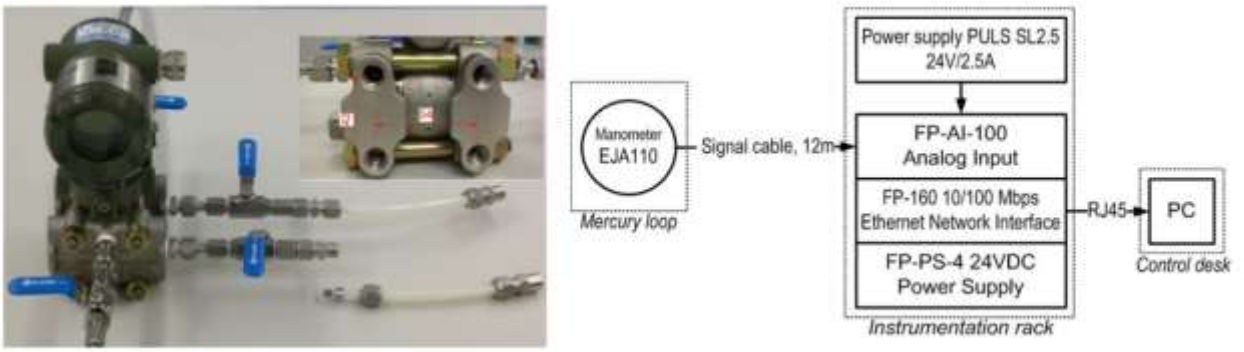

Figure 105: Differential manometer for hydraulic pressure drop measurement R. Milenkovic

A reliable flow-meter is also an important tool in monitoring the conditions in the loop. Ultra-sonic flow meters may well prove more reliable than electromagnetic flow meters which have been plagued by poor performance in the past. However they would require adequate testing under irradiation and the implementation and preparation of back up measure to cover possible failures. Such backups as thermocouple using enthalpy calculations have been proven reliable in the past.

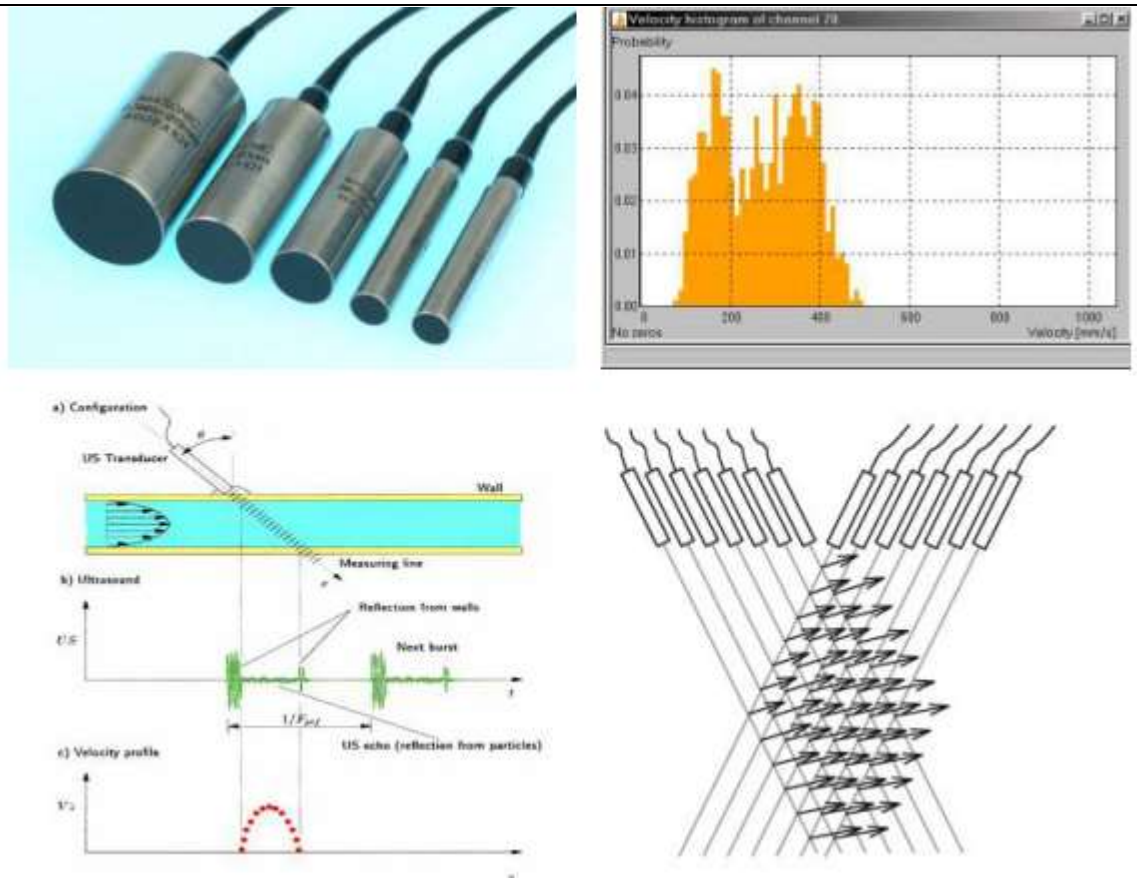

Figure 106: Ultrasonic flow meter acc. METFLOW / Y. Takeda

The issue of vibrations is less of a problem under constant beam conditions than with a pulsed beam. However generally, liquid metal is a good conductor of sound due to its incompressible nature. Cavitation or noise caused by irregularities in the flow would be easily picked up as vibrations in the piping and this form of health monitoring has been proven reliable in the case of the Eurisol test. An example of such implementation is pictured hereafter.

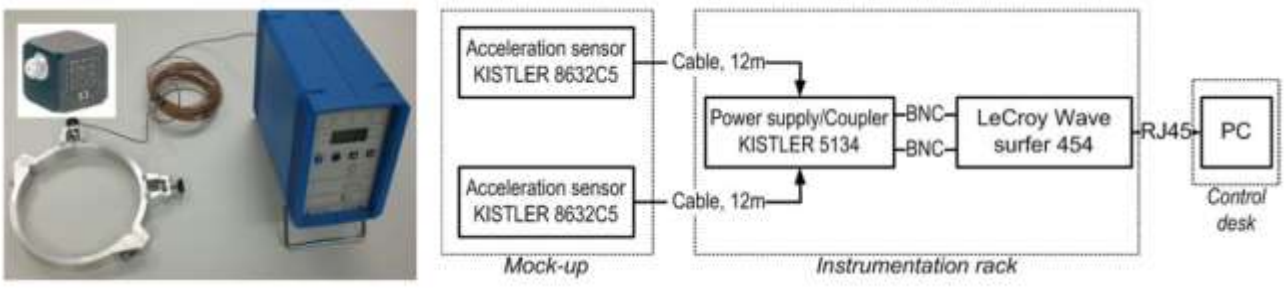

Figure 107: Acceleration sensor for vibration measurements R. Milenkovic

Finally, any possible leak must be monitored. Many strategies are possible such as monitoring the pressure in an interstitial gap between two vessels, a proposal mentioned here-above for the heat exchanger.

Another possibility is the use of resistive sensors which show a change in electric capacity in the presence of a fluid. This was show to be quite effective in Megapie and an example is shown below.

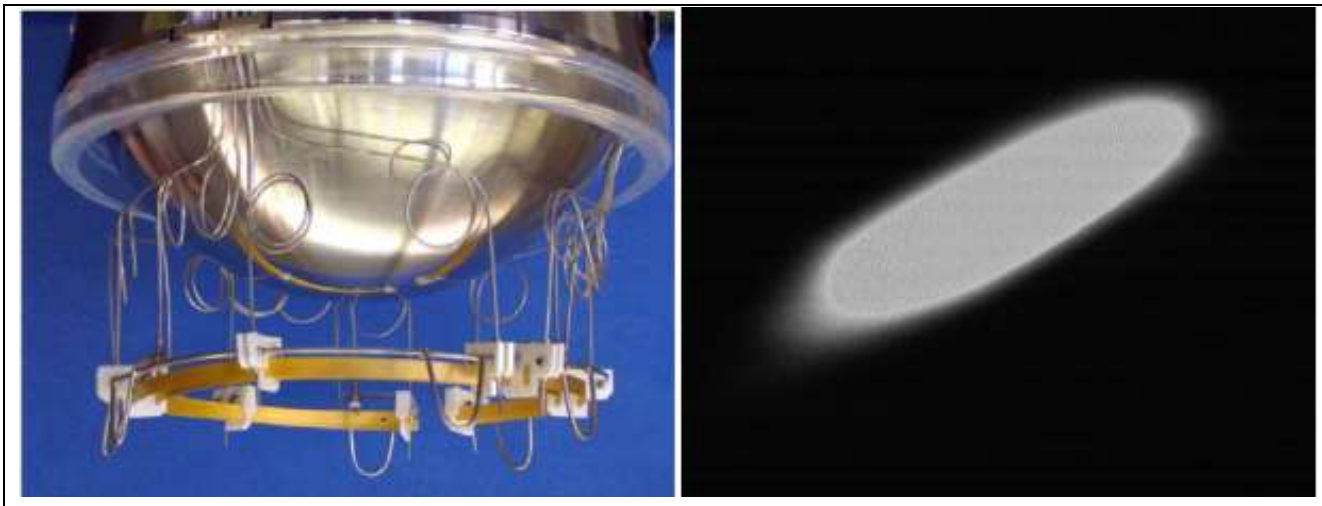

Figure 108: MEGAPIE Beam diagnostic devices (l.) and beam spot VIMOS camera (r.) [K.Thomsen

3.5.2 Flow control

Past experience has shown that the major issue with controlling the flow rate does not rest with the pump but with the measurement of the flow rate. This is complicated by virtue of the fact that such instrumentation must survive in a highly radioactive environment. The best strategy is to ensure redundancy of both the instrumentation and also diversification of the type of instrumentation. In this sense, thermo-couples are an indirect method of measuring the flow since the heat source is well known, measured by the current in the accelerator. If the difference between inlet and outlet temperature are known with sufficient accuracy, usually less than 1°C, a simple enthalpy calculation will result in a fairly accurate measurement of the flow rate.

3.5.3 Temperature control

Detailed CFD studies in section 4.3.2 demonstrate the possibility of ramping up the flow from 4 kg/s to 38 kg/s with no observable large-scale disturbance in the flow on the window or inside the incomer sections. These studies did not all include the samples since the numerics become unstable and require far longer convergence times, however a detailed model with the samples in section 4.3.1 showed that the flow between samples is essentially unhindered. Therefore it is possible to change the overall temperature in the samples simply by adapting the flow rate as shown in section 4.3. A higher flow rate of 38 kg/s means the sample will be exposed to a temperature around 400°C whereas at the other end of the scale, a slower flow rate of 4.1 kg/s will imply temperatures in the sample of some 550°C

The effect on the overall thermal-hydraulics of the system has been studied in terms of the performance of the heat exchanger as detailed in section 3.2.6, which shows the design is capable

of evacuating 100 kW with the lowest flow rate which is the most challenging for the design of the heat exchanger. At higher flow rates the heat exchanger becomes more efficient, therefore in order not to cool the liquid lead too much, the bypass valve will be used to divert some of the liquid metal away from the heat exchanger and directly back into the loop. This purposeful degradation of the performance of the heat exchanger will allow the temperature to remain controlled above freezing point in spite of the better heat transfer which will ensue from the higher flow rate.

The bypass valve which is shown in Figure 75 is an efficient means of controlling the temperature in the loop independently of the flow rate. In this manner the temperature inside the sample can be simply adjusted by adjusting the flow rate in the pump and the degree of flow bypass around the heat exchanger. The interplay between these two parameters would be the subject of further study using thermal-hydraulic codes such as Relap-5 or Trace and validated by testing on a thermal-hydraulic loop.

3.6 Concluding remarks on the proposed system

A design for the irradiation facility has been proposed and laid out in sufficient detail to demonstrate the feasibility from a technical standpoint. The level of detail is sufficient for a rough cost estimate of the facility to be made at project level, as per section 0. The design reflects the latest progress made in the neutronics which were documented in chapter 2 and in the hydraulic design of the target as per chapter 4.

The design features some innovative solutions such as the dismountable heat exchanger in which the secondary and primary loop are physically separate with no common wall. The secondary loop is easily removable from the facility, easing maintenance and the management of possible leaks. Another innovation lies in the target itself which can absorb a specially tailored elliptical profile beam, thus exposing the samples to a high DPA. This is made possible by the design of a window with an elliptical base which is optimised in terms of stress and cooling. The loading mechanism for the samples is also new. It can load samples cyclically using mechanisms which are easily dismountable from the target, thus enhancing its capability to accommodate many experiments.

4 Detail analysis of the neutron source

Source: The current chapter is reproduced from reference document 4.

4.1 Design of the T-MIF neutron source

The preliminary design report (Ref. 2) laid out in principle the design of the T-MIF neutron source inspired by prior experience in the EURISOL program. The possibility of irradiating samples under combined proton and neutron irradiation was investigated in the specification report (ref.2), which suggested using an elliptical beam impacting the sample side-on. In so doing, it was hoped a fairly homogeneous DPA distribution would be reached in the sample, a fact borne out by the neutronics analysis in chapter 2

The sample disposition and the necessity to house the loading mechanism meant the target had to be widened in the plane of the sample. Thus the elliptical section of the beam entailed that the original circular symmetry of the EURISOL target was deemed to be not optimal for minimising thermal stresses. Hence the EURISOL target beam window was changed from a circular symmetry to an elliptical cross-section in a plane at right angle to the beam. Along the beam direction however, the beam window section was kept the same as in the original neutron source.

These changes in the beam window, entail the local speed distribution along its wetted surface may be altered, thereby modifying the cooling characteristics and *in fine* the beam window temperature.

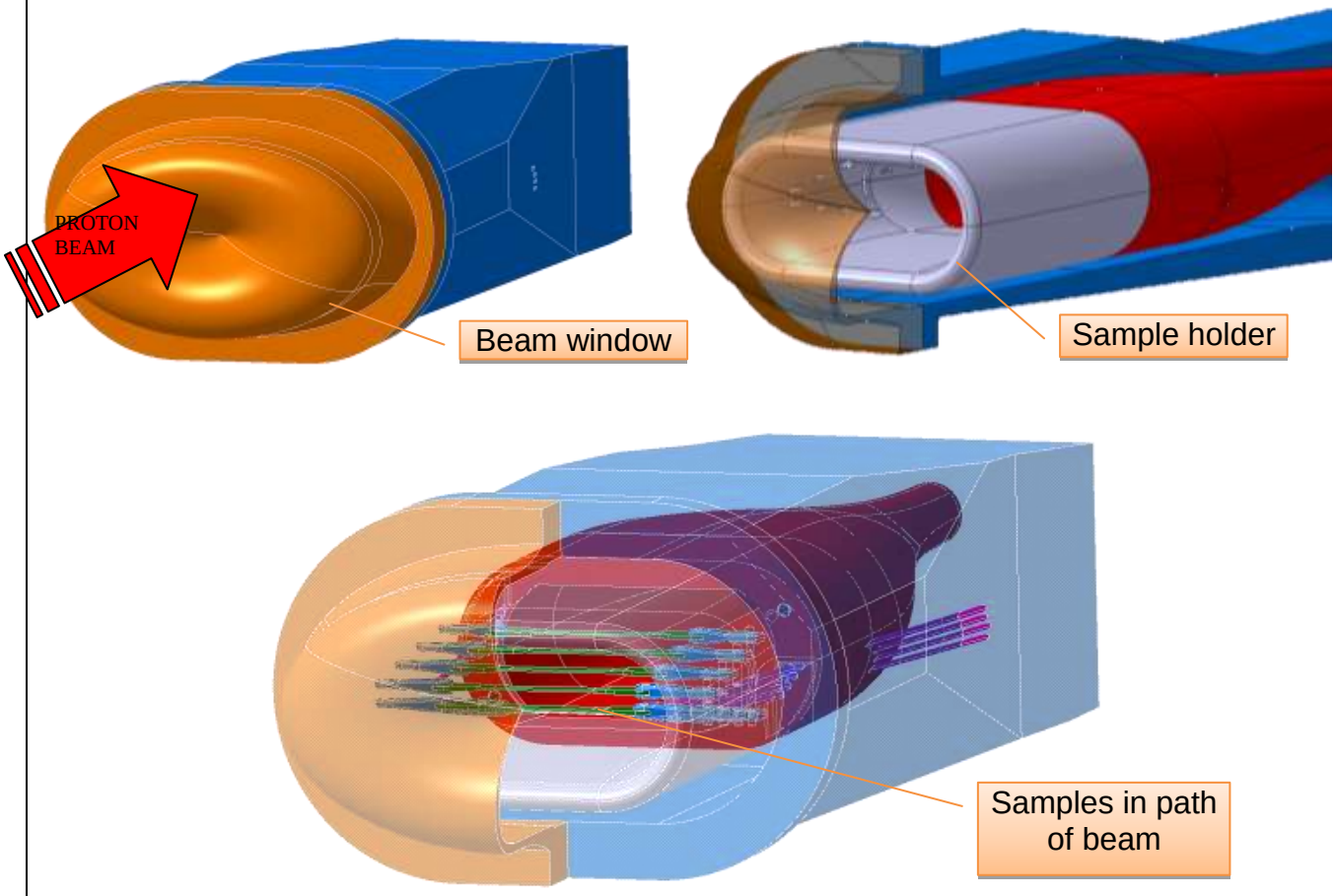

Figure 109: Target and sample locations (detail in section 3.2.1)

4.2 CFD analysis of the neutron source flow

4.2.1 Assumptions and Boundary conditions

The initial simulation focuses only on the hydraulics, i.e. ensuring stable flow exists over the window. For this purpose, it is not necessary to include the effect of the beam as the temperature increase in the liquid metal will be low enough to ensure that buoyancy effects are modest in relation to the overall speed of the liquid metal. Hence wherever the purpose of the analysis is to optimise the flow, heat deposition is not considered, as the additional equations which need to be computed, slow down numerical convergence

Heat deposition is considered when the temperatures in the window, sample and fluid are needed. Therefore, in order to further simplify the calculation, in some calculations where the heat deposition is not considered, the entire sample loading mechanism is removed from the CFD model as is the structure itself. The model then only contains the fluid domain bounded by what are essentially adiabatic walls. This is an appropriate simplification since the main objective of such optimisations is to verify the flow on the beam window and the mechanism is located downstream of the window.

Based upon the heat exchanger calculations documented in section 3.2.6, the following boundary conditions are applied in the CFD simulations hereafter:

Inlet mass flow rate is set at 4.1 kg/s to 38 kg/s

Inlet temperature is 380 °C.

Outlet: the static pressure is 0 bar

The nominal pressure of the fluid is 1 bar.

The turbulence model used is the SST

4.2.2 Design iterations to optimise the flow in the target

The design must be able to function over a wide range of speeds so as to allow the temperature in the sample to be varied. The source of heat, the beam, is constant as is the deposition in the sample. The simplest method of controlling the sample temperature is therefore to change the flow rate, another method would be to apply electric heating to the sample but this could be a challenge in an electrically conductive medium.

At first the design proposed in ref.2 is examined at a very high speed, sufficient to keep the samples at temperatures close to the DBTT of austenitic stainless steel under high irradiation dose. This will raise pressure losses in all components, most notably the target which is therefore the main focus of the CFD analysis. The heat exchanger can be expected to perform better at the higher flow rate and is therefore not examined in the current context.

4.2.2.1 Iteration 0

The analysis for this initial examination was conducted at maximum speed on the original design shown in Ref.2. The maximum speed corresponds to a flow rate of 38 kg/s. In doing so, the temperature in the sample can be lowered to 400°C (refer to chapter 3). The rationale for varying the speed is to vary the temperature in the sample and since the highest speed presents the greatest challenge in terms of stability, the initial iteration focused on this domain. Furthermore, the heat

exchanger can be expected to function far better at higher speeds and it is therefore only necessary to focus on the target, not on the rest of the system.

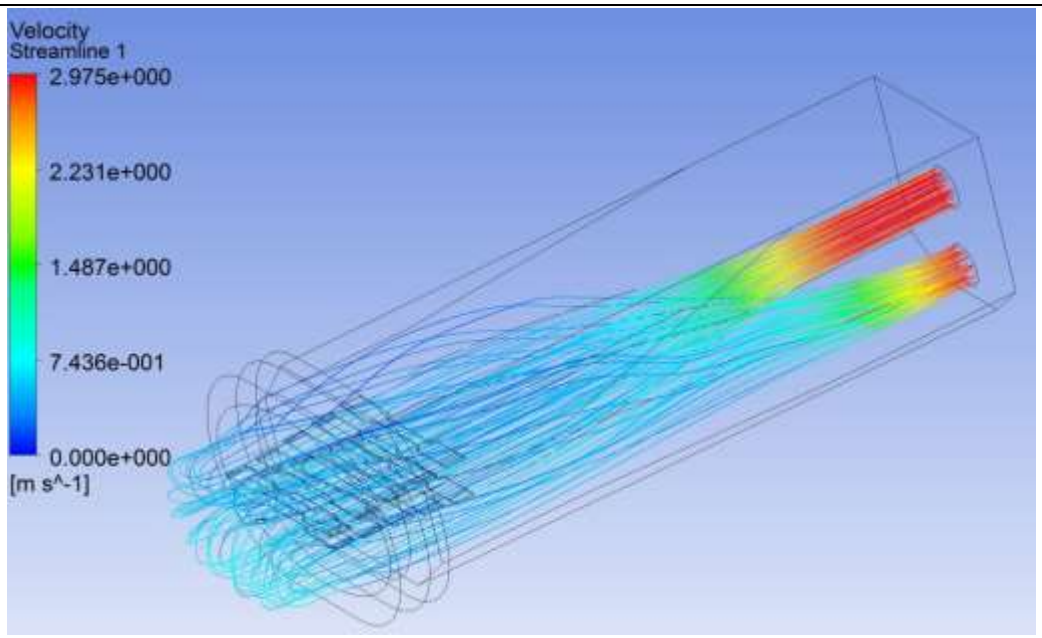

Figure 110: Velocity streamlines in the fluid

The initial calculation shows some interesting features in the flow pattern. Although this may not immediately visible in the figure above, closer examination of the flow field in the annular section just upstream of the window shows there is an imbalance between the lower an upper section. More fluid is conducted through the lower portion of the annulus which could result in an unsteady flow further downstream. Hence in order to ascertain the level of imbalance measurements thereof are taken along the beam axis in the model using sections perpendicular to the beam axis, shown in red in the figure below.

An attempt was made to find how to equalize this flow and it was suggested that lengthening the target would give the incoming flow in the annulus the space needed to equalize between the top and bottom of the channel. In order to quantify this proposition, the flow at different sections was examined as shown in the figure below,

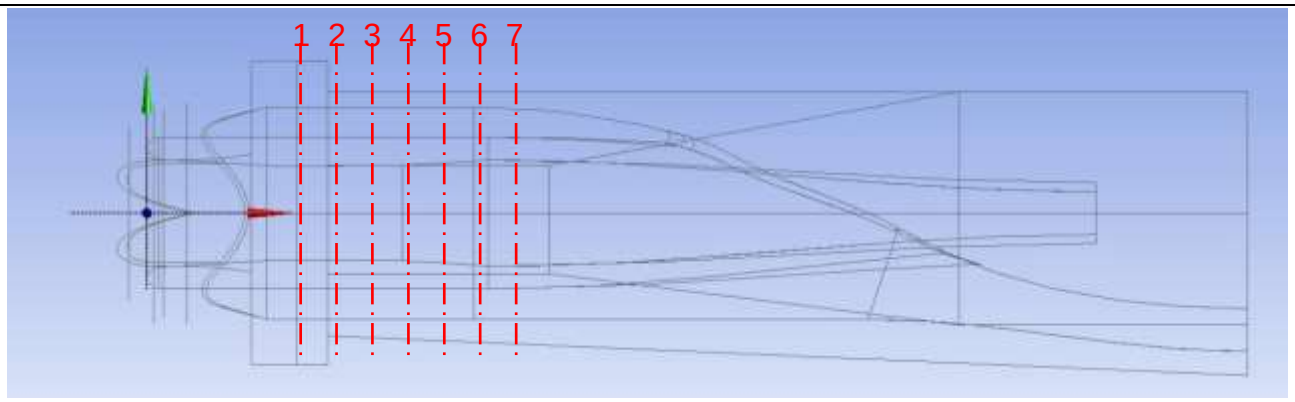

Figure 111: Side view showing section planes for calculating the flow imbalance

The velocity contours in the sections planes are shown in the next following figure, illustrating how the imbalance becomes progressively weaker along the incomer annulus, just before reaching the window. However the imbalance does not completely disappear, and is the focus of a detailed calculation.

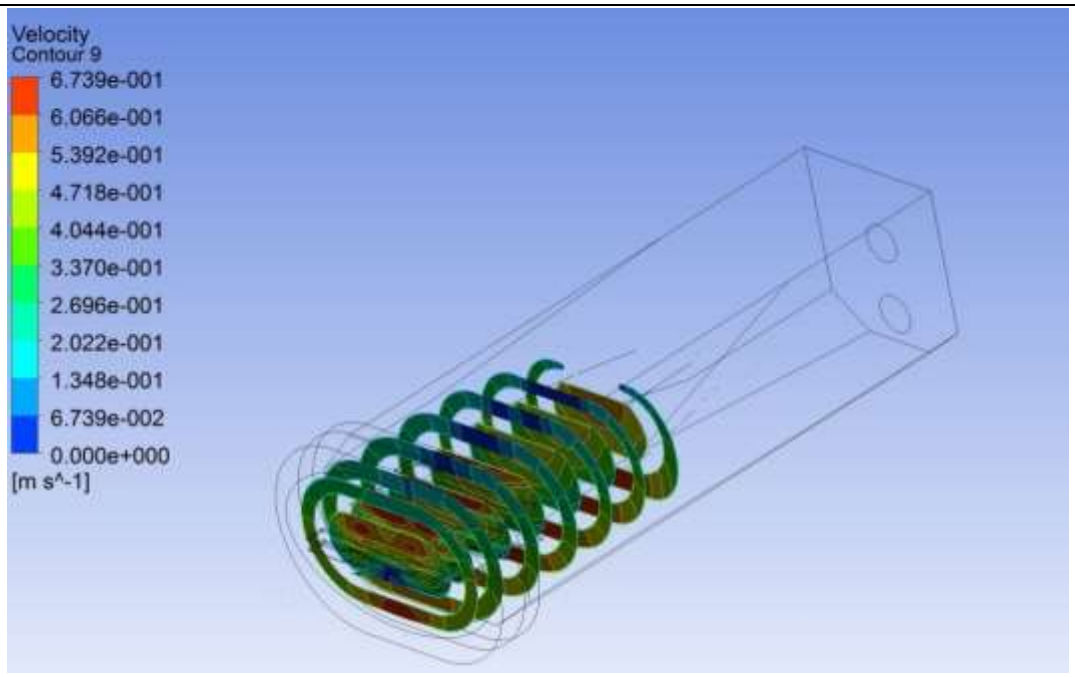

Figure 112: Velocity contour in the annulus and guide tube

In order to find the imbalance between the integrated flow in upper and lower regions of the incomer annulus, the average velocity is computed in each section plane, for the top and bottom as given in Table 1. Note that after plane 4, the ratio does not change.

To find the required additional length of the target, the “x” corresponding to an imbalance equal to 1 must be found, as this corresponds to a flow in the incomer annulus where there is no difference between the upper and lower flow. There are two possibilities top interpolate the results; an exponential or a linear interpolation. According to an exponential interpolation, the imbalance=1 is reached at coordinate 3.5cm. Based on a linear interpolation, imbalance is resolved at 4.5[cm]. This corresponds to a needed increase in length of 6[cm]. Conservatively, the target is lengthened by 10[cm].

	Y(cm)	Imbalance
Plane 1	7	2.19
Plane 2	10	2.83
Plane 3	15	5.50
Plane 4	20	19.0
Plane 5	25	18.8
Plane 6	30	19.0
Plane 7	35	19.0

Table 23: Flow Imbalance in each plane

The target is thus to be lengthened by an additional 10 cm to allow the flow more running length for equalising its distribution over the entire section of the annulus before the beam window. This should be sufficient to guarantee stable conditions on the window. Furthermore, on the whole, there seems

to be adequate cooling of all the structural parts particularly the samples which are at fairly constant temperature. Therefore subsequent iterations will focus on enhancing the stability of the flow on the window with the target increased by the required 10cm. A flow rate of 4.1 kg/s will be sued as this presents a challenge in terms of equalizing the flows.

4.2.2.2 Iteration 1

In this design configuration the fluid is entering into the target station from the side in order to allow greater depth for the shielding. Indeed, a greater thickness of polyethylene has to be added behind the target as compared to the sides of the target because the more energetic particles escape from the target rear section (see ref.3). Hence having straight pipes at the back would act as an escape route for gammas and neutrons leaking from the target.

Since the overall dimensions of the T-MIF facility are to be reduced as much as possible, bending the pipe just after the active section of the target may be thought to bring some advantage.

However the flow in the CFD simulation appear to show that this configuration makes the fluid turn on itself precisely in the regions where the samples are to be located and in addition creates a vortex in the window. Although the second aspect could in theory bring about a higher velocity on the window and thus better cooling it is also much more unstable. The vortex around the samples is far more problematic, it could lead to a high amount of turbulent detached flow on the samples which would then no longer be kept at constant temperature, a mandatory requirement for providing adequate data for material research purposes.

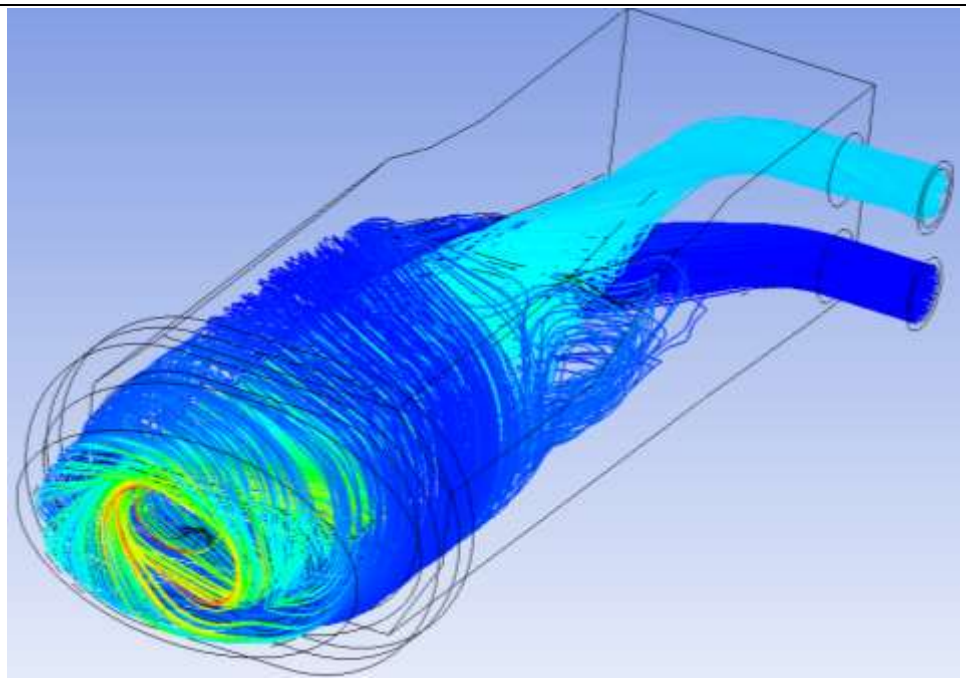

Figure 113: Velocity streamline with an interface facing sideways with flow rate at 4.1 kg/s

The conclusion from the previous calculation is that in- and outlet pipes have to be straight behind the target station to avoid this phenomenon. Furthermore, new results of the neutronics calculation show that a lead shielding would be more efficient than polyethylene behind the target as the liquid lead in the target itself would also be of benefit as a shielding against gammas, post shutdown.

4.2.2.3 Iteration 2

In the current iteration, the interface has been moved back to the rear of the target. A totally new flow field appears which although more steady is still highly complex.

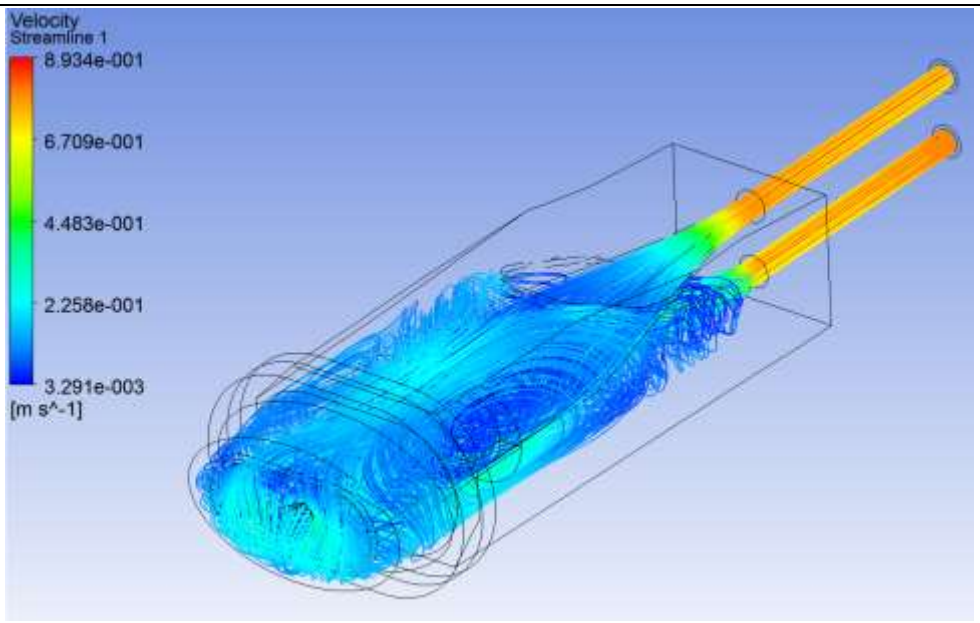

Figure 114: Velocity streamline with rear interface

Flow problems in the fluid point to additional areas needing improvement. First the inlet is too wide and forces the fluid to recirculate inside the incomer annulus tube instead of flowing steadily towards the window. The space between the exit collector and the chassis is too great compared to the incomer annulus such that the fluid cannot fill this space entirely and stays in the lower portion of the chassis instead of flowing back out the exit collector. Finally, the space between the window and the front of the sample holder is also too wide, so that the fluid flows over the sample holder but loops back towards the window instead of being guided into the sample holder. All these matters have to be resolved and the design needs to be improved in order to guide the fluid flow better.

4.2.2.4 Iteration 3

In this iteration, the annulus section is slightly raised and its axis follows an arching curve at the entrance to attempt to force the fluid to move upwards, around the exit collector and the sample holder. The illustration below shows that the fluid is accelerated along the lower section and most of the problems described above remain.

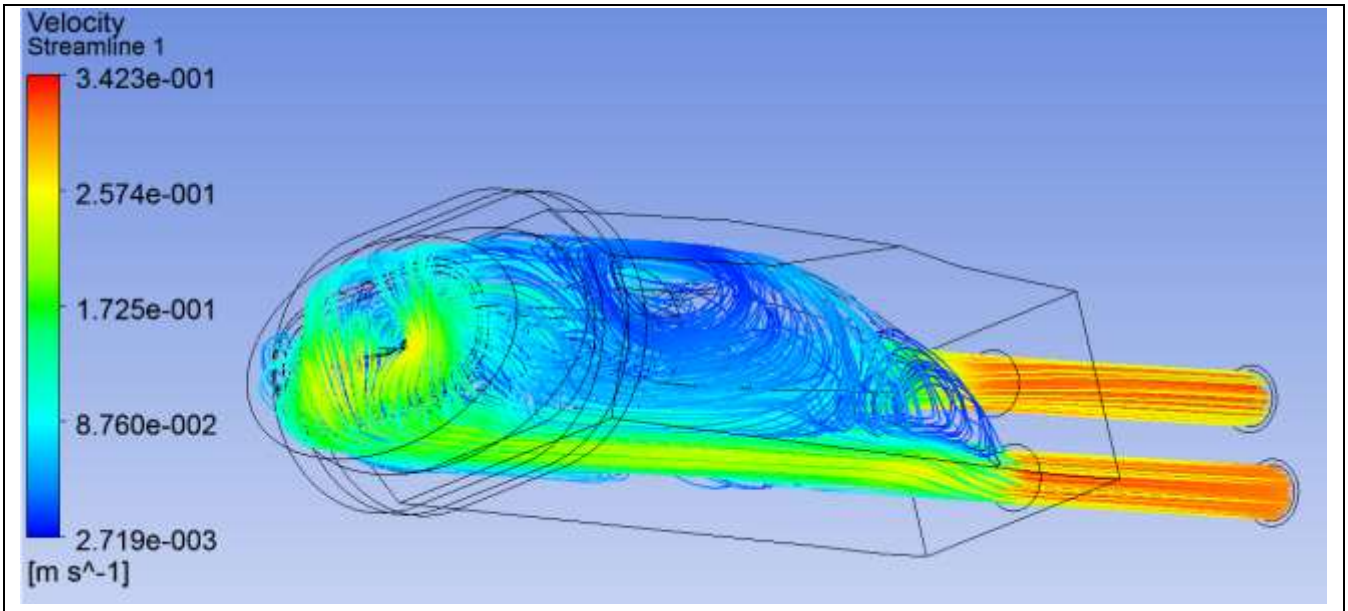

Figure 115: Incomer annulus shifted vertically upwards

4.2.2.5 Iteration 4

After a number of intermediate iterations which are not documented here, the incomer annulus is shifted to a position in vertical direction which seems to result in acceptable flow pattern. There is no direct recirculation and the fluid is directly fed more equally into the target. But the space after the window is still not filled entirely and the flow back from the window does not guide enough liquid equally all through the sample holder.

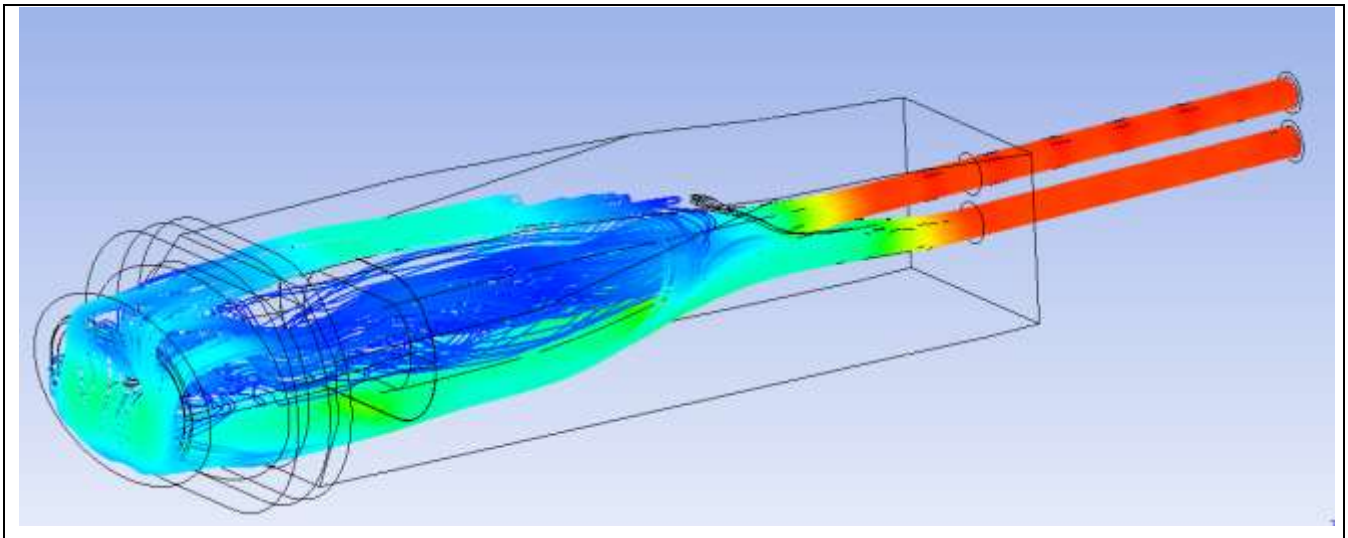

Figure 116: Optimised incomer annulus position

4.2.2.6 Iteration 5

Further modifications are implemented in the incomer annulus section, which is significantly reduced. Also the overall shape of the leading edge of the sample holder is modified to conform better to the elliptical section of the window. The fluid fills the whole volume of this modified incoming annulus and conforms to the window cusp as required in order to enter the sample holder smoothly.

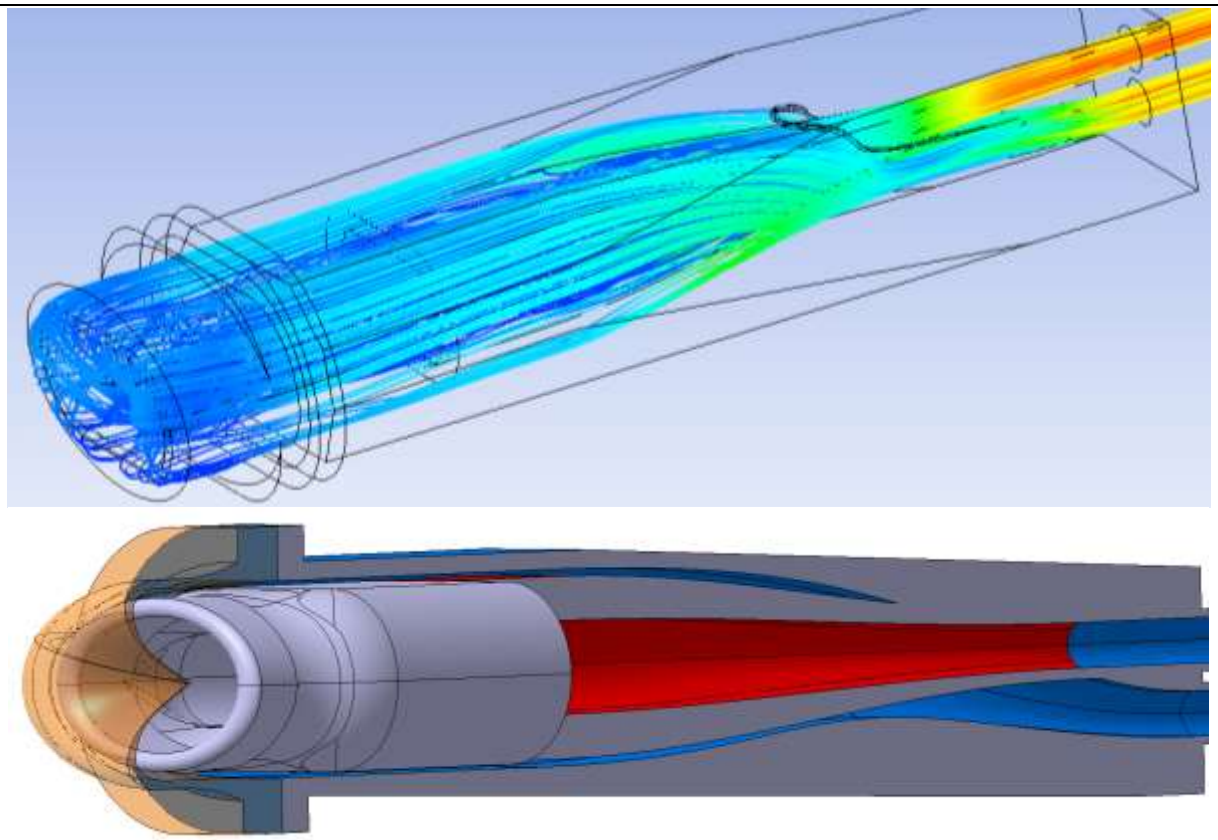

Figure 117: Optimised incomer annulus thickness (top) and redesigned section (bottom)

Having completed an optimisation on the inflow in the incomer annulus, some work is still needed on the outflow, beginning in the sample holder just after the window. Indeed, the following image shows a recirculation at the entrance of the sample holder, where the heat deposition is the highest.

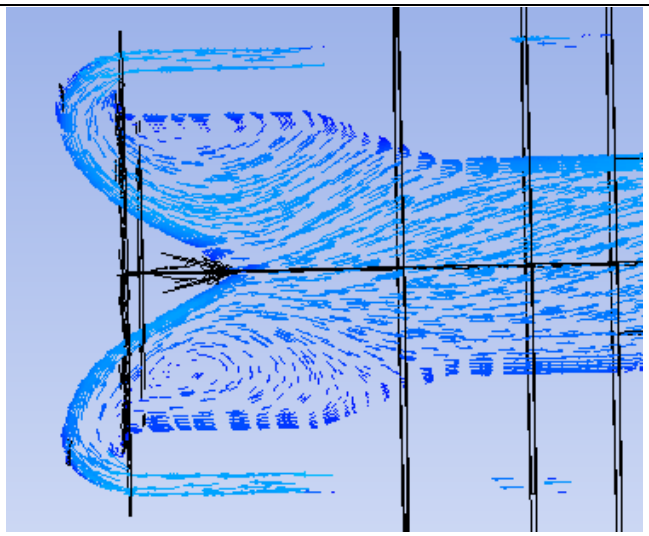

Figure 118: Recirculation in the sample holder

4.2.2.7 Iteration 6

The entrance surface of the sample holder is modified to avoid recirculation in the sample holder as shown above in the previous iteration. The new shape allows the flow to be guided back towards the exit more smoothly.

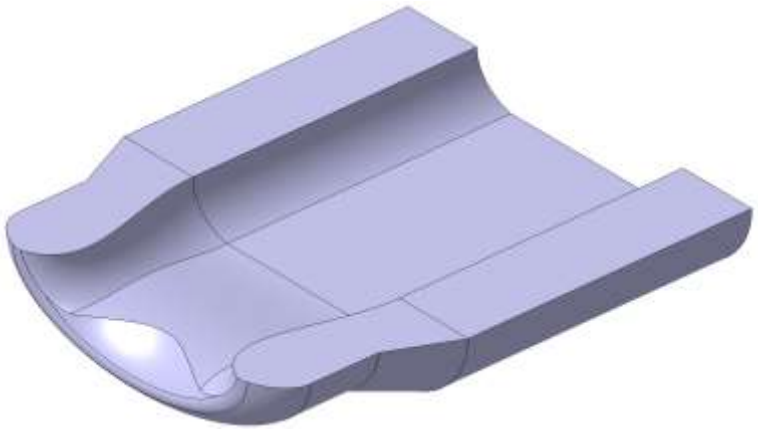

Figure 119: Redesign of the sample holder

This modification has a clear benefit in the vertical section but a significant recirculation is still observable in the horizontal section. As it occurs precisely in the region of the beam deposition, it would accumulate significant heat in the structure of the guide tube. Note however that in the absence of the samples, the recirculation is unhindered. This is a conservative model as the samples would effectively at the very least inhibit or perhaps even prevent such a recirculation from occurring.

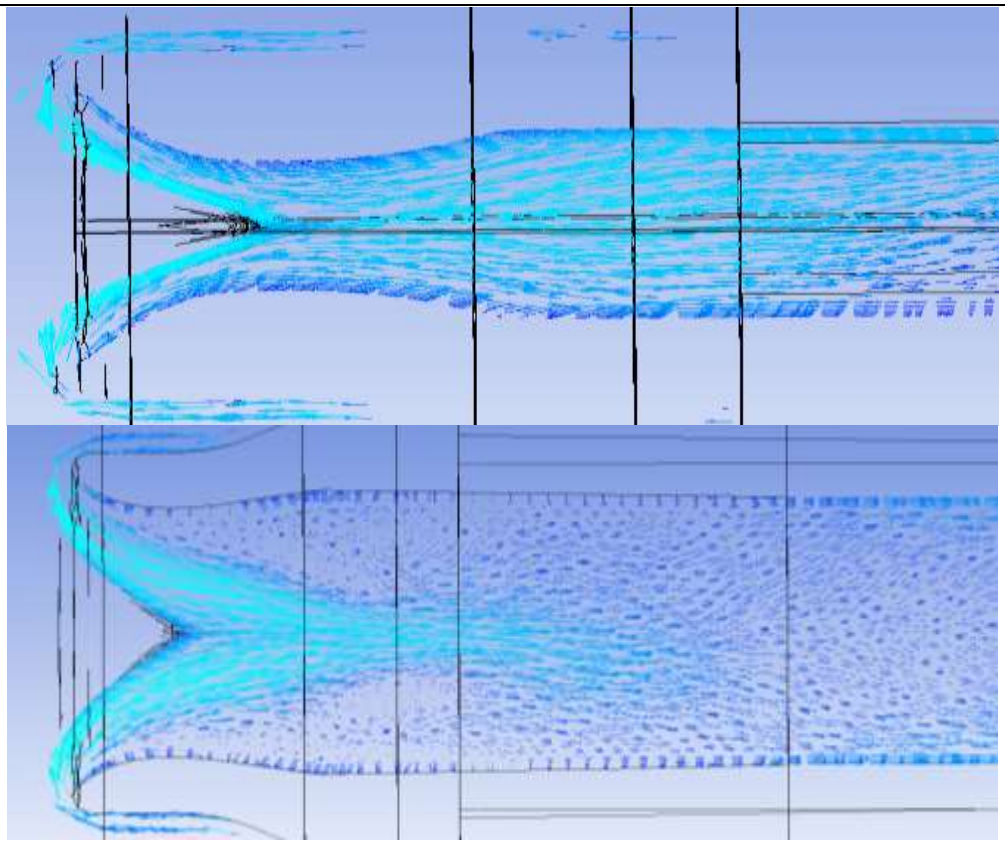

Figure 120: Flow in the optimised sample holder vertical (top) and horizontal (bottom) Plane

4.2.2.8 Iteration 7

In the next iteration, guide vanes are included to interfere with the recirculation pattern shown in the previous iteration. They succeed in isolating the high deposition region from the recirculation pattern, which thereby shifts towards the wall of the guide tube. Although this is not yet totally satisfactory, it yields a significant improvement. In the first example (left bottom in Figure 121), the position of the blade is not an optimum and does not maximise its impact on the flow distribution. New iterations are then undertaken (right bottom in Figure 121), to find the blade position which can generate a more stable flow.

From a structural point of view, these guide vanes are solidly anchored to the guide tube (see lower portion of figure below). They are an integral machined feature of the guide tube. It is therefore unlikely that they would rupture due to fatigue.

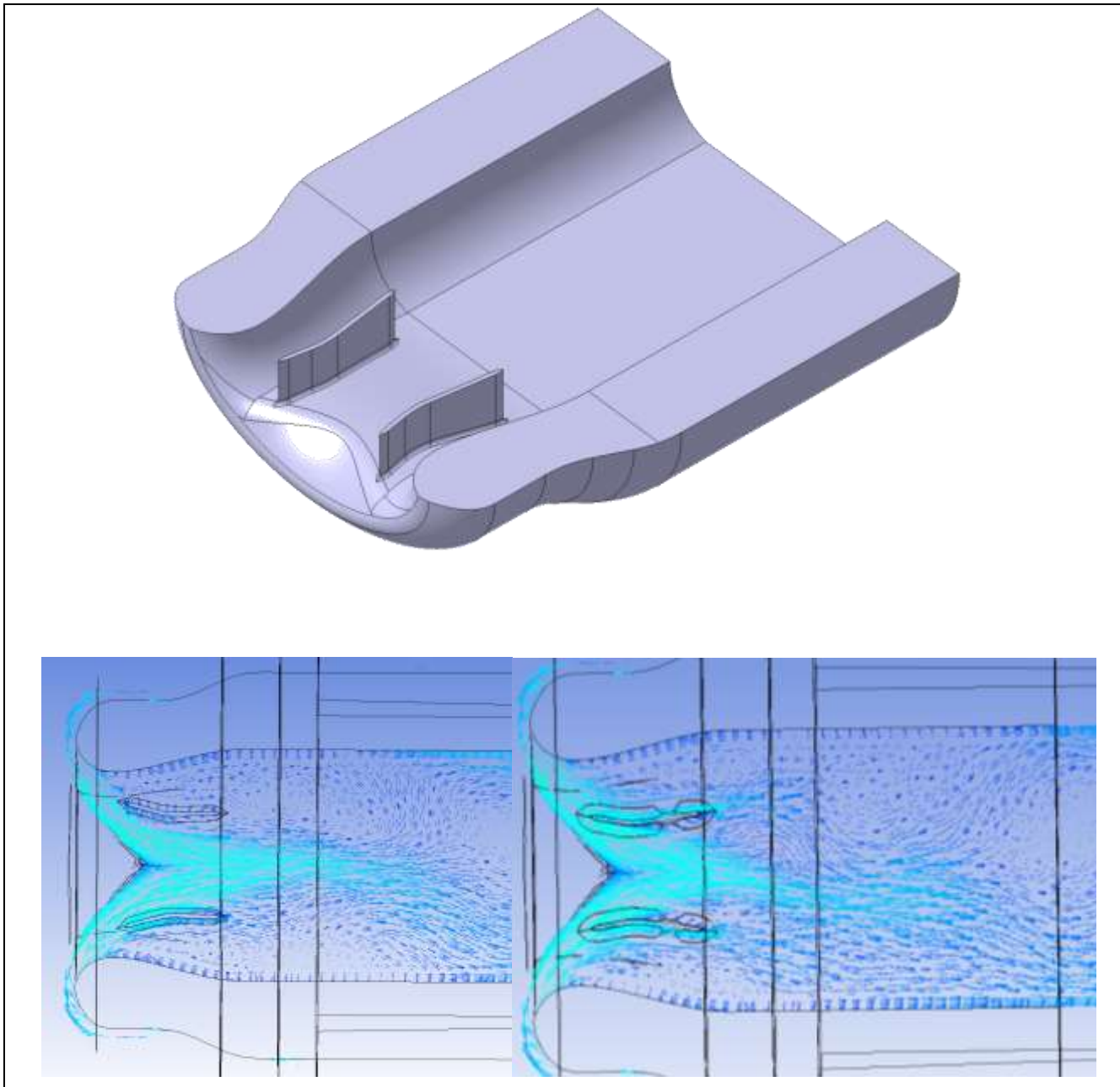

Figure 121: Flow with guide vanes (top) in the sample holder horizontal plane (bottom).

4.2.2.9 Iteration 8

Building on the previous attempt the guide vanes are doubled, which seems to have a favourable effect on the flow. Indeed the flow in the centre of the exit channel in the sample holder is now widened.

Again, a few iterations were necessary to derive the most efficient position as may be seen in the next following figure.

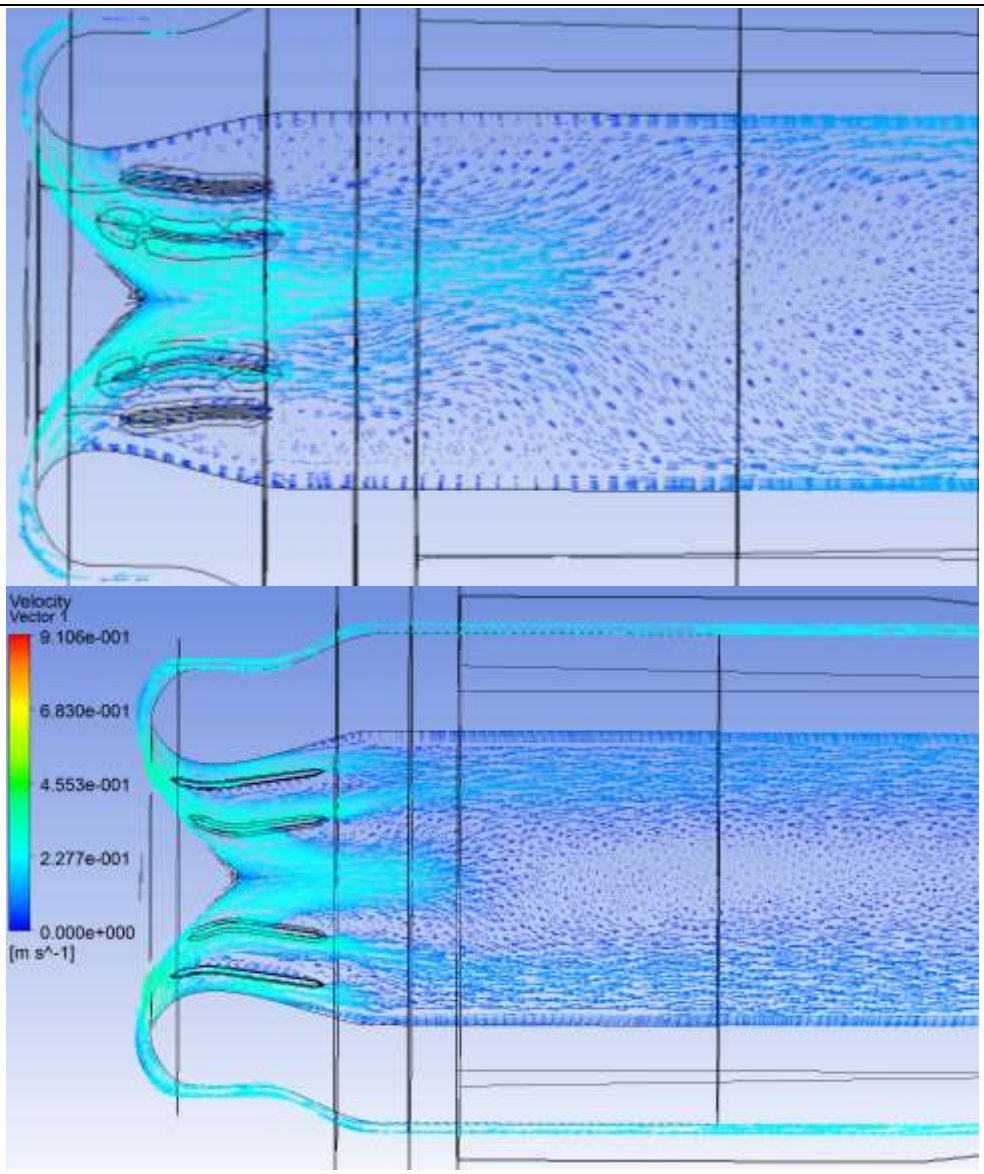

Figure 122: Flow in the sample holder horizontal plane with two guide vanes at different positions

It is now possible with the last iteration to suppress recirculation in the sample holder to avoid any overheating of the guide tube.

The resulting design is shown in the figure hereafter.

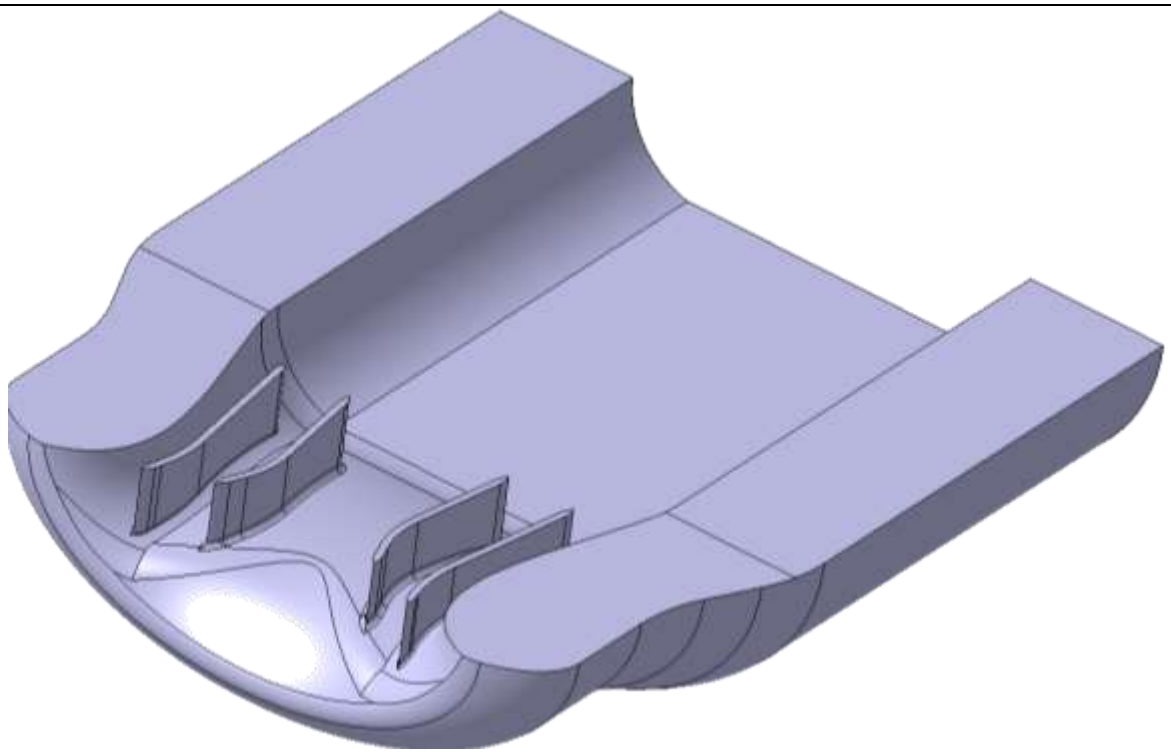

Figure 123: Sample holder design with two guide vanes

In light of the differences in hydraulic section between the window and the sample holder, the velocity decreases down to 0,1 m/s in the sample holder whereas it reaches 0.5 m/s at the inlet. The pressure into the fluid increases slightly during its passage in the target where it is fairly constant. Because of the low velocity the pressure drop is not significant although this may be an underestimation due the absence of the samples.

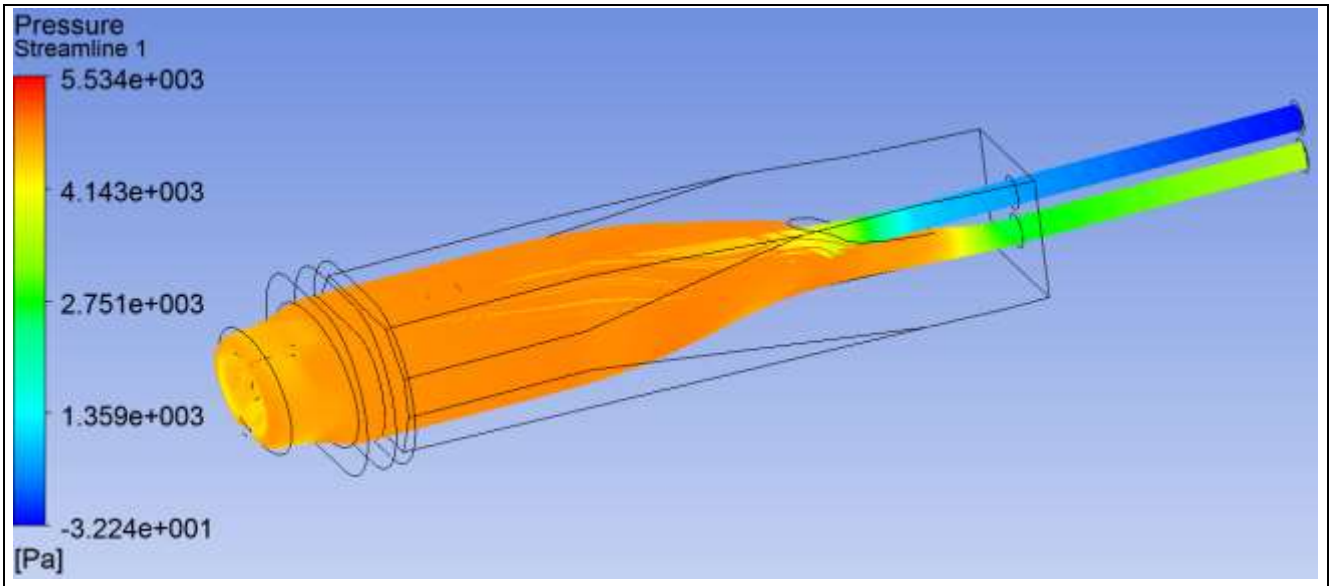

Figure 124: Pressure drop along streamlines in final configuration

Thus the final design of the target is derived, for which the sample mechanism will have to be slightly adapted. This could not be integrated in the systems study in section 3.2.1 but is not anticipated to present any significant difficulty.

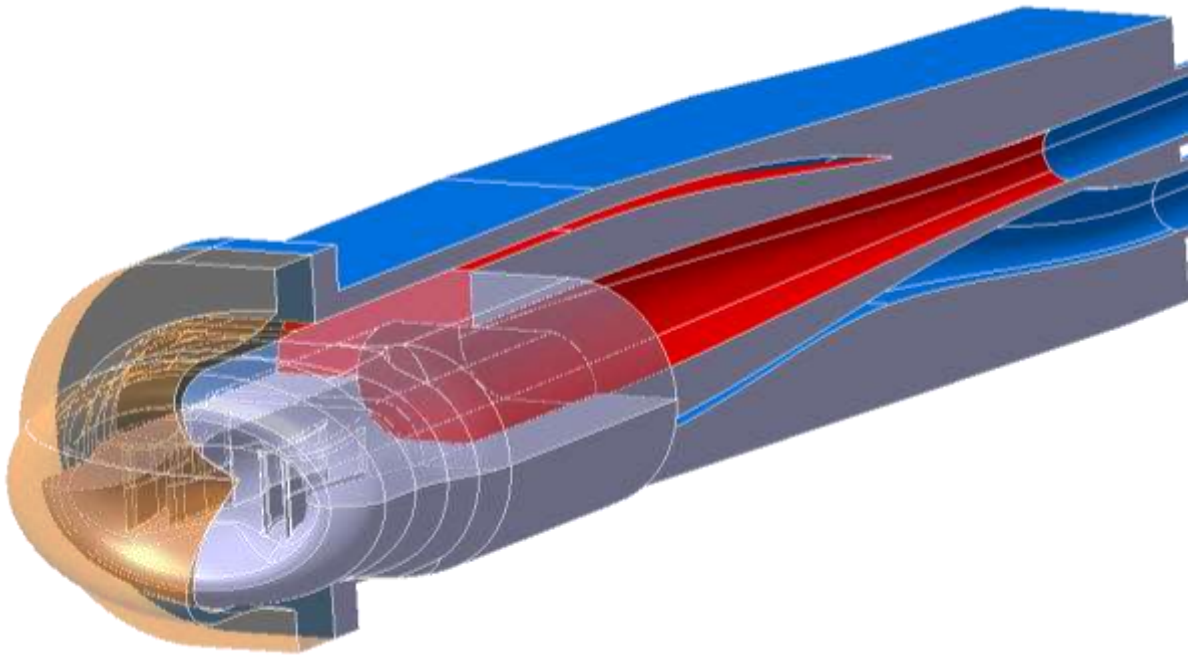

Figure 125: Final optimised target configuration

4.3 Thermal assessment of the design

4.3.1 Analysis of the initial design

The design proposed in ref. 2 is analysed in the current section. The purpose of this first calculation is to test the thermal-hydraulic performance at maximum speed. Results for lower speeds are then expanded so as to cover the full scope of the operational regimes. Indeed the speed of the flow is used to control the temperature of the sample.

The current analysis is therefore conducted using boundary conditions, which were modified compared to those of the iterations outlined in the previous chapter. In this section the flow rate is varied from 4.1 kg/s to 38 kg/s.

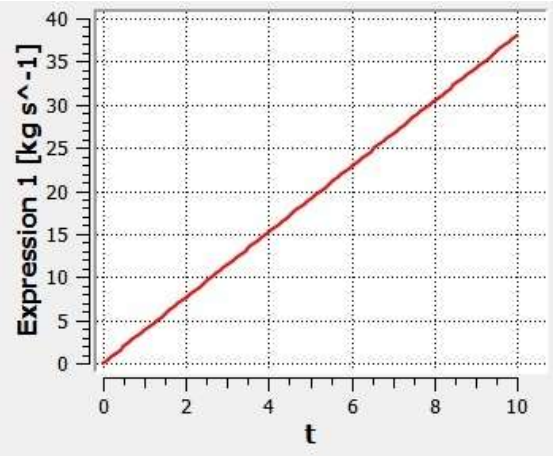

Figure 126: Time dependent mass flow rate for inlet in fluid domain

Transient analysis is used in order to help in the convergence as the flow with the heat deposition from the beam is quite complex, hence the fluid flow is analysed over a total time of 10 seconds with 0.005 time increments, ramping up the applied boundary conditions linearly as illustrated in the figure above. As the heat of the beam deposition is considered, the thermal energy model is applied for heat transfer analysis in the fluid domain.

In this analysis the energy deposition is a parameter which must be considered. There are three main regions in which heat is deposited, the window, the samples and the fluid. Two expressions have been defined in CFX setup corresponding to a:

- 100 kW , 600 MeV and 166 μA

The beam is a Gaussian profile with an elliptical cross-section, using a

- short axis of 1 cm

- long axis of 6 cm

As mentioned in section 2.10, many different options were examined from the point of view of increasing the DPA by varying the beam characteristics. Which set of parameters has the most advantages for the experimenter cannot be determined at the present stage. The scope of the current design study did not allow all configurations to be studied. Indeed apart from a variation of the beam also the flow rate may be changed. In the event of the design study leading to a full-scale development beam characteristics would be chosen and the flow rate would be adapted to suit this beam and allow the safe evacuation of heat and control of temperature. In the current section the beam characteristics listed here-above form the basis of the thermal hydraulic analysis and the flow rate is varied to demonstrate the effect on flow stability and temperatures.

Energy Deposition in the samples

Conservatively, the same deposition is used in the samples as in the fluid. In reality due to the lower density of most samples as compared to the fluid (Lead), the samples should be subjected to a lower heat deposition from the beam.

In the model, a patch-conforming method of meshing has been used in both solid and fluid parts; an inflation method is applied in the fluid region near the wall to capture the boundary layer.

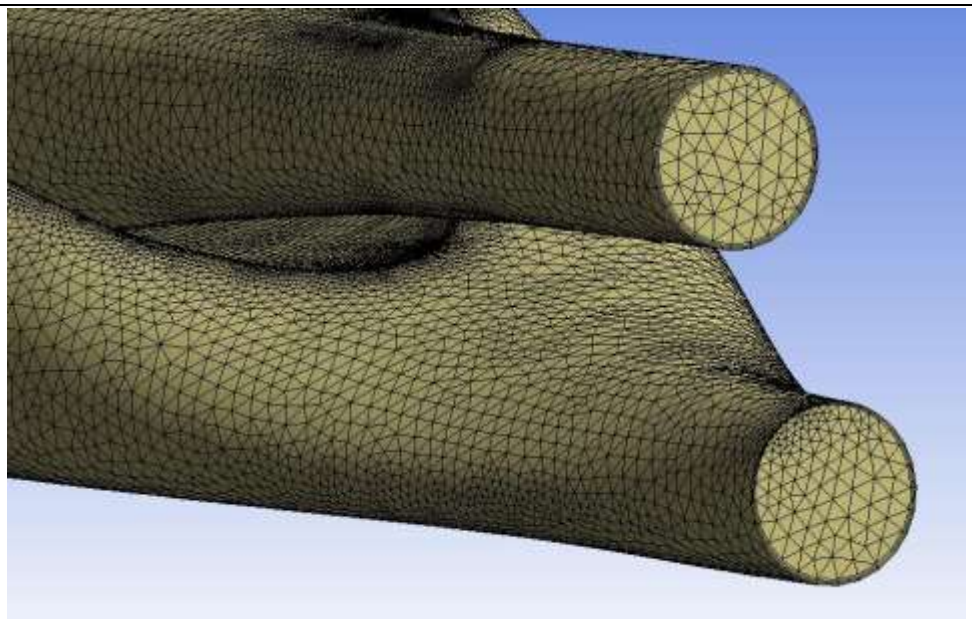

Figure 127: Mesh in the fluid domain

In a first calculation using the initial design, all assumptions here above including the heat deposition, are considered so as to verify whether the temperature lie in the desired envelope and whether system level parameters such as the pressure loss is acceptable. The results of this first calculation on the initial design re shown in the next following figures.

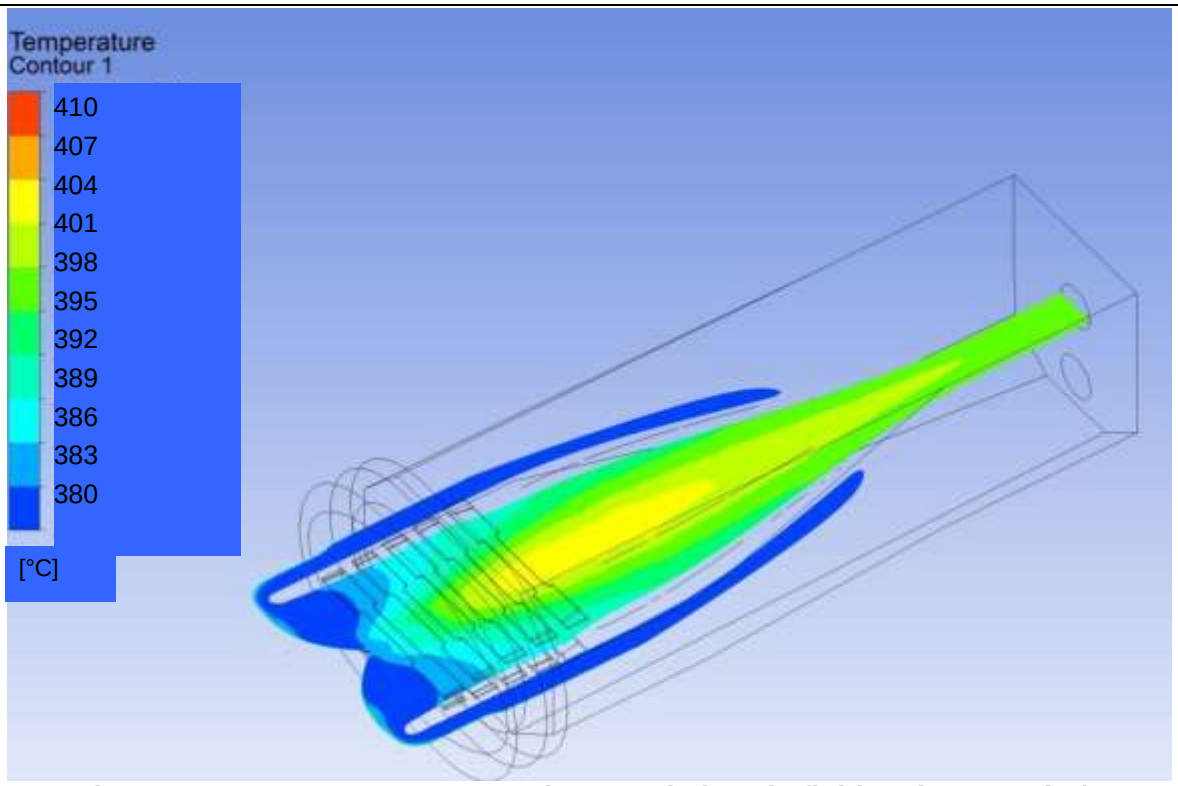

Figure 128: Temperature contour in central plane in fluid region at 38 kg/s

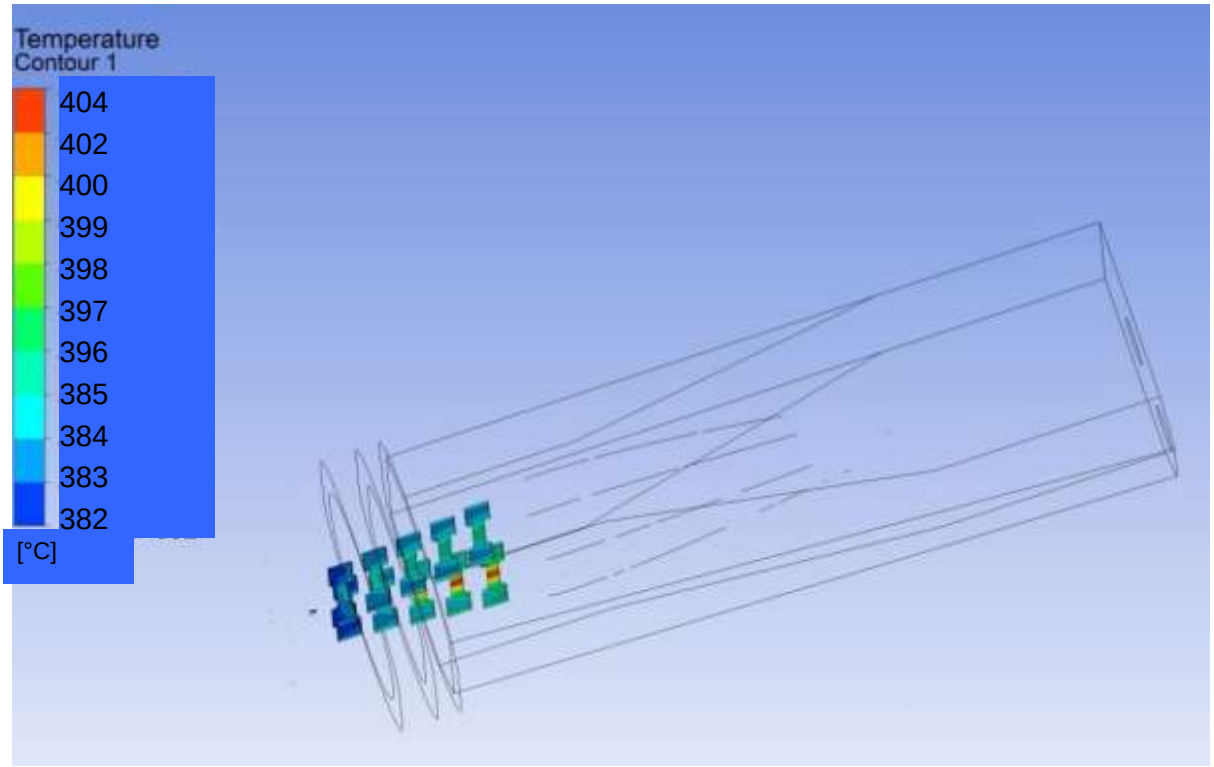

Figure 129: Temperature contour in the samples at 38 kg/s

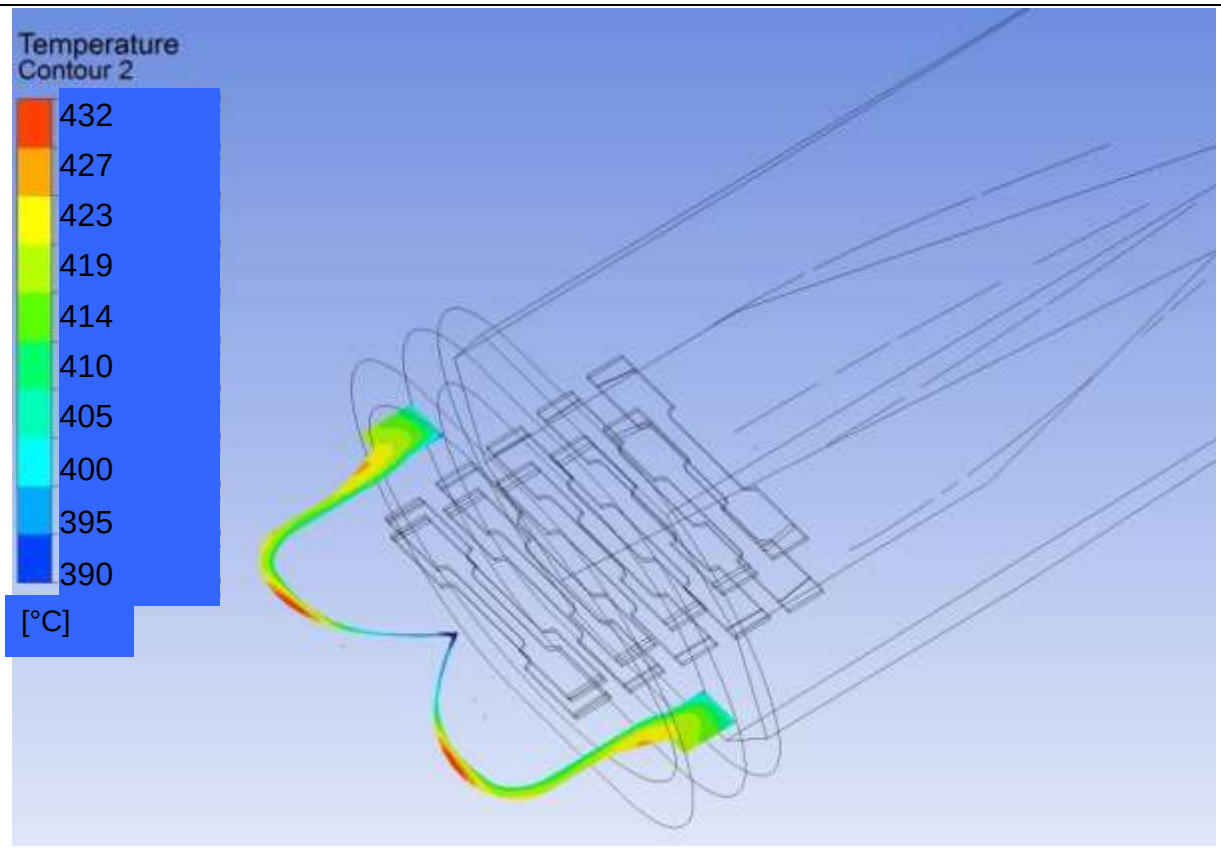

Figure 130: Temperature contour in the window at 38 kg/s

Finally, the pressure drop is calculated along the flow path, as shown below.

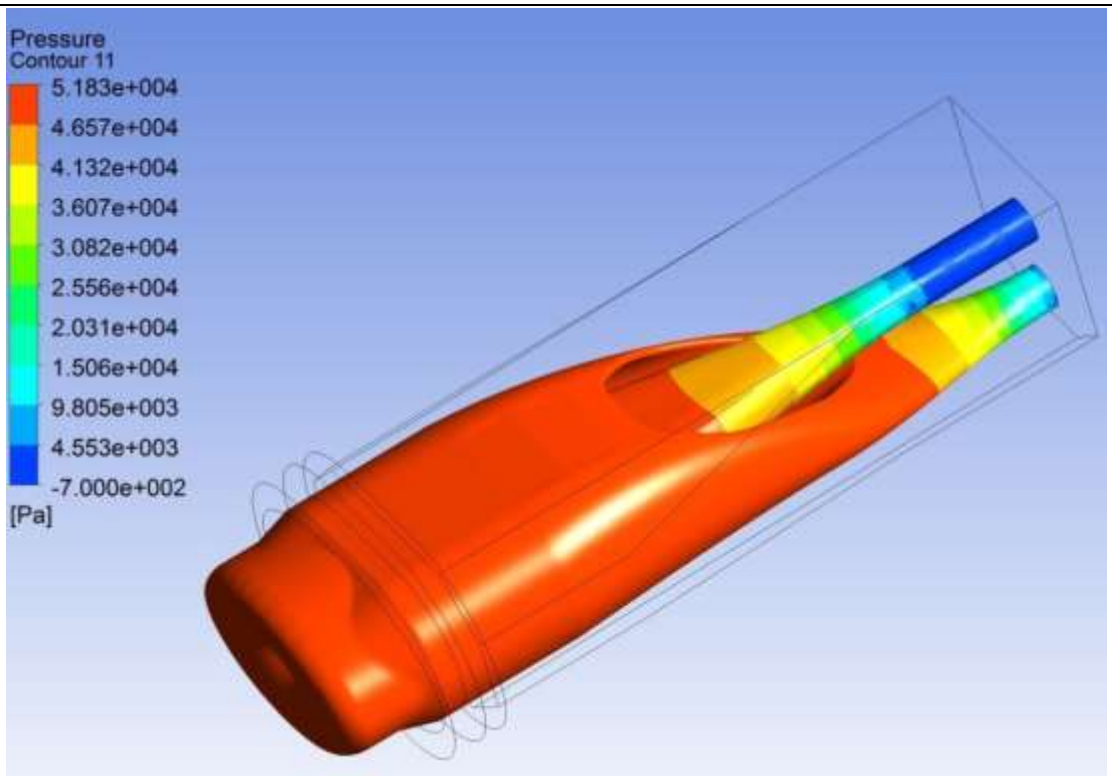

Figure 131: Pressure profile in fluid domain at 38 kg/s

The flow of liquid metal is shown in the figure below, from the inlet to the window and around the samples.

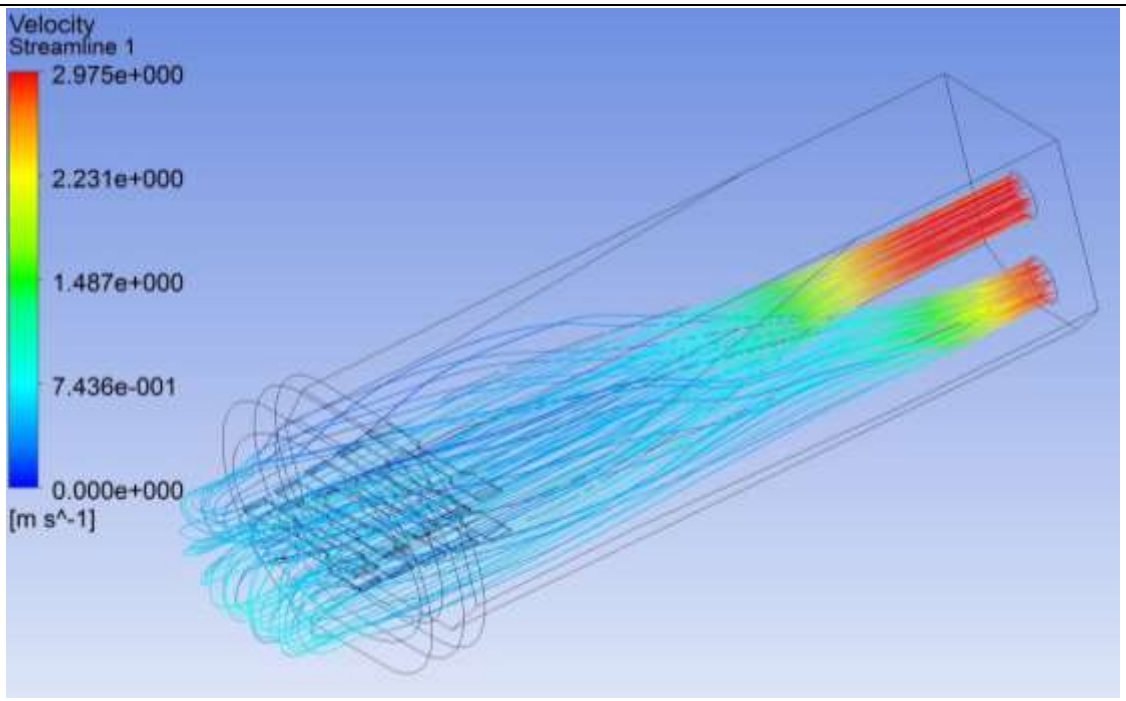

Figure 132: Velocity streamlines in the fluid at 38 kg/s

4.3.2 Analysis of the optimised design

In this section the optimised design shown in paragraph 4.2.2.9 is analysed thermally. The flow rate is varied from a minimum of 4.1 kg/s to a maximum of 38 kg/s in order to vary the sample temperature using the same beam power deposition.

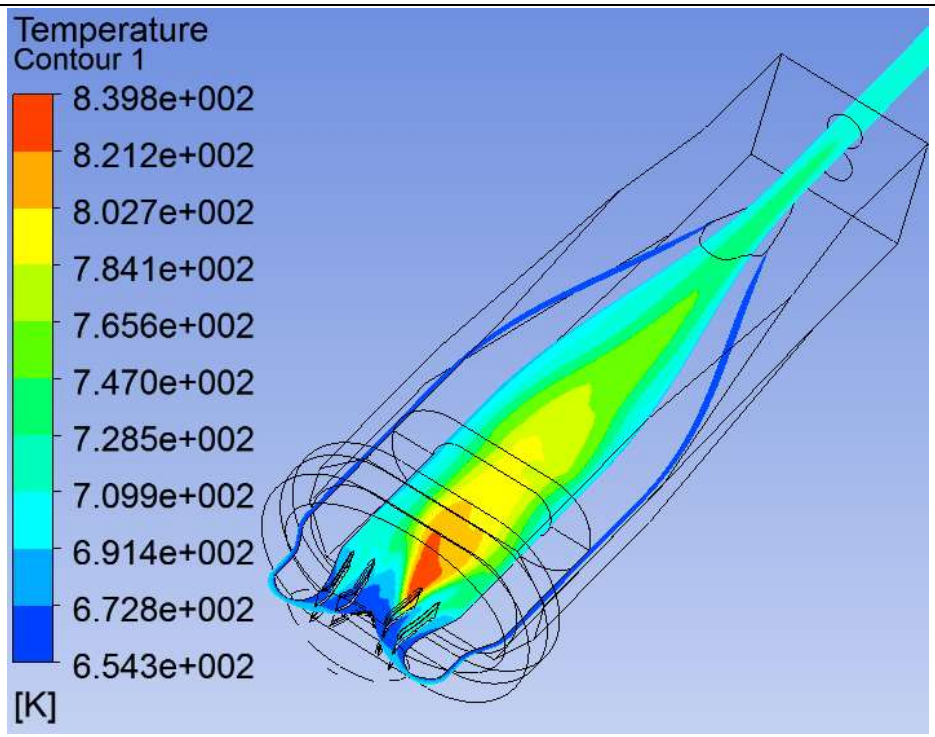

Figure 133: Temperature contour in central plane in fluid region at 4.1 kg/s

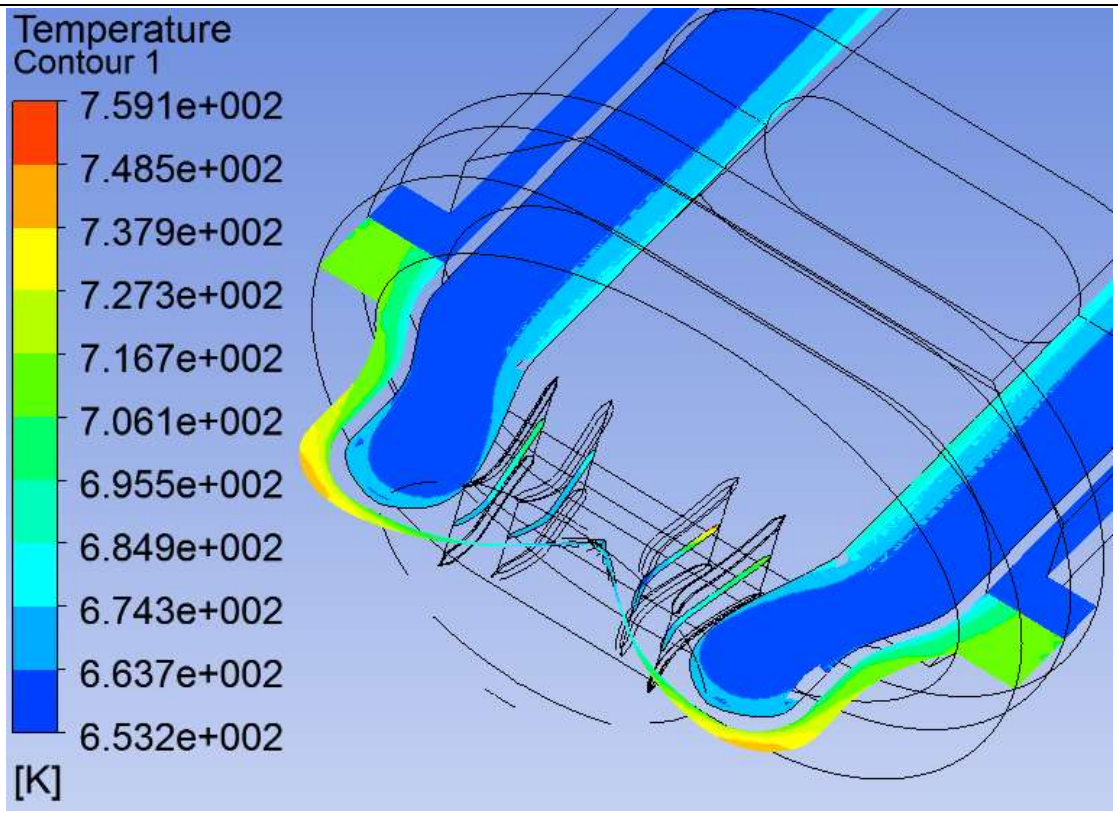

Figure 134: Temperature contour in central plane in window at 4.1 kg/s

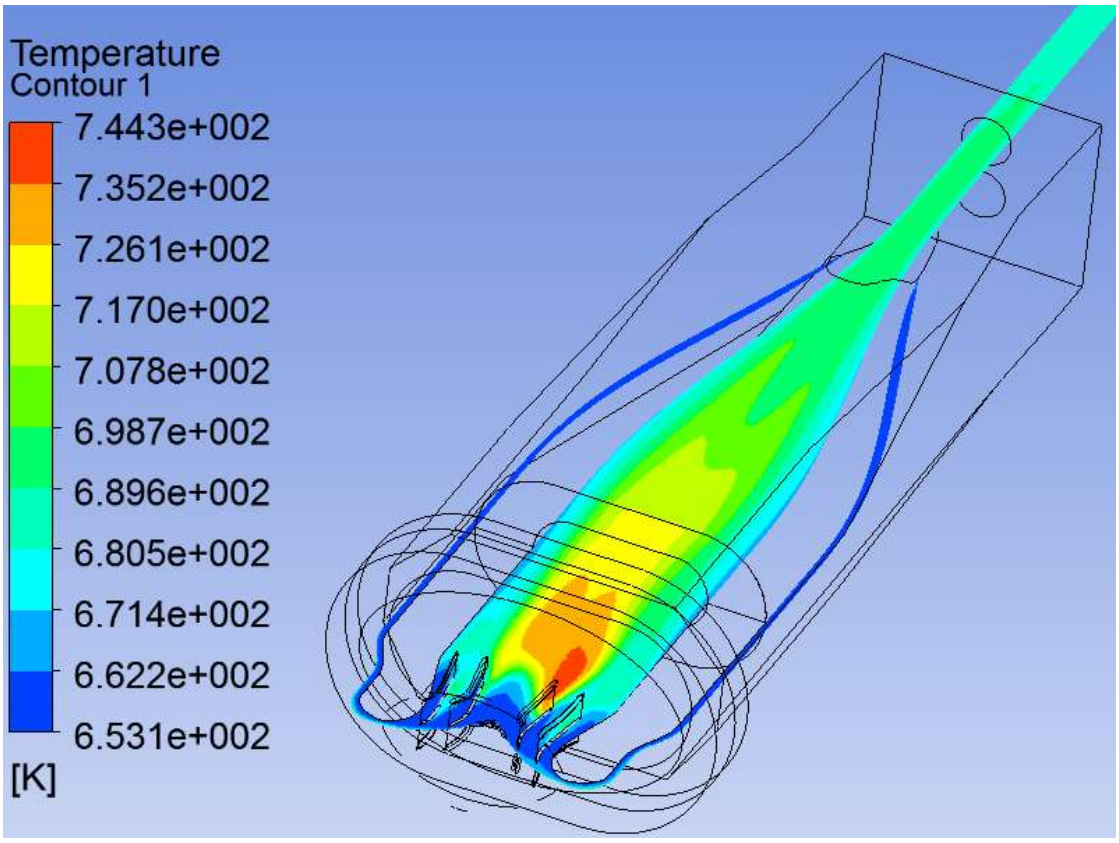

Figure 135: Temperature contour in central plane in fluid region at 12.3 kg/s

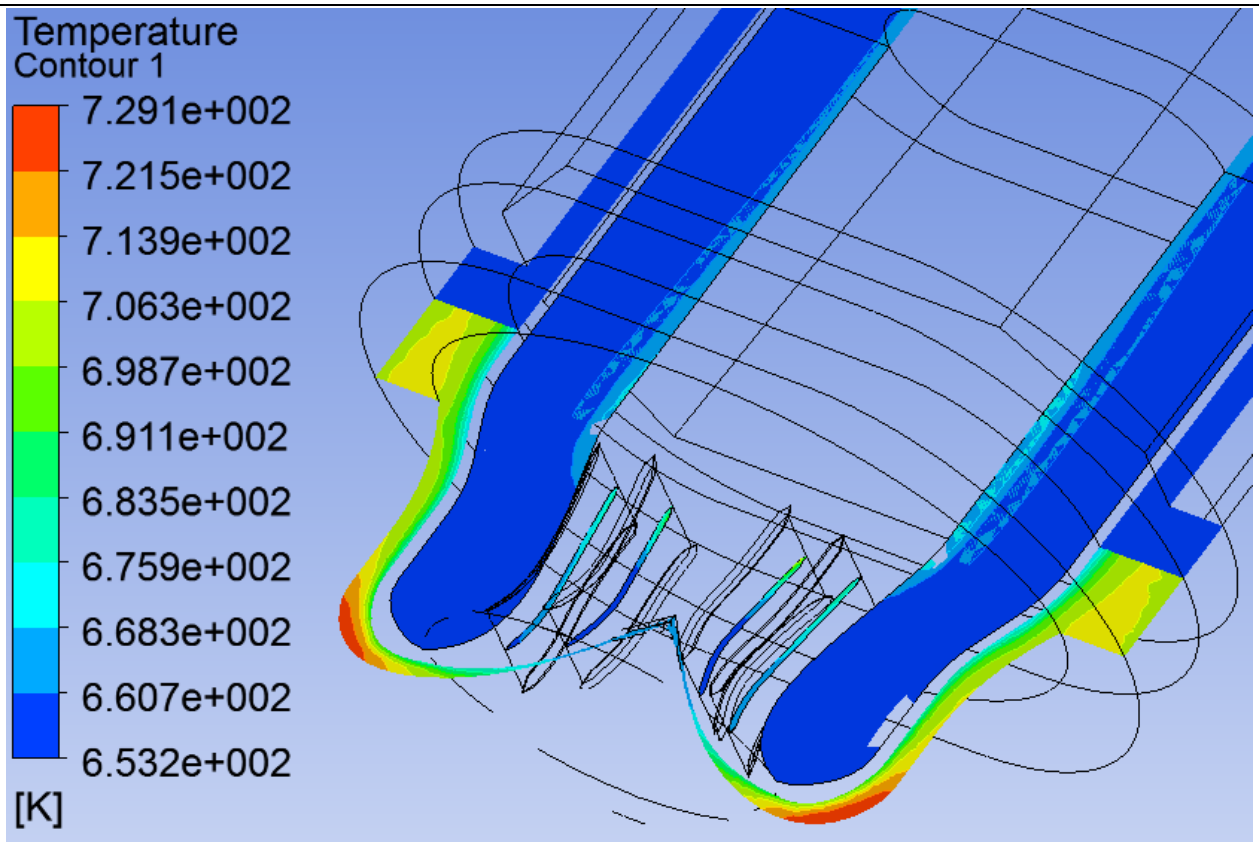

Figure 136: Temperature contour in central plane in window at 12.3 kg/s

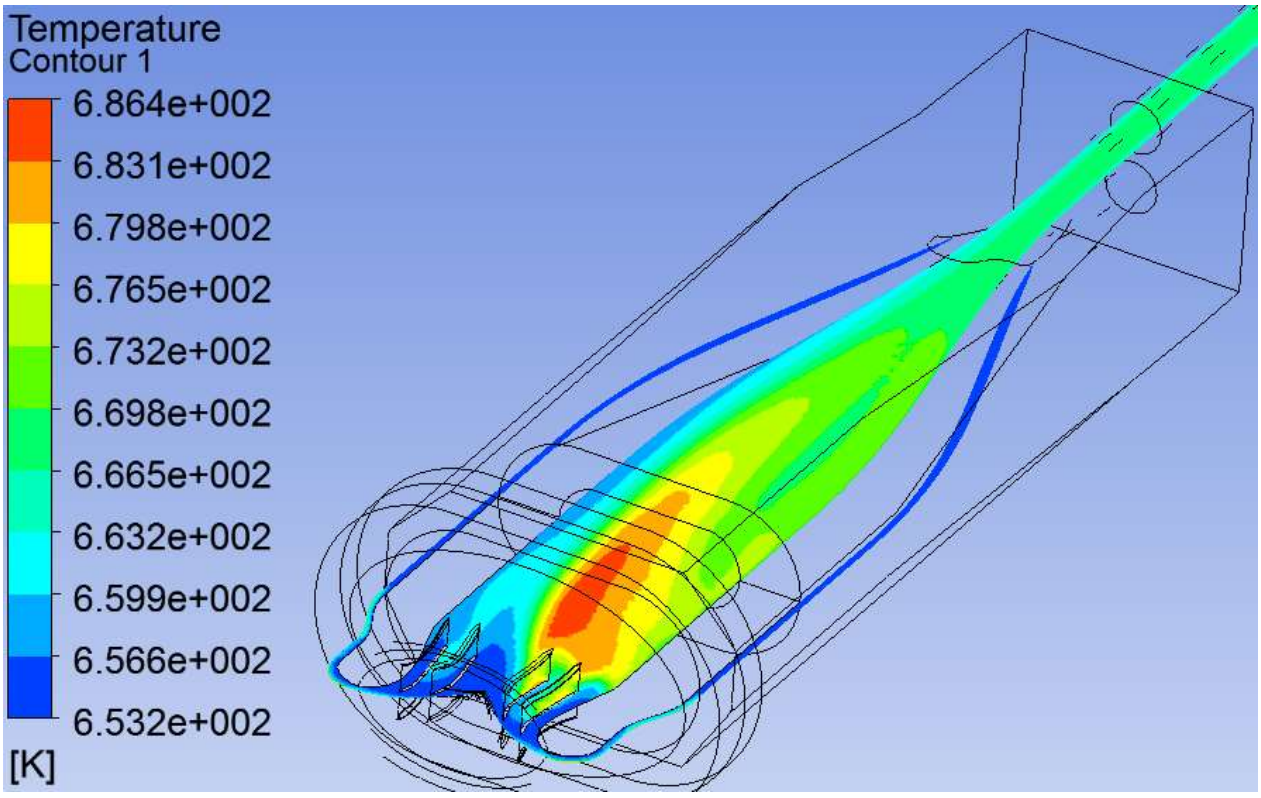

Figure 137: Temperature contour in central plane in fluid region at 38 kg/s

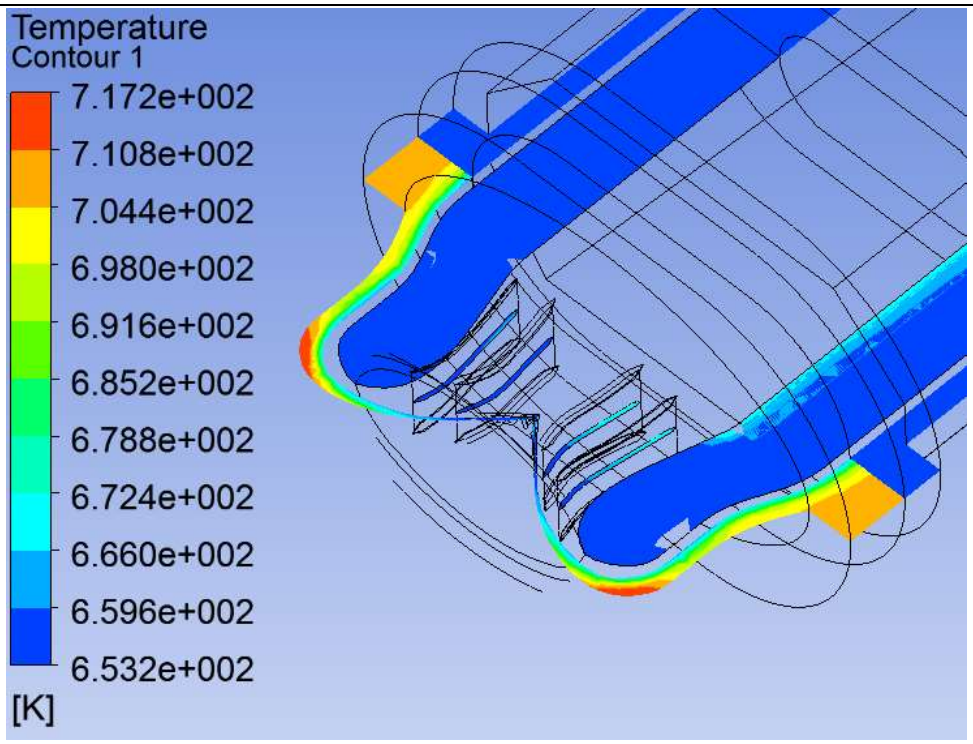

Figure 138: Temperature contour in central plane in window at 38 kg/s

As expected, reducing the flow rate in the target increases the temperature of the fluid and therefore the temperature of the samples. Decreasing the mass flow rate from 38 kg/s to 4.1 kg/s makes the temperature around the samples increase from 400 °C to 537°C. This increases also slightly the maximum temperature in the window from 440°C to 467°C.

The effect of increasing the flow rate on the pressure loss through is significant; it increase from 0.05 Bar to 4 bar, it remains however tolerable in terms of pumping capacity.

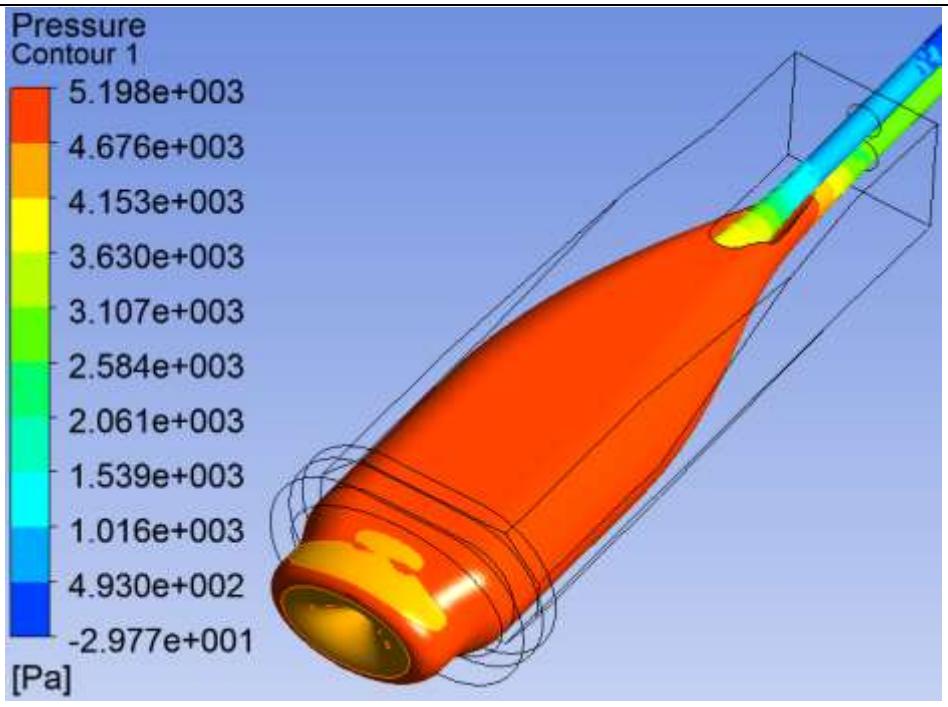

Figure 139: Pressure in the fluid at 4.1 kg/s

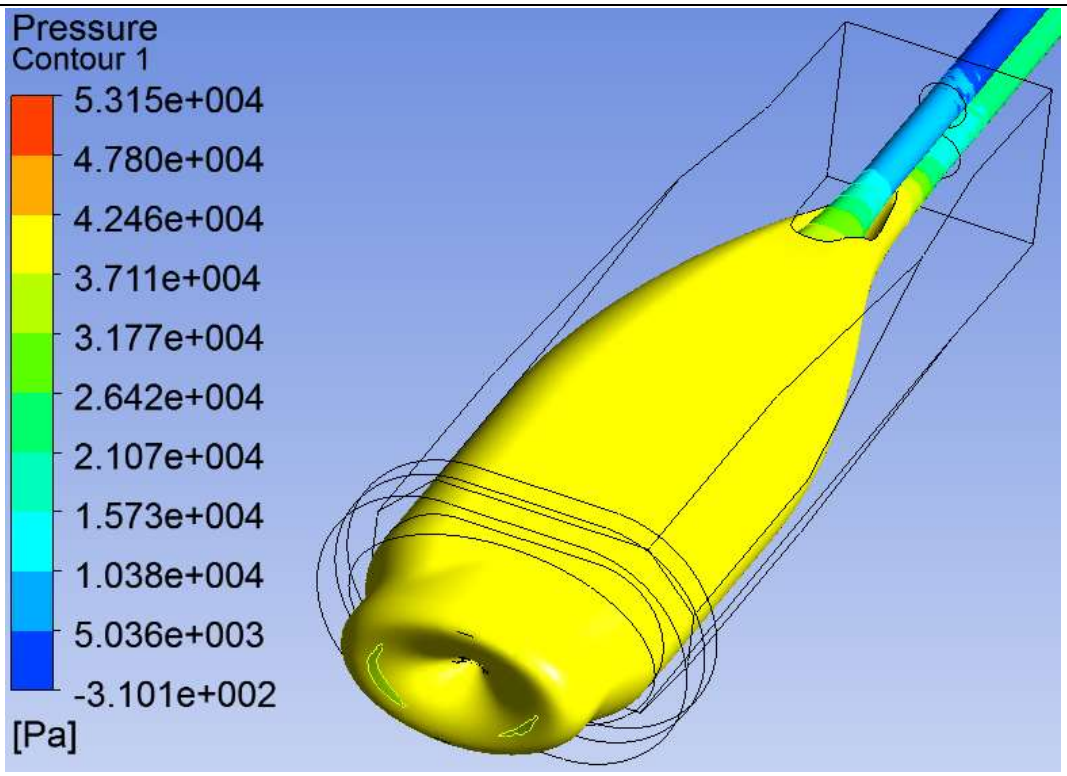

Figure 140: Pressure in the fluid at 12.3 kg/s

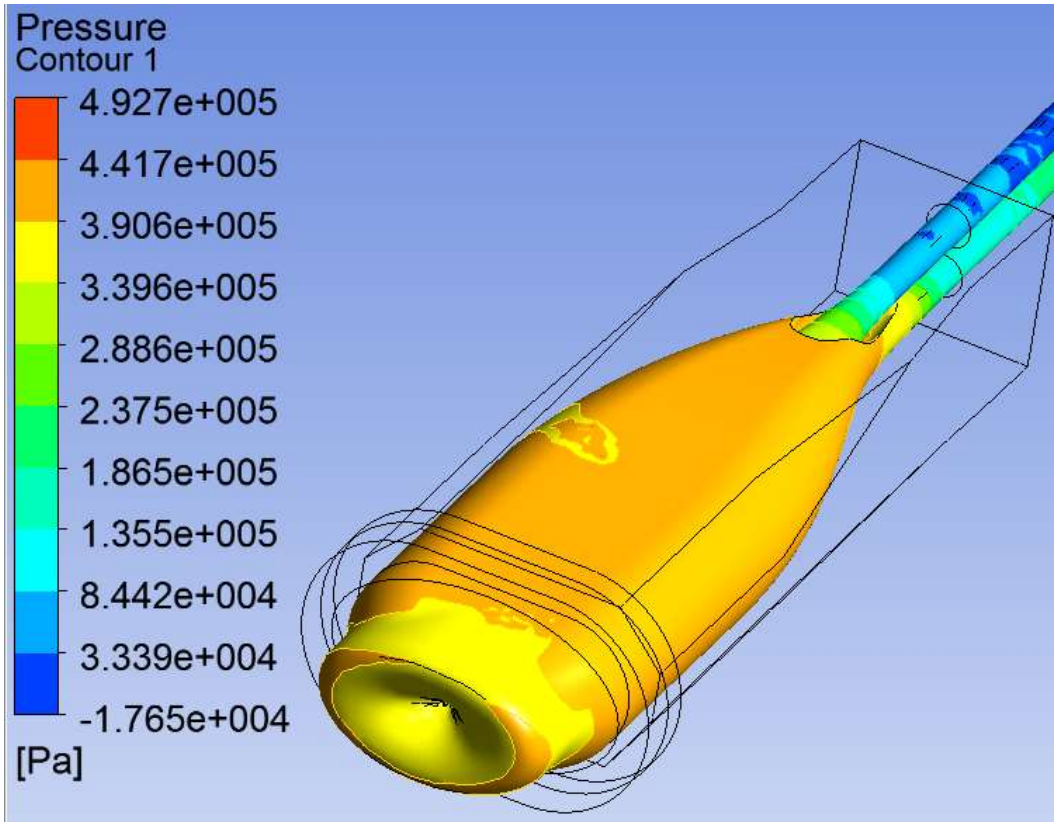

Figure 141: Pressure in the fluid at 38 kg/s

In spite of the great change in velocity of the fluid in the target, from 0.25 m/s to 3 m/s, the stability of flow remains unperturbed.

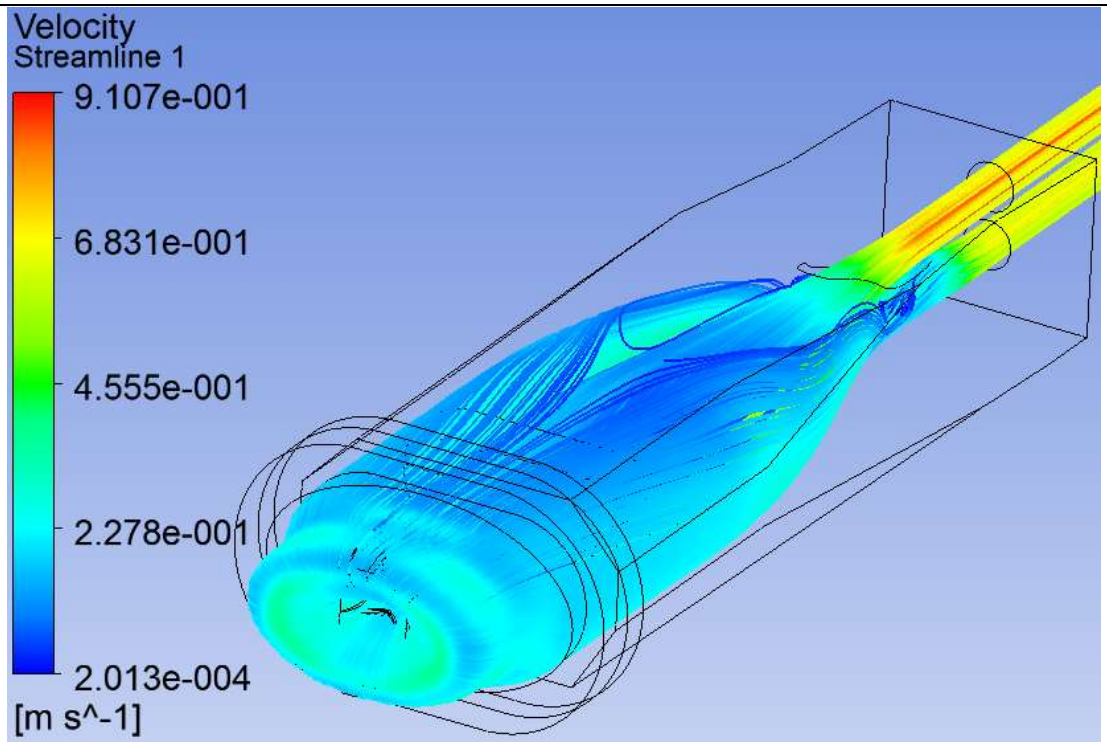

Figure 142: Velocity in the fluid at 4.1 kg/s

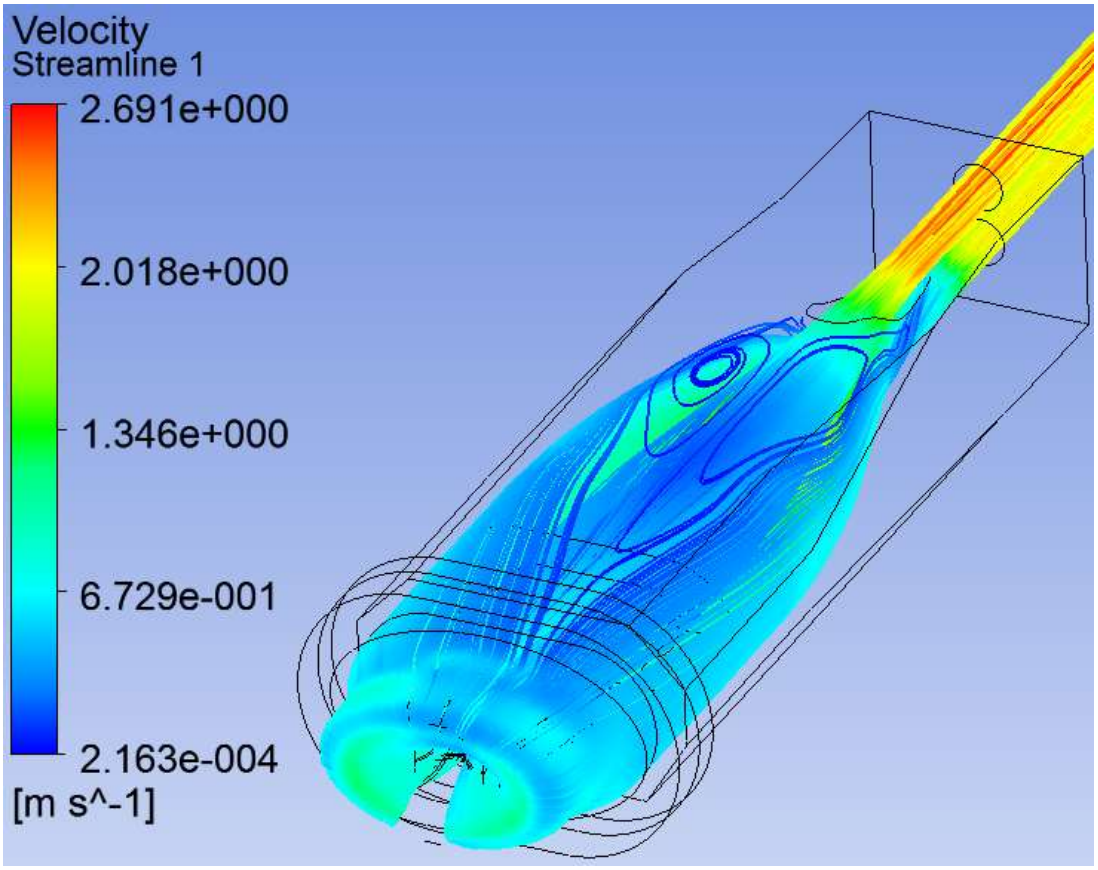

Figure 143: Velocity in the fluid at 12.3 kg/s

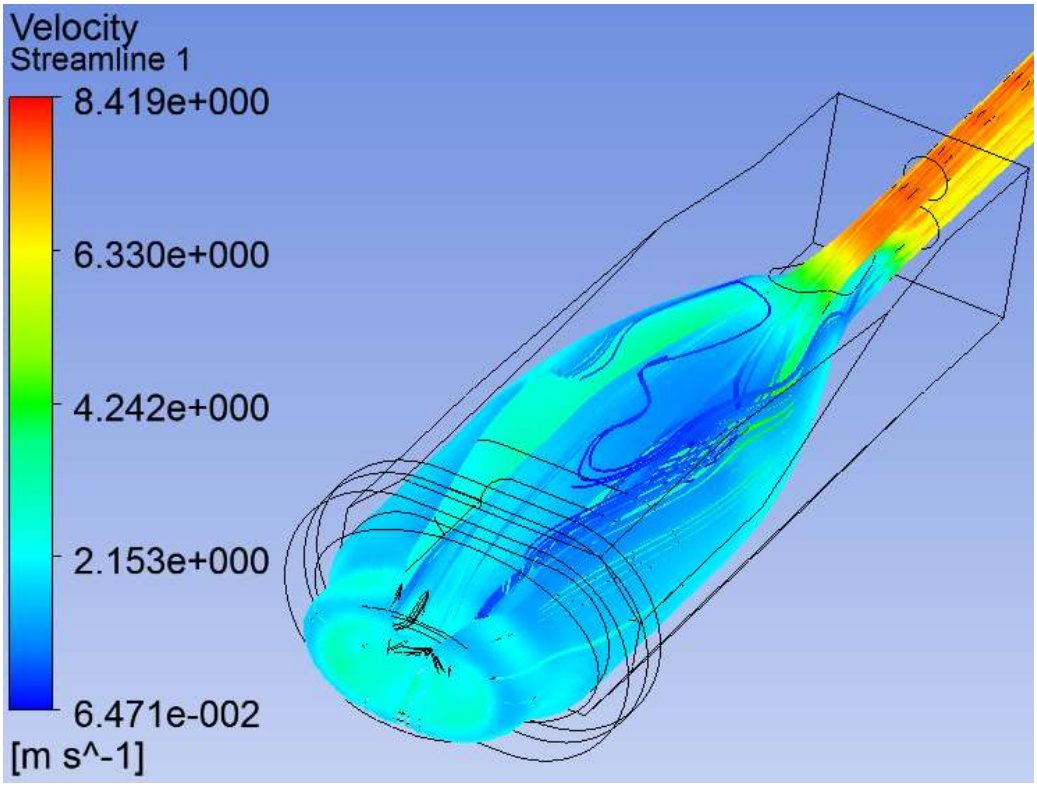

Figure 144: Velocity in the fluid at 38 kg/s

In view of these results, changing the flow rate to increase the samples temperature seems a viable option, which has the advantage of not requiring changing the power level in the beam.

4.4 Overall assessment of the target design

Hydraulic analysis of the target concludes that the essential parameters as laid out in the original preliminary design report (ref.2) are valid and stable conditions will be reached on the window allowing it to be cooled. The use of vanes in reversing the flow back into the guide tube is somewhat novel but due to their attachment method, this is not feared to result in any fatigue failure. Previous testing in the Eurisol program reinforces this belief.

5 Detail stress analysis

An essential part of the assessment of the current project is determining the degree to which it can operate safely, limited by its most exposed components. Safety aspects of the beam window are reviewed in the current chapter, as it is judged to be most critical.

5.1 Stress analysis of the beam window

The lifetime of the beam window has long been a source of major concern, leading some to propose its abandonment in favour of so-called windowless designs. However, in essence the beam must penetrate through a barrier at some point in order to isolate the very high vacuum of the beam line from the target. Even if the beam were to intersect a falling curtain of liquid metal, such a target would immediately pollute the beam tube if it were not materially isolated. Hence a beam window always exists although it may be relegated far from the target.

The next question which arises is, if a window has to exist, is it best to isolate it from the target or to use the liquid metal to cool it. In case it is uncooled, the window has to dissipate heat by thermal radiation and therefore needs to be very thin. The vacuum in the beam tube is therefore at very high risk from any rupture of this barrier, a rupture which is ever more likely, the higher the temperatures and stresses.

The method employed in the current design is therefore to adopt a target window that is cooled by the liquid metal. However rather than resort to the simple hemispherical geometries used in past projects such as Megapie, the proponents of this technology suggest the use of a concave conical beam window with a hyperbolic section which has been tried and tested in the Eurisol project. The design of the window has been derived from the Eurisol beam window and the current analysis will focus on this optimised beam window.

5.1.1 Properties of Beam window T91 stainless steel

Allowable design stress

The allowable stress documented in the French RCCMR standards are applicable to irradiation levels below 2 [dpa], a dose the window is guaranteed to exceed after a month. The values in the table below can be used for design purposes, as long as the elasto-plastic domain is avoided.

T	ºC	20	50	100	150	200	250	300	350	400	450	500	550	600
σ	N / mm^2	193	193	193	193	192	190	187	183	174	163	146	126	101

Table 24: Allowable design stress for T91 Martensite steel, temperature dependency

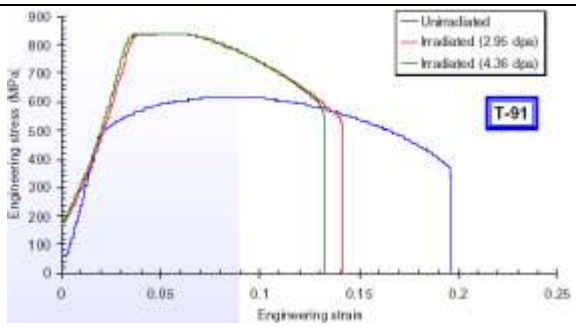

Source: D. Sapundjiev, E. Lucon, M. Matijasevic, S. Van Dyck, A. Almazouzi: Mechanical Behaviour of candidate steels in LBE after irradiation in BR2 at 200°C, Nantes Megapie TRM, May 2004

Figure 145: Effect of irradiation doses on stress-strain curves

Linear thermal expansion coefficient

The temperature dependency for the thermal expansion coefficient is as follows

T	ºC	20	100	200	300	400	500	600	700
α_m	10^{-6}/K	10.4	10.8	11.2	11.6	11.9	12.2	12.5	12.7
α_i	10^{-6}/K	10.4	11.1	11.9	12.4	13.0	13.6	13.8	

Table 25: Linear thermal expansion coefficient for T91 Martensite steel, temperature dependency

Where: α_m mean coefficient between 20ºC and T

α_i instantaneous coefficient at T

Young`s Modulus

The temperature dependency for the stiffness modulus follows is as follows

E [MPa] = 207300 – 64.58 T for 20ºC < T < 500ºC

E [MPa] = 295000 – 240 T for 500ºC < T < 600ºC

T	ºC	20	100	200	300	400	500	600	700
E	[MPa]	206000	199500	194400	187900	181500	175000	151000	127000

Table 26: Young's modulus for T91 Martensite steel, temperature dependency

Poisson Coefficient

The coefficient ν is 0.3 for all temperatures.

The shear modulus G [MPa] is calculated according to $G = E/2(1+\nu)$.

Density

The density of T91 steel as a function of temperature is described in the table below.

T	ºC	20	100	200	300	400	500	600
ρ	kg/m^3	7730	7710	7680	7650	7610	7580	7540

Table 27: Density for T91 Martensite steel, temperature dependency

Thermal capacity

The thermal capacity of T91 steel as a function of temperature is described in the table below.

T	ºC	20	50	100	150	200	300	400	500	600
Cp	J/kg/K	448.85	462.76	484.11	503.92	523.04	562.69	609.96	671.75	754.96

Table 28: Thermal capacity for T91 Martensite steel, temperature dependency

Conductivity

The thermal conductivity of T91 steel as a function of temperature is described in the table below.

T	ºC	20	100	200	300	400	500	600
λ	W / m	25.9	27.0	28.1	28.8	29.2	29.0	28.5

Table 29: Thermal conductivity for T91 Martensite steel, temperature dependency

5.1.2 Detail thermal analysis of T91 stainless steel beam window

The beam window is analysed using the temperature-dependent properties listed here above and simplified assumptions for the boundary conditions. Cooling by liquid metal assumes a flow past the window corresponding to 1 m/s, this is a minimum and is quite conservative for the higher flow rates studied in section 3.2.1.

- HTC = 15'000 W/m^{2}K
- T_{Bulk} = 380°C in annulus / 480 [°C] at window centre

The power deposition in the window uses beam parameters, ranging from the greatest to the smallest beam spot envisaged in the previous optimisation, particularly in chapter 2. The chosen ratio of short axis to long axis is wither 1:6 as per section 2.4 or 1:1.7 as in the smallest beam spot envisaged in section 2.10.

- σ_x = 6 cm, σ_y = 1 cm
- σ_x = 1.7 cm, σ_y = 1 cm

In both case the total beam power is 100kW. As was previously remarked in section 4.3 covering the thermal-hydraulic analysis, the exact beam parameters need to be discussed with the end users, after which a final optimisation is conducted. The shape of the power deposition from the beam is shown hereafter for the first beam spot dimensions; the peak corresponds to the values calculated in chapter 2 as in Figure 14.

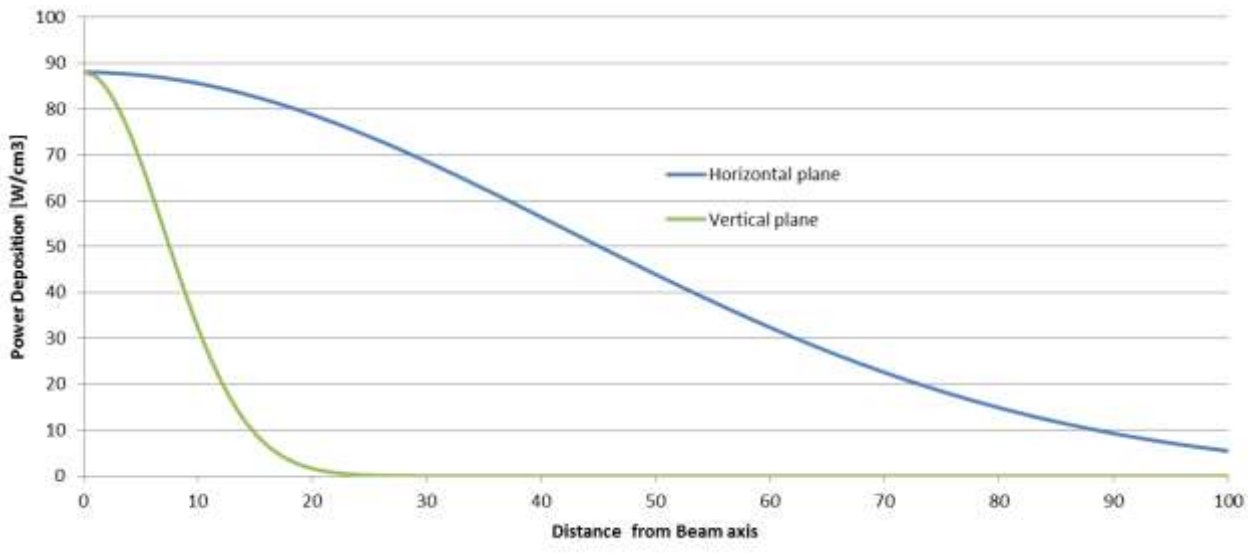

Figure 146: Power deposition along the two axes at right angle to the beam axis

These boundary conditions are programmed into an Ansys thermal model to produce a thermal map and are then output into a temperature map. The temperature map is then used as a boundary condition for calculating thermal stresses induced by thermal elongation. The temperature contours in the figure hereafter follow the overall shape of the elliptical beam window since the beam has the same geometric characteristics as the window. The original intent was in doing so to ensure a minimisation of stress. As can be seen in the next figures, this goal has not materialised as the stress pattern is more complex than in the Eurisol design which was rotationally symmetric and impacted by a symmetric beam.

5.1.3 Detail stress analysis of T91 stainless steel beam window

5.1.3.1 Detail stress analysis for a σ_x = 6cm, σ_y = 1cm, 100 kW beam

The thermal map calculated in the previous section is entered into a structural model of the quarter of the window using symmetry conditions. The temperatures are roughly similar on either surface, there is a slightly more elongated high temperature spot on the surface facing the beam as it is not as well cooled by the flowing liquid metal. The difference is however quite small due to the reduced wall thickness of the beam window.

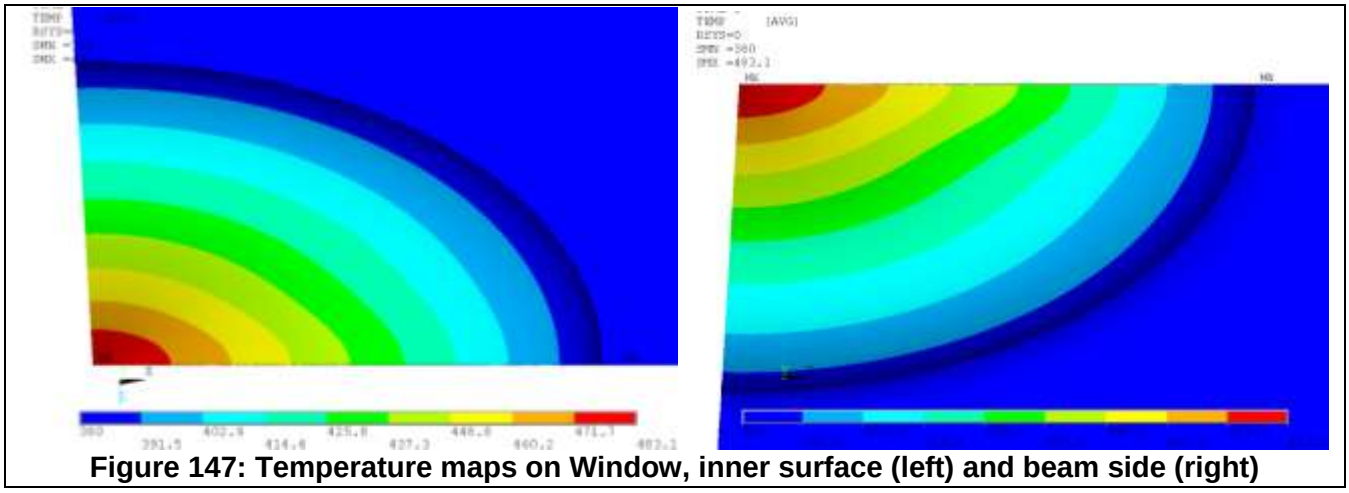

Figure 147: Temperature maps on Window, inner surface (left) and beam side (right)

The thermal elongation in the beam window is calculated by the program using these temperatures maps and the temperature-dependent properties listed in the previous section here above.The resulting stress components are shown in the figures hereafter; both on the inner and outer surface of the beam window.

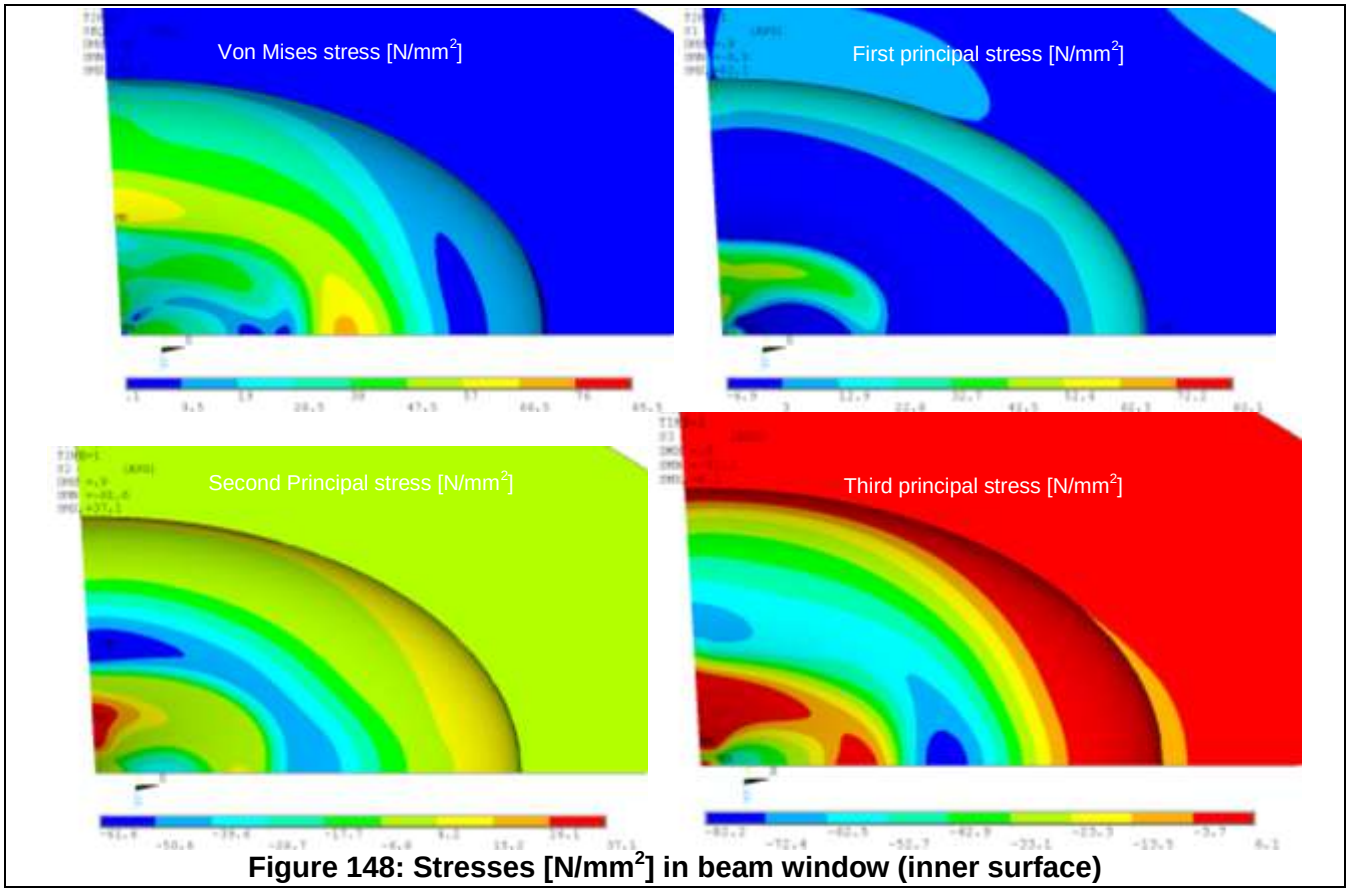

Figure 148: Stresses [N/mm^2] in beam window (inner surface)

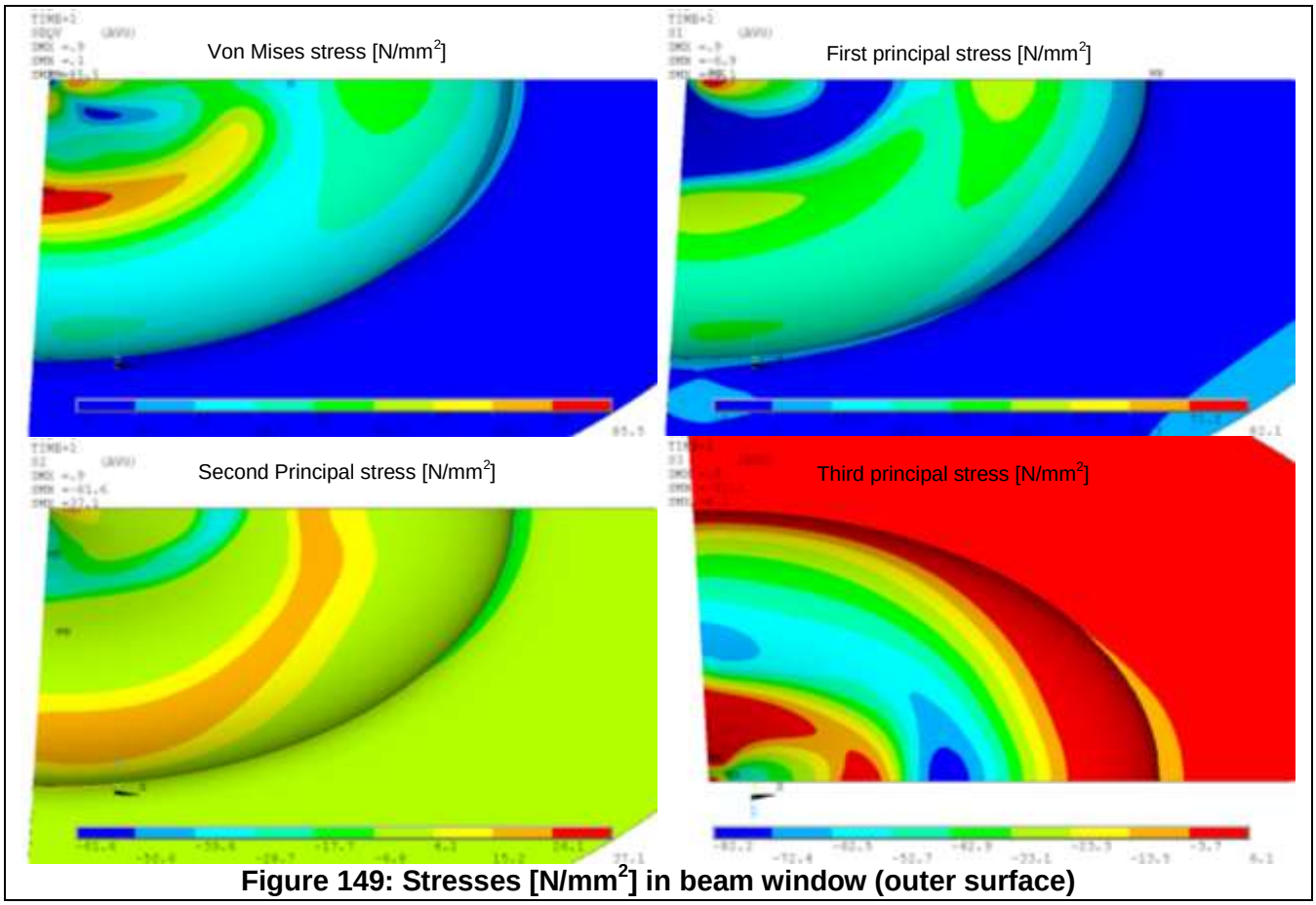

Figure 149: Stresses [N/mm^2] in beam window (outer surface)

A closer examination of the deformation plots explains the reason for the rather complex stress pattern, which is more complicated that in the Eurisol target. The thermal deformation is causing two types of bending; the primary motion is about the circumferential direction as in the case of Eurisol. Another bending motion arises however at right angle to this primary bending motion; it is likely caused by the elliptical shape of the window.

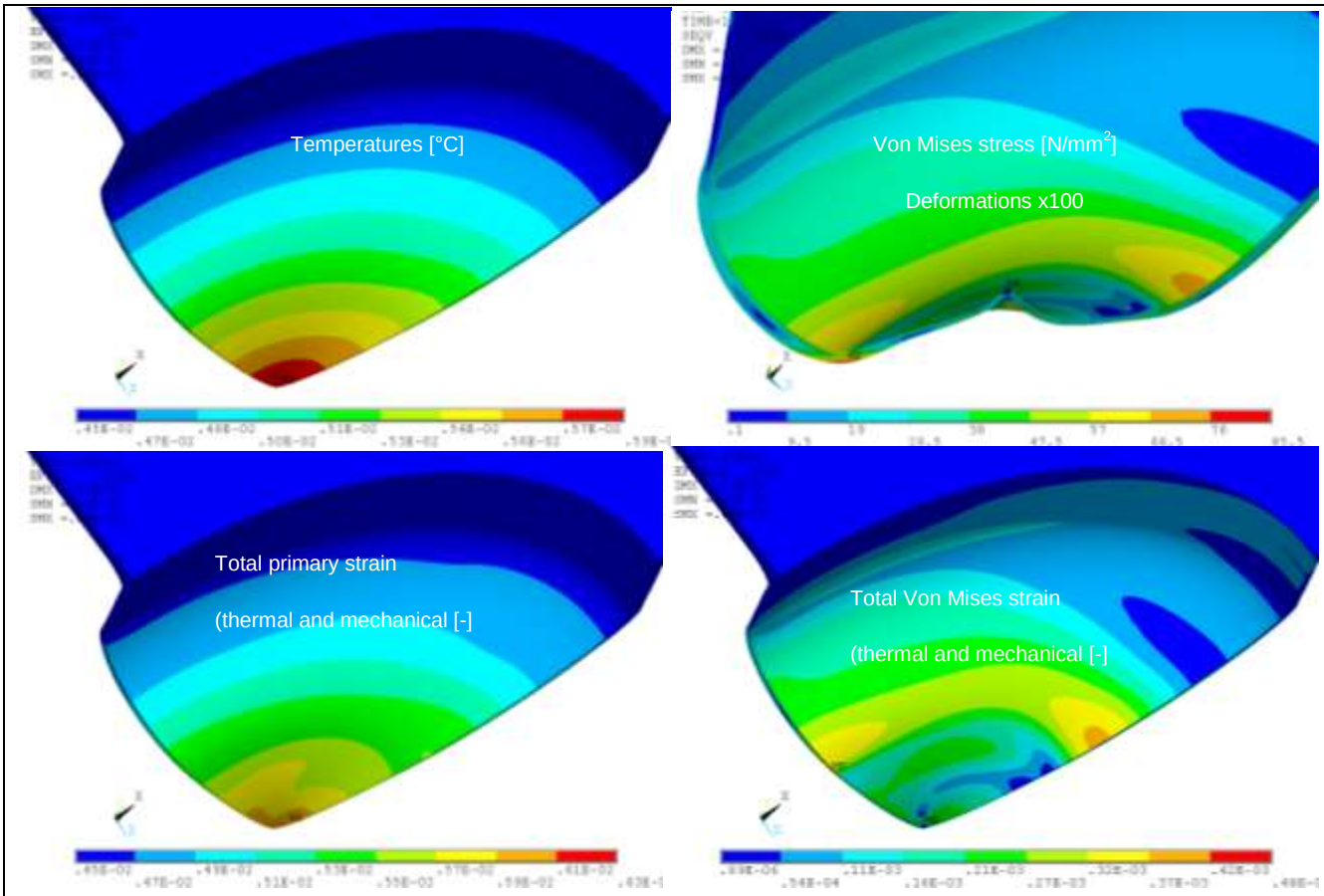

Figure 150: Deformations in beam window (top right, increased x100)

The highest Von Mises stress is 85.5 [N/mm^2]. This value corresponds to a tensile stress that is located on the outside of the beam window, as can be seen by comparing the Von Mises stress plot in the top left of Figure 149 with the first principal stress in the top right and second principal stress in the bottom left. On the inner surface of the window, the maximum tensile stress is approximately 50 [N/mm^2], comparing the Von Mises stress plot in the top left of Figure 148 with the first principal stress in the top right. The maximum Von Mises stress on the inner surface is 75 [N/mm^2] and is in compression.

Hence the stresses which are most dangerous in terms of the strength of the beam window is a tensile stress of 50 [N/mm^2], well below critical values which is around 160 [N/mm^2] for highly irradiated T91 stainless steel (Table 24) and above is clearly in the purely elastic domain of the stress-strain curve, including under increased irradiation doses as shown in Figure 145. A rough margin on the window can therefore be derived as;

Reserve factor = Maximum Stress / Allowable Stress = 160 / 50 = 3.2

5.1.3.2 Detail stress analysis for a σ_x = 1.7cm, σ_y = 1cm, 100 kW beam

The same calculations are repeated for a smaller spot size and the results are shown in the figure hereafter.

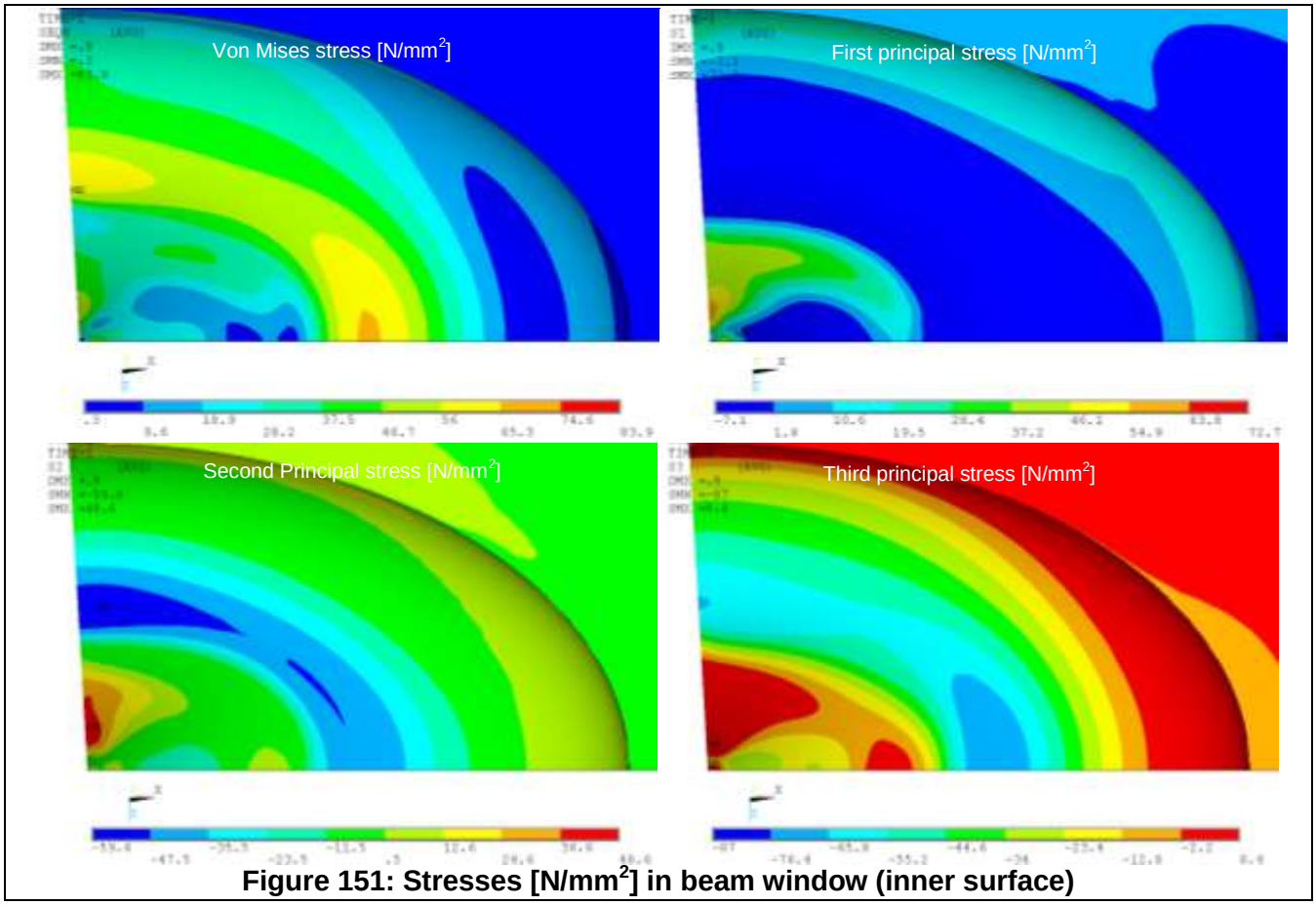

Figure 151: Stresses [N/mm^2] in beam window (inner surface)

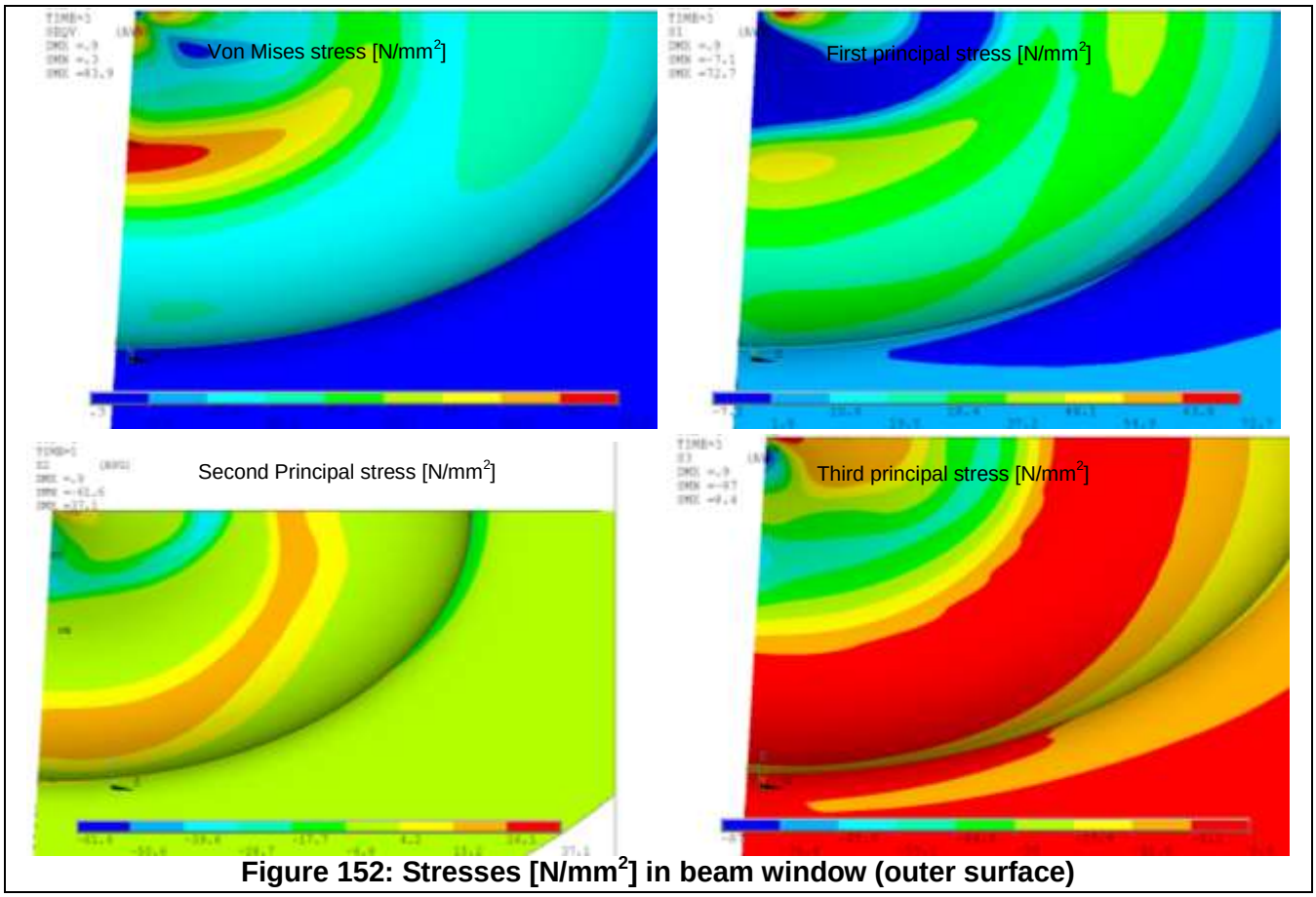

Figure 152: Stresses [N/mm^2] in beam window (outer surface)

The highest Von Mises stress is 84 [N/mm^2]. This value is quite close to the previous calculation with the more elongated beam spot. The stress values do not change much because the stress patterns is dominated by the bi-axial bending mentioned in the previous section and which is itself the product of the elliptical plan of the beam window.

It would seem that the capacity of the Eurisol beam window to evacuate high heat loads from a beam make it quite able to adapt to a variety of beam loading conditions. The elliptical plan which was adopted as a means of creating more space for the samples and the loading mechanism has not had too much of a detrimental effect in terms of the peak stresses.

The low stresses under all beam configurations are particularly comforting, considering the tight beam spot with dimensions 1cm / 1.7cm results in a peak deposition at the centre which is 6 times higher than that of the elongated beam spot with dimensions 6cm / 1cm. This entails that the design could withstand much higher beam power, although the entire neutronics / CFD calculations would have to be repeated for the corresponding increased power, something outside the current scope of the design study.

5.1.3.3 Detail stress analysis for a σ_x = 4.1 cm, σ_y = 2.4 cm, 100 kW beam

Finally, in order to check the assumption of symmetry a complete model of the beam window is calculated using a slightly larger beam spot with σ_x = 4.1 cm, σ_y = 2.4 cm under a 100 kW beam. The results are again quite similar.

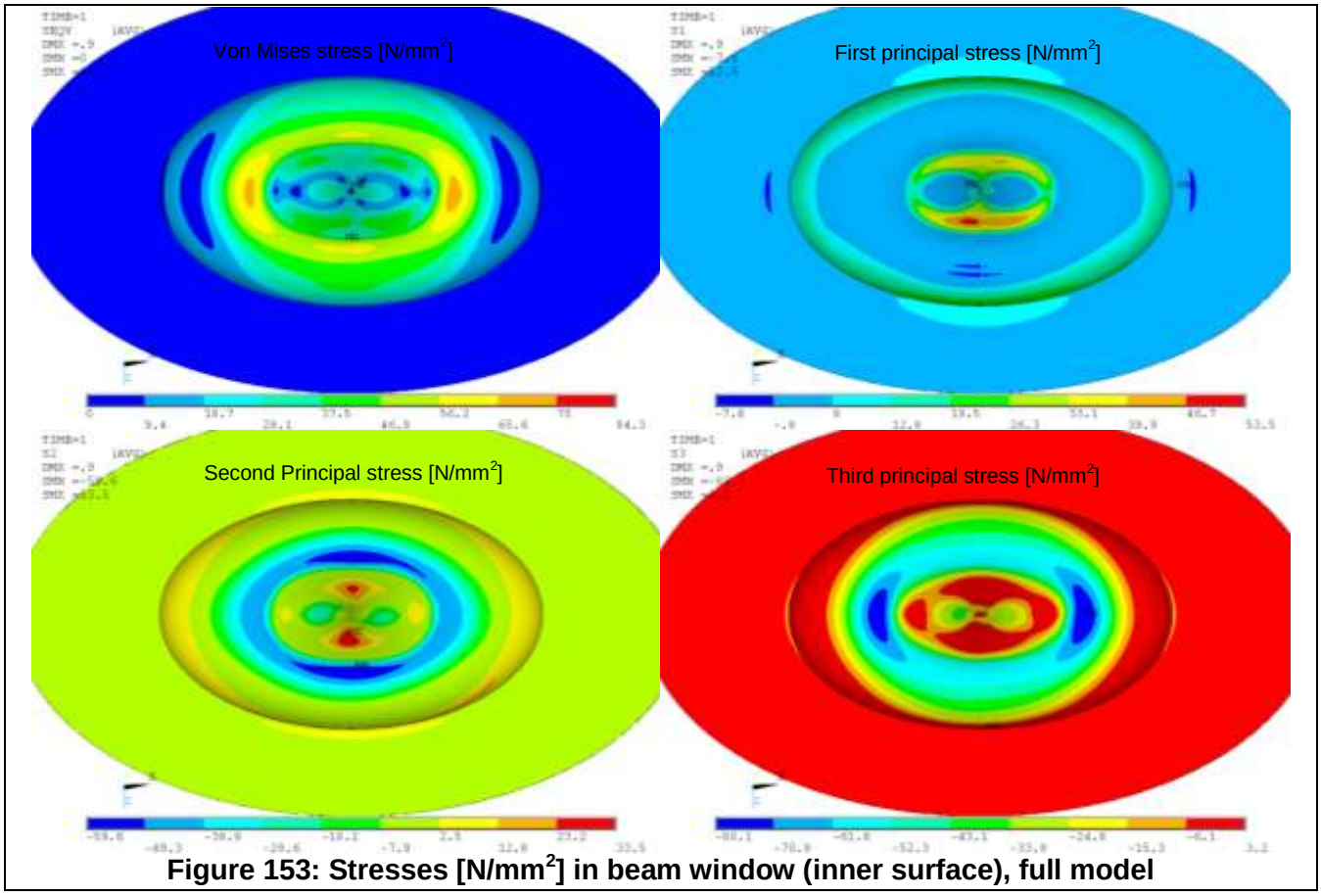

Figure 153: Stresses [N/mm^2] in beam window (inner surface), full model

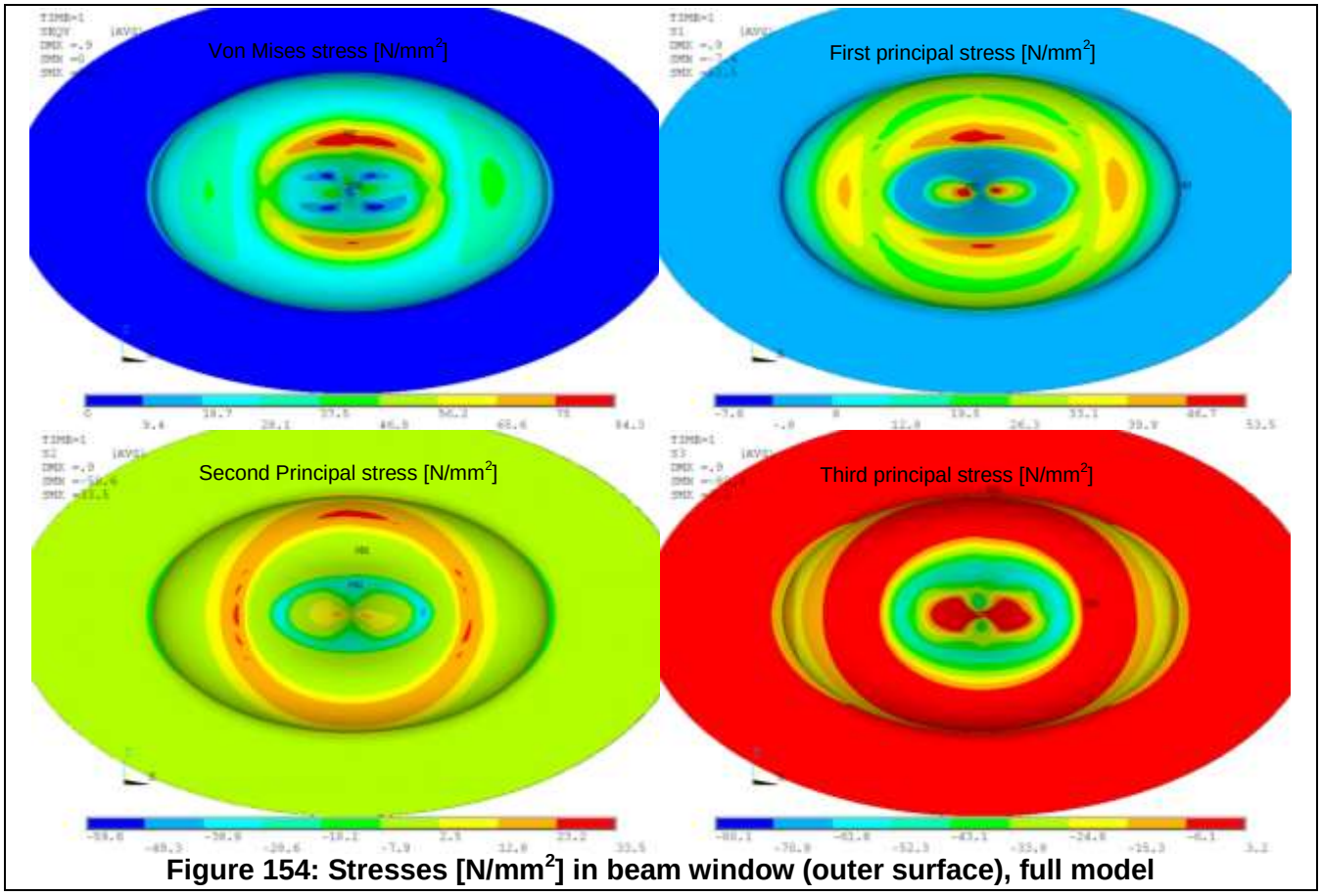

Figure 154: Stresses [N/mm^2] in beam window (outer surface), full model

5.2 Strength assessment

The detail stress analysis has been limited to the most critical item, the beam window. Other items such as the primary heat exchanger are not exposed to high stresses by virtue of their design. Indeed in the heat exchanger the primary pin is inserted inside the secondary barrel and separated by a flexible contact element which can absorb differential expansion between primary and secondary circuit. Likewise the spiral tubing at the exit of the target should absorb thermal expansion in the event of rapid transients.

Stress analysis concluded that the thermal loading caused by the beam on the window will not result in strength failure, taking into account the likely weakening of the structure caused by higher irradiation doses. The ability of stainless steel to sustain high DPA has been proven in experiments such as Megapie

6 Planning for the next phase in the development of T-MIF

The TIARA design study supported the development of a material irradiation facility at concept level using advance computational tools to optimise its performance, as described in the chapters above. The next step in the development of such a facility would be its implementation by a consortium of laboratories using their own resources, supported by FP7 funding. The purpose of the current chapter is to estimate the scale of the effort such a development would imply.

6.1 Work packages

The full development of T-MIF will be broken up into individual work packages and tasks, as is customary for sharing the cost of developing an infrastructure between participating institutes. The table below indicates how the project would be structured and which task could be assigned to specialised institutes. The institutes mentioned in the table are being approached at the time of writing. Wherever a specific task could foreseeably be carried out by an institute, this has been marked accordingly in orange. The tasks already finalised are marked in green. The individual tasks listed in the table are expected to be self-contained, with a main coordination body responsible for ensuring coherence. Although the tasks are all contributions to a complex facility, it may be expected that each task can evolve relatively independently with a modest amount of effort needed for interfacing between the different groups. Ideally the tasks should be allotted according to the experience of each institute with a view to minimising the need for interfacing.

Work Package	TASKS	Completion to date	1 CERN	2 EU-FP7	3 JAEA	4 IFMIF	5 MYRRHA	6 IPUL	7 EPFL	8 PSI	9 ESS
WP0	T0.1 Project management	0%	X		o		o			o	o
	T0.2 Communication	0%		X	o						
WP1	T1.1 Optimisation study establishing the overall layout of the facility	100%	X	covered by TIARA -Design Study							
	T1.2 Detail design study of facility	20%	X								
	T1.2.1 Design of the target and sample loading mechanism	30%	X								
	T1.2.2 Design of shielding	20%	x								
	T1.2.3 Design of ancillary systems	10%	x	o	o		o			o	
	T1.2.4 Aquisition & development of instrumentation	0%	o	o	o		o			o	
	T1.2.5 Design of beam interface	0%	o	o	o		o			o	
WP2	T2 Licensing	0%									
	T2 .1 Selection of representative accident case studies	1%	o								
	T2 .2 Accident analysis	0%	o	o	o		o			o	
	T2 .3 Safety case documentation	0%	o	o	o					o	
	T2 .4 Application for License	0%	o	o	o		o			o	
WP3	T3. Component Manufacturing	0%									
	T3.1 Manufacturing of the target and sample mechanism	0%	o		o	o	o			o	o
	T3.1.a Manufacturing target for thermal hydraulic testing	0%	o		o	o	o			o	
	T3.1.b Manufacturing of sample loading mechanism + test rig	0%	o		o	o	o			o	o
	T3.2 Manufacturing of the shielding & support structures	0%	o		o	o	o			o	
	T3.3 Manufacturing of Ancillaries	0%	o		o	o	o			o	
	T3.3.a Build thermal-hydraulic test bench	0%	o		o	o	o	o	o	o	
	T3.1.b Manufacture Heat exchangers for thermal hydraulic testing	0%			o			o			
	T3.1.c Manufacture Pumps for thermal hydraulic testing	0%			o			o			
	T3.3.d Integrate all ancillaries to thermal-hydraulic test bench	0%	o		o	o	o	o	o	o	
WP4	T4.1 Testing	0%									
	T4.1 Testing of individual components: target, heat exchanger, pumps	0%	o		o	o	o	o	o	o	
	T4.2 Thermal-hydraulic testing of assembled system on test bench	0%	o		o	o	o	o	o	o	
	T4.3 Facility integration	0%	o		o	o	o	o	o	o	
	T4.3 Qualification irradiation testing of integrated facility without samples	0%	o		o	o	o			o	
	T4.4 First sample irradiation testing	0%	o		o	o	o			o	
WP5	T5.1 Samples	0%									
	T5.1 Sample preparation	0%							o	o	o
	T5.2 Handling post irradiation	0%	o		o	o	o			o	o
	T5.3 Dissemination	0%	o	o	o	o	o			o	o
WP6	T6. Radio-isotopes	0%									
	T6.1 Design adaptation of facility to radio-isotopes	0%	o		o		o			o	
	T6.2 Manufacture equipment for Radio-isotope extraction and conditioning	0%	o		o		o	o	o	o	
	T6. 3 Qualification and licensing of radio-isotope production	0%	o		o		o	o	o	o	

Table 30: Work packages, breakdown of tasks

6.2 International cooperation

In terms of manpower and expenditure the proposed facility is roughly equivalent to a project such as Megapie for which it was necessary to form a consortium of interested laboratories. This philosophy has been adopted in the current project and contacts are on-going with funding organisations, research facilities and laboratories which may have an interest. They are listed below, with a short description of their possible contribution

1. CERN. Initiated the project and is seeking to find application for accelerator technology in the field of material science and isotope production. It possesses the necessary specialist for performing many of the analytical tasks.

2. EU-FP7 funded the design study and is seeking to encourage the development of accelerator-based technology in Europe

3. JAEA is developing a material testing facility using a spallation source at a power level very close to the proposed facility. It has extensive facilities in the nuclear field and experience spanning several decades both in accelerator technology and reactor technology.

4. IFMIF. The neutron spectrum it seeks to achieve could be matched by the proposed facility. Hence, the facility could serve as an interim solution for providing the irradiated material data needed for ITER, pending full-scale implementation of IFMIF

5. MYRRHA: is developing a facility which will need material data at high DPA, possibly with the inclusion of proton damage.

6. IPUL has developed the pumps for Megapie and the test loops for Eurisol along with a number of liquid metal projects. Their experience would be valuable in testing and developing liquid metal components

7. EPFL has developed expertise in thermal-hydraulic testing; it is also encouraging the development of life sciences of which radio-isotopes are an interesting component.

8. PSI hosted and managed the Megapie project, co-managed the Eurisol development and still possesses a significant nuclear department capable of handling irradiated materials. It could therefore participate in many of the tasks.

9. ESS is developing a high power spallation source for physics research and medical applications. The power of the installation at 5 MW would make it the most powerful spallation source to date and will require advanced materials validated under irradiation from protons and neutrons. It may have an interest in sample preparation and evaluation.

6.3 Schedule

A substantial factor in most development work involving cutting edge technology is the speed at which the project is conducted. Too fast and technical risks will be taken, too slow and the cost of manpower will escalate. Overall a similar project such as Megapie took 5 years to develop after the initial design study. The current project, although it contains some technical innovations builds on this existing prior experience. Furthermore, since the end of the Megapie significant experience has been gained in liquid metal technology and with materials under irradiation. Therefore a total duration for the development of just 3 years seems attainable.

Within this tight schedule there are some external factors which could slow down progress. The most significant is probably likely to be licensing. It seems essential to keep the licensing authorities abreast of the latest developments, but also to ensure that the facility remains an experimental object confined to laboratories. This is why the last task concerning radio-isotopes is isolated from the main development as the licensing hurdles can be expected to be far greater.

Work Package	TASKS	1st Project year												2nd Project year												3rd Project year											
		1	2	3	4	5	6	7	8	9	10	11	12	13	14	15	16	17	18	19	20	21	22	23	24	25	26	27	28	29	30	31	32	33	34	35	36
WP0	T0.1 Project management																																				
	T0.2 Communication																																				
WP1	T1.1 Optimisation study establishing the overall layout of the facility	covered by TIARA -Design Study																																			
	T1.2 Detail design study of facility																																				
	T1.2.1 Design of the target and sample loading mechanism																																				
	T1.2.2 Design of shielding																																				
	T1.2.3 Design of ancillary systems																																				
	T1.2.4 Aquisition & development of instrumentation																																				
	T1.2.5 Design of beam interface																																				
WP2	T2 Licensing																																				
	T2 .1 Selection of representative accident case studies																																				
	T2 .2 Accident analysis																																				
	T2 .3 Safety case documentation																																				
	T2 .4 Application for License																																				
WP3	T3. Component Manufacturing																																				
	T3.1 Manufacturing of the target and sample mechanism																																				
	T3.1.a Manufacturing target for thermal hydraulic testing																																				
	T3.1.b Manufacturing of sample loading mechanism + test rig																																				
	T3.2 Manufacturing of the shielding & support structures																																				
	T3.3 Manufacturing of Ancillaries																																				
	T3.3.a Build thermal-hydraulic test bench																																				
	T3.1.b Manufacture Heat exchangers for thermal hydraulic testing																																				
	T3.1.c Manufacture Pumps for thermal hydraulic testing																																				
	T3.3.d Integrate all ancillaries to thermal-hydraulic test bench																																				
WP4	T4.1 Testing																																				
	T4.1 Testing of individual components: target, heat exchanger, pumps																																				
	T4.2 Thermal-hydraulic testing of assembled system on test bench																																				
	T4.3 Facility integration																																				
	T4.3 Qualification irradiation testing of integrated facility without samples																																				
	T4.4 First sample irradiation testing																																				
WP5	T5.1 Samples																																				
	T5.1 Sample preparation																																				
	T5.2 Handling post irradiation																																				
	T5.3 Dissemination																																				
WP6	T6. Radio-isotopes																																				
	T6.1 Design adaptation of facility to radio-isotopes																																				
	T6.2 Manufacture equipment for Radio-isotope extraction and conditioning																																				
	T6. 3 Qualification and licensing of radio-isotope production																																				

Table 31: Proposed schedule for the development of facility

6.4 Cost estimates

Costs may be estimated in two manners, one is a top-down approach in which the cost of similar installations is plotted against a dimensioning parameter, the second, a bottom-up approach, attempts to itemize the cost of every significant component in an installation and sum them up.

Top-down approach.

In such an approach, three similar installations have been examined and are summarized in the table hereafter, most cost figures are approximately 3-5 years old; however inflation has been modest in the interim.

0.4 MW SF / MSU (Michigan)	M€
High-energy targets	16.2
Shared target services	10.7
Target Total	26.9
1 MW Megapie / PSI	M€
Target	20
Ancillaries	40
Target Total	60
1.4 MW SNS / ORNL	M€
Assemblies	9.7
Moderator Systems	5.8
Reflector Assemblies	5.3
Vessel Systems	7.9
Target Station Shielding	9
Target Utility Systems	7.2
Remote Handling Systems	9.6
Controls	2.1
Beam Dumps	2.1
Technical Support	8.6
ORNL Field Coordination	10.8
Target Total	78
Target Building	65

Table 32: Cost break-down of comparable spallation systems

The three data points are included in the figure hereafter, based on the table above and show a rough correlation between the power of the installation and its cost. A linear regression is applied, implying the cost of a 100 kW installation would be roughly 12 M€, while a more powerful machine at 200 kW would cost around 17 M€

Naturally a more refined method will have less uncertainty however the figures do point out that at the lower end of the scale there is a minimum price to pay of over 6 M€ below which it is not possible

to expect any economies from a smaller installation. This seems logical as much of the more expensive infrastructure needed to cope with the radiological constraints is incompressible.

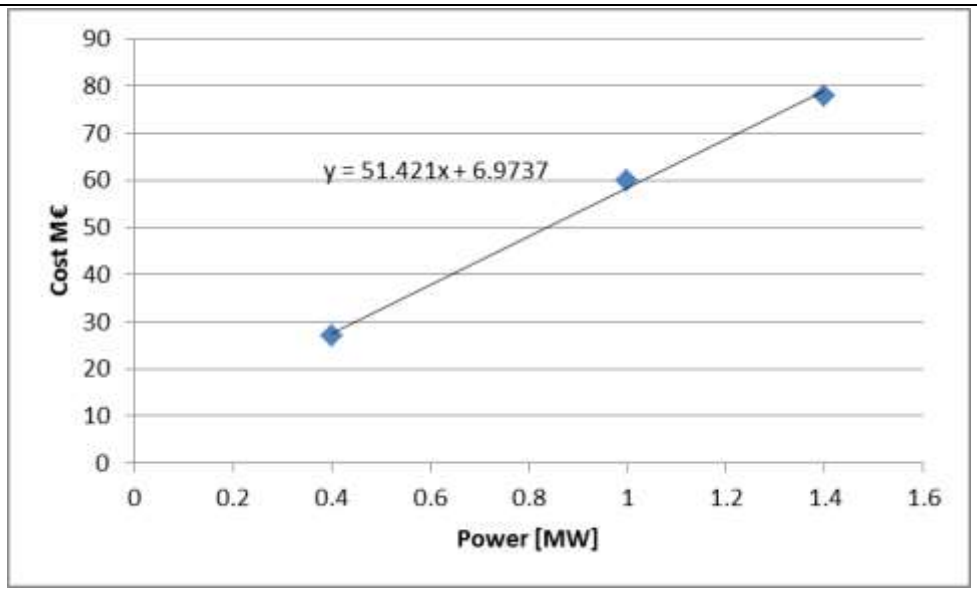

Figure 155: Cost of spallation source installations

The method delivers a rough estimate between 12 to 17 M€ depending on the power chosen.

Another method of establishing the costs may be to evaluate one of the installations such as SNS for which a more detail breakdown of the costs exists and focus on those packages that a project such as TIARA would definitely need. In the list given, the systems which would certainly be needed are:

- Vessel Systems 7.9 M€
- Target Station Shielding 9 M€
- Remote Handling Systems 9.6 M€
- Controls 2.1M€

In a laboratory facility the other systems are assumed to exist or would be provided by the experimenters. Hence a “minimal list” of items drawn from the SNS list would yield a total price of 28.6 M€ for a 1.4 MW machine. The cost derived from this “semi-top-down” approach may be seen as an absolute upper bound cost for TIARA which it is not likely to exceed.

Bottom-up approach.

In this approach, the work packages listed in the previous section 6.1 and the schedule in section 6.3 are examined to arrive at an approximate cost and manpower estimate. Note that in some instances, the manpower requirements are quite considerable despite the short duration due to the need for a large task force, as in the case of testing for example.

By separating clearly the manpower from the cost of the hardware, it is possible to gauge the necessary effort to be provided by each participant in the form of manpower. Indeed much of the source of funding for the hardware are the central research funding agencies, supplemented in part by the individual laboratories.

The total budget with and without the development of a radio-isotope production capability is listed hereafter, as WP6 is at this stage only an option.

Work Package	TASKS	Completion to date	Manpower	costs
			Man-years	k€
WP0	T0.1 Project management	0%	3	150
	T0.2 Communication	0%	0.5	20
WP1	T1.1 Optimisation study establishing the overall layout of the facility	100%	vered by TIARA -Design Stu	
	T1.2 Detail design study of facility	20%	8	630
	T1.2.1 Design of the target and sample loading mechanism	30%	2	10
	T1.2.2 Design of shielding	20%	1	10
	T1.2.3 Design of ancillary systems	10%	3	100
	T1.2.4 Aquisition & development of instrumentation	0%	1	500
	T1.2.5 Design of beam interface	0%	1	10
WP2	T2 Licensing	0%	2.5	120
	T2 .1 Selection of representative accident case studies	1%	0.5	0
	T2 .2 Accident analysis	0%	1	50
	T2 .3 Safety case documentation	0%	0.5	20
	T2 .4 Application for License	0%	0.5	50
WP3	T3. Component Manufacturing	0%	3.25	4'500
	T3.1 Manufacturing of the target and sample mechanism	0%		
	T3.1.a Manufacturing target for thermal hydraulic testing	0%	0.25	800
	T3.1.b Manufacturing of sample loading mechanism + test rig	0%	0.25	600
	T3.2 Manufacturing of the shielding & support structures	0%	0.25	1'000
	T3.3 Manufacturing of Ancillaries	0%		
	T3.3.a Build thermal-hydraulic test bench	0%	1	500
	T3.1.b Manufacture Heat exchangers for thermal hydraulic testing	0%	0.25	1'000
	T3.1.c Manufacture Pumps for thermal hydraulic testing	0%	0.25	500
	T3.3.d Integrate all ancillaries to thermal-hydraulic test bench	0%	1	100
WP4	T4.1 Testing	0%	7	900
	T4.1 Testing of individual components: target, heat exchanger, pumps	0%	2	100
	T4.2 Thermal-hydraulic testing of assembled system on test bench	0%	1	100
	T4.3 Facility integration	0%	2	500
	T4.3 Qualification irradiation testing of integrated facility without samples	0%	1	100
	T4.4 First sample irradiation testing	0%	1	100
WP5	T5.1 Samples	0%	2.25	1'300
	T5.1 Sample preparation	0%	1	200
	T5.2 Handling post irradiation	0%	1	1'000
	T5.3 Dissemination	0%	0.25	100
	Total without radio-isotope production capability		M.yr. 23.0	7'450 k€
WP6	T6. Radio-isotopes	0%	5	2'200
	T6.1 Design adaptation of facility to radio-isotopes	0%	2	
	T6.2 Manufacture equipment for Radio-isotope extraction and conditioning	0%	1	2'000
	T6. 3 Qualification and licensing of radio-isotope production	0%	2	200
	Total with radio-isotope production capability		M.yr. 28.0	9'650 k€

Table 33: Cost break-down for the development of the proposed T-MIF

7 Conclusions

The stated aim of the program has been achieved; a maximum irradiation dose in the sample of 26 DPA per annum can be achieved in a compact facility, measuring 2 metres on a side. The spectrum in the samples has been proven to resemble that needed for the fusion program ITER. A method for applying cyclical mechanical loads in addition to the corrosive effect of liquid metal and the irradiation dose has been proposed.

The most critical items in the facility, the target, the heat exchanger, the sample loading mechanism have been subject to detail analysis and have robust margins. The shielding has been examined and every effort has been made to lower the dose rate during operation which will be conducted in a shielded laboratory.

After irradiation, the samples are easily accessible using simple robotic tools and a new batch of test samples can be installed rapidly to reduce the down-time so as to maximise the irradiation periods. Once the samples are dismounted, they decrease rapidly in activity allowing them to be manipulated in gloves boxes after a week.

Hence a detailed engineering design is proposed, which fulfils all the requirements laid out in the specification, for a facility able to irradiate samples at high doses. This very robust solution addresses the need for testing materials at high irradiation doses, whilst keeping the overall facility compact enough for it to be transportable and adaptable to many diverse laboratories.

The full-scale development of the facility is estimated to cost 7.5 M€ over a short development period of 3 years, and the partners involved would have to provide a total level of manpower estimated to be 23 man-years over the three year period. In terms of scale, the effort required to develop T-MIF is not incommensurate with that which was needed to complete similar projects in the past, such as Megapie. A single research institute with existing nuclear facilities could probably even take on this task alone; ideally however two to three institutes operating in close cooperation could best develop a first prototype, thus minimising the risk and cost.